

TWO-SCALE THERMO-MECHANICAL ANALYSIS OF
MULTIDIRECTIONAL CARBON/CARBON COMPOSITES USING
IMAGE-BASED FINITE ELEMENT METHOD

A Thesis submitted

In fulfilment of the requirements for the degree of

Doctor of Philosophy

By

Mohammad Zahid

Scholar No.- DI6035



School of Engineering

Indian Institute of Technology Mandi, Mandi

Himachal Pradesh, India -175075

October 2020

© Indian Institute of Technology (IIT) Mandi, 2020

This Ph.D. work is dedicated to my Mother, Father and Teachers

Declaration by the Research Scholar

I hereby declare that the entire work embodied in this thesis is the result of investigations carried out by me in the School of Engineering, Indian Institute of Technology Mandi, under the supervision of **Dr. Rajneesh Sharma** (School of Engineering) and **Dr. Syed Abbas** (School of Basic Sciences), and that it has not been submitted elsewhere for any degree or diploma. In keeping with the general practice, due acknowledgements have been made wherever the work described is based on findings of other investigators.

Place:

Signature:

Date:

Name:

Declaration by the Research Advisors

We hereby certify that the entire work in the thesis entitled “**Two-Scale Thermo-Mechanical Analysis of Multidirectional Carbon/Carbon Composites using Image-Based Finite Element Method**” has been carried out by **Md Zahid** under our supervision in the School of Engineering, Indian Institute of Technology Mandi, and that no part of it has been submitted elsewhere for any degree or diploma. We further certify that this thesis has been prepared in conformity with the rules and regulations of the institute and has attained a standard required to award a Ph. D degree.

Signature:

Signature:

Name:

Name:

Date:

Date:

Acknowledgments

First of all, I would like to express my heartiest gratitude to my supervisors, Dr. Rajneesh Sharma (School of Engineering (SE)), and Dr. Syed Abbas (School of Basic Sciences (SBS)), IIT Mandi for their exemplary guidance, motivation, and kind support during the entire course of this programme. I also thank them a lot for giving me their valuable time and golden suggestions that helped me in the academic field and made me capable of handling the critical situations in my personal life.

I would also like to thank my doctoral committee members, Dr. Rajeev Kumar (SE), Dr. Rajesh Ghosh (SE), Dr. Vishal Singh Chauhan (SE), and Dr. Amit Jaiswal (SBS), for their support and constructive suggestions which helped me improve my work and research skills.

I am also thankful to Prof. Puneet Mahajan, IIT Delhi, for providing me with an image processing facility and his fruitful suggestions. I would also like to thank Dr. Rohini Devi (Asso. Director), Dr. R.K Jain (Tech. Director), and Dr. Atul R Bhagat (Scientist-D), ASL, DRDO Telangana for providing me the composite specimen and experimental facilities. I am also grateful to Dr. A. Ganju (Director) and Mr. Paramvir Singh (Scientist-C) SASE, DRDO, Manali, and India to provide the scanning facility.

I am also thankful to my lab mates and friends Abhilash Awasthi, Sonal Prasad, Ravi Sandal, Ashish Rehal, Sneha Das, Misbah Bashir, Farha Anjum, Kamran, Wasil, Chandar, Md. Amir, Ahmad Raza, Md. Shakir, and Md Sultan Alam for their support and making my stay joyful in the campus. Encouragement from friends of my graduation days, Nadeem, Saif (jangli), Meraj, Kashif (Chotka), Fahad, Kaify, and Shashi has always been like a positive source of energy for me and I will always remain thankful to them. I would also like to express my special thanks to my childhood friend Nuzhat Nahid (Goldy) for her continuous motivation and encouragement.

I am very grateful to my beloved wife, Hena Parween and my Son Mohammad Omar, for their love, motivation, patience, and being always there for me when I needed them the most. I am also thankful to

my in-law family members, relatives, especially my uncle Late Md. Zafaruddin, my cousin brother Arif bhaijaan, and my uncle Md Liyakat Ali for their admirable support and motivation.

I would like to express my deepest gratitude to my mother, Aqueela Begum, my father Md. Farooque, my younger brother Md. Shahid, my sweet sisters Nuzhat (Daisy) and Nikhat (Sana), for their love, motivation and support. I am also thankful to Akif Bhai, who is not less than my elder brother, for his selfless support to my family in my absence, which directly helped me in the smooth completion of my dissertation work. I am also thankful to my ustad, Qari Jahangir, my former teachers Mr. Ravi Panday, Mr. Zeeshan, Dr. Shahid Mahmood (NIT Patna) and Dr. Sikandar Azam (IIT Dhanbad), who continuously motivated me during my academic journey.

Above all, I thank Almighty Allah Subhanahu Wa Ta'ala for blessing me with all the happiness, kind people in the form of a guide, teachers, friends, family, relatives, and great opportunities and success in my life.

Mohammad Zahid

October 2020

Abstract

Carbon/Carbon (C/C) composites consist of carbon fibers and carbonaceous matrix as the main constituents. In these composites, the carbon fibers are oriented in different directions to achieve tailored properties. Two of such architectures are three-dimension hybrid (3DH) and four dimensions inplane (4DIN) C/C composites widely used in thermal protection systems in aerospace applications. These composites are very popular in the applications where the dimensional stability of structures is highly needed under severe thermo-mechanical loading conditions. Therefore, in the present study, these composites have been studied in detail using the image-based finite element method and two-scale asymptotic homogenization scheme. This includes some of the inherent geometrical imperfections directly in the finite element meshes and also accounts for the micro-structure hierarchy.

First of all, the 2D images of these composites were reconstructed using an X-ray computed tomography facility. The inherent imperfections that are primely raised during the heat treatment procedure of fabrication were explored. The inherent imperfections were categorized as voids (Micro voids and big voids), cracks (intra-bundle, matrix, and interfacial), and bundle distortions. With the help of 2D images of microstructure, a three-dimensional (3D) model of these composites was reconstructed and discretized into finite element mesh. The resulting finite element model of realistic microstructure successfully included some of the inherent imperfections such as irregularly shaped big voids and bundle distortion directly.

Further, two-scale asymptotic expansion homogenization was utilized under periodic boundary conditions to predict the effective thermo-mechanical properties such as effective thermal conductivity and effective thermal expansion coefficient. The Laser flash experiment was performed to measure the effective thermal conductivity of 3DH C/C composite in the in-plane direction up to 1000°C for the numerical model's validity. The measured TC is found in a very good agreement with predicted results that successfully validate the proposed IBFE model. The effect of interfacial debond was also incorporated in terms of effective thermal gap conductance that caused a decrease in the effective thermal conductivity of the composite. In the case of 3DH C/C composite, around 14.85% and 7.98 % reduction in the in-plane TC of the 3DH C/C composite was observed at 27°C and 1227°C respectively. However, the out-of-plane TC was reduced by 6.2 % and 2.8 % at the respective temperatures. On the other hand, TC was reduced by around 5% due to the imperfect interface for the full range of temperatures; thus, Interfacial debond shows a significant effect on the behavior of 3DH

C/C composite compared to 4DIN C/C composite. Further, it was observed that the local distribution of field variables (temperature and heat flux) is significantly affected due to the presence of imperfections. Next, the effective thermal expansion coefficients (CTEs) of these composites were studied. In the numerical predictions of effective CTEs of 4DIN C/C composite, the effect of the three interfacial conditions, namely i) perfectly bonded, ii) imperfectly bonded, and iii) completely debonded interface was included using surface-based cohesive behavior. The effective CTEs in x and z directions decreased significantly due to the imperfect interface, while opposite behavior was noticed for CTE in the y-direction. For the validation of numerical findings, effective CTEs of 4DIN C/C composite were measured experimentally in the temperature range of 200-2500 °C. The in-plane CTE varied from 0.56 to $2.66 \times 10^{-6}/^{\circ}\text{C}$. The predicted CTEs corresponding to the imperfect interface were found in very close proximity with experimental results. It was also found that interfacial damage initiates at around 247 °C with the corresponding strains of 0.008%, 0.06 %, and 0.009% in x, y, and z directions respectively.

Finally, the thermal shock resistance (TSR) of 4DIN C/C composite was predicted in terms of critical laser power density as a function of laser beam diameter using the finite element-based simulation of laser pulse irradiation technique. The temperature dependency and anisotropic behavior of material were included in the analysis. A homogenous cylindrical body was assumed as a test specimen, and shear strength as a failure criterion. The yz-plane was predicted as a critical plane. The locations near the laser beam periphery around 1.5-2 mm below the irradiated surface were observed as the critical location for shear failure. Apart from this, the temperature and shear stress distribution at critical LPD values were studied in detail. It was noticed that the TSR of 4DIN C/C composite is 10-18 times higher than that of 2D C/C composite.

The presented study concludes that the IBFE method is an effective route to include the inherent imperfections realistically into the FE analysis. The microstructural imperfections such as voids, bundle distortion, and imperfectly bonded interfaces cause a significant reduction in effective thermo-mechanical properties of multidirectional C/C composites.

Table of contents

Acknowledgment	v
Abstract	vii
Table of content	ix
I. Introduction	I
1.1 Carbon/Carbon composite	1
1.2 Classification of C/C composites	2
1.3 Multidirectional Carbon/Carbon composites.	4
1.4 Application of multidirectional C/C composites	5
1.5 Fabrication of C/C composite	5
1.6 The hierarchical microstructure of C/C composites	7
1.7 Thermo-mechanical properties of C/C composites	7
1.7.1 Analytical.	8
1.7.2 Experiments	8
1.7.3 Numerical	8
1.8 Motivation for research.	8
1.9 Layout of the thesis.	9
2. Literature survey	10
2.1 Thermal shock resistance	10
2.2 Effective thermal conductivity	12
2.3 Effective thermal expansion coefficient	17
2.4 Literature gap	20
2.5 Objective of the present study.	21
3 Image-based finite element model	22
3.1 Material reconstruction techniques	22
3.2 X-ray computed tomography	23
3.3 Material description.	24
3.4 Reconstruction of the C/C composites.	24
3.5 Morphology of 4D C/C composite.	25

3.6	Hierarchy in the C/C composite	29
3.7	Reconstruction of the 3D RVEs	30
3.8	Finite element model of multidirectional C/C composite	33
3.8.1	Reconstructed FE model of 4DIN.	33
3.8.2	Reconstructed FE model of 3DH.	37
4	Thermal conductivity of multidirectional C/C composite	41
4.1	Thermal conductivity.	41
4.2	Laser flash experiment	41
4.3	Two-scale homogenizations.	43
4.3.1	Asymptotic expansion homogenization.	43
4.3.2	Bundle level.	45
4.3.3	Composite level	46
4.3.4	Boundary conditions	47
4.4	Numerical analysis	50
4.5	Results and discussion	50
4.5.1	Microscale analysis (Effective thermal conductivity of bundles)	50
4.5.2	Effective thermal conductivity of 3DH C/C composite.	54
4.5.3	Effective thermal conductivity of 4DIN C/C composite	59
5	Thermal expansion coefficient of multidirectional C/C composite	64
5.1	Thermal expansion coefficient.	64
5.2	Experimentation.	65
5.3	Asymptotic expansion homogenization.	66
5.4	Modeling of imperfect interface	68
5.5	Numerical analysis.	70
5.5.1	Micro scale analysis (at bundle level).	70
5.5.2	Meso-scale analysis (at composite level).	73
5.6	Results and discussion	78
5.6.1	Results of 3DH C/C composite.	78
5.6.1.1	Effective properties of bundles.	78
5.6.1.2	Effective properties of 3DH C/C composite.	80
5.6.2	Results of 4DIN C/C composite	83
5.6.2.1	Effective properties of bundles.	83
5.6.2.2	Effective properties of 4DIN C/C composite.	86

6	Thermal shock resistance of 4DIN C/C composite	93
6.1	Thermal shock resistance	93
6.2	Governing equation and finite element formulation.	93
6.3	Material	96
6.4	Numerical model and thermal shock analysis.	97
6.5	Results and discussion	99
6.5.1	Critical laser power density and the critical plane	99
6.5.2	The critical time of laser irradiation	102
6.5.3	Shear stress and temperature distribution at critical laser power density.	103
7	Conclusions	107
7.1	X-ray computed tomography	107
7.2	Effective thermal conductivity	109
7.3	Effective thermal expansion coefficient.	110
7.4	Thermal shock resistance.	111
7.5	Scope for the Future	112

References

Appendix A

Appendix B

Appendix C

List of Figures

1.1	Fiber/yarn architectures of Carbon-Carbon composites	4
1.2	Different possible architectures of multidirectional C/C composite. (a) 3D orthogonal, (b) 3D in-plane woven (c) 3D orthogonal hybrid, (d) 4D in-plane (e) 4D in-plane hybrid (f) 4D in-plane woven (g) 5D-inplane and (h) 5D in-plane woven.	5
1.3	General diagram of the liquid precursor based fabrication process for C/C composite . . .	6
2.1	(a) Geometrical model of specimen (b) Boundary conditions of computations [23, 24]. .	12
3.1	Image acquisition through X-Ray computed tomography	23
3.2	(a) Projected image acquired through XCT, (b) Reconstructed 2D stack images, (c) 3D reconstructed image of microstructure of 4D C/C composite	25
3.3	Morphology of the 4DIN C/C composite	27
3.4	Hierarchical microstructure: a) homogenous at macro scale; b) heterogeneity represented by the matrix, bundle, and interface; c) distribution of the Fibers in the bundle; and d) heterogeneity represented by the matrix, Fiber, and interface	29
3.5	a) Reconstructed image of the microstructure of the multidirectional composite at 2 μ m resolution, b) Zoomed bundle cross-section and c) Zoomed intra-bundle cracks.	30
3.6	Greyscale value distribution over a 2D stack image.	31
3.7	(a) Unsegmented, (b) Segmented at threshold greyscale value of 80, and (c) Segmented at threshold greyscale value of 100.	31
3.8	((a), (b), and (c)) Cross-sectional 2D view of bundle segmentation and (d) 3D view of segmented bundles	32

3.9	(a) Segmented bundles, (b) Matrix pocket, (c) Big voids in matrix pocket, (d) Reconstructed 3D image of RVE, and (e) Discretized FE model of RVE eliminating voids.	34
3.10	(a) View from x-y plane, (b) View from the z-y plane, and (c) Opposite side of the view shown in (b).	34
3.11	Finite element models of the RVEs of the 4DIN C/C composite	35
3.12	Finite element discretization of the micro-unit cell	36
3.13	RVE of 3DH C/C composite containing big voids and bundle distortion.	38
3.14	Micro unit cells for bundles	38
3.15	FE model of (a) RVEs of 3DH C/C composite, (b) Micro unit cell for the circular bundle, and (c) Micro unit cell for the rectangular bundle.	39
4.1	Basic principle of Laser flash experiment.	42
4.2	Variation of (a) Measured thermal diffusivity and specific heat data of 3DH, (b) Calculated thermal conductivity data.	43
4.3	(a) A global heterogeneous domain (b) A local unit cell domain (c) Interface between two phases.	44
4.4	Temperature gradient as a boundary condition in (a) x-direction, (b) y-direction, and (c) z-direction and keeping other faces adiabatic.	48
4.5	Flow chart of the two-scale homogenization process	49
4.6	(a, b) Temperature profile in the transverse direction, (e, f) Temperature profile in the longitudinal direction, (c, d) Heat flux contour in the transverse direction, and (g, h) Heat flux contour in the longitudinal direction at 1500K	51
4.7	Temperature distribution in micro-unit cells at different thermal gap conductance values.	52
4.8	Variations of effective thermal conductivity of (a) Rectangular bundle and (b) Circular bundle of 3DH C/C composite.	53

4.9	Longitudinal and transverse thermal conductivity of bundles in 4DIN composite.	54
4.10	(a, b, and c) Temperature profile (d, e, and f) Heat flux contour at 1500K (g, h, and i) Heat flux contour at 300K in 3DH C/C composite (In x, y, and z direction respectively from left to right).	56
4.11	(a, b, c and d) Temperature profile and (e, f, g, and h) corresponding heat flux contour of 3DH (RVE 3C) composite unit cell at 1500K for different Thermal conductance values across the interface.	57
4.12	(a) Temperature profile in x-direction and path AF crossing the bundle/matrix interfaces and (b) Plot of temperature variation along the path A-F in RVE 3C at 1500K for different interface conditions.	58
4.13	Effective thermal conductivity of 3DH C/C composite in (a) In-plane direction and (b) Out-of-plane direction.	59
4.14	(a, b, and c) Temperature profile, (d, e and f) Heat flux contour at 1500K, and (g, h and i) Heat flux contour at 300K in 4DIN C/C composite (in x, y, and z directions respectively from left to right).	60
4.15	(a, b, c, and d) Temperature profile and (e, f, g, and h) corresponding heat flux contour of 4DIN composite unit cell at 1500K for different Thermal conductance (TC) values across the interface	61
4.16	Temperature profile in x-direction and path AF crossing the bundle/matrix interfaces and (b) Plot of temperature variation along the path AF in RVE4A at 1500K for different interface conditions	62
4.17	Effective thermal conductivity of 4DIN composite with perfect and imperfect interface in all three directions and their comparison with experimental results of [8]	62
5.1	Schematic diagram of the CTE measurement system based on the basic principle of dilatometer.	65
5.2	The variation of CTEs of 4DIN C/C composite with respect to temperature obtained through experiments.	66

5.3	(a) A global heterogeneous domain, (b) A local unit cell domain, and (c) Interface between two phases.	66
5.4	(a) Directions associated with the interface surface, (b) Traction separation law in the normal direction (pure Mode I condition), and (c) Traction separation law in tangential direction (Pure Mode II condition)	70
5.5	Micro unit cell under unit thermal load and constrained deformation BC in (a, b) Transverse and (c) Longitudinal directions	72
5.6	(a) Boundary conditions in the mesoscale analysis of 3DH C/C composite and (b) Coupling of rigid planes with the faces of RVE.	74
5.7	5.7 Boundary conditions in the mesoscale analysis of 4DIN C/C composite. Free thermal deformation in (a) x-direction, (b) y-direction, and (c) z-direction	75
5.8	Two-scale homogenization scheme for effective CTE of 4DIN C/C composite.	77
5.9	Thermal stress distribution in micro-unit cells at extremum temperatures in different directions.	79
5.10	Variation of effective CTE of bundles in 3DH C/C composite with temperature	80
5.11	Thermal deformation in (a) x-direction, (b) y-direction, and (c) z-direction of 3DH C/C composite RVE at 2227°C	80
5.12	(a) Paths (A-B and C-D) crossing different phases of RVE and variation of stress components along them in (b) x-direction, (c) y-direction, and (d) z-direction.	81
5.13	Stress distribution in 3DH C/C composite in (a, b, c) x-direction, (d, e, f) y-direction, and (g, h, i) z-direction at different temperatures.	81
5.14	(a) Localized stress concentration in the vicinity of irregularly shaped voids and (b) Uneven stress distribution in bundles due to bundle distortion imperfections	82
5.15	Variation of the effective CTEs of 3DH C/C composite with respect to temperature (Experimental [57]).	83

5.16	Thermal stress distribution in micro unit cell under unit temperature change at extremum thermal conditions (a, b, d, e) Transverse direction, (c, f) Longitudinal direction, (g, h) Longitudinal stress jump plot at the interface due to CTE mismatch at different temperatures	85
5.17	Effective CTE of bundles as a function of temperature	85
5.18	Free thermal deformation in (a, b, c) x-direction, (d, e, f) y-direction, and (g, h, i) z-direction for different interfacial conditions.	87
5.19	(a) Boundary condition applied on RVE (b) Boundary conditions contributed by oblique bundles.	87
5.20	Plot for interfacial displacement jump for three different interfacial conditions at 2227°C in (a,b) x-direction, (c,d) y-direction, and (e,f) z-direction in 4DIN C/C composite . . .	89
5.21	Cohesive surface damage variable (CSDMG) plot when RVE deform in (a) x-direction, (b) y-direction, and (c) z-direction	90
5.22	The effective thermal expansion coefficient of 4DIN C/C composite in three orthogonal directions	91
6.1	(a) Cylindrical specimen, (b) 2D approximation, (c) 2D approximated finite element model with associated loading and boundary conditions, and (d) Schematic diagram of the laser pulse irradiation technique	97
6.2	Representation of (a) xy-plane, (b) xz-plane, and (c) yz-plane by assigning different material orientations along the r and s direction of the 2D approximated model	98
6.3	(a) Shear stress contour plot in xy-plane and paths crossing the maximum stress point (b) Shear stress distribution along the path 'A-B' (c) Stress distribution along the path 'C-D'	100
6.4	(a) Maximum shear stress (τ_{xy}) Vs LPD curve and (b) Critical LPD curve	101
6.5	Critical LPD curve for 4D C/C composite associated with three orthogonal planes and their comparison with critical LPD curve for 2D laminated C/C composite (Li et.al. [24]).	102

6.6	(a) Shear stress vs time plot at the location of maximum stress and corresponding to critical LPD and (b) Critical time for different beam diameters	103
6.7	(a) Shear stress distribution and (b) Temperature distribution at critical LPD at the critical time	104
6.8	(a) Shear stress distribution in the radial direction along the path crossing critical location, (b) Shear stress distribution in the thickness direction along the path crossing critical location, and (c) Depth of critical location for different beam diameters	105
6.9	(a) Radial temperature distribution on the irradiated surface and (b) Central temperature distribution along the thickness	106

List of Tables

1.1	Carbon yield of various thermoset precursors [1].	2
2.1	Thermal conductivities of constituents [61].	17
2.2	Material properties of carbon Fiber (superscript f) and matrix (superscript m) [104].	19
3.1	Micro-CT scan parameters for C/C composite	25
3.2	Fiber volume fractions of 4D in-plane C/C composite RVEs in different directions.	35
3.3	FE description of micro-unit cells of different bundles in 4DIN C/C composite.	36
3.4	Fiber volume fractions of 3D orthogonal composite unit cells in different directions.	37
3.5	Finite element model description of micro unit cells.	39
4.1	Variations of effective thermal conductivity of bundles (of RVE3C) at 1500K with different interfacial gap conductance values.	52
4.2	Fluctuation in effective thermal conductivity of bundles in 3DH C/C composite.	54
5.1	Periodic boundary conditions [77, 119].	72
5.2	Bundle/matrix Interfacial parameters [76].	76
5.3	Mean effective elastic properties of bundles in 3DH C/C composite.	78
5.4	Mean effective elastic constants of bundles in 4DIN C/C composite.	84
6.1	Mean effective elastic constants of 4DIN C/C composite	96
6.2	specific heat of 4DIN C/C composite [130].	97

List of Abbreviations

C/C	Carbon-Carbon
FEM	Finite element method
IBFE	Image-based finite element
CTE	Coefficient of thermal expansion
TC	Thermal conductivity
ETC	Effective thermal conductivity
XCT	X-ray computed tomography
TSR	Thermal shock resistance
LPD	Laser power density
3DH	3-Dimensional hybrid
4DIN	4-Directional in-plane
FEM	Finite element method
VF	Volume fraction
AEH	Asymptotic expansion homogenization
PBC	Periodic boundary condition
RVE	Representative volume element
UC	Unit cell
FRC	Fiber reinforced composite

Chapter I

Introduction

This chapter contains a brief introduction of Carbon/Carbon (C/C) composites, their classification, and applications. The fabrication process involved in the manufacturing of these composites is also discussed for better understanding. There are many stages involved in the manufacturing of these composites that affect the evolution of microstructure. Hence, the final microstructure of these is also explored in detail. Later, the motivation and layout of the thesis are presented.

I.1 Carbon/Carbon composite

Composites are well defined in literatures as a material made by mixing two or more constituents at the microscopic level to produce materials with one or more enhanced properties than their constituents. Carbon, in the form of graphite, is the best candidate material for use at extremely elevated temperatures where inert atmosphere and ablative environment are dominant. The brittle nature of the monolithic carbon greatly limits its use at the component level. This limitation has been omitted in the recent past by the introduction of carbon in fiber form. Thus, new material has been introduced to the aerospace industry consisting of carbon fibers embedded in the carbonaceous matrix, known as Carbon/Carbon composite. This material aimed to replicate the advantages of the fiber-reinforced composites such as high specific strength, stiffness, high toughness, and high thermal resistance. Due to these enhanced properties, these composites were used during World War-II in rocket fins (Germany used polygranular synthetic graphite for the fins) [1]. Further developments of these composites have taken place slowly, and in the late 1960s, it has emerged as a new generation material. In the 1970s, the USA and European countries have extensively used these composites in military armor applications [1, 2]. There are a variety of Carbon/Carbon composites available nowadays depending on the different types of precursors used for fiber and matrix, fiber orientations, and various properties of constituents. The classification of these composites is discussed in detail below.

I.2 Classification of C/C composites

The composites can be tailored depending upon the specific requirements or needs by altering the basic physical and geometrical properties of the constituents. Therefore, there are various forms of Carbon/Carbon composites. These composites can be organized into four major categories as given below

I. Depending on the precursor used for matrix

The precursors used for the carbon matrix are broadly classified into two categories.

a. Thermosetting resin:

Thermosets are those materials that, once solidified, cannot melt upon reheating. The main advantages of the thermoset resin include easy impregnation in the fiber preforms of the composites, easy production of large structures and complex geometries, and a relatively large technological base already exists. There are numerous thermoset polymers which can be used as impregnates for C/C composites. The carbon yield of some thermoset precursors has been shown in the following Table I.I.

Table I.I Carbon yield of various thermoset precursors [1]

Precursor	Carbon yield in (%)
Phenolic resins	55-55
Furan resin	50-60
Oxidized polystyrene	55
Polyvinyl alcohol	50
Polyacrylonitrile	44
Polyvinylidene chloride	25
Cellulose	20
Epoxy resins	5
Polystyrene	5

b. Thermoplastics resin:

Unlike the thermosets, thermoplastic materials melt upon reheating. The pitches derived from the coal tar, petroleum, and polyaromatic resins are widely used as thermoplastic precursors for the carbon matrix. The main advantages of these precursors include the high yield of carbon, ease of graphitization, and lower processing cost.

2. Depending on the type of fibers used

a. The composites are generally characterized in two categories according to the length of the carbon fibers: short fiber-reinforced composite and long fiber-reinforced composite.

i. Short fiber-reinforced composite:

These are also known as discontinuous fiber-reinforced composites. The properties of these composites largely depend on the length of the fiber. Generally, the aspect ratio, i.e., a ratio of diameter to length, is kept between 1-100.

ii. Long fiber-reinforced composite:

These are also known as continuous fiber-reinforced composites. The length of the fiber extends to the component scale in these composites. The fiber is a principle load-bearing component in these composites as the load is directly transferred to fiber along the fiber axis.

b. According to the precursor material used for carbon fibers, these composites can be divided into three categories.

i. Rayon based:

Rayon is used here as a precursor for producing carbon fibers. Carbon fibers have been obtained through three heat treatment stages: namely, oxidization, carbonization, and graphitization. The properties of these fibers are generally inferior to the other two types.

ii. Polyacrylonitrile (PAN) based:

These fibers are obtained by the stabilization of the PAN structure using an oxidization process. These fibers have superior properties to those derived from rayon.

iii. Pitch based:

Another class of fibers which are derived from pitches such as coal-tar and petroleum. They are relatively low-cost and high-performance fibers.

3. Depending on the matrix impregnation route

The Matrix impregnation method has a significant effect on the properties of the composite. C/C composites can be broadly divided into three categories based on the matrix impregnation route.

i. Gas route

ii. Liquid route

iii. Combined route

4. Depending on the architecture

The long fibers are generally arranged in the form of bundles or yarns for the manufacturing of preforms of the composites. Many arrangements have been developed for the effective use of the fiber properties in the composite. These arrangements of the fiber bundles/yarns are also known as fiber architectures. Based on the arrangements of the bundles/yarns, C/C composites can be broadly divided into the following three broad categories [3].

i. One-dimensional (Unidirectional or Linear)

ii. Two-dimensional (Bidirectional or planer)

iii. Three dimensional (Multidirectional)

These three categories of composites are further subclassified based on the type of interlocking of fiber/yarn in the preform as shown in Fig. I.1.

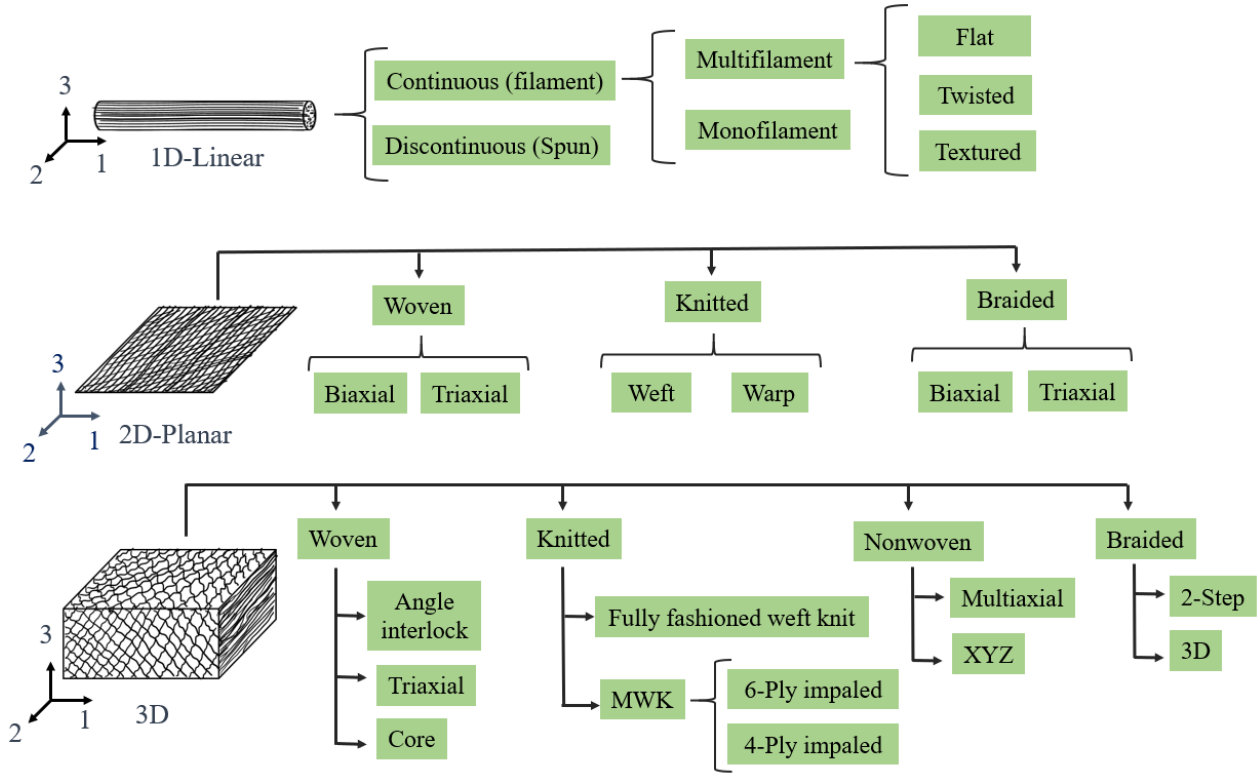


Fig. I.1 Fiber/yarn architectures of Carbon-Carbon composites.

I.3 Multidirectional Carbon/Carbon composites

In a composite, the fibers are the principal load-carrying elements and can be oriented in different directions to provide the specific needs of resistance in different directions. In aerospace industries, 2D preform reinforcements are generally adopted for the components under simple mechanical loading conditions [1]. But, under complex thermomechanical loading conditions (e.g., conditions at the time of re-entry), 2D architected C/C composites become the inappropriate choice due to their incapability to sustain the severe load in out of plane direction [1]. This limitation of 2D-composite has been overcome by introducing the reinforcement in the third (out of plane) direction, which finally constitutes a 3D architecture of reinforcement [2]. This is the simplest form of the multidirectional composite. In 3D composite, the fibers in the forms of yarns or bundles are oriented in three orthogonal directions, as shown in Fig. I.2 (a). The weaving of this architecture makes it possible to form fabric preforms, as shown in Fig. I.2 (b). 3D weaved architecture of the composite is also

known as 3D inplane woven composite. The most commonly used other multidirectional composites in the aerospace industry are presented in Fig I.2.

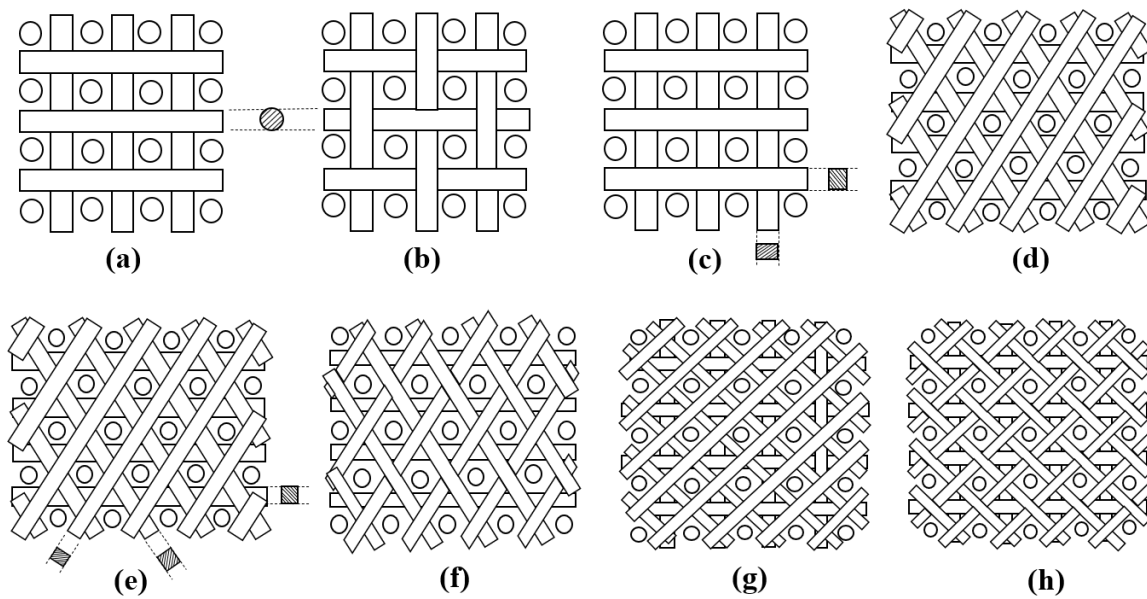


Fig. I.2 Different possible architectures of multidirectional C/C composite. (a) 3D orthogonal, (b) 3D inplane woven (c) 3D orthogonal hybrid, (d) 4D inplane (e) 4D inplane hybrid (f) 4D inplane woven (g) 5D-inplane and (h) 5D inplane woven.

I.4 Application of multidirectional C/C composites

Due to the high performance of these composites under extreme loading environments, they are widely used in the aerospace industry, automobile sectors, power generation industries, high-temperature glass and ceramic industries etc. [2, 4]. The following are some of the major applications of these composites.

- a. Braking pads
- b. Rocket nose cones
- c. Rocket motor throats
- d. Heat shields of re-entry shuttles
- e. Glass industry for guides, push-out pads, and transfer pads
- f. Hot dies and high-temperature furnace filaments
- g. Biomedical implants such as knee ligaments, ankles, and hip joints

I.5 Fabrication of C/C composites

The C/C composites are manufactured in three ways depending on the matrix impregnation [1, 2]. Generally, the preforms of the carbon fibers are first prepared in the desired shape and size, and then the matrix is impregnated in the fibers preforms. There are generally three ways of matrix impregnation.

- a. Liquid phase route
- b. Gas-phase route
- c. Combined route

In the gas-phase route, the chemical vapor infiltration or densification techniques are generally utilized. This method is the most suitable when the structure or component is thin. In contrast, the liquid phase route is more popular and generally used in industrial manufacturing. The thickness of the components is not an issue in this impregnation method. Sometimes, the liquid phase route is followed by the gas-phase impregnation or vice versa to achieve more densification. The most commonly used precursors in the liquid phase route are coal-tar, petroleum pitches, and high char-yielding thermoset resins.

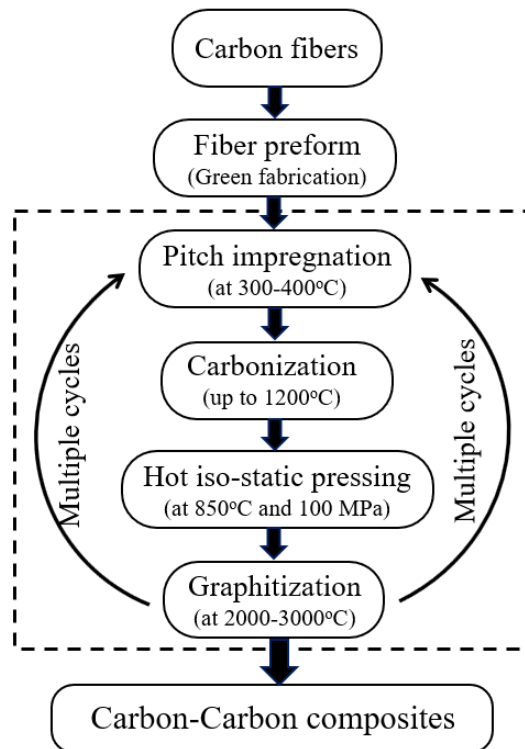


Fig. I.3 General diagram of the liquid precursor based fabrication process for the C/C composite.

Fig. I.3 shows the flow chart of the C/C composite manufacturing process [4]. Firstly, the preforms of the fibers are made according to the desired architecture and volume fraction. This process is also called green fabrication. Next, the desired liquid precursor is impregnated into the fibers' preforms at a temperature ranging between 300–450°C. In the third step, carbonization of the liquid phase is carried out at a temperature around 1200°C under high pressure. The pressure affects the yielding of the carbon in the matrix [1]. It has been observed in other studies that the grains are coarser and isotropic due to higher pressure during carbonization. The last process is the graphitization of the carbon preforms. This is achieved by applying high temperatures in the range of 2000–3000°C at the same pressure. This whole process is known as a graphitization cycle. As there are many voids left in the composite after one cycle, the fabrication process starting from the liquid impregnation

up to the graphitization is repeated to get the required degree of the densification. The final microstructure of the composite has been discussed in detail in the next section.

I.6 The hierarchical microstructure of C/C composites

Multi-directional fiber-reinforced composites are generally made of fiber in the form of bundles embedded in the matrix in more than two directions. Therefore, the typical micro-structure at the mesoscale consists of fiber bundles, matrix, the interface between matrix/bundles, and imperfections. These imperfections at this scale consist of matrix cracks, voids in the matrix, interfacial cracking, misalignment, and distortions of the bundles [5, 6]. The porosity in the C/C composites is generally due to the cavities remaining during the matrix's impregnation or introduced by the generation of gases during the graphitization process. On the other hand, the micro-cracks in the matrix and at the interface originated due to the shrinkage or differential thermal stresses produced during the manufacturing process. Although several cycles of infiltrations have been used to achieve the dense material, the micro-cracks and porosity are unavoidable in the C/C composites.

Apart from this, the bundles consist of fibers embedded in the same matrix. This arrangement of fibers in the matrix produces a unidirectional composite. Imperfections like micro-cracks, porosity, and fiber misalignment preexist at this scale. They are generally referred to as local imperfections or intra-bundle defects. These hierarchical microstructures present at these two-scales affect the thermo-mechanical behavior of C/C composites. The presence of defects like voids and cracks reduces composite strength and sometimes enables crack propagation due to stress concentration. The effect of these defects on the thermo-mechanical behavior of these composites has been explored in the present study using X-ray tomography and reconstruction techniques.

I.7 Thermo-mechanical properties of C/C composites

The excellent thermo-mechanical properties like specific strength (strength/density), toughness, specific modulus (modulus/density), specific thermal conductivity (thermal conductivity/density), low thermal expansion coefficient, and resistance to thermal shocks have been reported for C/C composites [1]. These remarkable properties make the C/C composites the most advanced form of carbon compared to conventional graphite. The thermo-mechanical properties, along with inherent reactivity to oxygen, make these composites an extraordinary candidate for aerospace applications like turbine components and heat shields to resist high temperatures for long durations. There are many variables, such as selecting the fibers, fabrication of green forms, matrix precursor, densification methods, number of cycles, etc. involved in achieving these properties [4]. Therefore, these properties of the C/C composites have always appealed to the interest of researchers in the past to carry out the investigations experimentally, analytically, or through numerical simulations.

1.7.1 Analytical

The different approaches, such as the strength of the material, theory of elasticity, bounding methods, self-consistent models or Eshelby method, and semi-empirical relations, usually come under this category. These methods are mostly based on the assumption of perfect bonding at the interface and can be applied to only limited problems that make it inappropriate for complex architected composite.

1.7.2 Experiments

Mostly reported experiments are Laser flash experiments, Dilatometry, Quenching tests, laser irradiation tests, etc. at the room and elevated temperatures. These tests have been conducted to characterize the behavior of the composite under thermal, thermo-mechanical, and thermal shock kind of loading conditions. The experimental studies are destructive, more expensive, and require highly experienced and skilled individuals. It is also challenging to determine the properties at elevated temperatures for the multidirectional composites through experiments. However, the experiments are necessary for the validation of numerical and analytical solutions.

1.7.3 Numerical

In contrast, the numerical methods are the most efficient tools to simulate the complex microstructures and boundary conditions of any material. Numerical techniques such as finite difference, finite volume, spring lattices, boundary element method, finite element method (FEM), extended finite element method, etc. are the tools generally utilized by various researchers to handle the complexity of the problems. FEMs in which the micro and macro geometrical complexities of a composite can be directly incorporated have been utilized in the present study. Also, the asymptotic homogenization technique has made much advancement in the last decade to predict the homogenized properties of heterogeneous materials. In this approach, a representative volume element (RVE) or unit cell is analyzed by applying the periodic boundary conditions to evaluate the effective or homogenous properties. This method is discussed in detail in chapter-4.

1.8 Motivation for research

During the re-entry into the atmosphere, the missiles nose-tips experience a severe aero-thermal environment. A special thermal barrier is provided at the nose cone to protect the critical components and vehicle from the high-temperature exposure [3]. The material used in the nose cone of the re-entry vehicle structure (RVS) generally contains carbon phenolic and C/C composites. The failure analysis of these materials under high temperatures is always an active area of the research. These materials are generally studied by simple experiments at the laboratory level. For the component scale thermomechanical analysis, an accurate and multi-

scale numerical model is needed, which can predict the overall damage and degradation in thermo-mechanical properties due to high temperature.

As discussed earlier that thermo-mechanical properties of C/C composite are of the main interest of the aerospace industry. These properties are greatly affected by the different processing and manufacturing variables. Some of these factors were investigated by various researchers in the past using idealized unit cell analysis. The hierarchical microstructure of the multi-directional composites has rarely been given any attention. In the recent past, some researchers have explored the material microstructure including the inherent defects such as cracks, voids, bundle misalignment, etc. using X-ray tomography. The motivation of the present research is the assimilation of the hierarchical microstructure along with micro defects in FEM for the study of the thermo-mechanical properties of commercially available multidirectional C/C composites.

I.9 Layout of the thesis

In the present thesis, the material microstructure of the multi-directional C/C composites has been reconstructed using the X-ray tomography. Two-scale homogenization has been performed for the prediction of the thermo-mechanical properties. Previous studies were explored in the discussed areas and they are presented in chapter 2. Chapter 3 covers the development of an Image-based FE model. Chapter 4 and chapter 5 contain the thermo-mechanical characterization of C/C composite. Finally, the applications of these properties to determine the thermal shock resistance have been presented in chapter 6. The study is concluded in chapter 7.

Chapter 2

Literature survey

In this chapter, a brief review of existing studies on the characterization of thermal, thermo-mechanical, and thermal shock behavior of C/C composites are presented. The literature review is briefed into three separate sections. In each of these sections, the work done by the researchers is classified as experimental, analytical, and numerical. The chapter ends with the findings of the research gaps in the existing literature and the objectives of the present study.

2.1 Thermal shock resistance

It is well known that C/C composites are the most popular materials for the aerospace industry that utilizes such composites to manufacture spacecraft's components such as rocket nozzles, nose cone for re-entry vehicle, heat shields, disc brakes, etc. [1]. These components fail mostly due to the thermal stresses induced under sudden exposure to a high-temperature or thermal shock type of loading [2]. Therefore, the exploration of material behavior under thermal shock type of loading is one of the most important research areas. In the last few decades, researchers have shown their interest to explore the thermal shock resistance (TSR) behavior of composites that belongs to the ceramic family through theoretical [7-11], experimental [13-26], and numerical [27-30] studies.

In the theoretical investigation, Kingery [7] found that the thermal shock resistance (TSR) of ceramic materials depends on the factors such as geometry of the sample, material strength, material properties, and heat transfer rate. Based on the heat transfer rate, Kingery [7] proposed two TSR parameters, R and R' as follows.

For an infinite rate of heat transfer:

$$R = \frac{\sigma_t(1-\nu)}{E\alpha} \quad (2.1)$$

For a finite rate of heat transfer:

$$R' = \frac{k\sigma_t(1-\nu)}{E\alpha} = kR \quad (2.2)$$

Where R and R' are the thermal shock resistance parameters (also termed as material index parameters), σ_t is the strength, k is the thermal conductivity (TC), E is the young's modulus, α is the coefficient of thermal expansion (CTE), and ν is the Poisson's ratio. These parameters of the materials are generally obtained through experiments [8]. Lu and Fleck [9] have discussed the dependency of Biot number (Bi) (which is the indication of a high rate of heat transfer) and material porosity on the TSR of solids in detail. Lu and Fleck [9] suggested two TSR parameters based on the value of 'Bi' given as.

For an infinite rate of heat transfer($Bi = \infty$):
$$R = \frac{\sigma_t}{E\alpha} \quad (2.3)$$

For infinite rate of heat transfer($Bi < 1$):
$$R' = \frac{k\sigma_t}{E\alpha} \quad (2.4)$$

The parameter R and R' defines the resistance against crack initiation rather than crack propagation. Deng et al. [8] used the equation (2.4) to obtained the TSR parameter for carbon felt reinforced C/C composite. Later, Hasselman [10, 11] introduced two different thermal shock parameters in unified form for crack initiation and propagation by combining the thermoelastic and fracture mechanics approaches. In later studies [12, 27], it was found that the above discussed theoretical TSR parameters (equation (2.1)-(2.4)) are well valid for monolithic and isotropic materials possessing temperature-independent material properties only.

Conventionally, the thermal shock test of ceramics and composites was carried out through arc discharge [13], direct electric current [14], and quenching of heated specimens in different quenching media [15- 20]. The direct electric current heating method [14] is more appropriate for the materials having pores and flaws where failure originates at a flaw (rather than the outer edge of the disc sample as in [13]). Li et al. [15] observed that the coefficient of thermal expansion (CTE) is the most critical factor among all that are used to determine the thermal shock resistance of ceramics. Wang et al. [17] concluded that the composite's failure due to thermal shock is not catastrophic as in the monolithic ceramics through the water quenching test of 2D woven C/SiC composite. Yin et al. [19] observed that around 83% strength of 3D C/SiC composite was retained even after 50 cycles of the thermal shock of 1000°C through air quenching. In similar testing, Leanos et al. [20] found that the compressive stiffness of 2D C/C composite decreases with the peak temperature of thermal shock, and composite fails mostly in shear and interfacial debonding.

In quenching techniques, thermal shock resistance is measured in terms of relative degradation of strength due to the shock and the critical temperature difference that can be sustained without fracture. Also, the heat transfer mechanism is highly unstable; thus, it makes the measurement of temperature distribution in the material and the evaluation of damage mechanisms are very difficult. This difficulty has been overcome by an alternate experimental technique called the laser irradiation method, which many researchers have used to measure the *TSR* of the composites [21-26]. Thermal shock strength of several ceramic materials, including pyrolytic graphite, was measured by Benz et al. [21] through photon, proton, and electron beam irradiation techniques and considering a new measure of shock strength as $\phi\sqrt{t}$ (The damage threshold). Here ϕ is the flux density, and t is the pulse duration. Qi et al. [22] have investigated the thermal shock resistant capability of the ceramic coating through the CO₂ laser irradiation technique. The critical power density of the laser was set as a new measure of thermal shock resistance that is nothing but a laser power density at which the first crack is observed. Critical power density also varies with the diameter of the laser pulse beam. The same CO₂ laser irradiation technique was utilized by Amada et al. [23] and Li et al. [24] to measure the thermal shock resistance of 2D C/C composites in terms of critical laser power density and laser beam diameter. Kim et al. [25, 26] utilized

the CO₂ laser irradiation technique along with the analytical formulation of (Sato et al. [13]) to evaluate thermal shock resistance and thermal shock fracture toughness of graphite that are obtained in the range of 22.1-23 W/mm and 20.6-22.3 W/mm^{0.5} respectively. Amada et al. [23] and Li et al. [24] has obtained a critical power density curve through finite element simulation of laser irradiation experiment that was found to be in good agreement with experimental findings. The geometrical model and boundary conditions used in the finite element simulation are presented in Figs 2.1 (a) and (b), respectively. The application of the numerical framework of finite element method has also been found for other materials such as; Wang et al. [27] evaluated the thermal shock resistance of fiber-reinforced SiC/Borosilicate laminated composite, Li et al. [28] predicted the thermal shock resistance of porous ceramics, Burlayenco [29] studied the thermomechanical behavior and crack propagation of functionally graded material under thermal shock loading, and Hennberg et al. [30] explored the damage growth in refractory material under thermal shock.

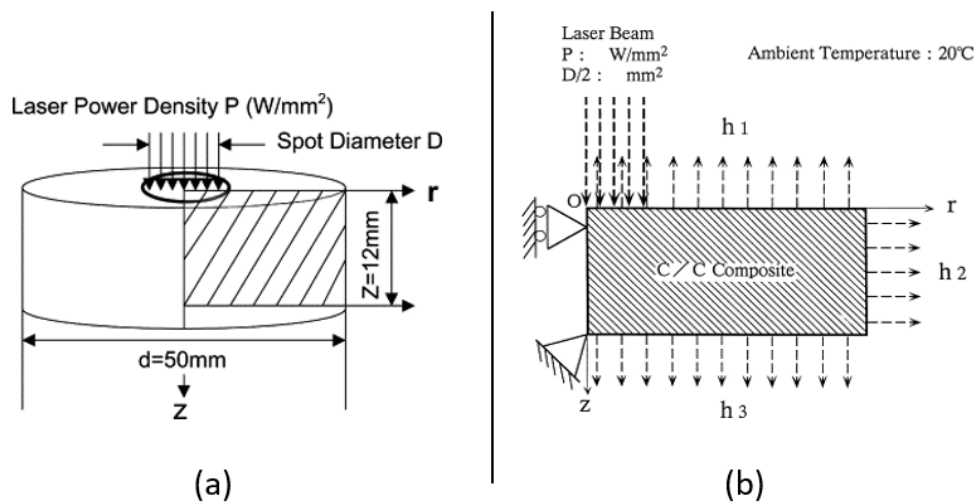


Fig 2.1 (a) Geometrical model of specimen (b) Boundary conditions of computations [23, 24]

It has been noticed through these studies that the microstructure of composite plays a vital role [26-27,30] in the crack development and propagation under the thermal shock. Also, it has been reported that the thermomechanical properties (i.e., thermal conductivity and coefficient of thermal expansion (CTE)) of the composites also affect the performance of the material behavior, especially at high-temperature gradients [16-21, 30].

Since the composites are produced in various forms depending on their basic constituents, these properties were studied in detail one by one for C/C composites in next sections.

2.2 Effective thermal conductivity

As discussed earlier, the thermal conductivity of the materials plays a vital role in high-temperature applications. In the case of composites, the properties are characterized in an apparent/effective manner, and

these depend on the various parameters of their constituent materials (matrix and fibers) such as type of precursor, fabrications process, heat treatment temperature, morphology, volume fraction/orientations of the fibers, etc. Thus, it has been a challenging task for researchers to develop a method that can yield accurate effective thermal conductivity of multiphase composite materials, including all the affecting parameters. In the last few decades, several experimental [31-38], analytical [39-54], and numerical [55-66] methods have been developed due to this challenge. The experimental studies have primarily focused on the measurement of thermal properties like thermal diffusivity (TD), specific heat (SH), and thermal conductivity (TC). Whittakar et al. [31] measured the thermal diffusivity of unidirectional and bidirectional C/C composite in the temperature range of 500-3000K using the Laser Flash method. They concluded that TD of both architectures decreases with temperature and increases with an increasing number of densification cycles. The data of the TD from experiments was further used in another work of Whittakar et al. [32] for the reverse estimation of the constituent's thermal properties. Luo et al. [33] studied the effect of preform architecture as well as matrix morphology on the TC of the C/C composites. The composites with rough laminar pyrocarbon (PyC) structure was found to possess higher thermal conductivity as compared to the smooth laminar PyC structure. Manocha et al. [34, 35] discussed the dependency of matrix microstructures on the thermophysical properties of the C/C composites with the help of the phonon interaction mechanism. It was concluded that the degree of the orientation of graphite around the fibers directly affects the thermal conductivity of the C/C composites, i.e., composites with highly oriented graphite possess high thermal conductivity.

Bhatt et al. [36] found that oxidation and gaseous conduction at the debonded interface has a negligible effect on longitudinal TC of UD composite and decreases the transverse TD by a factor of 2. He also concluded that 90% of the heat across the interface is transferred through gaseous conduction; thus, significantly affecting the transverse TC of composite even at 300°C. Farhan et al. [37] measured the TD of the 4D architecture of C/C composite up to 1250°C using the Laser Flash method. They found that TD in all three orthogonal directions is almost the same and the volume fraction of the bundles is the major factor for the change in TD in any direction. Kumar et al. [38] measured the TD of 3D orthogonal C/SiC composite up to 1200°C in three orthogonal directions using the Laser Flash experiment. It was concluded that micropores present at the interface adversely affect the thermal property of the composite at low temperatures. However, the radiation dominates the heat transfer through pores at high temperatures.

Alternately, many researchers have developed analytical models based on either analogy techniques such as shear force analogy [39], thermo-electrical analogy [40-43], or micro-mechanics approach [44-53]. Springer et al. [39] compared the two analogical techniques (shear loading analogy and electrical analogy) to predict the effective thermal conductivity of the unidirectional fibrous composite. It was found that the thermal analogy model under predicts the effective TC of composites as compared to the shear analogy model for the fiber volume fractions higher than 75%. It was further noticed that the square arrangement of the filaments with circular cross-section yields more accurate results as compared to the hexagonal arrangement of the same filaments. Zou et al. [40] developed an analytical expression for the transverse effective thermal conductivity of

the unidirectional cylindrical fibrous composite using a unit cell model that included the effect of the thermal barrier resistance at the interface. In another study, the thermal-electrical analogy approach was used for the unit cell model by Dasgupta and Aggrawal [41]. They have predicted the effective thermal conductivity of woven composite in inplane and out-of-plane directions. Ning and Chou [42] used a similar approach to the development of a micromechanics-based model. They have evaluated the inplane (in the warp and fill direction) effective thermal conductivities of the woven fabric composite. Kulkarni and Brady [43] used a thermal-electrical analogy approach to calculate the global effective thermal conductivity of laminated composite composed of angle lamina. Firstly, longitudinal and transverse TC's of each lamina were evaluated by the rule of mixture and Char's model, respectively. Then, the overall TC of the composite was obtained using the electrical analogy. The effects of the volume fraction (varied from 0 to 50%) and the ratio of TCs of the constituents (varied from 2 to 1000) were discussed in the study. Benveniste and Miloh [44] developed an analytical model for effective TC of composite, where the reinforcement was considered as spherical inclusion. The effect of thermal boundary resistance as temperature discontinuity at the interface has been included in the model. This model is valid for the dilute concentration of the inclusions only. Benveniste [45] used two micromechanics-based models (Mori-Tanaka and Generalized Self-Consistent) to overcome this limitation. The expressions for effective TC of the particulate composite were derived, including the effect of thermal contact resistance. Hatta and Taya [46] used the equivalent inclusion method to derive the analytical expression for the effective thermal conductivity of coated filler composite. The effects of the coating thickness, coating conductivity, and filler volume fraction were discussed in their study. It was found that ETC of the composite could be enhanced with highly conductive fillers. Similarly, Hasselman and Johnson [47] developed an analytical model for the thermal conductivity of unidirectional composite, including thermal barrier resistance at the fiber-matrix interface. This formulation is valid for isotropic constituents and diluted concentrations of fiber (i.e., <50% and no mutual interaction between inclusions). The same author further used the model for orthotropic fiber in an isotropic matrix [48]. In this study, the proposed model and experimental data were utilized to calculate the interfacial heat transfer coefficient through reverse calculation. Benveniste et al. [49] derived an expression for effective thermal conductivity of composite that contains coated fibers based on the Mori Tanaka mean-field approach. The fibers are considered to be transversely isotropic cylindrical inclusions in the matrix. In another study, Lee et al. [50] have included the effect of interfacial contact conductance in his analytical model to predict the effective TC of the particulate and fibrous composite. Here, the interface was assumed to be a thin coat around the inclusion. Similarly, Sejnoha and Zeman [51] analyzed the imperfect textile composite, including the geometrical and material imperfections using the Mori-Tanaka approach. Vorel and Sejnoha [52] used the analytical formulation based on the same approach to evaluate the homogenized thermal conductivity of imperfect 2D C/C textile composite. Schuster [53] found that the out-of-plane TC of 3D orthogonal composite depends on TC of adjoining materials and needled fiber density. A modification in the simple rule of the mixture was done in this study by introducing two parameters corresponding to the influence of TC of adjoining material and needled fiber density. The modified analytical model was found to

yield accurate results when compared with the experimental values. It is also concluded that out-of-plane TC can be enhanced by the factor of 8 with the addition of 6% of needled fiber. Feng et al. [54] developed another analytical model based on an equivalent circuit approach to predict the transverse thermal conductivity (TTC) of unidirectional fiber-reinforced composites (FRC). The effects of interface thickness and porosity fraction at the interface and composite region was concluded in the study. It was found that the TTC of the composite is adversely affected by these parameters.

Most of the analytical models are generally confined to simple geometries. They are unable to directly model the complex microstructural features such as the orientation of fibers in multi-directions, imperfections, defects, etc. Despite these limitations, the analytical models are useful to obtain the constituent's thermal properties [32] and interfacial conductance [36, 48] using reverse calculations that are sometimes difficult to obtain directly using experiments.

The numerical technique, like the finite element method, has proven to be the most cost-effective alternative for predicting the thermal behavior of complex structured composites. FEM was used by many researchers to study the thermal conductivity of different architectures of C/C composites such as the unidirectional [55-57], 2D-woven and laminated composites [58, 59], 3D orthogonal [60, 61], and multidirectional braided composites [62-66].

Islam and Permila [55] predicted the effective transverse thermal conductivity of unidirectional composite using FEM. Klett et al. [56] performed a steady-state heat transfer finite element analysis on two types of unidirectional C/C composite at two different temperatures. Their study concluded the effects of fiber morphology, matrix morphology, and imperfections (pores, voids, and interfacial debond) on the thermal conductivity of the composite. Grujicic et al. [57] extended the work of Klett et al. [56] by performing the 3D finite element, steady-state heat transfer analysis. This study included the effects of gaseous heat conduction and radiation heat transfer across the voids, cracks, and interfacial gap. Apart from this, the effects of fiber volume fractions and porosity levels on effective thermal conductivity were also discussed. It was found in the study that the imperfections mostly affect the transverse thermal conductivity of composite and have a negligible effect in the longitudinal direction. Puglia et al. [58] included the major manufacturing imperfections in a two-scale finite element study for the effective thermal conductivity of the 2D laminated composite. The computer-aided design (CAD) based idealized unit cells were used in the study. It was found that the matrix cracking is a dominating factor in the reduction of in-plane effective thermal conductivity. The thermal conductivity of 2D woven fabric in the thickness direction was predicted by Siddiqui and sun [59] using finite element based unit cell analysis that includes the fiber yarns as reinforcement in the air (as a matrix). The TC in the thickness direction increased with the temperature rise and an increase in the fiber volume fractions. Alghamdi et al. [60] calculated the thermal conductivity of 3D orthogonal C-SiC composite using the finite element method. They have considered four types of porosity defects at different levels of length scales. They concluded that the large voids in the matrix significantly degraded the thermal properties of 3D C-SiC composites. Shigang et al. [61] predicted the effective thermal conductivity of 3D hybrid C/C composite up to 2500K using finite element based two-scale

analysis. The idealized CAD-based model of composite unit cells was used in the study. The temperature-dependent thermal conductivity of PAN-based carbon fiber and carbon matrix reported in this study are listed in Table 2.1. In another study, the effective thermal conductivities of 3D braided C/C composite was measured by Liu et al. [62] through FEM. The effect of the braiding angle of the fiber reinforcement was studied. It was concluded that the transverse TC increases with an increase in braided angle, whereas the longitudinal TC has the opposite effect. Jiang et al. [63] made a similar observation regarding the effect of braiding angle on effective TC of 3D braided composite using FE based sub-unit cell model. Lu et al. [64] investigated the effect of interfacial property on thermophysical properties (TC and CTE) of 3-dimensional 4-directional (3D4D) and 3-dimensional 5-directional (3D5D) braided composites performing multiscale 3D finite element analysis under periodic and non-adiabatic boundary conditions. In this study, a suitable TC and CTE of 0.1 μm thick yarn/matrix interface were obtained with the help of experimental results. It was concluded that interfacial properties have an obvious effect on effective transverse TC of 3D4D composite. However, effective transverse TC of 3D5D composite shows sensitivity only for the interfacial conductivity less than 0.4325W/mK.

Table 2.1 Thermal conductivities of constituents [61]

Temperature (K)	Longitudinal TC of fiber (W/mK)	Transverse TC of fiber (assumed) (W/mK)	TC of matrix (W/mK)
300	202.4	20.24	150.5
500	197.1	19.71	118.5
700	191.8	19.18	88.4
900	186.5	18.65	73.6
1100	183.4	18.34	63.9
1300	175.3	17.53	56.7
1500	166.7	16.67	51.2

Inplane and out-of-plane effective thermal conductivity of 3D braided and 2.5D knitted C/C composite was obtained by Dong et al. [65, 66]. Sequential two-scale FE unit cell analysis was performed under periodic temperature boundary conditions. Based on experimental validation, it was concluded that the equivalent gap conductance value of $1.5 \times 10^5 \text{ W/m}^2\text{K}$ was appropriate for the modeling of imperfect interfaces at two-scale levels. Besides, behavior of 3D braided C/C composite was reported to be transversely isotropic with higher out-of-plane TC than that of in-plane components. Almost all the numerical studies discussed utilized the idealized CAD-based model of the microstructure, ignoring the imperfections (such as irregular shaped voids, bundle distortion and misalignment, cross-sectional warping, etc.).

Recently, the irregular shaped voids in the composite have been included through equivalent ellipsoids using principal component analysis by Tsukrov et al. [67] and Piat et al. [68]. Simultaneously, many researchers [6,

69-74] have utilized X-ray computed tomography (XCT) to explore the inherent microstructure of the C/C composites. In recent past, a comparatively new approach has been developed by different researchers [75-79] that included the inherent imperfections of the material microstructure directly in the geometry based on the tomographs obtained through XCT. This approach is also known as an image-based finite element (IBFE). IBFE was used for the mechanical characterization of 3DH and 4DIN C/C composite by Sharma et al. [76-79], unidirectional C/C composite by Qi et al. [80], and 2D woven C/C composite by Ali et al. [81]. This technique was also utilized for the estimations of effective thermal conductivities of 2D woven C/C composite by Alghamdi et al. [82]. IBFE technique is able to include the realistic inherent imperfection of C/C composites and architectural complexities into the numerical models. However, this technique has yet to be tested for the thermo-mechanical characterization of complex architected C/C composites.

Next, the literature review on the study of the thermal expansion behavior of C/C composites is reported in the next section.

2.3 Effective thermal expansion coefficient

The thermal expansion coefficient is the second most important property of high thermal application composite materials. Low CTE of the composite materials assures the thermal stability of a structure under severe thermal loading conditions. At extreme conditions, the failure of the composite structure generally occurs due to the mismatch of the CTE of constituents at the interfacial [1-3]. Thus, the detailed study of the thermal expansion behavior is essential for the efficient design of composite structures used at elevated temperatures. In the last few decades, various studies covering experimental [33-34, 37-38, 83-85], analytical [86-95], and numerical [96-110] are reported on the development of an efficient methodology to estimate the effective CTE of composite materials. Luo et al. [33] studied the effect of three different preform architectures of C/C composite using experiments. They concluded that the slope of the variation of CTEs with respect to temperature is almost similar for all.

Manocha et al. [34] discussed the effect of carbon fibers as well as the graphitic orientation on CTE of C/C composites. It was found that the composite with high strength fiber (PAN-T300) and highly oriented graphitic matrix possess the lowest CTE ($-0.85 \times 10^{-6}/^{\circ}\text{C}$). Farhan et al. [37] measured the effective CTE of 4D in-plane (4DIN) C/C composite in inplane and out-of-plane directions. It was reported that the CTE in all three orthogonal directions is nearly the same and is around $1.8 \times 10^{-6}/^{\circ}\text{C}$ at 1250°C . Kumar et al. [38, 83] have studied the CTE of 3D orthogonal and 3D stitched C/SiC composites. It was found that the effective CTE varied between 0.5 to $4 \times 10^{-6}/^{\circ}\text{C}$ for temperature range 25 - 1050°C . An inverse effect of siliconization temperature was observed in the case of out-of-plane CTE of 3D stitched C/C composite. At the same time, the in-plane CTE has a negligible dependency on siliconization temperature. Liao et al. [84] concluded through the experimental study on the 2D and 3D stitched C/C composites that the effective behavior of CTE of these composites greatly depends on the architecture, temperature, heat treatment, and porosity. Effective CTEs of

2D and 3D composites were found to vary from -1.5×10^{-6} to $4.3211 \times 10^{-6}/^{\circ}\text{C}$ for a temperature range of 25-1300°C. Wang et al. [85] discussed the effect of heat treatment temperature on the CTE of the C/C composite by varying the graphitization temperature from 850 to 2500°C.

Among analytical studies, the simplest upper bound approximation for effective CTE of composite with two isotropic phases was given by Voigt [86] and Reuss [87] based on uniform strain and uniform stress concept, respectively. These models are also termed as Rules of the mixture. Voigt model gives reasonable results in the longitudinal direction for unidirectional composite, whereas the Reuss approximation is poor because of the existence of interfacial stress due to CTE mismatch [99]. Turner [88] accounted for the mechanical interaction between phases resulting in a lower bound approximation of effective CTE. Based on the elastic energy principle, Schapery [89] and Levin [90] developed an analytical model for longitudinal and transverse effective CTE of a unidirectional composite consisting of isotropic constituents. In the Schapery's model [89], the expression for longitudinal CTE is similar to the Voigt model with some modifications. Further, the transversely isotropic behavior of fibers has been included in the model by Chamis [91] and Chamberlain [92]. The expression for longitudinal CTE in both of these models is the same as Schapery's model. Chamberlain [92] also included the effect of the square and hexagonal packing of fibers into his model. Rosen and Hashin [93] further extended Levin's work for the multiphase composite, preserving constituents' anisotropy using a thermo-elastic energy-based approach. This model was then simplified for unidirectional composite with transversely isotropic constituents by Hashin [94]. Gowayed et al. [95] included the effect of voids and interfacial coating (considering it as a third phase) on effective CTE of a unidirectional composite. Again, It is observed from the literature that the analytical studies are confined to very simple geometry.

The finite element based numerical model is one of the most effective alternatives to study the thermal expansion behavior of the complex architecture composites. Many researchers adopted this technique to calculate the effective CTE of different composites such as unidirectional [96-101], 2D woven [102-103], 3D orthogonal [104-105], and multidirectional braided [64, 106-110] composites. Bowles and Tompkin [96] investigated the effective CTE of unidirectional composites using FEM on the periodic 2D unit cell model for square and hexagonal packing. It was found that the fiber properties are significantly responsible for longitudinal CTE, while matrix properties play the leading role for transverse CTE of composites. Islam et al. [97] used a 2D unit cell model with periodic boundary conditions to predict the transverse CTE of unidirectional composite along with the effect of partial interfacial crack. A significant effect of interfacial cracks was observed on the transverse CTE of the composite. Karch C [98] obtained the effective CTE of UD composite through FEM using three different approaches characterized by different boundary conditions, i.e., periodic, the plane remains plane and displacement boundary condition. All three approaches gave almost similar results, and the periodic boundary condition was found to consume more computational time than the other two. Karadeniz et al. [99] developed a quarter 3D unit cell model of a unidirectional composite to predict the effective CTE. The predicted results were compared with various analytical models. In this study, an over-constrained condition, i.e., plane remain plane, has been imposed. Also, a similar constrained condition has been used by Ran et al. [100] for

unidirectional composite and Shigang et al. [I04] for 3D orthogonal C/C composite. The effective thermo-mechanical properties of PAN-based carbon fiber and carbon matrix are given in Table 2.2. Dong et al. [I01-I02] used periodic displacement and temperature boundary conditions on unit cell analysis to predict the effective CTE of unidirectional and plain-woven composite, respectively. They concluded that such boundary conditions have the ability to include thermal to mechanical coupling in the analysis. The asymptotic expansion homogenization (AEH) approach along with finite element analysis, was utilized by different researchers such as Dasgupta et al. [I03] for woven fabric composite, Nasution et al. [I05] for 3D textile, and Zhai et al. [I06] for 3D braided composite. Zhai et al. [I06] found a particular angle of braiding yarn for which composite possesses zero effective CTE.

Table 2.2 Material properties of carbon fiber (superscript f) and matrix (superscript m) [I04]

Temp (°C)	E_L^f (GPa)	E_T^f (GPa)	G_{LT}^f (GPa)	G_{TT}^f (GPa)	ν_{LT}^f	ν_{TT}^f	α_L^f	α_T^f	E^m	ν^m	α^m
27	233.13	23.11	8.97	8.23	0.2	0.4	-2.41	6.41	97.38	0.2	1.2
227	232.82	23.08	8.96	8.22	0.2	0.4	-1.57	7.19	98.53	0.2	1.45
427	231.79	22.98	8.92	8.18	0.2	0.4	-0.94	7.64	99.67	0.2	1.85
627	231.17	22.92	8.89	8.16	0.2	0.4	-0.56	7.8	100.82	0.2	2.15
827	230.78	22.88	8.88	8.15	0.2	0.4	-0.27	7.8	101.96	0.2	2.36
1027	229.36	22.74	8.83	8.10	0.2	0.4	-0.04	7.86	103.57	0.2	2.54
1227	227.15	22.52	8.74	8.02	0.2	0.4	0.18	7.93	107.58	0.2	2.7
1427	221.81	21.99	8.53	7.83	0.2	0.4	0.32	7.89	107.97	0.2	2.86
1627	210.63	20.88	8.10	7.44	0.2	0.4	0.48	7.95	106.84	0.2	3.02
1827	186.41	18.48	7.17	6.58	0.2	0.4	0.58	7.86	107.15	0.2	3.18
2027	157.3	15.59	6.05	5.55	0.2	0.4	0.71	7.84	97.37	0.2	3.34
2227	128.2	12.71	4.93	4.53	0.2	0.4	0.8	7.75	86.95	0.2	3.5

E=Young's modulus, ν =Poisson's ratio, G = Shear modulus, L = longitudinal direction, T =transverse direction and α = CTE. Here α = (tabulated value) x $10^{-6}/^{\circ}\text{C}$

A similar observation was also made in the work of Wang et al. [I07] in which a FE-based multi-unit cell model (MUCM) was developed to investigate the effect of the yarn braiding angle on effective CTE. A critical braiding angle was obtained at which composite possesses zero effective CTE.

Sequential multiscale finite element analysis under periodic non-adiabatic temperature boundary conditions was used by Lu et al. [64] to predict the effective CTEs of 3D4D and 3D5D composites, including the effect of

the interface. The effect of the interface was found significant for the effective CTE of 3D4D, but it has a negligible effect on 3D5D braided composites.

It is observed from the literature that the effective properties of the multidirectional C/C composites largely depend on the hierarchical distribution of the carbon fibers in the matrix, temperature, heat treatment process, and porosity. Also, it suggests that the defects like interfacial debonding, cracks, and voids have a significant role in thermo-mechanical behavior. It is further noticed that the CTE of the constituents (especially matrix) is highly dependent on the temperature and morphology. Literature survey on thermal shock behavior and the thermo-mechanical properties of C/C composite is concluded in the next section.

2.4 Literature gap

Since the multi-directional C/C composites are subjected to high thermal gradients in a very short time that creates thermal shock-like conditions during their service life, it becomes important to predict their thermal shock resistance accurately. Conventionally, the thermal shock resistance of ceramics and composites is measured through experiments like arc discharge [13], direct electric current [14], and quenching of heated specimens in different quenching media [15-20]. In quenching techniques, thermal shock resistance is obtained in terms of relative degradation of strength due to the shock and the critical temperature difference that can be sustained without fracture. The heat transfer mechanism in this technique is highly unstable; thus, it makes the measurement of temperature distribution and the evaluation of damage mechanisms very difficult in these materials. The alternate experimental technique called a laser irradiation test has overcome this difficulty [23-24]. In this technique, the TSR is defined in terms of the critical power density at which the first crack is observed in the composite. The heat transfer mechanism in this test is relatively simple and is modeled by the researchers using the finite element method [23-24]. It is observed through the literature that the thermo-mechanical properties used for the simulation of the laser irradiation test are considered as isotropic, and the effect of the temperature on the properties is ignored. The literature on the two most important properties of these composites, e.g., TC and CTE, is further explored in detail. It has been observed that the factors such as material anisotropy, temperature dependency of the constituent's material properties, fiber orientations in green composites, and voids have a significant effect on the effective behavior of these composites.

It is noticed in the literature that the analytical models developed so far are still limited to simple geometries such as unidirectional fiber-reinforced, particulate, and 2D composites. Analytical models are completely incapable of dealing with the geometrical complexity of composites and real inherent imperfections in them. However, these models are quite useful for the reverse estimation of constituent properties, as it is very difficult to measure them directly through experiments. Finite element based numerical approaches have overcome the limitation of analytical approaches and are capable of dealing with the geometrical complexity of composite materials. It is further observed that almost all numerical studies performed in the past are based on the idealized

unit cell analysis. In the CAD-based unit cell models of composite, the effect of imperfections such as bundle distortion, bundle misalignment, and irregular shaped big voids are completely ignored. Most recently, these imperfections are successfully included in the numerical model through IBFE modeling techniques [77-79, 82]. The main differences in the real and ideal geometries of microstructure are as follows:

- Real microstructure contains inherent imperfections such as misalignments, cross-section distortions, irregularity in the distribution phases, etc.
- Inherent damage originated during the manufacturing process, such as irregularly shaped big voids, cracks in the matrix, and partial debonding of the bundle/matrix interface.

It is also observed in the literature that the effective properties of the composites are greatly affected by the imperfections like voids and interfacial cracks, temperature, and hierarchical distribution of the microstructure. Therefore, a hierarchical numerical model that includes realistic microstructural features is needed to predict the local distribution of the field variables (e.g., temperatures, heat fluxes, strain, and stresses) and effective global properties of these composites accurately. The experiments, such as a laser flash test for thermal conductivity and a dilatometer test for the measurement of CTEs, can be performed for the validation of the model.

2.5 Objective of the present study

The aim of the present study is to determine the thermal shock resistance of the 4D-inplane multi-directional C/C composite using a hierarchical finite element-based model that includes the realistic features of microstructure and temperature-dependent material properties. The following objectives are defined for the development of the model.

- 1) To study the inherent microstructural features and explore the inherent damage network within the 4D In-plane C/C composite through X-ray computed tomography-based reconstruction techniques.
- 2) Reconstruction of the 3D finite element mesoscale unit cells from the 2D reconstructed images and rebuilding of the micro-scale unit cells based on the actual volume fraction details of fibers in the bundle.
- 3) Development of the image-based finite element model using two-scale hierarchy and asymptotic homogenization technique along with suitable boundary conditions.
- 4) Application of the image-based two-scale finite element model to predict the effective thermal conductivity, temperature-dependent effective CTE, and thermal shock resistance capability of multi-directional C/C composites.
- 5) To conduct the different experiments such as laser flash test and dilatometer test at the macro level to validate the numerical model.

Chapter 3

Image-based finite element model

In this chapter, the development of the image-based finite element model is discussed in detail. Firstly, the image reconstruction techniques are discussed; then, the application of the X-ray computed tomography (XCT) to the reconstruction of Carbon/Carbon composites is presented. Later, the morphology of the reconstructed microstructure is explored in detail through the obtained XCT images of the 4DIN C/C composite. Lastly, the hierarchy in the microstructure of composites is discussed, and representative volume elements (RVEs) of the composites are established at two-scales (macro and micro).

3.1 Material reconstruction techniques

These are the techniques by which the geometrical information of an inherent material's microstructure can be extracted in the form of images. The images of the microstructure of any material can be obtained in 2D or 3D forms from the original material sample. There are many reconstruction techniques reported in the literature to reconstruct various materials and can be broadly classified into two categories: destructive and non-destructive.

i. Destructive reconstruction methods

This is a surface scanning method. In this technique, the top surface of the material is scanned using one of many suitable means such as scanning electron microscopy, photography, reflective microscopy, micro-radiography, etc. The geometrical information of the microstructure of the surface is stored in the form of 2D images. Afterward, a very thin film of the top surface will be removed using any polishing approach to expose the microstructure underneath for further surface scanning. These methods are also known as serial sectioning methods because a very thin layer of the material is required to be removed from the material's surface. Optical tomography was the most widely used example of the destructive method in the early days [111]. A very high-resolution 2D image of the material's microstructure is obtained that includes the details from sub nanometers to a few microns [73]. However, the information in the third direction is generally compromised due to the trimming process. Another limitation of this technique is that the registration of the 2D images for 3D reconstruction requires a lot of work [111].

ii. *Non-destructive reconstruction methods*

As the name suggests, these methods do not need any material trimming or microstructural destructions. Therefore, they are known as non-destructive methods. In these techniques, a radiation source is utilized for the exploration of the inherent material structure. Whenever a radiation ray passes through an object, its properties are attenuated due to the molecular interactions within any material. These interactions are generally directly proportionate to the density of the material. Therefore, the material density profiles can be captured with the help of any suitable radiation source and attenuation detector. These profiles are converted into 2D images, and these images are used to reconstruct the material microstructure using different reconstruction algorithms. These techniques are further divided into the following categories based on radiation sources:

- a. X-ray computed tomography
- b. Γ -rays computed tomography
- c. Neutron computed tomography
- d. Magnetic resonance imaging
- e. Ultrasound imaging

3.2 X-ray computed tomography

X-ray is used as a radiation source in this technique. As X-rays pass through the material, properties such as diffraction coefficient and absorption index attenuate due to molecular interactions. These indices were recorded with the help of suitable detectors, as illustrated in Fig 3.I. There are two further classifications of this technique based on the detector type.

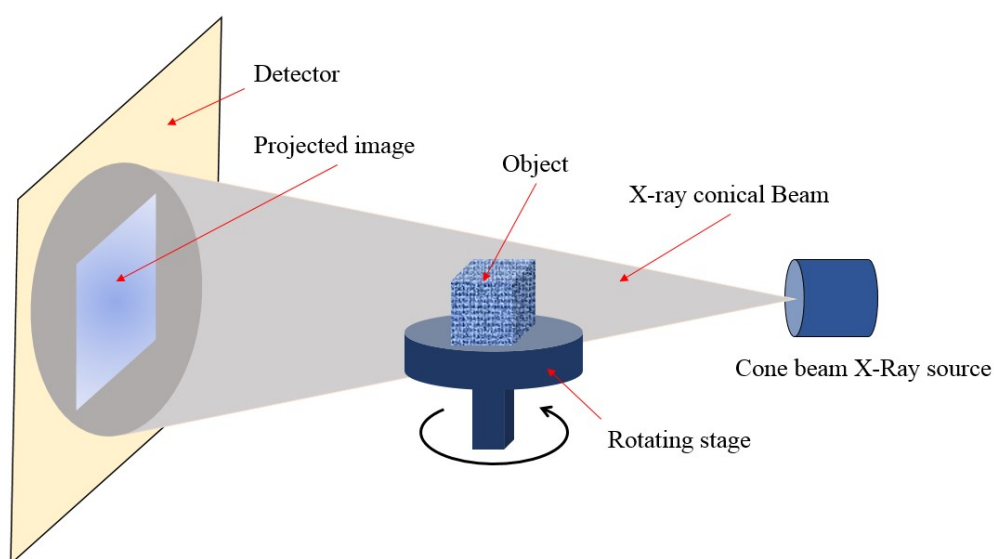


Fig. 3.I Image acquisition through X-Ray computed tomography

These detected indices are correlated to the density profiles and finally, an image of the profile is obtained. This image is also known as a shadow or a projection image. The absorption-based technique is frequently used in medical applications to detect the fracture of bones. This is also known as classical X-ray tomography or computed tomography.

3.3 Material description

Two multi-directional composites, namely three-dimensional hybrid (3DH) and four-dimensional in-plane (4DIN) C/C composites, were considered for investigation in this study. 3DH composite is made of rectangular fiber bundles in in-plane directions and circular rods in the out-of-plane direction. Nearly 24k fibers are embedded in the rectangular bundle, and the circular rod contains 15K fibers approximately. On the other hand, the 4DIN composite contains circular rods in three in-plane (0° , 60° , and 120°) and one out-of-plane direction. PAN-based fiber (T300) and coal tar pitch-based matrix were utilized as precursors for the fabrication of these composites. The diameter of a single fiber is around $6.8 \mu\text{m}$. The total volume fraction of fibers is maintained at around 48% and 38%, respectively in 3DH and 4DIN C/C composite. The liquid impregnation technique was used along with three graphitization cycles up to a temperature of 2200°C [1, 2] to achieve the required density of composites.

3.4 Reconstruction of the C/C composites

In the present study, the X-ray source available at SASE, DRDO Manali, India, was used to reconstruct the multi-directional composite. As previously discussed, the specimen was exposed to radiation and the density profile is captured as an image during the reconstruction process. The specimen was rotated with a fixed increment. An exposure time of a few milliseconds was given to capture the profile image of the specimen from different angles during the scanning process. In this way, the density variation within the specimen can be obtained as a function of 'r' and ' θ ' coordinates where 'r' is the radial distance, and ' θ ' is the angular position of any of the material points. This information was converted to Cartesian coordinates with the help of the filter back-projection algorithm. Sharma et al. [6, 76-79] have more details on the reconstruction procedure. Fig 3.2 shows the transformation process of the density profiles to 2D stacked images, and then from 2D images to 3D image for 4D C/C composite.

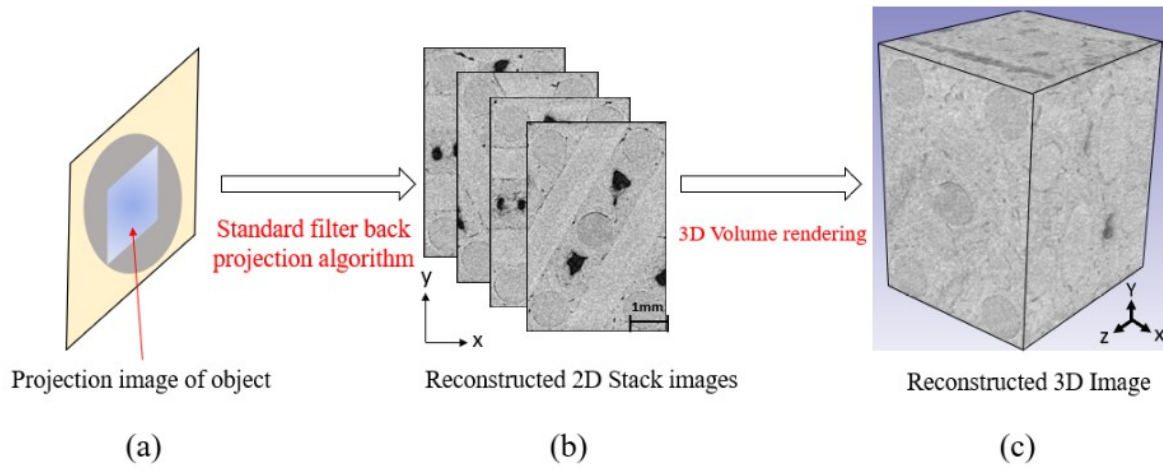


Fig. 3.2 (a) Projected image acquired through XCT, (b) Reconstructed 2D stack images, (c) 3D reconstructed image of microstructure of 4D C/C composite.

The final reconstructed 2D image resolution depends on different factors such as the density of the material, specimen size, X-ray intensity, angular displacement, and exposure time. A specimen of the size of $9 \times 9 \times 9 \text{ mm}^3$ was scanned to get the best contrast and resolution at $8 \mu\text{m}$. Different scanning parameters were tried based on the trial and error approach. The details of the scanning parameters which offered satisfactory results are given in Table 3.1.

Table 3.1 Micro-CT scan parameters for C/C composite

X-ray tube: energy/intensity		Radiograph acquisition		Reconstruction area	
Voltage (kV)	Current (mA)	Angular displacement ($^\circ$)	Exposure time (ms)	Pixel size (μm)	
				3DH	4DIN
80	100	0.30°	1178	$8\mu\text{m}$	$8\mu\text{m}$

Fig. 3.2 (b) shows the 2D stacked greyscale images of the 4DIN C/C composite, and a 3D image is presented for the same in Fig. 3.2 (c). It is clear from these images that very important structural information about the inherent microstructure is captured non-destructively. The captured morphology of the microstructure is discussed in detail in the next section.

3.5 Morphology of 4D C/C composites

The reconstructed 2D images of 4D C/C composite are shown in Fig 3.3. Morphological features such as bundle cross-sections, cracks, voids, and bundles' misalignments were investigated through these images. Figs. 3.3(a), (b), and (c) show the images of x-y planes at different locations in the z-direction. Fig 3.3 (a) shows the

2D image of one of the planes across z-direction in which the bundles inclined at 120° appear. Fig 3.3 (b) shows the 2D image of one of the planes across z-direction in which bundles inclined at 60° appear. Fig 3.3 (c) shows the image of the plane where bundles of 0° appear. Here, the inclination of the bundles measured with respect to the x-direction. It is observed from the images that the voids and cracks are presented as dark black, while bundles in 120° directions are in light grey. The circular patterns, as visible in Fig. 3.3 (a), (b), and (c), are the bundles in the z-direction. Fig. 3.3(d) shows the y-z plane to cover the longitudinal section of the z-bundle and the cross-section of the in-plane bundles. The bundles in the z-direction are clearly dissuadable in the image as they appear slightly darker compared to the in-plane bundles. The contrast between the matrix and the bundle is not high, and sometimes it appears to be more or less of the same intensity. Still, the cross-sections due to peripheral cracking patterns can be easily distinguished (see Fig.3.3(d)). The cross-sections of the bundles in 60° and 120° appear to be elliptical (see as marked with red in Fig 3.3 (d)) because the image slice cuts them at an oblique plane.

It is clear from Fig 3.3 that substantial cracks and voids network exists in the microstructure of the C/C composite in the virgin state (before any loading). This network is very complex and highly interconnected with each other. All these defects based on the size, shape, and location are characterized in the following categories.

- I. *Voids*: There are two types of voids visible in these images.
 - a. *Big voids*: These voids generally appear at the center of the matrix pockets. The maximum size of these voids is comparable to the size of the bundle (i.e., greater than 0.2 diameters); thus, they are clearly distinguishable from other voids. Hereafter, these voids are referred to as big voids or pocket voids.
 - b. *Micro voids*: These voids are much smaller than the big voids (i.e. less than 0.2 diameters) and are present in the other areas .i.e. not in the center, of the matrix bundles. These are further classified into three categories based on their location: 1) micro voids in the matrix, 2) micro voids at bundle/matrix interface, and 3) micro voids in bundles. The location of these voids is crucial when a separate study is conducted at micro length scales. In most studies, the researcher considers the effect of the macro-porosity in the matrix by degrading its mechanical properties. However, the effect of the micro voids present at the interface is taken as the average behavior of the interfacial properties.

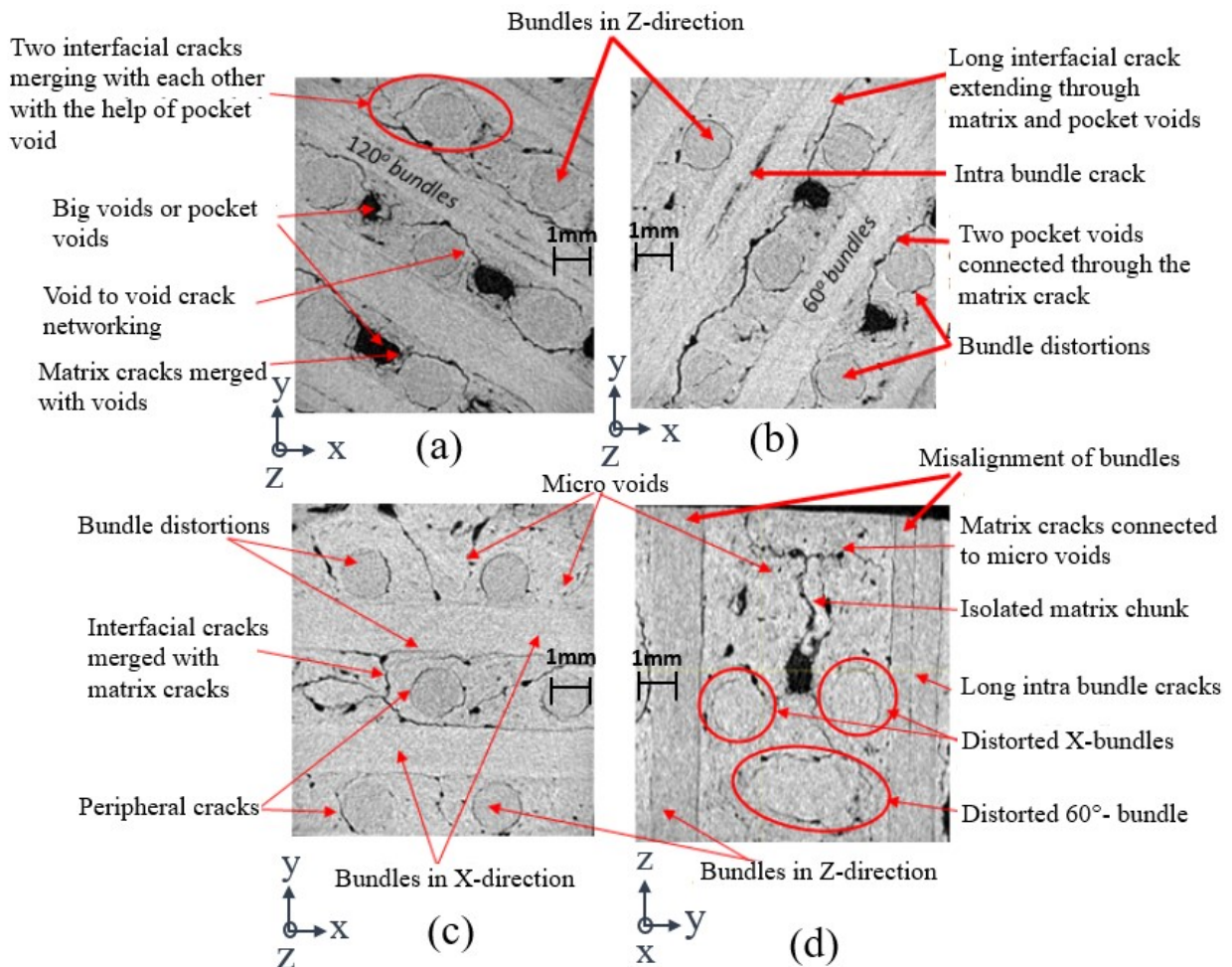


Fig 3.3 Morphology of the 4DIN C/C composite

2. *Cracks*: Cracks are very thin sheet-like or slender pipe-like features present in the morphology. Generally, cracks are distinguished from voids as one of their dimensions is usually quite larger or smaller than the other two. It is explained using only two dimensions as their network is very complex in 3D.

They are classified as follows:

a. Based on the length of the crack:

- i. *Long crack*: The crack is classified as long if one of its dimensions is longer than the smallest dimension of the phase (i.e. either matrix pocket size or bundle diameter).
- ii. *Short crack*: The crack is said to be short if its largest dimension is four times lesser than the least dimension of the matrix pocket or bundle.
- iii. *Intermediate cracks*: Cracks that fall in between these two previous categories are called intermediate cracks.

b. Based on the location:

- i. *Matrix cracks*: These exist in the matrix pockets between the bundles. These generally originate due to the shrinkage of the matrix during the processing.

- ii. *Intra-bundle cracks*: The cracks present in the bundles of C/C composites are intra-bundle cracks. These cracks are clearly marked in Fig 3.3(a), (b), and (d). These cracks are generally caused due to the improper impregnation of the matrix or the high stresses generated during the processing of preforms.
 - iii. *Interfacial cracks*: The cracks present at the interface of the matrix and bundle are called interfacial cracks. These cracks originate due to the mismatch of the thermal expansion coefficient of the matrix and the bundle. Most of the peripheral cracking depicted in Fig 3.3(a), (b), and (c) fall under this category.
- c. Based on the propagation:
- Once a crack originates at a place, it tends to propagate under different environments and conditions. Therefore, the cracks can also be characterized in different categories based on their propagation. The following categories of the cracks are observed in the images based on the propagation.
- i. Cracks originated and propagated only in the matrix.
 - ii. Cracks originated from the matrix and merged in the voids (both pocket and micro).
 - iii. Cracks originated from the matrix and merged in another matrix crack.
 - iv. Cracks originated from the matrix and merged in the interfacial crack or vice versa.
 - v. Interfacial cracks of two different bundles propagated and merged with the same pocket voids.
 - vi. Interfacial cracks originated at one bundle, then propagated through the matrix, and merged in the interfacial crack of another adjacent bundle.
3. *Bundle distortions*: During the manufacturing process, the bundles experienced different stress conditions under different loading environments, which generally lead to distortions in their size, shapes, alignments, etc. These distortions are well captured in the 2D images of the XCT and broadly are classified in the following three categories.
- a. *Distortion of cross-section*: The circular bundles due to processing and stress handling are not able to maintain a perfect circular shape. (refer Fig 3.3)
 - b. *Distortion of longitudinal-section*: The bundles which were initially straight lost their straightness during the manufacturing process. It is clear from Fig 3.3 (d) that some undulations are present in the bundles along the longitudinal axis.
 - c. *Distortion of alignment*. This means that the bundles that are initially parallel to each other lose their parallelism after processing. This type of distortion is mostly caused during the preform manufacturing or matrix impregnation process. Again, it is evident from Fig 3.3 (d) that the bundles are not perfectly parallel and orthogonal to each other. This defect dominates in composites where the bundle volume fraction is less than 33%.

Some of these morphological features repeatedly occur within the bundles at lower length scales, and they can be found at higher resolution images. Apart from this, the microstructure of the multi-directional C/C

composites represents a hierarchy in the length scale as the bundles in these composites themselves are a unidirectional composite made of matrix and fiber phases. This hierarchy is explored in detail at higher resolutions in the next section.

3.6 Hierarchy in the C/C composites

A hierarchy is an arrangement of ordered groupings within a system that is again reflected at other levels either above or below. In the microstructure of the multi-directional C/C composites, the material phases can be divided into three categories. These are the inclusion phase, the binder phase, and the interface between both. This arrangement of the inclusion, binder, and interface at the macro scale is known as the mesostructure of the composite. It is represented by the bundles, matrix, and interface between them.

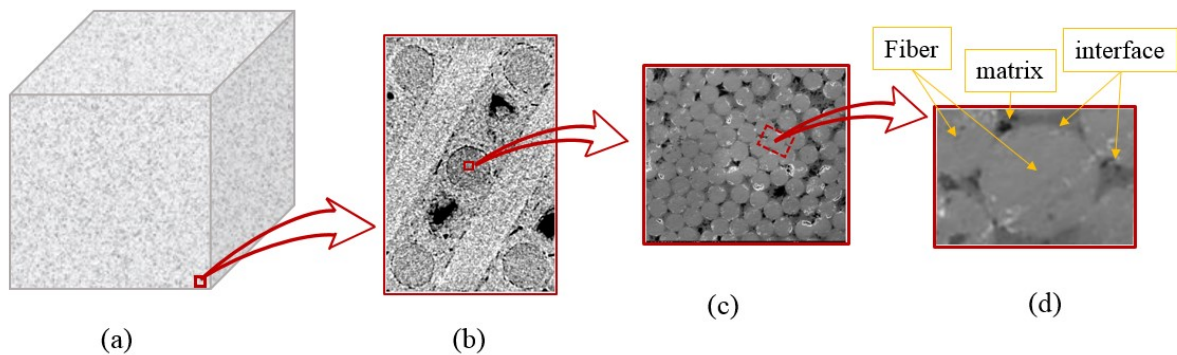


Fig 3.4 Hierarchical microstructure: a) homogenous at macro scale; b) heterogeneity represented by the matrix, bundle, and interface; c) distribution of the fibers in the bundle; and d) heterogeneity represented by the matrix, fiber, and interface

The same arrangement can be found at the lower length scale (micro-scale) i.e., at bundle length scale. Here, this arrangement is represented by the fibers as inclusion, matrix as the binder, and fiber-bundle interface as the interface between two phases. Fig 3.4 shows the hierarchical microstructure of the C/C composite at both scales.

Apart from these, some of the defects discussed in the morphology section are also repeated in the microstructure hierarchy. Fig 3.5 explores the defects at the bundle level through XCT images taken at $2\mu\text{m}$ resolution. Fig 3.5 (a) shows the microstructure of 3DH C/C composite at $2\mu\text{m}$ resolution in one of the x-y planes. In this composite, the circular bundles are needed in the z-direction, and rectangular bundles are used in x and y directions. Fig 3.5 (b) shows the zoomed-in cross-section. The micro-porosity within the bundle is clearly distinguishable, but it is very difficult to locate the fibers at this resolution. The micro-cracks within the bundles are clearly visible in Fig 3.5(c) (which is an enlarged view of the rectangular fiber bundle). Also, it is very difficult to include such minute details in the finite element

analysis. The direct inclusion of these details will lead to a computationally inefficient method [48]. Therefore, some compromise was made during the reconstruction of the 3D RVEs. The details of the reconstruction of the RVEs are discussed in the next section.

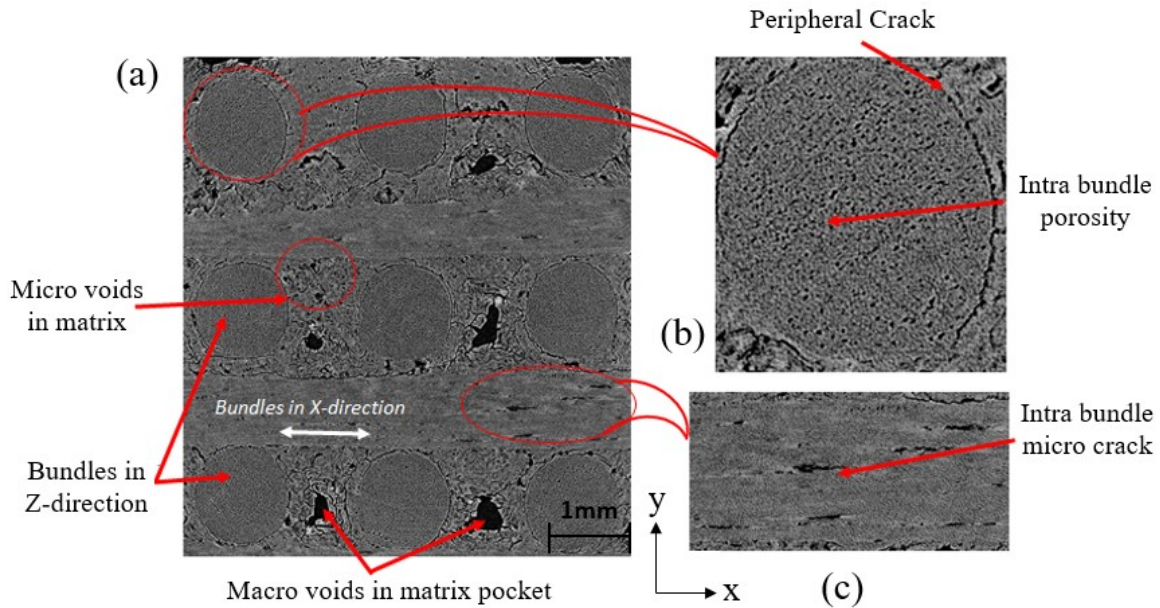


Fig. 3.5 a) Reconstructed image of the microstructure of the multidirectional composite at $2\mu\text{m}$ resolution, b) Zoomed bundle cross-section, and c) Zoomed intra-bundle cracks.

3.7 Reconstruction of the 3D RVEs

The 2D images were processed for the segmentation of the phases and the 3D reconstruction of the RVEs. A typical histogram of the distribution of the greyscale values in the images of one of the specimens is shown in Fig 3.6. It is clear from Fig.3.6 that the grey levels have a combined distribution in the different phases. This condition generally arises in neighboring density materials. Here, the grey level 0 shows the least density material particle, which is air, and 255 shows the densest particle of C/C composite. The segmentation of the voids in the composite can be done based on the greyscale threshold value. However, it is not easy to decide a threshold value, but an estimation of the value can be done using the trial and error approach. The initial guess of the threshold is considered to be between 50-150 by looking at the histogram. The initial guess of 50 is assumed, and the value is increased with an increment of 10. The corresponding covered area is observed by the pixel.

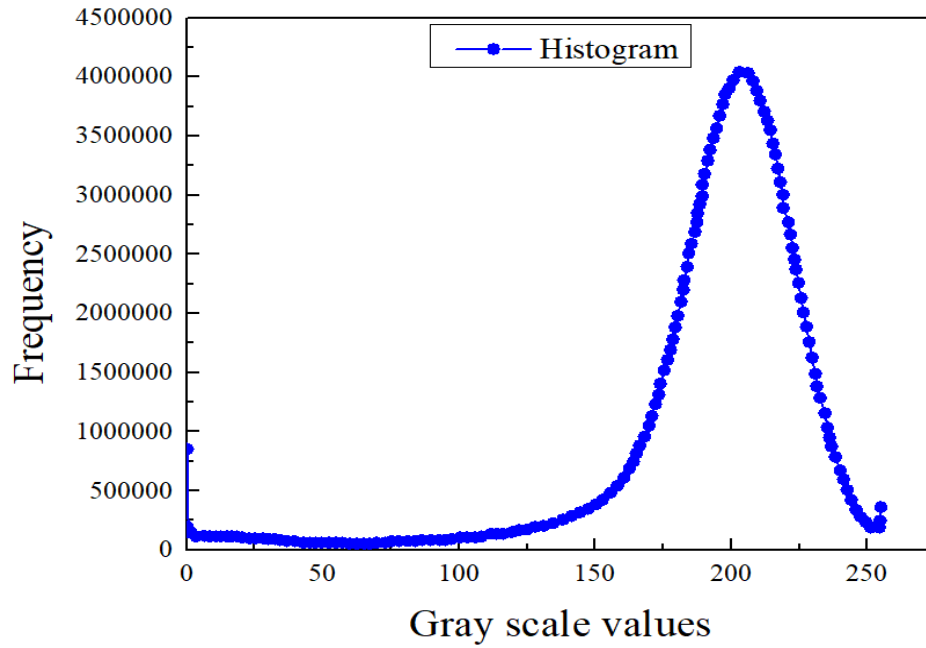


Fig. 3.6 Greyscale value distribution over a 2D stack image

Fig. 3.7 shows the segmentation procedure of the big voids in composite using greyscale values. Fig. 3.7(a) represents the original image. The area covered by the pixels of greyscale values up to 80 is marked yellow in Fig. 3.7(b). The area covered by the pixels for a threshold value 100 is shown in Fig. 3.7(c). It is observed that the big voids were covered satisfactorily at a greyscale threshold value of 80 (see Fig. 3.7(b)).

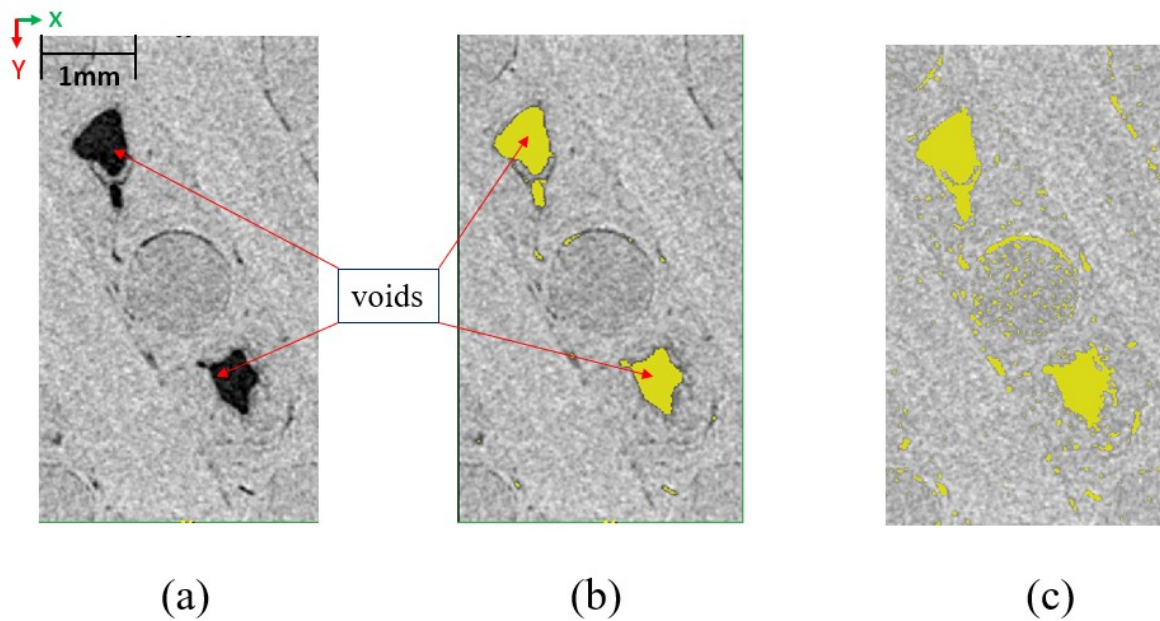


Fig. 3.7 (a) Unsegmented, (b) Segmented at threshold greyscale value of 80, and (c) Segmented at threshold greyscale value of 100.

It is clear from Fig. 3.7(c) that a further increase in the threshold value covers some undesired extra areas in the image. Therefore, it was decided that a threshold value of 80 is sufficient for the segmentation of voids in the images of the specimen.

As there is a combined distribution of greyscale values of pixels in the other two phases (matrix and bundle), it is very difficult to segment these phases using existing image processing algorithms. Therefore, a semi-manual procedure was adopted for the segmentation. The ‘ScanIP’ commercial software available at the Applied Mechanics Department, IIT Delhi, India, was used for the segmentation and reconstruction of the finite element meshes. The algorithm of the segmentation procedure is given below.

- 1) Identify the cross-sections of the bundles in one of the planes, i.e. mark the bundle cross-sections in one of the orthogonal planes in one mask (Mask refers to a collector bin in this study).
- 2) Improve the marking in other planes. There will be some cross-sections of the bundle that will be difficult to differentiate in the particular marking plane. These missing cross-sections are completed by identifying them in the other two planes.
- 3) Return to the original marking plane and improve the markings by using smoothing filters or doing it manually.
- 4) Repeat the procedure two or three times for each bundle to reduce the manual marking errors.
- 5) Once the bundles were reconstructed, make a new mask that covers the entire volume. Subtract the segmented masks from it using a Boolean operation.

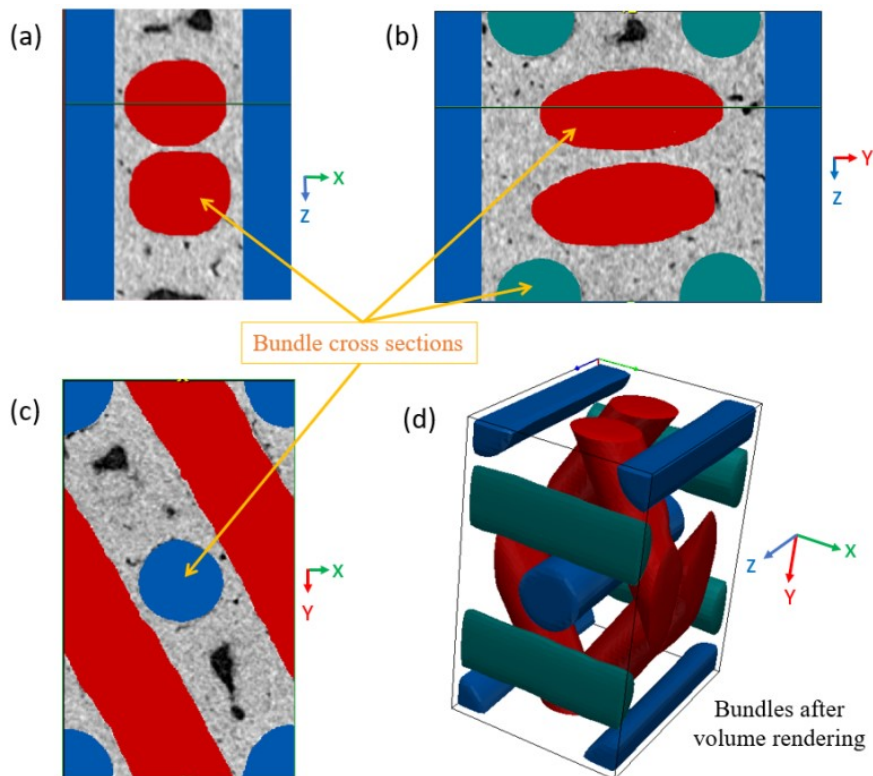


Fig. 3.8 ((a), (b), and (c)) Cross-sectional 2D view of bundle segmentation and (d) 3D view of segmented bundles

Fig. 3.8 shows the 3D image of the segmented bundles along with the marking of their cross-sections in all three orthogonal planes for 4DIN C/C composites. There are some assumptions made during the reconstruction of the 3D image and finite element mesh of the RVEs of these composites to make them computationally efficient. These assumptions are given below.

Assumptions:

1. Fiber bundles and matrix are considered homogenous materials at the mesoscale level.
2. It is assumed that fiber bundles are free from voids, cracks, and other inhomogeneities.
3. Micro voids are ignored in the geometry and big voids are directly modeled in the matrix phase.
4. The resolution was compromised and reduced to 36 μm to make the reconstruction process more accessible and the FE mesh workable.
5. The uneven surface of the interface was optimized for the finite element meshing. Hence, very sharp features were ignored and made smoother.
6. The segmentation of the phases was carried out using semi-automatic operations. Therefore, there always are some manual errors to be associated with the processor.
7. The micro-unit cells are assumed to be of ideal geometry due to the lack of their complete microstructural information.

3.8 Finite element models of multidirectional C/C composites

3.8.1 Reconstructed FE models of 4DIN

A good workable finite element mesh for the unit cell of the composites can be obtained by utilizing the discussed procedure and assumptions. Fig. 3.9 shows the reconstructed features of the segmented images of different phases, which were directly included in the finite element model of 4DIN C/C composite.

The final segmented images of bundles, matrix, and voids are shown in Fig 3.9 (a), (b), and (c). Fig. 3.9 (d) shows the 3D image of the composite RVE. Fig. 3.9 (e) is the finite element mesh of the RVE, excluding voids. Fig. 3.10 shows that most of the bundle distortions were preserved during the segmentation and successfully included in the finite element mesh. There are some small uncertainties associated with the geometric parameters of the phases due to geometrical variables like size, shape, and orientation that are not uniform throughout the composite.

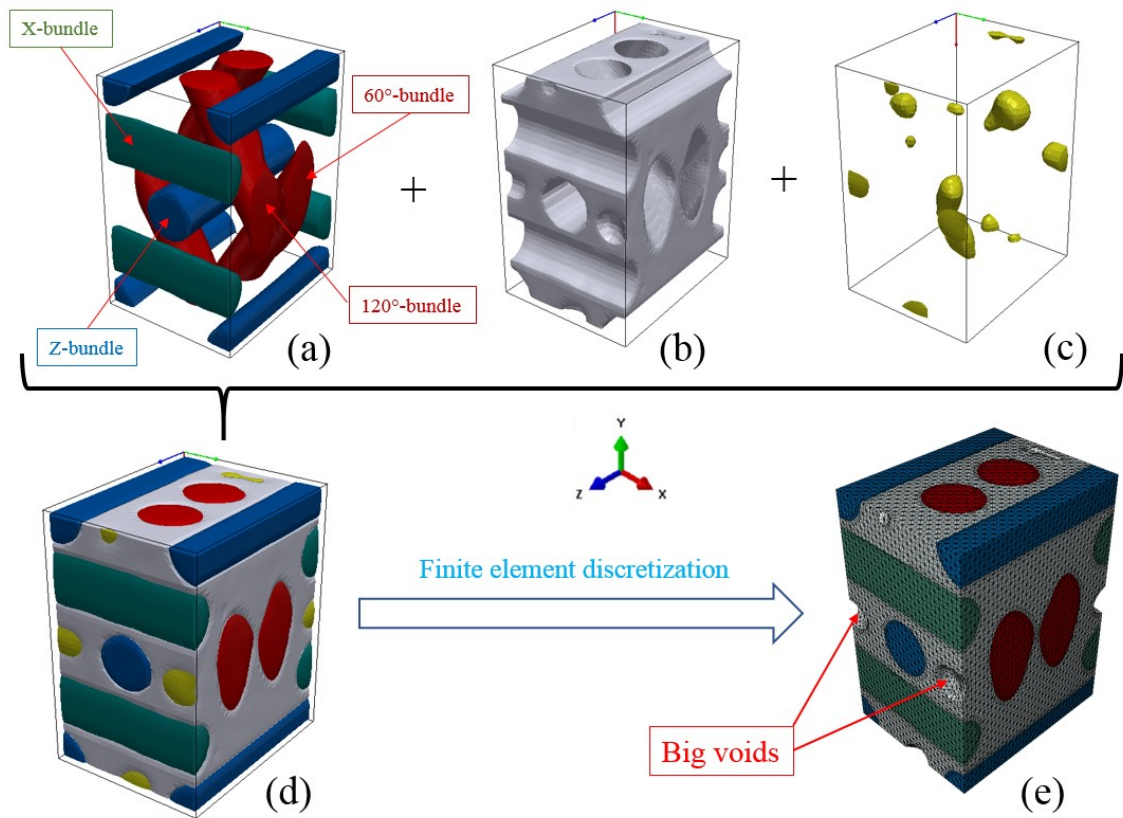


Fig.3.9 (a) Segmented bundles, (b) Matrix pocket, (c) Big voids in matrix pocket, (d) Reconstructed 3D image of RVE, and (e) Discretized FE model of RVE eliminating voids

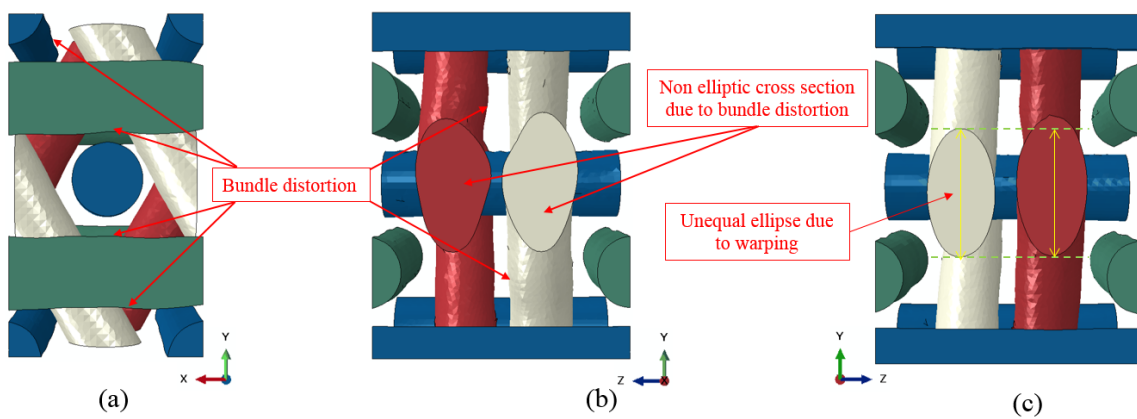


Fig. 3.10 (a) View from x-y plane, (b) View from the z-y plane, and (c) Opposite side of the view shown in (b)



Fig. 3.II Finite element models of the RVEs of the 4DIN C/C composite.

Table 3.2 Fiber volume fractions of 4D in-plane C/C composite RVEs in different directions

RVEs		RVE 4A	RVE 4B	RVE 4C	MEAN/SD
Dimensions (mm)		2.586 × 4.397 × 3.362	2.5 × 4.397 × 3.276	2.586 × 4.3973 × 3.276	-
V.F In-plane (x-y plane) bundles (%)	X-bundle	10	8	9	9/1
	60° Bundle	8.5	8.2	9.3	8.67/0.57
	120° bundle	8.3	7.8	9.5	8.53/0.87
V.F of z-bundle (%)		12	11.8	11.8	11.87/0.12
Total fiber V.F (%)		38.8	35.8	39.6	38.06/2
Void V.F (%)		1.7	2	2.4	2.03/0.35

V.F: Volume fraction

Three-unit cells of the 4DIN C/C composite named RVE4A, RVE4B, and RVE4C are considered from random locations to consider the effect of the uncertainties associated with the distribution parameters. The finite element meshes of these RVEs are shown in Fig 3.II. The detailed information regarding FE meshing, volume fractions, and the dimensions of these RVEs are given in Table 3.2.

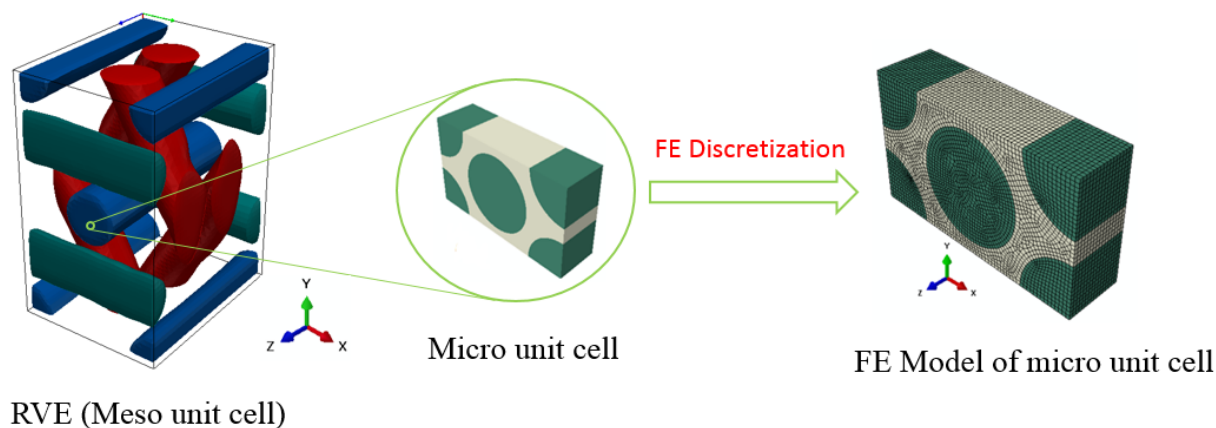


Fig. 3.12 Finite element discretization of the micro-unit cell

It was discussed in section 3.6 that the multidirectional C/C composites have a hierarchical microstructure at two length scales. The fiber bundles are also a unidirectional composite at the lower length scale (i.e. micro-scale). Here, it is assumed that it is a hexagonal packing of fibers in the carbonaceous matrix at this length scale based on the high-volume fraction of fibers in the bundles.

Table 3.3 FE description of micro-unit cells of different bundles in 4DIN C/C composite.

RVEs	Bundles	Fiber volume fraction (%)	Dimension (μm)	No. of elements/Nodes
RVE 4A	X	78.83	$12.63 \times 7.29 \times 4$	57700/67284
	XY60	89	$11.88 \times 6.86 \times 4$	96650/110578
	XY120	86.8	$12.04 \times 6.95 \times 4$	53460/62727
RVE 4B	Z	83.62	$12.26 \times 7.08 \times 4$	54200/63525
	X	90	$11.82 \times 6.83 \times 4$	148654/167100
	XY60	81.99	$12.38 \times 7.15 \times 4$	55540/64974
	XY120	81.02	$12.46 \times 7.19 \times 4$	56280/65751
RVE 4C	Z	87.64	$11.98 \times 6.92 \times 4$	53560/62832
	X	83.39	$12.28 \times 7.09 \times 4$	55020/64386
	XY60	79	$12.62 \times 7.29 \times 4$	57700/67284
	XY120	80.58	$12.49 \times 7.2 \times 4$	56740/66234
	Z	70.75	$13.33 \times 7.7 \times 4$	63380/73374

In the present study, the fiber volume fraction of bundles is calculated by considering 15k fibers (straight cylinder of diameter 6.8 μ m) and the actual reconstructed volume of the bundles. The separate micro-unit cell for each bundle was considered as the fiber volume fraction differs in each bundle due to distortions. The typical finite element mesh of one of the micro-unit cells is shown in Fig 3.12. The calculated fiber volume fraction was found to be 82.72 ± 5.12 %, which confirms the highly-dense packing of fibers. In this way, the effect of bundle distortion on the effective properties is included according to the corresponding fiber volume fractions. The details of fiber volume fraction and finite element meshes of different bundle unit cells are given in Table 3.3.

3.8.2 Reconstructed FE models of 3DH

A similar procedure described in the earlier section is adopted to reconstruct the finite element meshes of RVEs of 3D-Hybrid (3DH) C/C composite. Three images of the unit cells named RVE3A, RVE3B, and RVE3C are reconstructed and discretized into finite elements mesh. Fig 3.13 shows the 3D image of one of the RVEs. It is clear from Fig 3.13 that the imperfections such as bundle distortion, misalignments, and big voids are preserved in the reconstructed microstructure of 3DH C/C composite.

Table 3.4 Fiber volume fractions of 3D orthogonal composite unit cells in different directions

RVEs	RVE3A	RVE3B	RVE3C	MEAN/SD
Dimensions (mm)	2.21 \times 2.21 \times 5.4	2.41 \times 2.41 \times 5.804	2.32 \times 2.5 \times 5.89	-
V.F of x-bundle (%)	16.92	14.76	16.79	16.16/0.99
V.F of y-bundle (%)	18.04	15.85	18.54	17.47/1.17
V.F of z-bundle (%)	16.17	13.46	15.74	15.12/1.19
Total fiber V.F (%)	51.13	44.07	51.07	48.76/3.31
Void V.F (%)	2.38	1.62	2.39	2.64/0.95

V.F: volume fraction. Bundles are named according to their alignment in respective coordinate directions

The statistics of voids and the bundle volume fraction of the three RVEs are presented in Table 3.4. It is known that in-plane bundles (x and y) are rectangular (in shape) and out of plane bundles are circular in the 3DH C/C composite. The rectangular bundles contain around 24k fibers, and the circular bundle contains 15k fibers approximately.

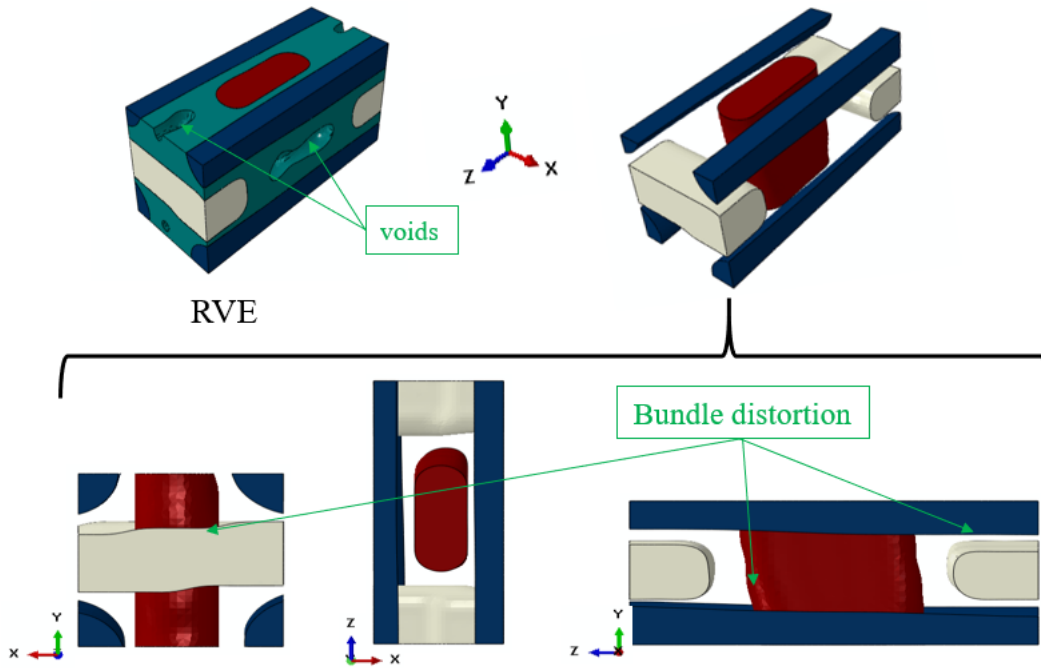


Fig. 3.13 RVE of 3DH C/C composite containing big voids and bundle distortion

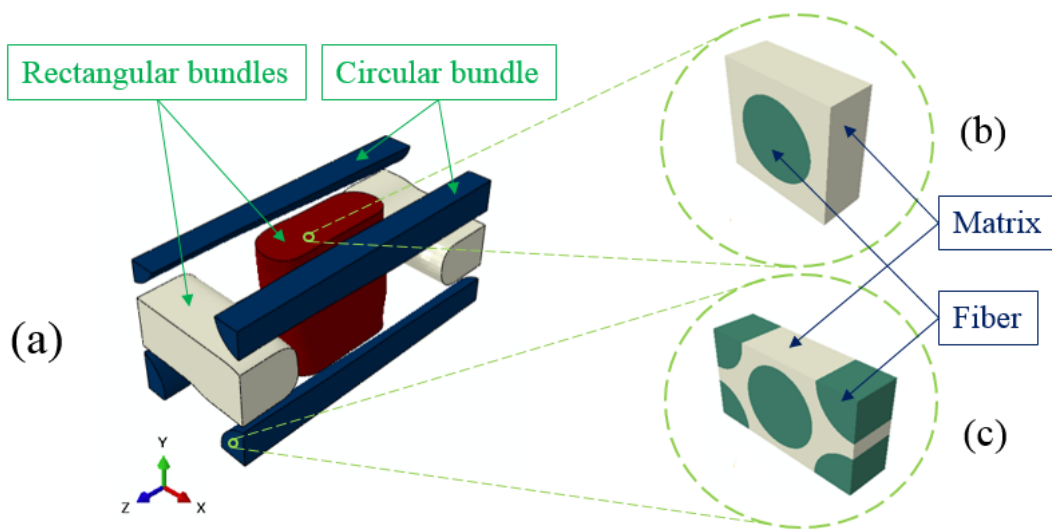


Fig 3.14 Micro unit cells for bundles

The fiber volume fraction for each bundle was separately obtained to decide the packing of fibers. Due to the distortion effect, fluctuations in calculated fiber volume fractions were observed. Fiber volume fraction came out to be $39.42 \pm 3.18\%$ and $66.08 \pm 4.56\%$ respectively for rectangular bundles and circular bundles. Based on the degree of tightness, square packing and hexagonal packing for the fibers were assumed for rectangular

and circular bundles, respectively. The images of the typical micro-unit cells for each packaging arrangement are shown in Fig 3.14 (b) and (c).

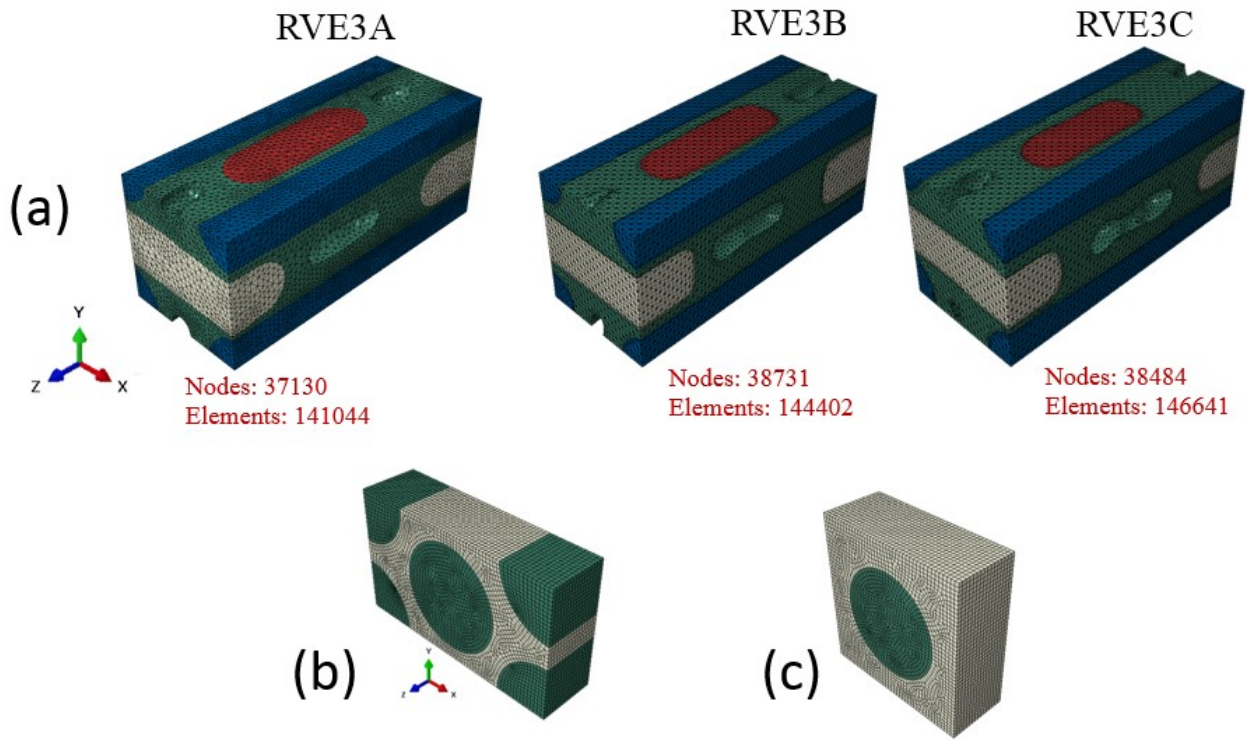


Fig 3.15 FE model of (a) RVEs of 3DH C/C composite, (b) Micro unit cell for the circular bundle, and (c) Micro unit cell for the rectangular bundle

Table 3.5 Finite element model description of micro-unit cells

RVEs	Bundles	Packing Fractions (%)	Dimension (μm)	No. of elements/Nodes
RVE3A	X	43.53	$9.13 \times 9.13 \times 4$	15158/17178
	Y	40.89	$9.42 \times 9.42 \times 4$	15990/18102
	Z	69	$13.51 \times 7.79 \times 4$	19019/21462
RVE3B	X	42.21	$9.28 \times 9.28 \times 4$	15522/18606
	Y	39.29	$9.61 \times 9.61 \times 4$	16510/19698
	Z	69.62	$13.44 \times 7.76 \times 4$	18629/23114
RVE3C	X	35.25	$10.15 \times 10.15 \times 4$	18720/22134
	Y	35.37	$10.13 \times 10.13 \times 4$	18265/21644
	Z	59.64	$14.53 \times 8.38 \times 4$	21567/26362

Finally, the 3D images of the different unit cells at meso and micro levels were discretized into finite element meshes. Fig 3.15 shows the finite element model of unit cells at these two length scales (meso and micro). The mesh statistics of all the micro-unit cells along with their dimensions, are presented in Table 3.5. In the present study, composite RVEs were discretized using tetrahedral elements. These unit cells or RVEs of the multidirectional C/C composites (3DH and 4DIN) were utilized to predict the thermo-mechanical properties in the next chapters.

Chapter 4

Thermal conductivity of multidirectional C/C composite

Thermal conductivity is a basic property of any material and is a measure of its ability to conduct heat. The requirement of a very high specific thermal conductivity is the most desired property in aerospace materials. This chapter starts with introducing thermal conductivity and the Laser Flash experiment for the C/C composite. Later, a two-scale framework for the prediction of the effective homogenized properties of multi-directional C/C composites is presented. The numerical analysis of the multi-directional C/C composites (3DH and 4DIN) is performed based on the two-scale framework and image-based finite element meshes. In the last section, the predicted FE results are compared with existing models and experiments.

4.1 Thermal conductivity

Thermal conductivity is the ability of any material to transfer the heat through the conduction mechanism. This is one of the most evaluated properties of C/C composites for aerospace material applications. Also, it is well known that the thermal behavior of the composites depends on the various parameters of the constituents (matrix and fibers) such as the type of precursor, fabrications process, heat treatment temperature, morphology, volume fraction, orientations of the fibers, etc. Here, our focus is on the development of an effective numerical solution that can include the hierarchical arrangements of the basic constituents (fibers and matrix) of the multidirectional C/C composites and can be validated through experiments.

Many researchers have made an effort for the characterization of the thermal behavior of C/C composites using experimental [31-38], analytical [39-54], and numerical techniques [55-66]. The experimental work is primarily focused on the measurement of thermal properties such as thermal diffusivity, specific heat, and thermal conductivity. Laser Flash experiment, which has been frequently performed to measure the effective thermal conductivity of C/C composites, is used to explore the behavior of 3DH C/C composite. The details are discussed in the next section.

4.2 Laser flash experiment

A very popular method called the Laser Flash method proposed by Parker et al. [112] was used to measure the thermal diffusivity of the 3DH composite. In this method, one surface of a sample is heated by the laser

pulse for very small intervals of time, and the temperature rise on the parallel opposite surface is measured (refer Fig. 4.1). On assuming one-dimensional heat flow and adiabatic conditions, the half rise time ($t_{1/2}$ (refer Fig. 4.1)) is obtained from the time-temperature profile. Then, thermal diffusivity can be calculated using the following expression

$$\alpha = 0.1388 \times L^2/t_{1/2} \quad (4.1)$$

Where α is the thermal diffusivity of the composite, and L is the thickness of the sample. In the present study, the in-plane diffusivity of 3D orthogonal C/C composite was measured using the Laser Flash instrument developed by NETZSCH over the temperature range of 50°C to 1000°C in Argon atmosphere. It is assumed that no loss of mass occurred during the experiment (no ablation or oxidation). Therefore, the following expression can be used to find out the effective thermal conductivity of the composite.

$$k = \alpha \times \rho \times c_p \quad (4.2)$$

where k is the thermal conductivity, ρ is the density (1.96 gm/cm³), and c_p is the specific heat of the composite.

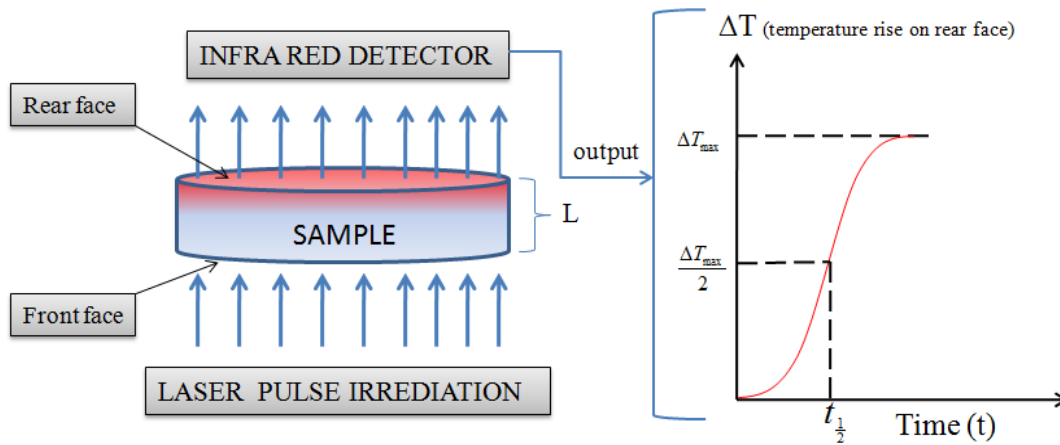


Fig. 4.1 Basic principle of Laser flash experiment

The results obtained for thermal diffusivity and conductivity are presented as a function of temperature in Fig. 4.2 (a) and (b) respectively. The maximum thermal diffusivity is 71.5 mm²/s at 51.5°C and then decreases exponentially to 14.4 mm²/s at 997.2°C.

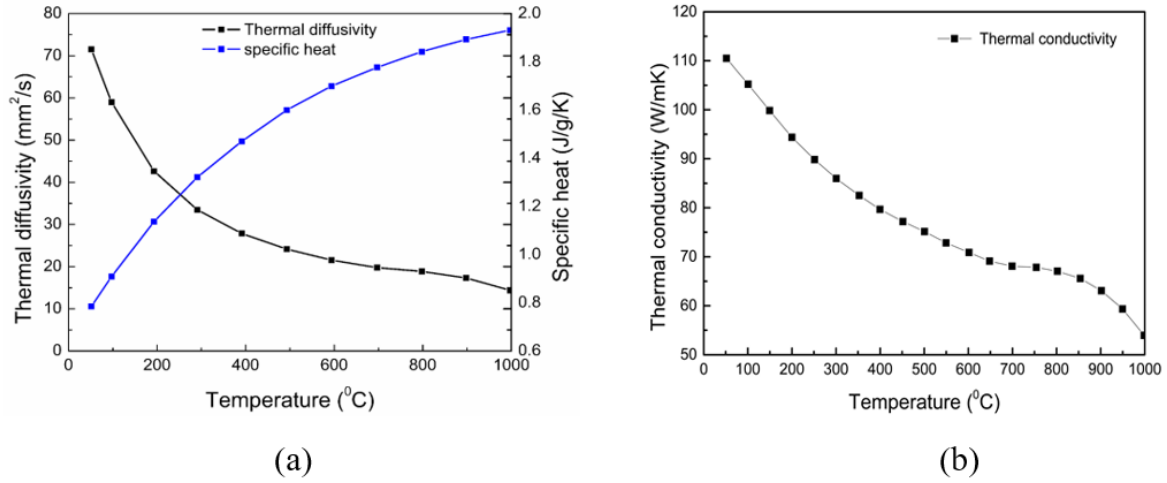


Fig. 4.2 Variation of (a) Measured thermal diffusivity and specific heat data of 3DH, (b) Calculated thermal conductivity data

The two-scale homogenization process for predicting the thermal properties is presented in detail in the following section.

4.3 Two-scale homogenizations

As discussed earlier, there are two hierarchical length scales present in the multi-directional C/C composites. The problems in the length scale can be split into two, namely: 1) bundle level and 2) composite level. Different homogenization techniques were utilized by researchers to find the effective response of heterogeneous materials, as seen in the literature review (Chapter 2). The effective response of heterogeneous materials is also known as the homogenous response, and the technique to replace a heterogeneous material with an equivalent energized homogenous material is called homogenization. The framework of the asymptotic homogenization given by Bensaoussan et al. [113], along with finite element formulation, is one of the most effective approaches. The next section covers the formulation of the asymptotic homogenization at both length scales to predict the effective macroscopic response of the composites based on these techniques.

4.3.1 Asymptotic expansion homogenization

AEH is one of the most popular homogenization techniques widely used in the multiscale analysis of periodic heterogeneous structures for finding effective properties and scale bridging [113-115]. In such a method, the heterogeneous domain is split into two levels of length scale as global (of the order of dimension of structure) and local scale (of the order of microstructure). Fig. 4.3 shows such local and global domains. let x_i and y_i (with $i=1, 2, 3$) are the coordinate systems describing the global and local state of field variables, respectively. Then, the scale bridging parameter ξ can be defined as

$$\xi = \frac{x_i}{y_i} \quad \text{where } i = 1, 2 \text{ and } 3 \quad (4.3)$$

The two-scales can be effectively bridged if the scaling parameter $\xi \ll 1$. The small value of ξ ensures that the effect of heterogeneities will vanish on the boundaries ($\partial\Theta$) of the local domain (Θ) [114] (see Fig. 4.3(b)).

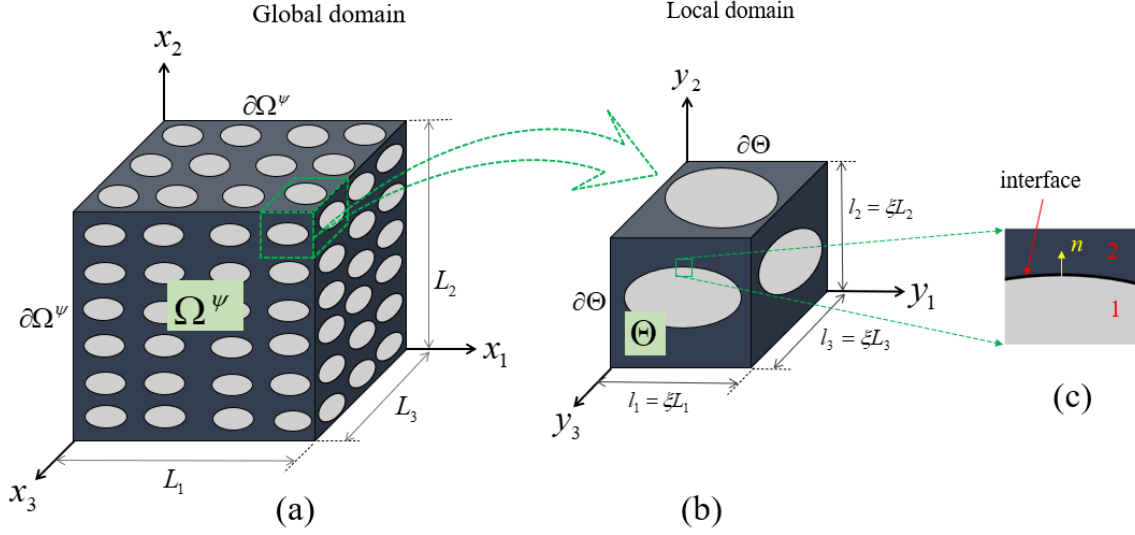


Fig. 4.3 (a) A global heterogeneous domain (b) A local unit cell domain (c) Interface between two phases.

Consider a thermal boundary value problem in a 3-dimensional heterogeneous domain $\Omega^\psi \in R^3$ having an outer boundary $\partial\Omega^\psi$, as shown in Fig. 4.3 (a).

$$\text{Steady-state heat equation:} \quad -\frac{\partial}{\partial x_i} \left(K_{ij}^\psi \frac{\partial T^\psi}{\partial x_j} \right) = f \quad \text{in } \Omega^\psi \in R^d \quad (4.4)$$

$$\text{Temperature BC:} \quad T^\psi = c_1 \quad \text{on } \partial\Omega_1^\psi \quad (4.5)$$

$$\text{Heat flux BC:} \quad K_{ij}^\psi \frac{\partial T^\psi}{\partial x_j} n_i = c_2 \quad \text{on } \partial\Omega_2^\psi \quad (4.6)$$

$$\text{Fourier's law of conduction:} \quad q_i^\psi = -K_{ij}^\psi \frac{\partial T^\psi}{\partial x_j} \quad \text{in } \Omega^\psi \quad (4.7)$$

Where, $\partial\Omega_1^\psi$ and $\partial\Omega_2^\psi$ are the temperature and heat flux prescribed boundaries respectively such that $\partial\Omega_1^\psi \cup \partial\Omega_2^\psi = \partial\Omega^\psi$.

The asymptotic expansion approximation of temperature field can be written as

$$T^\psi(x) = T_0(x) + \xi T_1(x, y) + \xi^2 T_2(x, y) + \dots \quad (4.8)$$

Here, the first term of the expansion is the globally varying temperature field, while further terms are the local fluctuations in the temperature field due to the presence of heterogeneity. Heterogeneity may be in the form of

reinforcements or voids. Using the expansion (4.8) into (4.4) and (4.6) and simplifying them using some mathematical manipulation under periodicity boundary condition [115], one can obtain the Fourier's law in terms of average quantities and homogenized constant thermal conductivity given as [41]

$$\langle q_i \rangle = -K_{ij}^H \left\langle \frac{\partial T}{\partial x_j} \right\rangle \quad (4.9)$$

Where, $\langle q_i \rangle$ is the average heat flux, $\left\langle \frac{\partial T}{\partial x_j} \right\rangle$ is the average temperature gradient and K_{ij}^H is the homogenized thermal conductivity. Average quantities in two-phase domains are defined as

$$\langle q_i \rangle = \frac{1}{V} \left[\int_{V_1} q_i^{(1)} dv_1 + \int_{V_2} q_i^{(2)} dv_2 \right] \quad (4.10)$$

$$\left\langle \frac{\partial T}{\partial x_j} \right\rangle = \frac{1}{V} \left[\int_{V_1} \frac{\partial T^1}{\partial x_j} dv_1 + \int_{V_2} \frac{\partial T^2}{\partial x_j} dv_2 + \frac{1}{S} \int_s [T] n_j ds \right] \quad (4.11)$$

Where ' V ' is the volume of the unit cell domain ' Θ '. The superscript '1' and '2' represent the local phases at any scale. $[T]$ is the temperature jump occurs at the interface (due to imperfectness) of two phases having interfacial surface area " S " and " n_j " as a unit outward normal (See Fig. 4.3(c)). The third term in equation (4.11) disappears for the perfectly bonded interface. Homogenized thermal conductivity K_{ij}^H is defined as

$$K_{ij}^H = \frac{1}{|\Theta|} \int_{\Theta} K_{ij}(y) \left(\delta_{jk} + \frac{\partial \chi_j(y)}{\partial y_k} \right) d\Theta \quad (4.12)$$

Here, $\chi_j(y)$ is temperature influence function which establishes the relation between local temperature and global temperature gradient as follows

$$T_1 = \chi_j(y) \frac{\partial T_0}{\partial x_j} \quad (4.13)$$

The detailed description of every term, as well as a complete derivation of equation (4.9) through the AEH method, is given in **Appendix-A**. Implementation of equation (4.9)-(4.11) at two levels of length scales of multidirectional C/C composite is discussed in the following subsequent sections.

4.3.2 Bundle level

The basic constituents of the Carbon/Carbon bundles are carbon fibers and a matrix that makes a unidirectional composite. The effective Fourier Law of Heat Transfer in terms of the asymptotic homogenization method (AHM) at the bundle level can be expressed as

$$\langle q_i^{(b)} \rangle = -K_{ij}^{bH} \left\langle \frac{\partial T^b}{\partial x_j} \right\rangle \quad (4.14)$$

Here, $\langle q_i^{(b)} \rangle$ is the average uniform heat flux in the bundle, $\left\langle \frac{\partial T^b}{\partial x_j} \right\rangle$ is the average temperature gradient in the bundle, and K_{ij}^{bH} is the effective conductivity matrix for the bundle. The average quantities are calculated as

$$\langle q_i^{(b)} \rangle = \frac{1}{V} \left[\int_{vf} q_i^{(f)} dv_f + \int_{vm} q_i^{(m)} dv_m \right] \quad (4.15)$$

$$\left\langle \frac{\partial T}{\partial x_j} \right\rangle^b = \frac{1}{V} \left[\int_{vf} \frac{\partial T^f}{\partial x_j} dv_f + \int_{vm} \frac{\partial T^m}{\partial x_j} dv_m + \frac{1}{S_{fm}} \int_s [T] n_j ds \right] \quad (4.16)$$

Here, $q_i^{(f)}$ and $q_i^{(m)}$ are the local variations of heat flux in fiber and matrix, respectively. Similarly, $\frac{\partial T^f}{\partial x_j}$ and

$\frac{\partial T^m}{\partial x_j}$ are the local variations of the temperature gradients, respectively. vf and vm stand for the volume of

the fiber and the matrix, respectively. $[T]$ indicates the temperature jump at the fiber/matrix interface having a surface area S_{fm} with unit normal n_j . Thus, the effective response of the bundle can be found using the properties of the constituents and utilizing the equations from 4.14 to 4.16.

4.3.3 Composite level

The main material constituents at the composite level are fiber bundles and matrix. Similar to the bundle scale, the effective Fourier law for the composite at mesoscale can be expressed as

$$\langle q_i \rangle^c = -K_{ij}^{cH} \left\langle \frac{\partial T}{\partial x_j} \right\rangle^c \quad (4.17)$$

Here, $\langle q_i \rangle^c$ is the average heat flux, $\left\langle \frac{\partial T}{\partial x_j} \right\rangle^c$ average temperature gradient, and K_{ij}^{cH} is the effective conductivity of the composite unit cell. The average quantities can be expressed as

$$\langle q_i \rangle^c = \frac{1}{V} \left[\int_{vb^k} q_i^{(b)} dv_{b^k} + \int_{vm} q_i^{(m)} dv_m + \int_{vv} q_i^{(v)} dv_v \right] \quad (4.18)$$

$$\left\langle \frac{\partial T}{\partial x_j} \right\rangle^c = \frac{1}{V} \left[\int_{vb^k} \frac{\partial T^{b^k}}{\partial x_j} dv_{b^k} + \int_{vm} \frac{\partial T^m}{\partial x_j} dv_m + \int_{vv} \frac{\partial T^v}{\partial x_j} dv_v + \frac{1}{S_{bm}} \int [T] n_j ds \right] \quad (4.19)$$

Here $q_i^{(b)}$, $q_i^{(m)}$ and $q_i^{(v)}$ are the local variations of heat flux in the fiber bundle, matrix, and voids. Similarly,

$\frac{\partial T^b}{\partial x_j}$, $\frac{\partial T^m}{\partial x_j}$, and $\frac{\partial T^v}{\partial x_j}$ are the local variations of the temperature gradients respectively. vb^k is the volume

of the k^{th} bundle and S_{bm} is the surface area of the bundle/matrix interface with the unit normal n_j . $[T]$ is the temperature jump occurring at the bundle/matrix interface due to partial debonding of the interface. One can easily find the effective response of the composite using equation 4.17 to 4.19 along with suitable boundary conditions.

These two levels are connected by using the effective response of the bundles obtained at the micro-level as an input to the composite level's homogenization analysis. This can be done in two ways, either simultaneously (coupled) or sequentially (uncoupled) [116]. Recently, Xu et al. have used a multilevel finite element approach with the real-time coupling of scales for the analysis of the super-elasticity behavior of shape memory alloy (SMA) [117] and pseudo-elastic behavior of SMA fiber-reinforced composite [118]. Dasgupta et al. [41] have utilized the AHM to solve the unit cell problem for effective thermal conductivity of plain-weave fabric composite in an uncoupled way. In the present study, the RVEs were reconstructed from the realistic microstructure. Therefore, it includes complex shapes which inherently increase the degrees of freedom of the system.

Here, it is assumed that the problem is piecewise linear and utilizes the uncoupled process of homogenization. An algorithm of the procedure is presented later in Fig. 4.5. AHM is clubbed with finite element discretization and periodic boundary conditions for two-scale analysis.

4.3.4 Boundary conditions

Since the asymptotic homogenization method is used to derive the effective properties of each unit cell, it is hypothesized that the mesoscale properties of the composite are the periodic functions of microlevel heterogeneities. This means that all the fluctuations will vanish at the boundaries of the unit cells. Thus, the following boundary conditions can be obtained by imposing the symmetry and anti-symmetry conditions on the heat flux and temperature gradients, which will be similar to the work of Li [119].

When heat flow is in the x-direction,

$$\left. \begin{aligned} \frac{\Delta T_x}{\Delta l_x} = 1 \text{ for faces perpendicular to the } x - \text{direction} \\ \frac{\Delta T_y}{\Delta l_y} = \frac{\Delta T_z}{\Delta l_z} = 0 \text{ for others} \end{aligned} \right\} \quad (4.20)$$

When heat flow is in the y-direction,

$$\left. \begin{aligned} \frac{\Delta T_y}{\Delta l_y} = 1 \text{ for faces perpendicular to } y - \text{direction} \\ \frac{\Delta T_x}{\Delta l_x} = \frac{\Delta T_z}{\Delta l_z} = 0 \text{ for others} \end{aligned} \right\} \quad (4.21)$$

When heat flow is in the z-direction,

$$\left. \begin{aligned} \frac{\Delta T_z}{\Delta l_z} = 1 \text{ for faces perpendicular to the } z - \text{direction} \\ \frac{\Delta T_y}{\Delta l_y} = \frac{\Delta T_x}{\Delta l_x} = 0 \text{ for others} \end{aligned} \right\} \quad (4.22)$$

Here, $\frac{\Delta T_x}{\Delta l_x}$, $\frac{\Delta T_y}{\Delta l_y}$, and $\frac{\Delta T_z}{\Delta l_z}$ are the temperature gradients; and Δl_x , Δl_y , and Δl_z are unit cell dimensions in x, y, and z directions respectively. Fig. 4.4 shows the systematic representation of the boundary conditions. Fig. 4.4 (a) corresponds to the boundary condition (4.20) where the temperature gradient is in the x-direction only. The face 'x=0' is kept at a higher temperature and face 'x= Δl_x ' at a lower temperature along the x-direction, whereas the faces perpendicular to other directions are adiabatic. This allows the heat to flow in positive x-direction only. Similarly, Fig. 4.4 (b) and (c) represent the boundary conditions in y and z directions corresponding to the boundary conditions (4.21) and (4.22) respectively. One can easily obtain the effective thermal conductivities for each unit cell by using the boundary conditions one by one. An algorithm of the process is also presented in Fig. 4.5 for a better understanding of the readers.

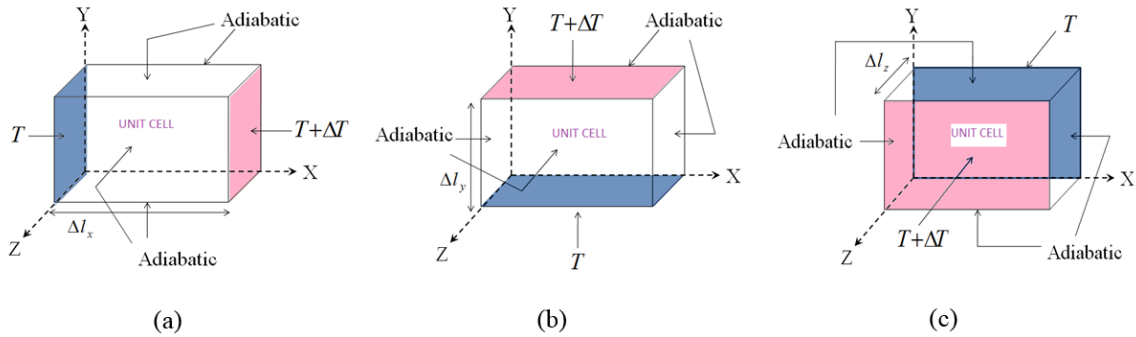


Fig. 4.4 Temperature gradient as a boundary condition in (a) x-direction, (b) y-direction, and (c) z-direction and keeping other faces adiabatic

For a global increment in temperature, the micro-unit cells were first solved for three independent load cases to determine the effective properties of bundles. Then the effective properties of the bundles were used in the analysis of the meso unit cells. At the meso level, three randomly selected unit cells of the composite were analyzed for three load cases, and the average of these three-unit cells is considered as the effective property for the composite. This procedure is repeated for every temperature increment to find the effective homogenized thermal conductivities of the composites as a function of temperature.

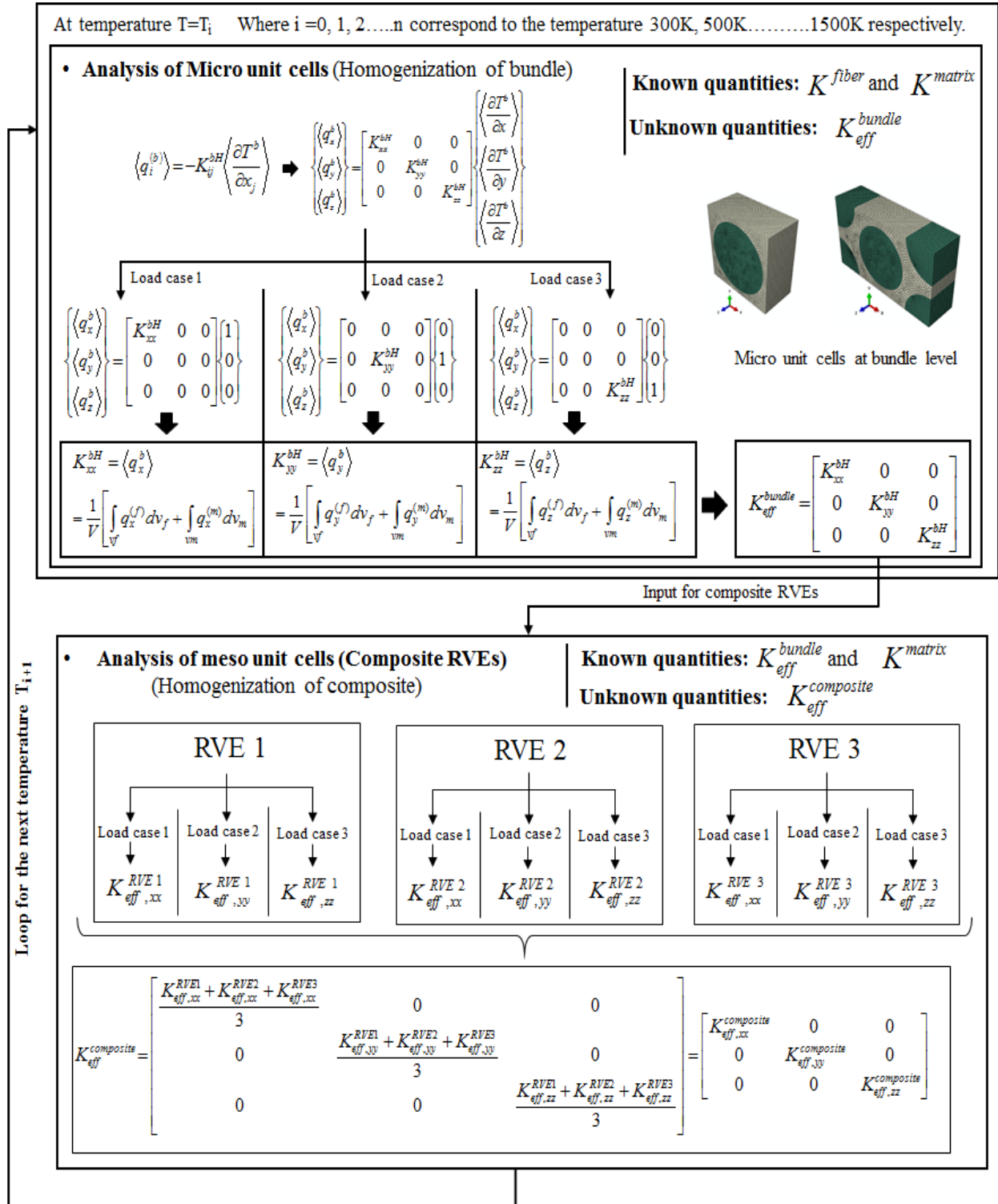


Fig. 4.5 Flow chart of the two-scale homogenization process.

4.4 Numerical analysis

The sequential homogenization process is considered in the present study as it allows us to conduct separate analyzes at both scales. The numerical work consists of performing a steady-state heat transfer analysis at both scales (micro and meso) using the previously discussed boundary conditions in the finite element method to calculate the effective response. The finite element models of 3DH and 4DIN C/C composites along with their micro-unit cells as developed in the last section of the chapter-3 are considered in this study. The temperature-dependent thermal properties of constituents (fiber and matrix) are considered from the literature [61] and can be found in Table 2.1 (chapter-2).

The effect of the imperfect interface was considered through the modeling of the interface with a discrete surface attached to each phase at both scales. The equivalent gap conductance was utilized to represent the effect of the imperfectness at such interfaces. The thermal gap conductance (TGC) is considered as $1.5 \times 10^5 \text{ W/m}^2\text{K}$ that was reported by Dong K et al. [65-66]. It should also be noted that as the reconstructed FE meshes contain big voids (as discussed in chapter-3), an assumption was made at mesoscale that the big voids are inactive in the heat transfer.

4.5 Results and discussion

4.5.1 Micro-scale analysis (Effective thermal conductivity of bundles)

The micro-scale unit cells of the fiber bundles of 3DH and 4DIN C/C composite are analyzed under the previously discussed periodic boundaries individually to get effective properties using asymptotic homogenization. Temperature distribution and heat flux contour within the phases of the hexagonal and the square packed unit cells are shown in Fig. 4.6. By exploiting the advantage of the symmetry in transverse directions, two cases will be discussed: 1) one parallel to the fibers axis and 2) perpendicular to the fibers axis. Fig. 4.6 (a) and (b) show the temperature profile in the transverse direction of the hexagonal and the square packed unit cells respectively and their corresponding heat fluxes are shown in Fig. 4.6 (c) and (d). Similarly, Fig. 4.6 (e) and (f) present the temperature profile in the longitudinal direction of the hexagonal and the square packed unit cells respectively and their corresponding heat fluxes are given in Fig. 4.6 (g) and (h) respectively. It is very clear that the matrix is the major carrier of heat in transverse directions. This is obvious as the thermal conductivity of the matrix is much larger than the transverse thermal conductivity of the fiber. In the longitudinal direction, the heat transfer capacity of the fiber and the matrix is based on their volume fractions as shown in Fig. 4.6 (g) and (h).

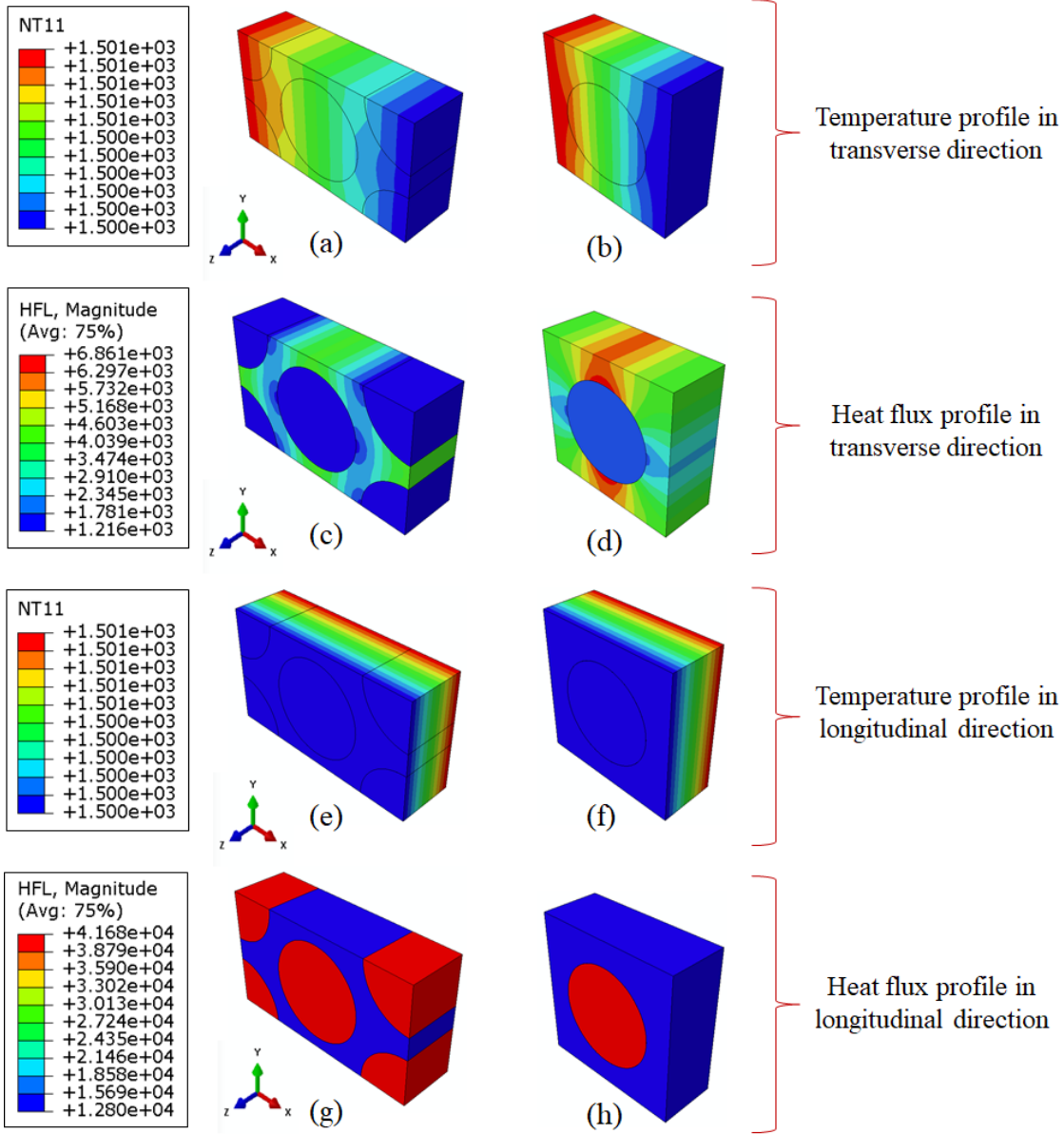


Fig. 4.6 (a, b) Temperature profile in the transverse direction, (e, f) Temperature profile in the longitudinal direction, (c, d) Heat flux contour in the transverse direction, and (g, h) Heat flux contour in the longitudinal direction at 1500K

To model the effect of the imperfect interface, it is assumed that heat was effectively transferred through a very close gap between two surfaces of different phases. The effective conductance of the gap region varies from $1.5 \times 10^5 \text{ W/m}^2\text{K}$ (represents an almost perfect condition) to $1.5 \times 10^3 \text{ W/m}^2\text{K}$ (represents the purely deboned condition). The obtained temperature profiles for the square and the hexagonal unit cells are shown in Fig. 4.7 (a, b, c, and d) and 4.6 (e, f, g, and h) respectively.

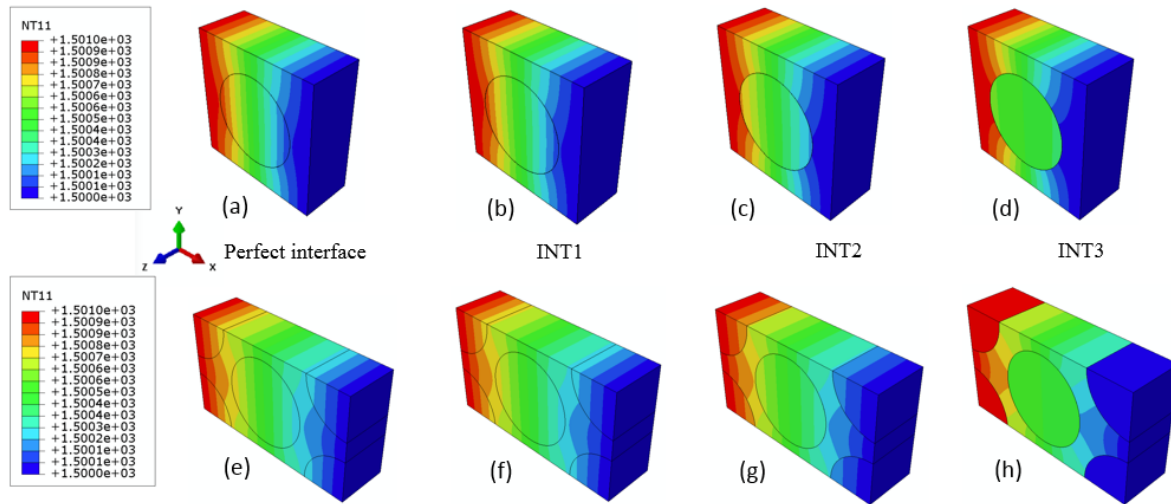


Fig. 4.7 Temperature distribution in micro-unit cells at different thermal gap conductance values.

From Fig. 4.7, it is revealed that the temperature profile for the thermal conductance value $1.5 \times 10^5 \text{ W/m}^2\text{K}$ (INT1) is almost similar to the profile for the perfect interface (P). There is an appreciable temperature jump at the fiber/matrix interface that occurs as the value is decreased by one order ($1.5 \times 10^4 \text{ W/m}^2\text{K}$ i.e. INT2). A further decrease of the thermal conductance of the gap by one order ($1.5 \times 10^3 \text{ W/m}^2\text{K}$ i.e. INT3) causes the fiber to be almost isolated which means there is a complete debonding at the interface. The effective thermal conductivities of bundles in the longitudinal and the transverse directions for different values of thermal gap conductance are obtained through the homogenization process and are presented in Table 4.1.

Table 4.1 Variations of effective thermal conductivity of bundles (of RVE3C) at 1500K with different interfacial gap conductance values

Thermal gap conductance value ($\text{W/m}^2\text{K}$)	Thermal conductivity of square packing (W/mK)		Thermal conductivity of hexagonal packing (W/mK)	
	Longitudinal	Transverse	Longitudinal	Transverse
Perfect interface	91.91	35.58	120.08	27.37
1.5×10^5	91.91	35.25	120.04	26.95
1.5×10^4	91.89	32.71	120.01	24
1.5×10^3	91.86	26.92	120.01	16.49

The study concludes that the effect of the imperfect conditions on the effective longitudinal conductivity is not predominant as compared to the effective transverse conductivity. The percentage change in effective transverse conductivities of square packed bundles is approximately 1%, 8%, and 25% for gap conductance values $1.5 \times$

10^5 , 1.5×10^4 , and 1.5×10^3 W/m²K, respectively. The same for the hexagonal packed bundles is 1.5%, 12.3%, and 40% for gap conductance values 1.5×10^5 , 1.5×10^4 , and 1.5×10^3 W/m²K respectively.

Secondly, it is observed through reconstructed images that the cross-sections of the fiber bundle were distorted during processing that leads to the changes in fiber volume fractions. To include these fluctuations, separate RVEs were considered for the individual bundles based on the fiber volume fraction. Each RVE is analyzed for the full range of temperature, and the interface is modeled by considering the gap conduction value of 1.5×10^5 W/m²K throughout the simulations. The results are separately presented for rectangular and circular bundles of 3DH in Fig. 4.8 (a) and (b), respectively. The effective thermal conductivities of the bundles have maintained the decreasing trend of the basic fiber or matrix properties with temperature. The difference in the longitudinal and transverse TCs of circular bundles is larger as compared to the rectangular ones. It is observed that the fluctuation in the values of longitudinal TCs increases with temperature increase while it decreases with temperature increase for transverse TCs. The standard deviation (SD) in longitudinal TCs of rectangular bundles is about 3.73 at 300 K and 8.3 at 1500K. The same for circular bundles is noticed as 2.92 and 6.48 at respective temperatures.

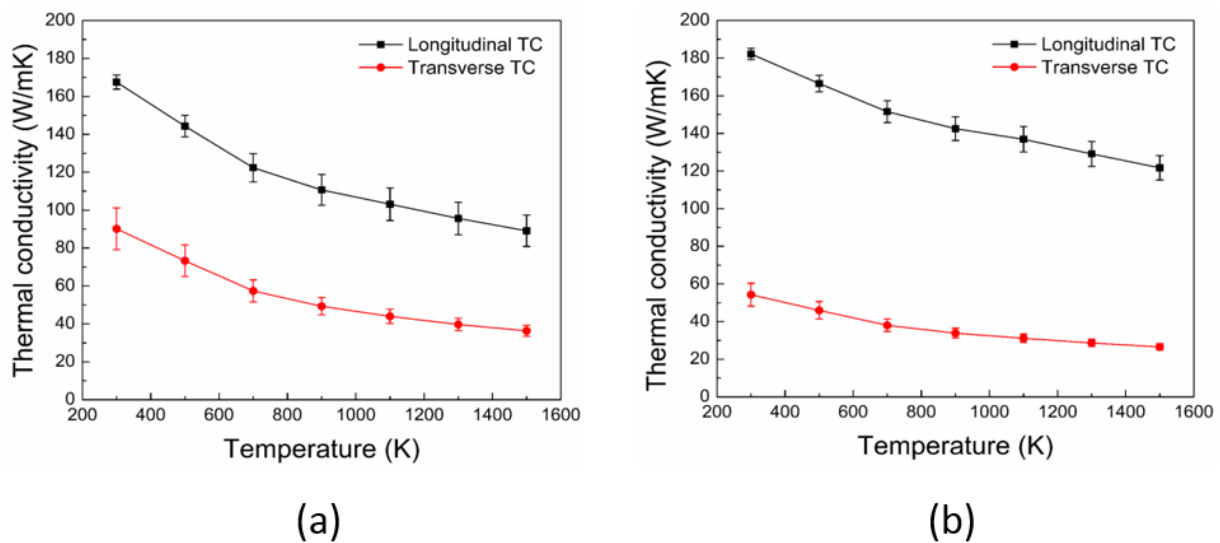


Fig. 4.8 Variations of effective thermal conductivity of (a) Rectangular bundle and (b) Circular bundle of 3DH C/C composite.

In the case of transverse TCs, the trend was reversed and the SD in rectangular bundles is 10.98 at 300K and 2.86 at 1500K, respectively. However, the SD in circular bundles is 6.04 and 1.7 for respective temperatures. The results of the TC at corresponding temperatures are presented in Table 4.2.

All the circular bundles of 4DIN C/C composite have a higher volume fraction than 3DH and they are closely packed. A similar approach was adopted to include the bundle distortion effects in the unit cells and the results of TCs for the full range temperature are presented in Fig. 4.9.

Table 4.2 Fluctuation in effective thermal conductivity of bundles in 3DH C/C composite

Direction	Temperature	ETC of the rectangular bundle		ETC of the circular bundle	
		Mean (W/mK)	SD	Mean (W/mK)	SD
Longitudinal	300 K	167.54	3.73	182.18	2.92
	1500 K	89.11	8.3	121.72	6.48
Transverse	300 K	90.17	10.98	54.3	6.04
	1500 K	36.35	2.86	26.56	1.7

ETC: effective thermal conductivity

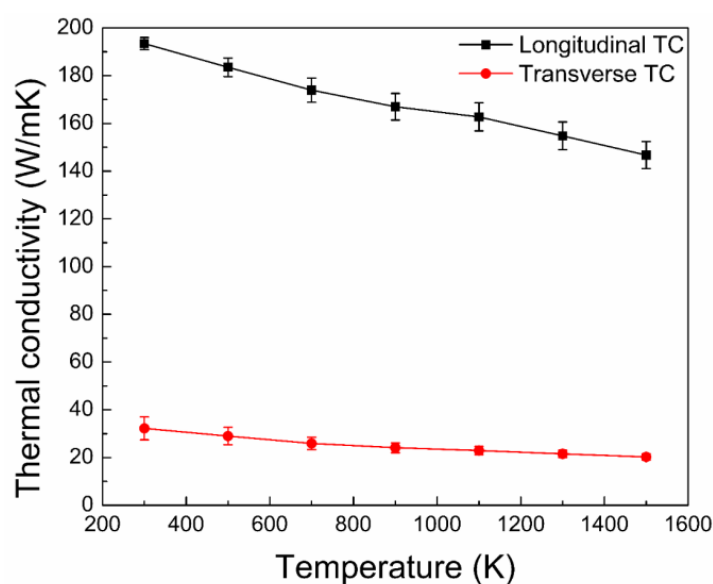


Fig. 4.9 Longitudinal and transverse thermal conductivity of bundles in 4DIN composite.

A similar trend for the variation of the effective TCs with respect to the temperature increase is observed in 4DIN. The SD in longitudinal TC of bundles is approximately 2.55 at 300 K and 5.68 at 1500K, and the same for transverse TC is obtained as 4.80 at 300K and 1.32 at 1500K. Next, these effective properties are used as an input for the upper scale analysis. The results of the upper-scale analysis are discussed in detail in the next section.

4.5.2 Effective thermal conductivity of 3DH C/C composite

The steady-state heat transfer analysis was performed on three unit cells of 3DH C/C composite. Figs. 4.10 (a, b, and c) correspond to the temperature variation in x, y, and z directions from 1500K to 1501K, and the corresponding heat fluxes are shown in Figs. 4.10 (d, e, and f). It is clear from the figures that the fiber in the longitudinal direction is the major carrier of the heat. It is obvious as the TC in the longitudinal direction

is almost 4 times higher than the transverse TC and nearly two times higher than the matrix TC. Fig. 4.10 (g), (h), and (i) show the heat flux distribution at low temperature (i.e., from 300K to 301K). It is clear from these figures that the matrix has almost equal participation in heat transfer at low temperatures compared to the longitudinal bundles and that the transverse bundles have the least heat flux. Apart from this, some patches of low heat flux are also observed near the void boundary. Moreover, the heat transfer mechanism for the 3DH is complex and cannot be explained through analogies such as the rule of mixture, shear stress, and electrical analogy.

To evaluate the effect of the interfacial gap conductance on the effective thermal conductivity of the composite, the analysis was performed on the same unit cell at 1500K. The thermal gap conductance value is varied in the same range as in the case of the lower length scale (i.e., from 1.5×10^3 to 1.5×10^5 W/m²K). Fig. 4.11 shows the obtained temperature profile and heat flux contour. Fig. 4.11 (a), (b), (c), and (d) show the temperature profile in the different phases of the unit cell when the heat is transferred in the x-direction for different gap conductance values. In the first two cases (i.e., perfect bonding and TGC= 1.5×10^5 W/m²K), the contours of the temperature are similar while a significant jump is observed in the next two cases. Figs. 4.11 (e), (f), (g), and (h) show the corresponding contours of the heat flux within the composite phases. As discussed earlier, longitudinal bundles are the major carriers of the heat in the composite while the matrix is moderately active in heat transfer. The contribution of the transverse bundles is the least in all. As the gap conductance is decreased, the contribution of the transverse bundles further decreases. Even the surrounding regions of the voids are affected by the gap conductance value as the heat flux is reduced nearly by a factor of 2 in the last two cases (i.e., TGC= 1.5×10^4 and 1.5×10^3 W/m²K). To elaborate on the effect of interface gap conductance on temperature distribution, a path 'A-F' is chosen in the direction of heat flow, as shown in Fig. 4.12(a). The temperature profiles along 'A-F' at different conductance values are shown in Fig. 4.12(b). It is clear from this figure that as the gap conductance is reduced, the temperature gradient in the different phases also drops and the jump in the temperature values increases at the interface.

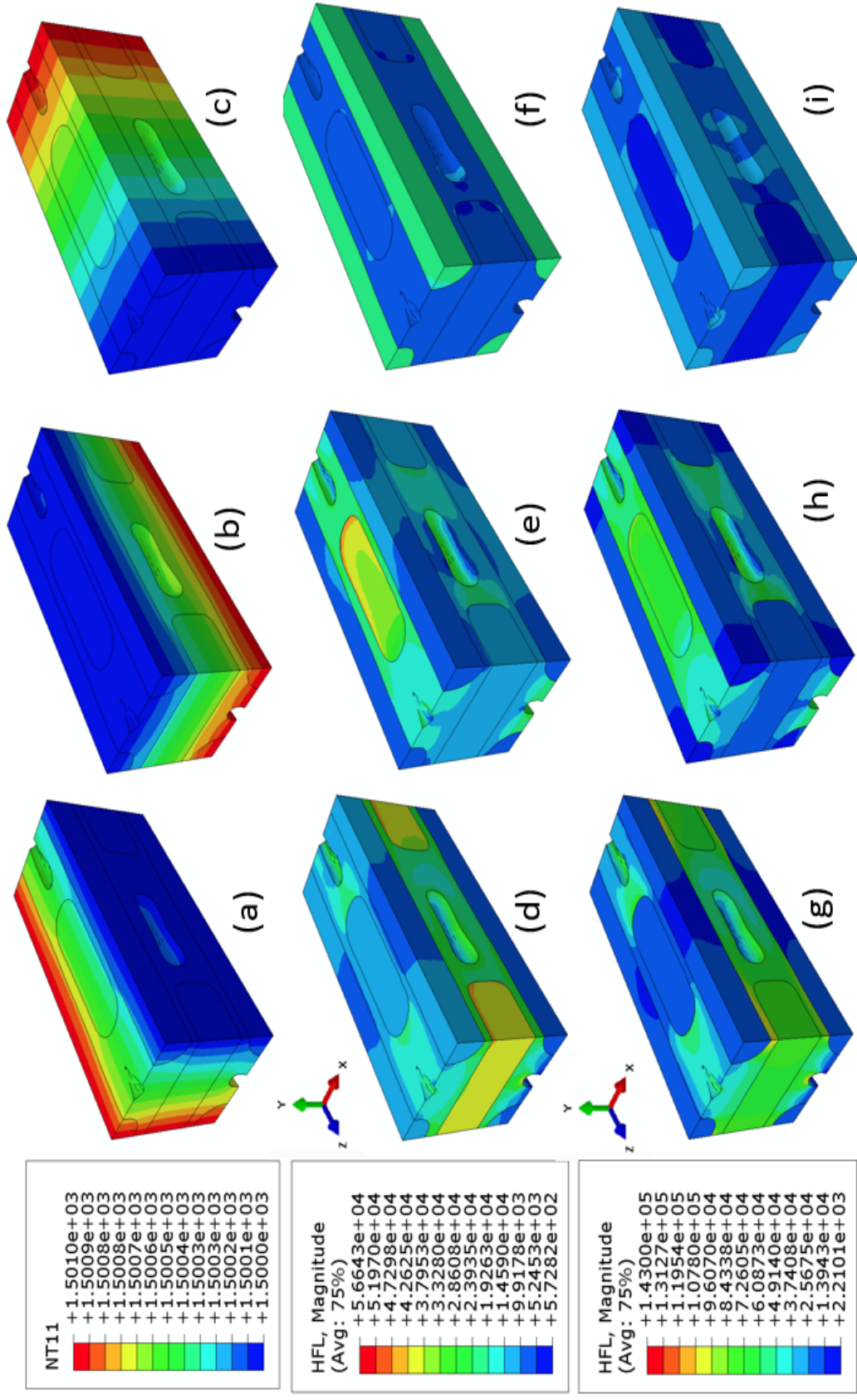


Fig. 4.10 (a, b, and c) Temperature profile (d, e, and f) Heat flux contour at 1500K (g, h, and i) Heat flux contour at 300K in 3DH C/C composite (In x, y, and z direction respectively from left to right).

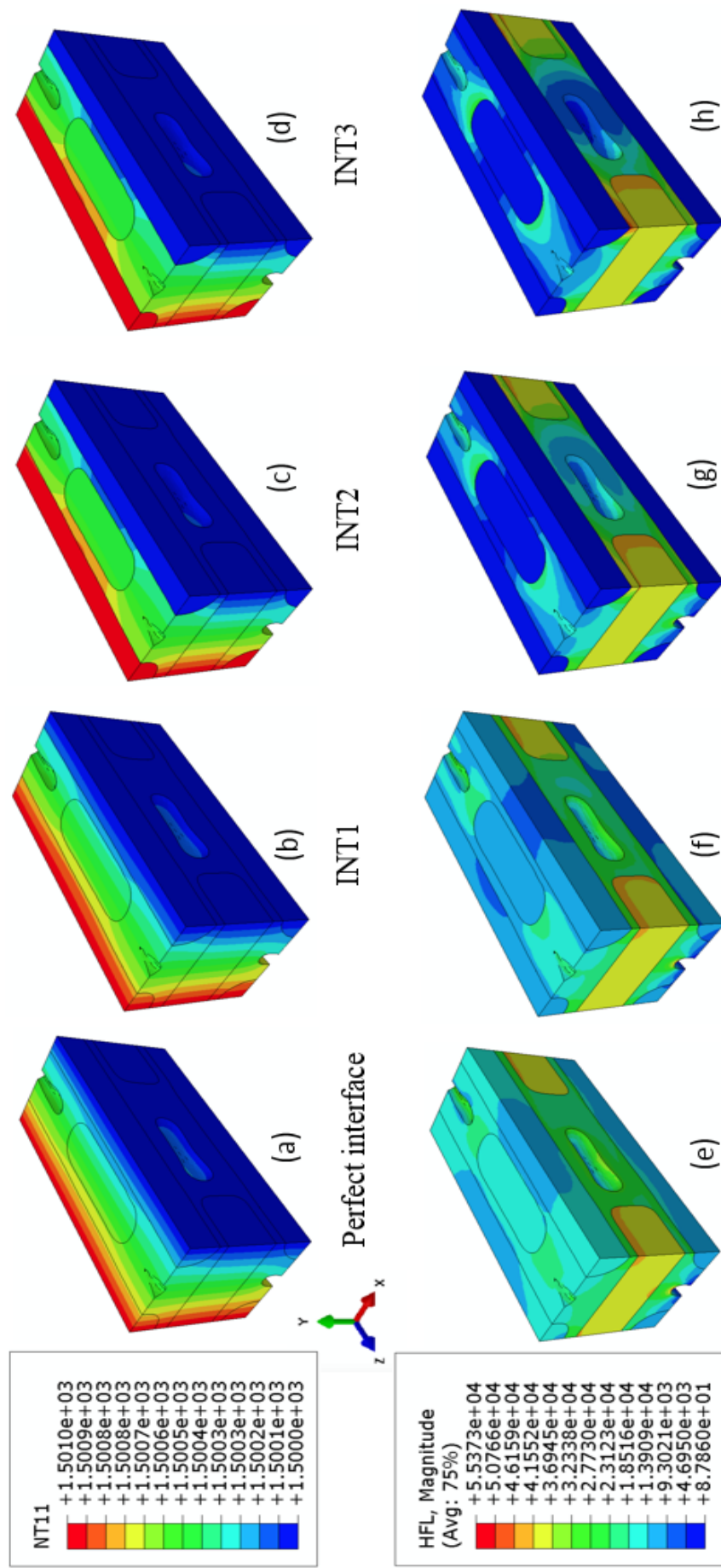


Fig. 4.11 (a, b, c and d) Temperature profile and (e, f, g, and h) corresponding heat flux contour of 3DH (RVE 3C) composite unit cell at 1500K for different interface types. Thermal conductance values across the interface.

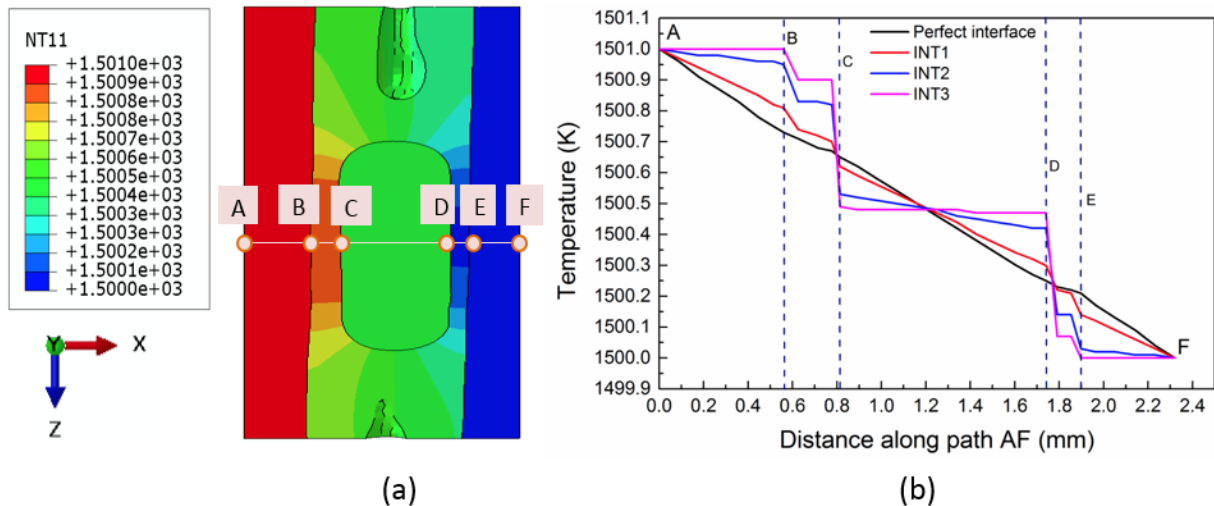


Fig. 4.12 (a) Temperature profile in x-direction and path AF crossing the bundle/matrix interfaces and (b) Plot of temperature variation along the path A-F in RVE 3C at 1500K for different interface conditions.

The steady-state simulations for the effective thermal conductivities are performed on all three RVEs of 3DH C/C composite for the full range of temperature (300-1500K). The two interface conditions i.e., perfectly bonded and imperfectly bonded (partially debonded), were considered. It was assumed that the bundle interfaces are partially debonded and their behavior closely modeled by taking the gap conductance equal to 1.5×10^5 W/m²K. The mean values of the TC for respective temperatures are plotted in Fig. 4.13 and the results of the in-plane direction are compared with the one those obtained from the experiment.

In Fig. 4.13(a), it is observed that the perfect bonded condition at the upper scale has closely predicted the thermal behavior of the composite at some temperatures while the partially debonded condition has slightly underestimated the TC values. The overall trend of the curve is similar to the one obtained experimentally. Fig. 4.13(b) shows the predicted values of the transverse TC for the entire temperature range and it was noted that both conditions (perfectly and imperfectly bonded) are converging towards each other at higher temperatures. This suggests that the effect of the interfacial gap on effective TCs is more at low temperatures and reduces considerably at high temperatures. The TC in the in-plane direction was reduced by 7.98%, while out-of-plane TC is reduced by 2.8% compared to the perfect bonded case at 1500K. The values of the reduction for the same at 300K are 14.85% and 6.14%, respectively. It has also been noted that the fluctuations associated with the RVEs reduced with an increase in temperature. This shows that the uncertainties are well accounted for at lower length scales. The TC in the out-of-plane direction (Fig. 4.13(b)) is slightly greater than the in-plane directions that make the 3DH architecture nearly transversely isotropic.

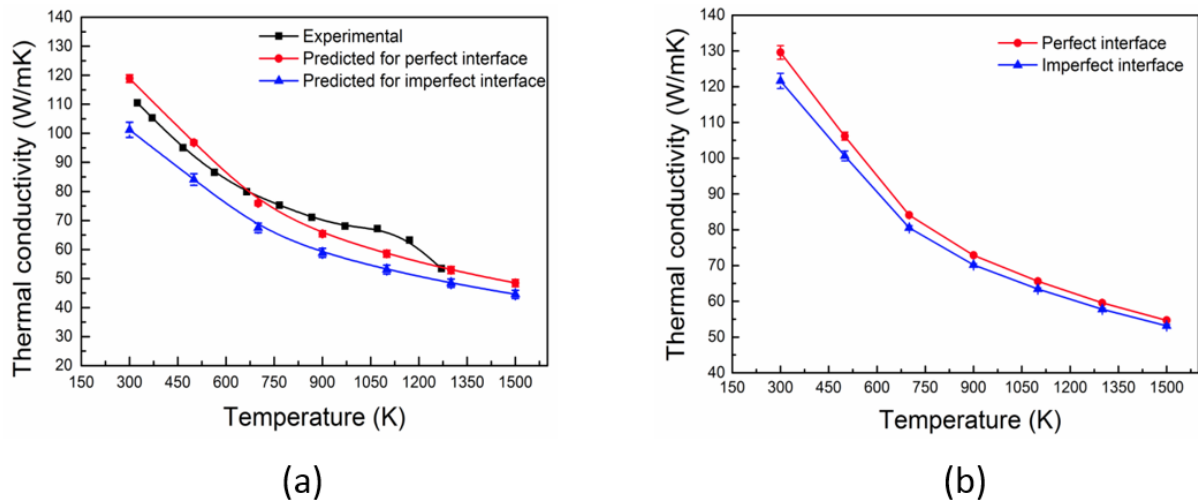


Fig. 4.13 Effective thermal conductivity of 3DH C/C composite in (a) In-plane direction and (b) Out-of-plane direction

4.5.3 Effective thermal conductivity of 4DIN C/C composite

A similar steady-state analysis was carried out to study the performance of the unit cells of 4DIN architecture. The obtained temperature distributions in x , y , and z direction are shown in Fig. 4.14(a), (b), and (c) for a perfectly bonded case. The temperature contours are more or less similar to the 3DH case. Similar to the earlier observations, longitudinal bundles are the major carrier of heat in these composites also (see Fig. 4.14(d)-(i)). It is clear from Fig. 4.14(d) that the in-plane bundles have also actively participated in the heat transfer in addition to the longitudinal bundles. In the 4DIN composite, there are no longitudinal bundles in the y -direction; hence, the major carriers of heat are in-plane bundles (refer Fig. 4.14(e)). In the case of the low-temperature heat transfer, the contribution of the in-plane bundles matches the matrix phase in x and y direction (see Fig. 4.14 (g) and (h) respectively). Due to the in-plane orientation of these bundles, the effective TC is higher than the transverse one. In the case of the z -direction, the matrix has higher heat flux values than the transverse and in-plane bundles (see Fig. 4.14(i)). The contours of the heat flux in the 4DIN composite are more complex than the 3DH composite.

Next, the effect of gap conductance was also evaluated in 4DIN C/C composite by taking the different values of the interfacial gap conductance. Four cases of the interface, similar to the 3DH composite, were considered and the results are presented in Fig. 4.15. Figs. 4.15 (a), (b), (c), and (d) show the temperature distributions for perfectly bonded, INT1, INT2, and INT3 interface conditions. In the first two cases, the temperature profiles are similar to each other. In the case of INT2, the in-plane bundle has a significant temperature jump at the interface due to which the contours within the bundles and the nearby matrix changed. For the INT3 case, the in-plane bundles are mostly isolated from the surrounding matrix. A path 'A-F' was considered as shown in Fig. 4.16(a) to study the temperature profiles. Similar to the 3DH case, reduction in the gap conductance value

caused a significant jump at the interface. The first two cases (i.e., perfect bonded and INT1) are very similar to each other. There is a significant reduction in the temperature of in-plane bundles in the last two cases, i.e., INT2 and INT3 (see Fig. 4.16(b)). The heat flux contours obtained for all four cases are presented in Fig. 4.15(e), (f), (g), and (h). It is clear from these figures that as the gap capacitance values are reduced, the heat-carrying capacity of the in-plane bundles is also lowered. It was also observed from this study that the heat flux distribution with the composite is complex due to the presence of voids and orientation of the bundles (refer Fig. 4.15(e)-(h)).

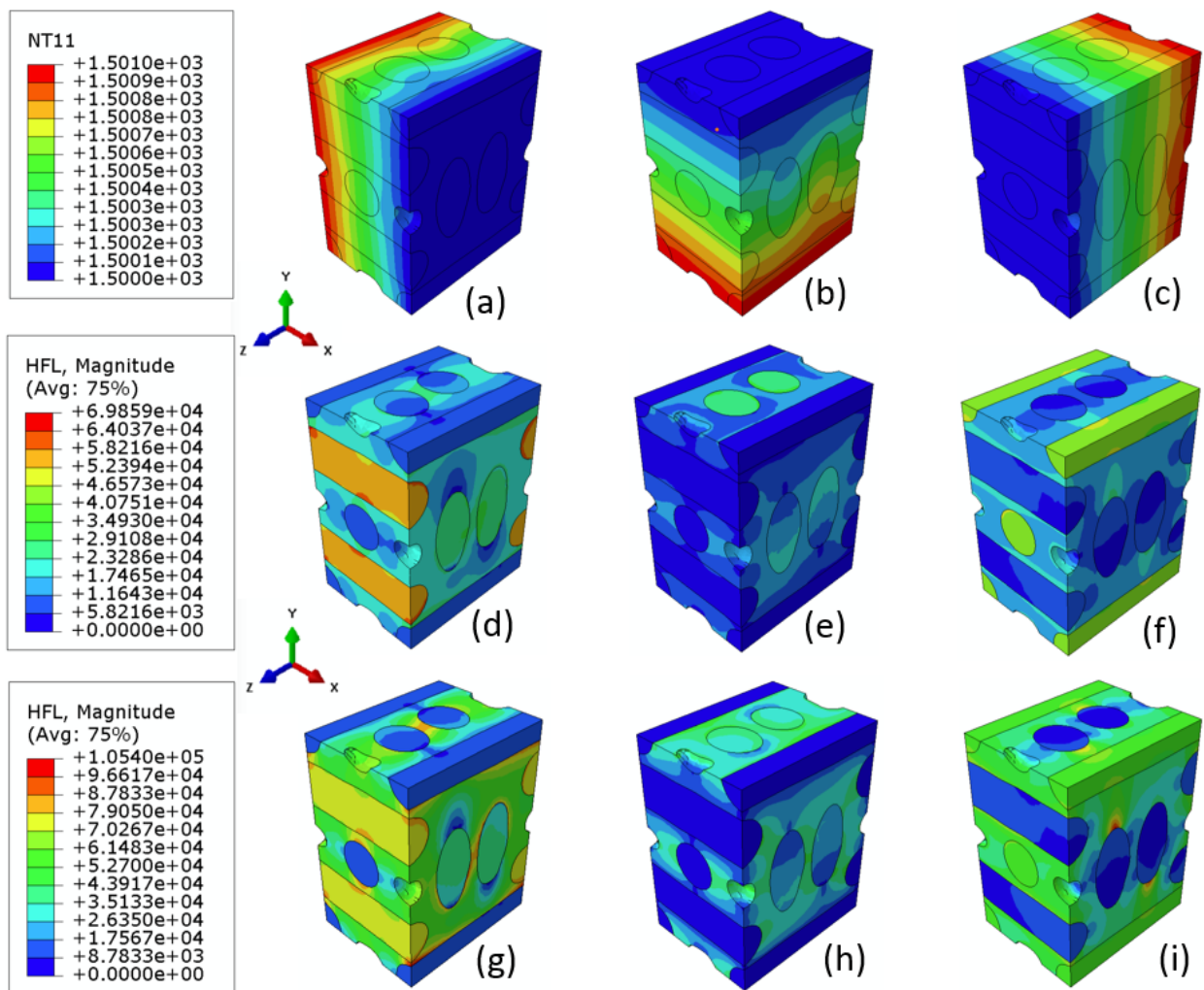


Fig. 4.14 (a, b, and c) Temperature profile, (d, e and f) Heat flux contour at 1500K, and (g, h and i) Heat flux contour at 300K in 4DIN C/C composite (in x, y, and z directions respectively from left to right).

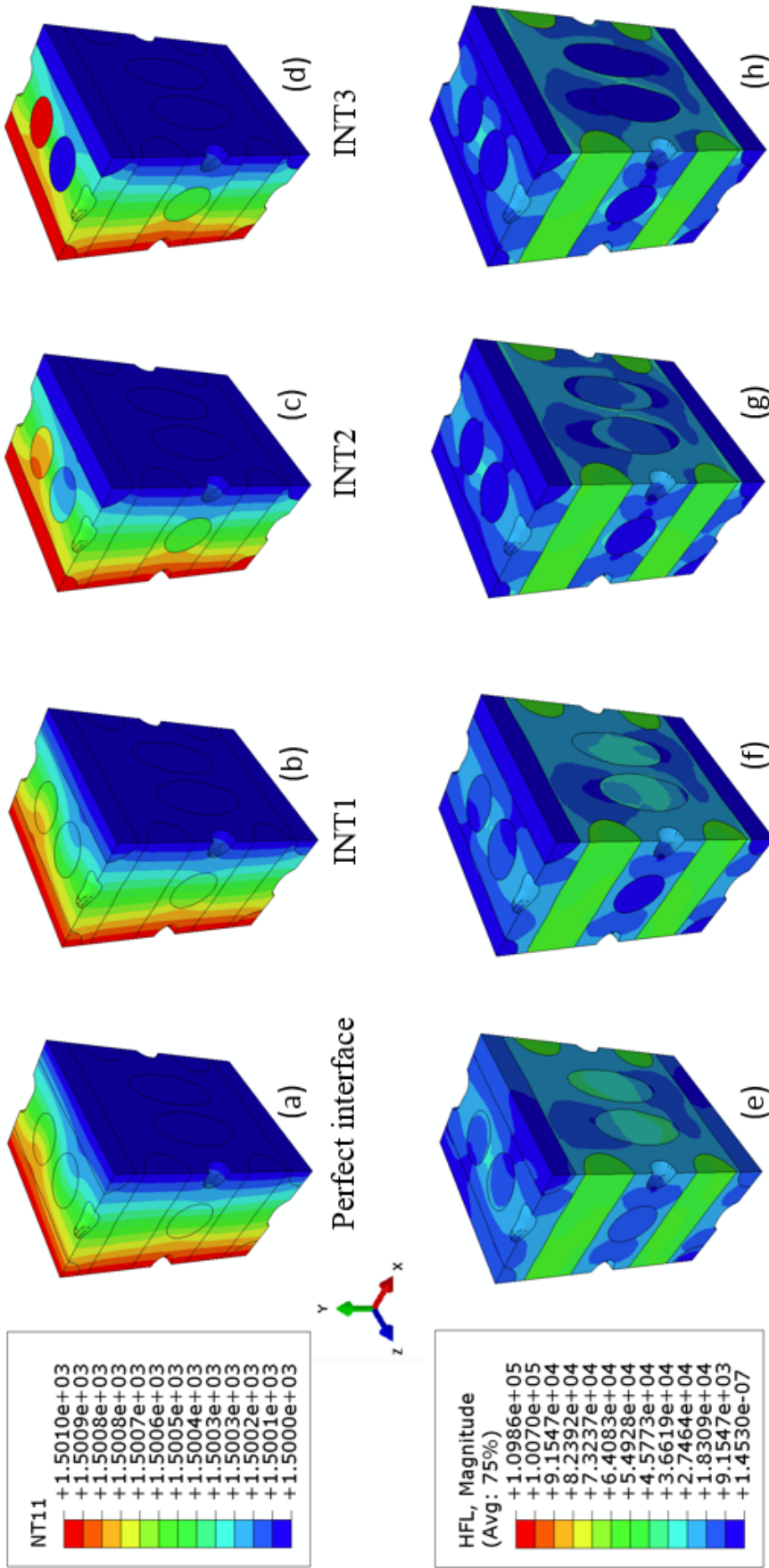


Fig. 4.15 (a, b, c, and d) Temperature profile and (e, f, g, and h) corresponding heat flux contour of 4DIN composite unit cell at 1500K for different Thermal conductance (TC) values across the interface.

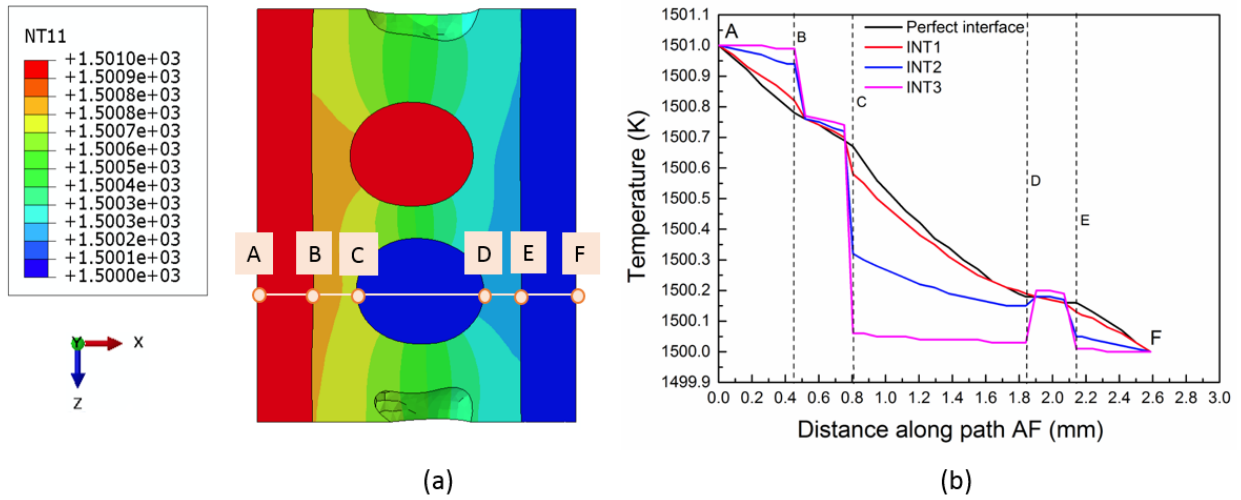


Fig. 4.16 (a) Temperature profile in x-direction and path AF crossing the bundle/matrix interfaces and (b) Plot of temperature variation along the path AF in RVE4A at 1500K for different interface conditions.

Finally, the effective TCs of the 4DIN C/C composite were evaluated for the full range of temperatures. The results for perfectly bonded and INT1 conditions are presented in Fig. 4.17.

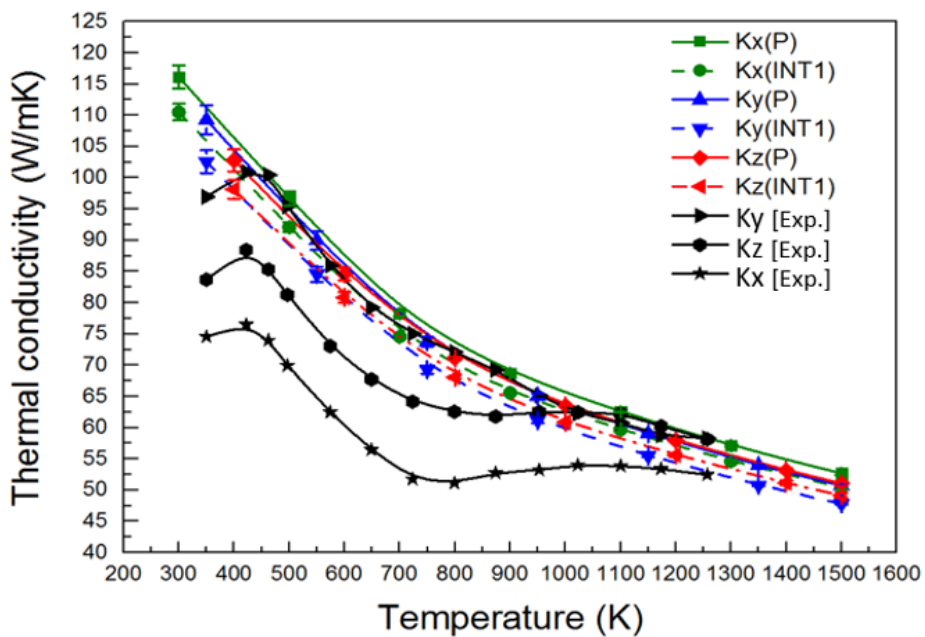


Fig. 4.17 Effective thermal conductivity of 4DIN composite with perfect and imperfect interface in all three directions and their comparison with experimental results of [37]

It was observed that the TC value for x, y, and z direction are very close to each other and the difference between them is further reduced with an increase in temperature. INT1 condition reduces the value of effective TC around 5% compared to the TC of perfectly bonded case.

The effective thermal conductivities of these composites will be used to study their behavior at severe environmental conditions like thermal shock in chapter-6. Before that, there is a need to characterize the composites for other effective properties such as an effective thermal expansion coefficient, effective elastic modulus, etc. A similar two-scale approach is considered for the prediction of effective thermal expansion coefficients of these composites in the next chapter-5.

Chapter 5

Thermal Expansion Coefficient of Multidirectional C/C Composite

In this chapter, the coefficients of thermal expansion (CTE) of the multi-directional C/C composites are explored using a two-scale asymptotic homogenization method. Firstly, the experimental procedure to determine the CTE of the C/C composites is explained. The values of CTE as a function of temperature are obtained for the 4DIN C/C composite. Then, the two-scale framework of asymptotic homogenization for the prediction of the effective CTE of a multidirectional C/C composite is presented. Later, the numerical analysis of 3DH and 4DIN C/C composites is presented using image-based finite element meshes. In the last section, the predicted FE results are compared with the existing models and experiments.

5.1 Thermal expansion coefficient

CTE is the property of any material which decides the degree of deformation under thermal loading conditions. It is another most desired property of the materials required in the structural design of the components in the aerospace industries. For materials used in high thermal applications, the CTE should be considerably low to maintain the dimensional stability. In most cases, the failure of the composite structures under severe thermal loading conditions occurred due to the mismatch of the CTEs of constituents. Therefore, it is important to explore the thermal expansion behavior of the composite materials in detail prior to designing the composite structures. In the past, researchers have put valuable effort to obtain the effective CTE of composites experimentally [33-34, 37-38, 83-85], analytically [86-95], and numerically [96-110].

In the experimental studies, a classical dilatometer is generally used to measure the elongation of the samples when they are subjected to any temperature change. Here, the same experimental setup was utilized to measure the effective behavior of multidirectional C/C composites. The details of the experiments are discussed in the next section.

5.2 Experimentation

Two cylindrical specimens: one from the in-plane (along 60° direction) and another from the out-of-plane direction, are prepared for experimental investigations. All the specimens are of a square cross-section (10x10 mm²) and around 100mm in length. An in-house developed dilatometer at Advance System Laboratory (ASL), Hyderabad, India is used to measure the CTE of composite samples in the temperature range of 200-2500°C. The schematic diagram of the CTE measurement system is presented in Fig 5.1. The experiments were conducted in an inert (N₂) atmosphere by raising the temperature of the specimen gradually at a rate of 5°C/min.

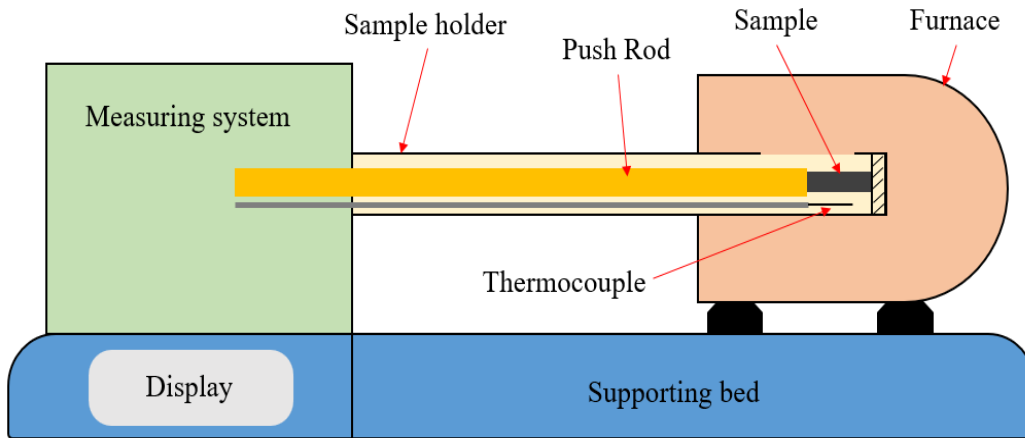


Fig. 5.1 Schematic diagram of the CTE measurement system based on the basic principle of dilatometer

The change in specimen length due to the temperature rise is measured as $\Delta L = L(T) - L(T_0)$. Here, $L(T)$ and $L(T_0)$ are the lengths of the specimen at current temperature (T) and reference initial temperature (T_0) respectively. Then, the CTE of the composite (α) for a temperature rise of ΔT is calculated using equation 5.1.

$$\alpha(T) = \frac{\Delta L}{L(T_0) \times \Delta T} \quad (5.1)$$

The average curves of the CTEs as a function of temperature are presented in Fig 5.2 for in-plane (U) and out-of-plane (Z) directions. For a temperature range of 200-2500°C, the in-plane CTE is found to be in the range of 0.56 to 2.66 x 10⁻⁶/°C, while the out-of-plane CTE varies between 0.28 to 2.5 x 10⁻⁶/°C.

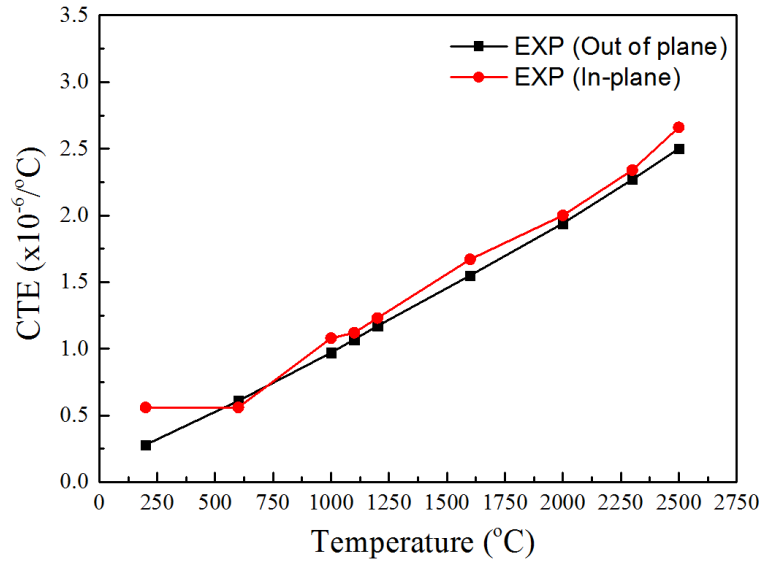


Fig. 5.2 The variation of CTEs of the 4DIN C/C composite with respect to temperature obtained through experiments

5.3 Asymptotic Expansion Homogenization

AEH is one of the most popular homogenization techniques and is widely used in the multi-scale analysis of periodic heterogeneous structures for finding the effective properties and scale bridging [114]. In this method, the heterogeneous domain is split into two levels of length scale, i.e., global (of the order of dimension of structure) and local scale (of the order of microstructure).

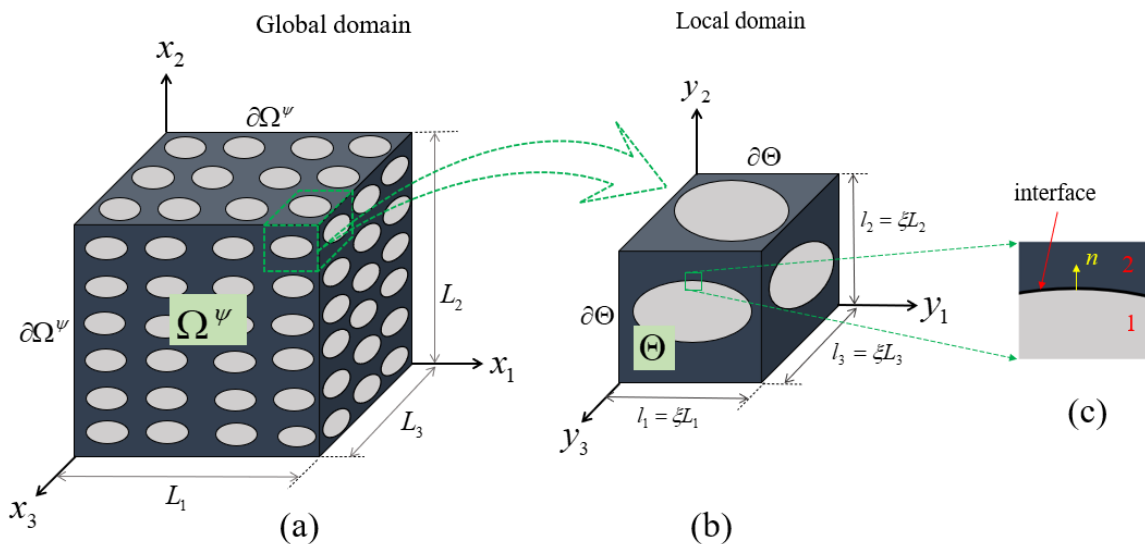


Fig. 5.3 (a) A global heterogeneous domain, (b) A local unit cell domain, and (c) Interface between two phases

Fig. 5.3 shows such local and global domains. Let x_i and y_i (with $i=1, 2, 3$) be the coordinate systems describing the global and the local state of field variables respectively. Then, the scale bridging parameter ξ can be defined as

$$\xi = \frac{x_i}{y_i} \quad \text{where } i = 1, 2, \text{ and } 3 \quad (5.2)$$

The two-scales can be effectively bridged if the scaling parameter $\xi \ll 1$. The small value of ξ ensures that the local fluctuations due to heterogeneities vanish on the boundaries ($\partial\Theta$) of the local domain (Θ) [114] (see Fig. 5.3(b)).

Consider the following equations describing the elastostatics state of the composite domain $\Omega^\psi \in R^3$ having an outer boundary, $\partial\Omega^\psi$ as shown in Fig. 5.3 (a).

$$\sigma_{ij,j}^\psi + F_i^\psi = 0 \quad \text{in } \Omega^\psi \quad (5.3)$$

$$\sigma_{ij}^\psi = C_{ijkl}^\psi \left((\varepsilon_{kl}^\psi)_{Tot} - (\varepsilon_{kl}^\psi)_{Th} \right) = C_{ijkl}^\psi \left((\varepsilon_{kl}^\psi)_{Tot} - \alpha_{kl}^\psi \times \Delta T \right) \quad \text{in } \Omega^\psi \quad (5.4)$$

$$(\varepsilon_{kl}^\psi)_{Tot} = u_{k,l}^\psi = \frac{1}{2} (u_{k,l}^\psi + u_{l,k}^\psi) \quad \text{in } \Omega^\psi \quad (5.5)$$

Equation (5.3), (5.4), and (5.5) are the stress equilibrium equation, stress-strain constitutive relation, and strain displacement relation, respectively. Here, the superscript ψ is an indication of the composite domain. σ_{ij}^ψ is the stress field, F_i^ψ is the body force, C_{ijkl}^ψ is the fourth-order elastic stiffness tensor, ε_{kl}^ψ is the strain field, u_i^ψ is the displacement field, α_{kl}^ψ is the thermal expansion coefficient, and ΔT is the temperature change. i, j, k , and l are the indices along Cartesian coordinate axes. ‘,’ represents the spatial derivatives of field variables. The subscripts of the strain field, ‘Tot’ and ‘Th’, stand for the total and the thermal parts of the strain field, respectively. For a linear thermo-elastic case,

$$(\varepsilon_{kl}^\psi)_{Total} = (\varepsilon_{kl}^\psi)_{Thermal} + (\varepsilon_{kl}^\psi)_{Elastic} \quad (5.6)$$

As per the AEH method, the displacement field in the composite domain can be approximated through its asymptotic expansion about the small bridging parameter as follows

$$u_i^\psi(x) = u_i^{(0)}(x) + \xi u_i^{(1)}(x, y) + \xi^2 u_i^{(2)}(x, y) + \dots \quad (5.7)$$

The first term of the expansion is the globally varying displacement field, while the other terms are the local fluctuations in the displacement field due to the presence of heterogeneity. Heterogeneity may be in the form of reinforcements or voids.

The following constitutive relation can be obtained in terms of average quantities and effective material properties by substituting the expansion (5.7) in equation (5.5) and simplifying the equations (5.3) and (5.4) using mathematical manipulations under periodicity conditions [120].

$$\langle \sigma_{ij} \rangle = \langle C_{ijkl} \rangle \langle (\varepsilon_{kl})_{Tot} \rangle - \langle \alpha_{kl} \rangle \Delta T \quad (5.8)$$

where “< >” stands for the average effective quantities. The effective stress and strain fields in the two-phase domain are defined as

$$\langle \sigma_{ij} \rangle = \frac{1}{V} \left[\int_{V_1} \sigma_{ij}^{(1)} dv_1 + \int_{V_2} \sigma_{ij}^{(2)} dv_2 \right], \quad (5.9)$$

$$\langle \varepsilon_{ij} \rangle = \frac{1}{V} \left[\int_{V_1} \varepsilon_{ij}^{(1)} dv_1 + \int_{V_2} \varepsilon_{ij}^{(2)} dv_2 + \int_S \llbracket u_i \rrbracket \cdot n_j ds \right] \quad (5.10)$$

where ‘V’ is the volume of the unit cell domain ‘ Θ ’. The superscripts ‘1’ and ‘2’ represent the local phases at any scale. $\llbracket u_i \rrbracket$ is the displacement jump occurring at the interface (due to imperfectness) of two phases having interfacial surface area “S” and “ n_j ” as a unit outward normal (See Fig. 5.3 (c)). The third term in equation (5.10) disappears for the perfectly bonded interface. One can refer to **Appendix-B** for the complete derivation of equation (5.8) through the AEH approach.

In this study, the constitutive relation (equation (5.8)) derived from the AEH approach was utilized sequentially at two levels of length scales: 1) bundle level (micro-scale) and 2) composite level (mesoscale). At the microscale, bundles are treated as a unidirectional composite having fiber and matrix as its constituents. However, the bundles and matrix are the constituents of the composite at the mesoscale level. The finite element analysis was performed at both levels of length scales to obtain effective properties by solving equation (5.8) under different loading/boundary conditions. Another important condition in the analysis is the modeling of the interface between the bundle/matrix. Here, the interface is represented using two discrete surfaces and their mechanical behavior and is discussed in detail in the next subsections.

5.4 Modeling of imperfect interface

The interface between the bundles and the matrix plays an important role in the thermomechanical behavior of C/C composites. The differential thermal stresses are induced in the constituent phases due to the mismatch of their CTEs when these composites were subjected to thermal loads. It is also evident from the previous studies

that these thermal stresses lead to severe interfacial damage. It is also observed in the tomographic images that the interface between the bundle and the matrix is not perfectly bonded. Significant damage in the form of cracks and micro-voids is observed at the bundle/matrix interface. Therefore, in the present study, the imperfect interfacial behavior was modeled using the surface-based cohesive contact interaction. In cohesive interaction, it is assumed that the effective traction forces at the interface represent all mechanisms such as crack initiation, crack propagation, crack bridging, adhesive force, frictional forces, and anchorage. The work done by these forces at the interface is equal to the fracture energy release rate (G_f) required to produce two fractured surfaces. The constitutive behavior of the interface is given through a traction separation law, which states that all the traction components at the interface are directly proportional to the separations between them. Initially, the traction is related to separation using high stiffness of the interface, and once the peak stress is attained, the stiffness is reduced using suitable damage evolution law. Let, t_N and t_T be the traction components in normal (N) and tangential (T_1 and T_2) directions respectively at a point on the interface as shown in Fig. 5.4 (a). Let δ_N , δ_{T_1} and δ_{T_2} be the corresponding value of separations in the respective directions. Then, the traction separation laws in the normal direction can be represented with the help of equations (5.11) and (5.12) [76].

$$t_N(x) - (1 - \omega_{int}(x))K_N\delta_N(x) \leq 0; \quad (5.11)$$

or
$$\delta_N(x) \geq 0;$$

and
$$\{t_N(x) - (1 - \omega_{int}(x))K_N\delta_N(x)\}\delta_N(x) = 0; \quad (5.12)$$

Similarly, the traction separation law in the tangential direction considering both adhesion and friction conditions can be expressed through equations (5.13) - (5.15).

$$t_T(x) = t_{T_a}(x) + t_{T_f}(x) \quad (5.13)$$

$$t_{T_a}(x) = (1 - \omega_{int}(x))K_T\delta_T(x) \quad (5.14)$$

$$t_{T_f}(x) = \omega_{int}(\mu t_N) \quad (5.15)$$

where ω_{int} , K_N , K_T , and μ are the interface damage parameter, stiffness in the normal direction, stiffness in tangential directions, and coefficient of friction respectively. The interfacial damage parameter ω_{int} can be defined as

$$\omega_{int} = \frac{\delta - \delta^o}{\delta^f - \delta^o} \left(\frac{\delta^f}{\delta^o} \right) \quad (5.16)$$

A graphical representation of the traction separation law in normal (Mode I) and tangential (Mode II) conditions is given in Fig. 5.4 (b) and (c), respectively [76].

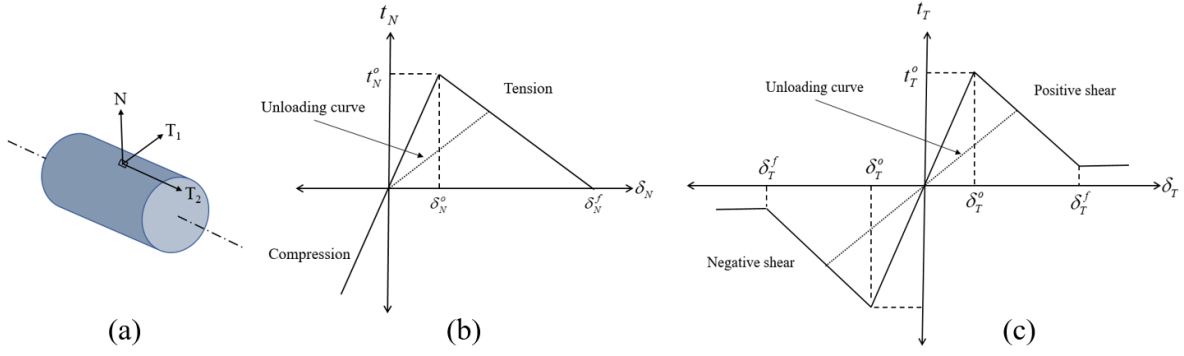


Fig. 5.4 (a) Directions associated with the interface surface, (b) Traction separation law in the normal direction (pure Mode I condition), and (c) Traction separation law in the tangential direction (Pure Mode II condition)

Here, a quadratic traction criterion is used for damage initiation and the linear softening law for damage propagation. According to quadratic traction initiation criteria, the interfacial damage initiates when the following condition is met

$$\left\{ \frac{\langle t_N \rangle}{t_N^o} \right\}^2 + \left\{ \frac{t_{T_1}}{t_{T_1}^o} \right\}^2 + \left\{ \frac{t_{T_2}}{t_{T_2}^o} \right\}^2 = I \quad (5.17)$$

Where t_N^o , $t_{T_1}^o$ and $t_{T_2}^o$ are the critical values of the tractions. Symbol “< >” is called the Macaulay bracket, which signifies that there is no interfacial damage under pure compression. The numerical implementation of these two sub-sections is presented in the next section.

5.5 Numerical analysis

A sub-sequential methodology was considered in the two-scale framework of the homogenization scheme. The problem was divided into two parts: 1) analysis of the bundle and 2) analysis of the composite. Firstly, the effective properties of the bundles were obtained through micro-scale analysis at the bundle level. Secondly, these effective properties were used as inputs at mesoscale level analysis to obtain the effective response of the composites.

5.5.1 Micro-scale analysis (at bundle level)

As was mentioned earlier, separate micro-unit cells of each bundle were constructed assuming the hexagonal packing of fibers for circular bundles and square packing for rectangular bundles. The linear hexahedral coupled temperature-displacement element (C3D8T in ABAQUS) was used for the discretization of unit cells. Coupled temperature-displacement step under steady-state condition was performed for the

thermo-mechanical analysis. The geometrical and finite element details of the models were already presented in chapter-2.

At the bundle level, the constitutive relation can be rewritten as

$$\langle \sigma_{ij} \rangle^b = \langle C_{ijkl} \rangle^b \langle (\varepsilon_{kl})_{Tot} \rangle^b - \langle \alpha_{kl} \rangle^b \Delta T \quad (5.18)$$

The average quantities are defined as

$$\langle \sigma_{ij} \rangle^b = \frac{1}{V_{microUC}} \left[\int_{V_f} \sigma_{ij}^{(f)} dv_f + \int_{V_m} \sigma_{ij}^{(m)} dv_m \right] \quad (5.19)$$

$$\langle \varepsilon_{ij} \rangle^b = \frac{1}{V_{microUC}} \left[\int_{V_f} \varepsilon_{ij}^{(f)} dv_f + \int_{V_m} \varepsilon_{ij}^{(m)} dv_m \right] \quad (5.20)$$

where i, j, k , and l are directed along Cartesian axes x, y , and z . ‘ b ’, ‘ f ’, and ‘ m ’ represent the bundle, the fiber, and the matrix phase respectively. At this level, equation (5.18) was solved under two separate conditions: under zero thermal load (i.e. $\Delta T = 0$), and then under pure thermal load.

For the first condition, the thermal strain part in equation (5.18) vanishes. Six independent load cases in the form of average strain (1%) along with periodic boundary conditions (PBC) (as derived by Li [119] based on symmetry condition) were applied on the unit cells for the calculation of homogenized stiffness tensor $\langle C_{ijkl} \rangle^b$. The six independent load cases are given as

$$\begin{Bmatrix} \langle \varepsilon_{xx} \rangle \\ \langle \varepsilon_{yy} \rangle \\ \langle \varepsilon_{zz} \rangle \\ \langle \varepsilon_{yz} \rangle \\ \langle \varepsilon_{xz} \rangle \\ \langle \varepsilon_{xy} \rangle \end{Bmatrix} = \begin{Bmatrix} \langle \varepsilon_{xx} \rangle = 0.01 \\ 0 \\ 0 \\ 0 \\ 0 \\ 0 \end{Bmatrix}, \begin{Bmatrix} \langle \varepsilon_{yy} \rangle = 0.01 \\ 0 \\ 0 \\ 0 \\ 0 \\ 0 \end{Bmatrix}, \begin{Bmatrix} \langle \varepsilon_{zz} \rangle = 0.01 \\ 0 \\ 0 \\ 0 \\ 0 \\ 0 \end{Bmatrix}, \begin{Bmatrix} \langle \varepsilon_{yz} \rangle = 0.01 \\ 0 \\ 0 \\ 0 \\ 0 \\ 0 \end{Bmatrix}, \begin{Bmatrix} \langle \varepsilon_{xz} \rangle = 0.01 \\ 0 \\ 0 \\ 0 \\ 0 \\ 0 \end{Bmatrix}, \begin{Bmatrix} \langle \varepsilon_{xy} \rangle = 0.01 \\ 0 \\ 0 \\ 0 \\ 0 \\ 0 \end{Bmatrix} \quad \text{and} \quad \begin{Bmatrix} 0 \\ 0 \\ 0 \\ 0 \\ 0 \\ \langle \varepsilon_{xy} \rangle = 0.01 \end{Bmatrix} \quad (5.21)$$

The periodic boundary conditions corresponding to the different loads are shown in tabular form in Table 5.1, where equation (5.22) is used for normal loads and the equations (5.23), (5.24), and (5.25) are used for shear load conditions. In this way, the six columns of the effective stiffness matrix are obtained through the six conditions of average stress using equation (5.18). Next, the average compliance tensor $\langle S_{ijkl} \rangle^b$ is obtained by taking the inverse of stiffness tensor. The effective homogenized engineering constants are then calculated as $E_{xx} = 1/S_{xxxx}$, $E_{yy} = 1/S_{yyyy}$, $E_{zz} = 1/S_{zzzz}$, $G_{xy} = 1/S_{xyxy}$, $G_{yz} = 1/S_{yzyz}$, $G_{xz} = 1/S_{xzxz}$, $\nu_{xy} = -(S_{xyxy}/S_{xxxx})$, $\nu_{xz} = -(S_{xzxz}/S_{xxxx})$ and $\nu_{yz} = -(S_{yzyz}/S_{yyyy})$. Here, E , G , and ν are Young’s modulus, shear modulus, and Poisson’s ratio, respectively.

In the second condition, the unit cells were analyzed under pure thermal load in three principal directions. A unit temperature rise is used in finite element based steady-state thermo-mechanical analysis of the unit cells to calculate the average/effective stress. The mechanical boundary conditions used for three cases are presented in Fig. 5.5 (a), (b), and (c) respectively.

Table 5.1 Periodic boundary conditions [77, 119]

Under normal loading (x, y, and z directions)	$\left. \begin{aligned} u _{x=0} = 0 \text{ and } u _{x=l_x} &= \langle \varepsilon_{xx} \rangle l_x \\ v _{y=0} = 0 \text{ and } v _{y=l_y} &= \langle \varepsilon_{yy} \rangle l_y \\ w _{z=0} = 0 \text{ and } w _{z=l_z} &= \langle \varepsilon_{zz} \rangle l_z \end{aligned} \right\} \quad (5.22)$	
Under shear loading (XY plane)	$\left. \begin{aligned} v _{x=0} = w _{x=0} &= 0 & v _{x=l_x} = w _{x=l_x} &= 0 \\ u _{y=0} = w _{y=0} &= 0 & u _{y=l_y} = \langle \varepsilon_{xy} \rangle l_y \text{ and } w _{y=l_y} &= 0 \\ w _{z=0} &= 0 & w _{z=l_z} &= 0 \end{aligned} \right\} \quad (5.23)$	
Under shear loading (YZ plane)	$\left. \begin{aligned} u _{x=0} &= 0 & u _{x=l_x} &= 0 \\ u _{y=0} = w _{y=0} &= 0 & u _{y=l_y} = w _{y=l_y} &= 0 \\ u _{z=0} = v _{z=0} &= 0 & u _{z=l_z} = 0 \text{ and } v _{z=l_z} &= \langle \varepsilon_{yz} \rangle l_z \end{aligned} \right\} \quad (5.24)$	
Under shear loading (XZ plane)	$\left. \begin{aligned} v _{x=0} = w _{x=0} &= 0 & v _{x=l_x} = w _{x=l_x} &= 0 \\ v _{y=0} &= 0 & v _{y=l_y} &= 0 \\ u _{z=0} = v _{z=0} &= 0 & u _{z=l_z} = \langle \varepsilon_{xz} \rangle l_z \text{ and } v _{z=l_z} &= 0 \end{aligned} \right\} \quad (5.25)$	

Here, l_x , l_y , and l_z are the dimensions of the unit cell and u , v , and w are the displacements in x, y, and z directions respectively.

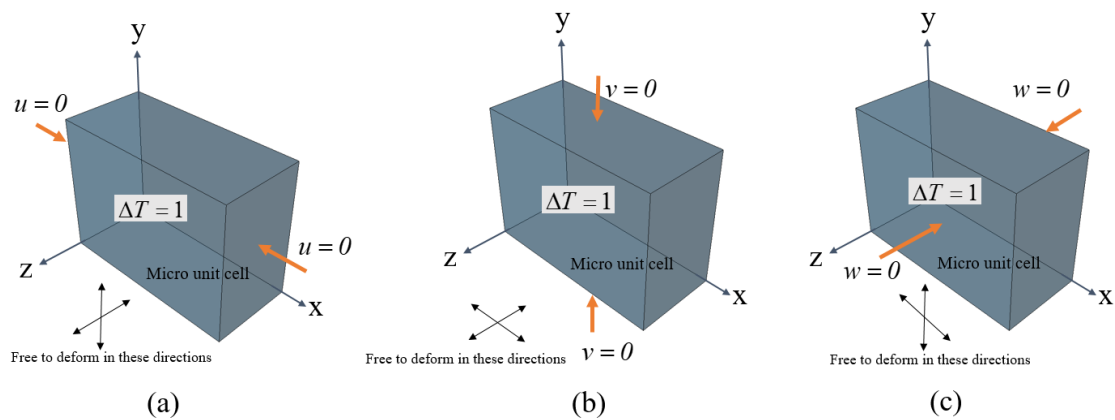


Fig. 5.5 Micro unit cell under unit thermal load and constrained deformation BC in

(a, b) Transverse and (c) Longitudinal directions

The average/effective stress induced in the unit cells for the unit temperature rise can be calculated using equation (5.19) one by one for all of the three cases. Therefore, the CTEs of the bundles can be calculated easily by using equation (5.18) for known values of $\langle C_{ijkl} \rangle^b$. This procedure was repeated for the entire temperature range and the bundle properties were determined as a function of temperature. These properties are then used as input for mesoscale analysis. The details are discussed in the next subsection.

5.5.2 Meso-scale analysis (at Composite level)

Four noded linear tetrahedral coupled temperature-displacement elements (C3D4T in ABAQUS) are used in the discretization scheme. The details of the FE mesh of the RVEs were already discussed in chapter-2. The effective constitutive relation at this length scale using AEH can be rewritten as

$$\langle \sigma_{ij} \rangle^C = \langle C_{ijkl} \rangle^C \left(\langle \epsilon_{kl} \rangle_{Tot}^C - \langle \alpha_{kl} \rangle^C \Delta T \right). \quad (5.26)$$

Here, average quantities are defined as

$$\langle \sigma_{ij} \rangle^C = \frac{I}{V_{RVE}} \left[\left(\sum_{r=1}^n \int_{V_{b^r}} \sigma_{ij}^{(b^r)} dv_{b^r} \right) + \int_{V_m} \sigma_{ij}^{(m)} dv_m \right] \quad (5.27)$$

$$\langle \epsilon_{ij} \rangle^C = \frac{I}{V_{RVE}} \left[\left(\sum_{r=1}^n \int_{V_{b^r}} \epsilon_{ij}^{(b^r)} dv_{b^r} \right) + \int_{V_m} \epsilon_{ij}^{(m)} dv_m + \int_{S_{int}} [u_i] \cdot n_j ds \right]. \quad (5.28)$$

The symbol ‘ b^r ’ stands for ‘ r^{th} ’ bundle, and ‘ n ’ is the number of bundles present in the composite (n=3 for 3DH and n=4 for 4DIN). Finite element analysis was performed on meso unit cells (RVEs) under suitable boundary conditions. Here, two different architectures (3DH and 4DIN) are analyzed separately under two different boundary conditions.

1. Plane remain planer boundary condition in case of 3DH C/C composite
2. Periodic boundary condition in case of 4DIN architecture

The boundary condition used for the analysis of the 3DH C/C composite unit cell is presented in Fig 5.6 (a). Here, the RVE was allowed to expand freely under unit temperature increase in all three orthogonal directions. The parallel faces of the RVE are constrained in such a way that there will not be any warping of the planes under thermal load, i.e., the planes which are plane and parallel to each other before the thermal load will remain plane and parallel after deformation.

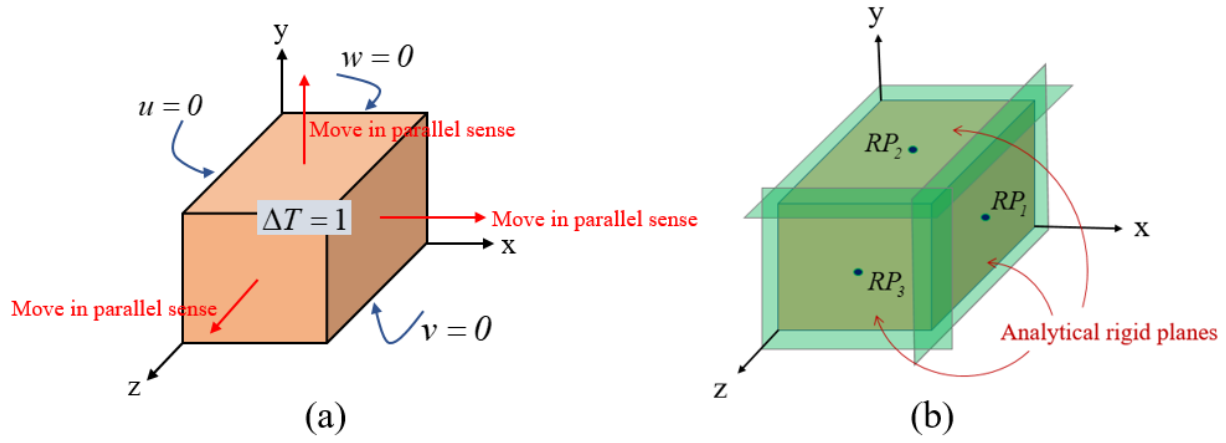


Fig. 5.6 (a) Boundary conditions in the mesoscale analysis of 3DH C/C composite and (b) Coupling of rigid planes with the faces of RVE

To ensure that the parallel planes remain parallel during deformation, the following constraints were implemented:

- Analytical rigid planes were created and rigidly coupled with their corresponding reference points (RP) as shown in Fig. 5.6 (b).
- Rigid planes were attached to the positive faces of RVE through surface-to-surface hard contact providing a small relative sliding relaxation between contacts, as shown in Fig. 5.6 (b).
- The distributing couplings were used between the unit cell surfaces and the corresponding rigid plane's reference points to ensure the uniform deformations of the faces.
- Lastly, the rotation of rigid planes was restricted, and planes were allowed to translate linearly in a particular direction.

Such constraints ensured the parallel movement of the positive faces during the deformation of the meso unit cell. The bundle/matrix interface was assumed to be perfectly bonded in this case.

In the case of the 4DIN C/C composite, Finite Element Analysis was performed on meso unit cells (RVEs) under the periodic boundary conditions, as depicted in Fig 5.7. The temperature of the whole RVE is increased quasi-statically from 27°C to 2227 °C and the thermal deformations are computed individually in three orthogonal directions. The periodic boundary condition used on the faces of the unit cell ensures the unidirectional deformation. For example, consider Fig 5.7(a), the unit cell face at $x=0$ is restricted to move in the x-direction (i.e., $u=0$) and the opposite face at $x=L_x$ is free to move. The unit cells facing the transverse direction (i.e., $y=0$, $y=L_y$, $z=0$, and $z=L_z$) are restricted to move in the corresponding directions (i.e., y and z directions respectively). They are free to move in the x-direction. These conditions ensure a uniform deformation of the unit cell in the x-direction. Similarly, Fig. 5.7(b) and (c) show boundary conditions in the other two directions. Here, L_x , L_y , and L_z are the geometric length of meso unit cells in x, y, and z directions, respectively.

In this situation, the use of an analytical rigid plane (as discussed in the last section) confirms the parallel movement of free surfaces of meso unit cells in three orthogonal directions individually.

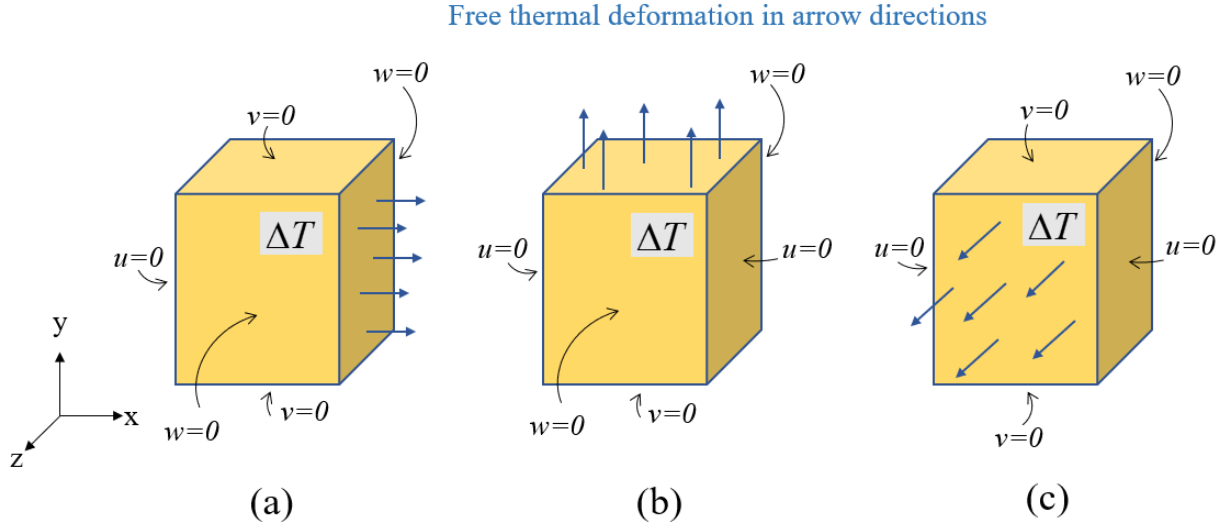


Fig. 5.7 Boundary conditions in the mesoscale analysis of the 4DIN C/C composite. Free thermal deformation in (a) x-direction, (b) y-direction, and (c) z-direction.

In both cases (3DH and 4DIN C/C composites), the average or effective thermal stress induced in the deformation direction equals zero due to free thermal deformation. Thus, the equation (5.26) can be modified as below to obtain an effective CTE.

$$\langle \langle \varepsilon_{ii} \rangle_{Tot} \rangle^C - \langle \alpha_{ii} \rangle^C \Delta T = 0.$$

or

$$\langle \alpha_{ii} \rangle^C \Delta T = \langle \langle \varepsilon_{ii} \rangle_{Tot} \rangle^C = \frac{\Delta L_i}{L_i}$$

or

$$\langle \alpha_{ii} \rangle^C = \frac{\Delta L_i}{L_i} \times \frac{1}{\Delta T} \quad (5.29)$$

Here, ΔL_i is the thermal deformation of RVE in i^{th} direction. Using equation (29), the effective CTEs of the composite are obtained in three orthogonal directions.

In the meso level simulations of 4DIN architecture, three types of interfacial conditions, namely: 1) perfect bonding, 2) imperfect bonding, and 3) complete debonding were used to obtain the effective CTE as a function of temperature. Properties of the bundle/matrix interface were considered from the previous studies of Sharma et al [76] and are presented in Table 5.2.

Table 5.2 Bundle/matrix Interfacial parameters [76]

Debond stress in normal mode (τ_N) (N/mm ²)	Debond stress in shear mode (τ_T) (N/mm ²)	Coeff. of friction (μ)	Critical fracture energy (G_{IIC}) (N/m)
6	6	0.75	5

Mix Mode Theory was implemented that assumes the same critical fracture energy and debond strength of interface for all three modes (Mode I, Mode II, and Mode III). The numerically predicted results at two length scales are presented in the next section.

An algorithm of the two-scale homogenization scheme adopted for the 4DIN C/C composite is presented in Fig. 5.8 to illustrate the point. A similar algorithm was followed to predict the effective CTE of the 3DH C/C composite.

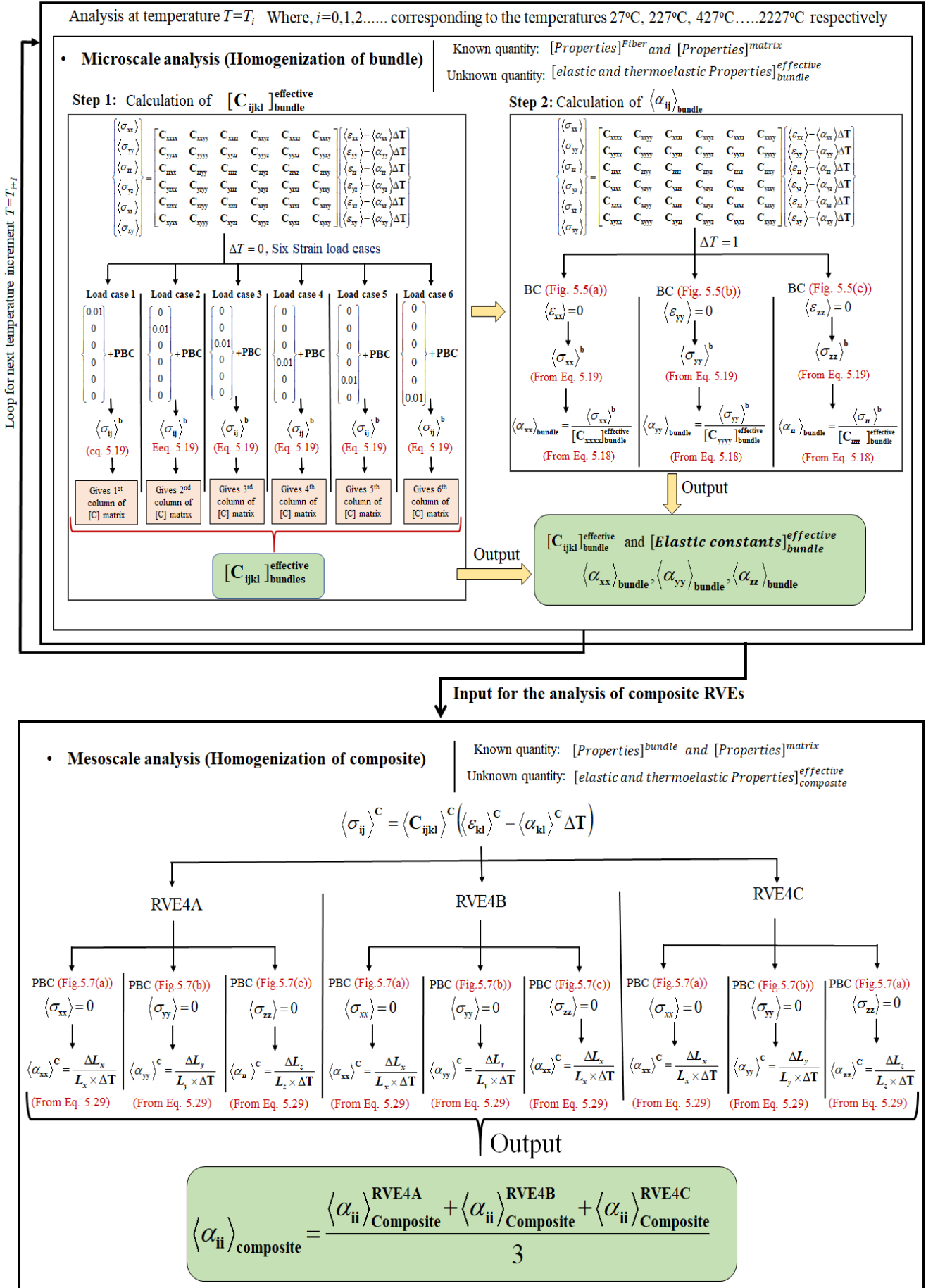


Fig. 5.8 Two-scale homogenization scheme for effective CTE of 4DIN C/C composite

5.6 Result and discussion

5.6.1 Results of 3DH C/C composite

5.6.1.1 Effective properties of bundles

Finite Element Analysis of the micro-unit cell was performed under the previously discussed loading and boundary conditions (section 5.5.1) to obtain the effective CTE of the bundles. The temperature-dependent properties of constituents are considered from the literature [104], as given in Table 2.2 (in chapter 2). Firstly, the homogenized effective elastic engineering constants of bundles for the temperature range starting from 27°C to 2227°C were obtained through finite element analysis at the microscale level and are listed in Table 5.3. The effective longitudinal modulus obtained for circular bundles is always larger than the rectangular bundles due to possessing high volume fraction.

Table 5.3 Mean effective elastic properties of bundles in 3DH C/C composite

Temperature (°C)	EL (GPa)	ET (GPa)	GLT (GPa)	GTT (GPa)	νLT	νTT
	Rect/circ	Rect/circ	Rect/circ	Rect/circ	Rect/circ	Rect/circ
27	145.29/178.34	59.2/42.24	25.66 / 18.21	22.88 / 15.81	0.2 / 0.2	0.2917 / 0.3343
227	145.93/178.62	59.63/42.45	25.89 / 18.33	23.06 / 15.89	0.2 / 0.2	0.2916 / 0.3342
427	146.29/178.47	60.02/42.59	26.09/ 18.42	23.22/ 15.93	0.2 / 0.2	0.2915 / 0.334
627	146.83/178.56	60.45/42.77	26.32/ 18.52	23.39 / 16.01	0.2 / 0.2	0.2914 / 0.3339
827	147.43/178.79	60.9/42.97	26.54/ 18.64	22.88 / 16.08	0.2 / 0.2	0.2913 / 0.3337
1027	147.97/178.59	61.45/43.17	26.84/ 18.77	22.74 / 16.16	0.2 / 0.2	0.2911 / 0.3335
1227	149.78/178.89	62.93/43.78	27.6/ 19.13	24.36 / 16.39	0.2 / 0.2	0.2907 / 0.3329
1427	148.16/175.86	62.65/43.34	27.55/ 18.99	24.25 / 16.24	0.2 / 0.2	0.2905 / 0.3326
1627	143.48/168.74	61.26/42.02	27.04/ 18.51	23.73 / 15.75	0.2 / 0.2	0.2901 / 0.3321
1827	135.12/154.42	59.34/39.72	26.48/ 17.74	22.99 / 14.91	0.2 / 0.2	0.2891 / 0.3305
2027	118.52/133.11	52.88/34.89	23.75/ 15.71	20.50 / 13.11	0.2 / 0.2	0.2884 / 0.3295
2227	101.51/111.55	46.14/29.94	20.89/ 13.62	17.91 / 11.26	0.2 / 0.2	0.2876 / 0.3282

Rect = Rectangular bundle, Circ = Circular bundle, L = longitudinal and T = transverse.

The Von-mises stress contours induced due to thermal load are presented for extremum temperatures (27°C and 2227°C) in Fig 5.9. The stress distribution over micro-unit cells when deformation is constrained in the longitudinal direction (z-direction) is shown in Fig. 5.9 (a), (e), (c), and (g) for both temperatures. Fig. 5.9 (b), (f), (d), and (h) present the thermal stress distribution when deformation is constrained in the transverse direction (x-direction). It is clear from Fig.5.9 that the stresses are almost uniformly distributed in the fibers

and the matrix for the longitudinal case. The interface also has a significant effect on stress distribution in the phases for the transverse case. At lower temperatures, the mismatch between the CTEs of fiber and matrix is predominant which caused higher stress fluctuations near the fiber/matrix interfaces.

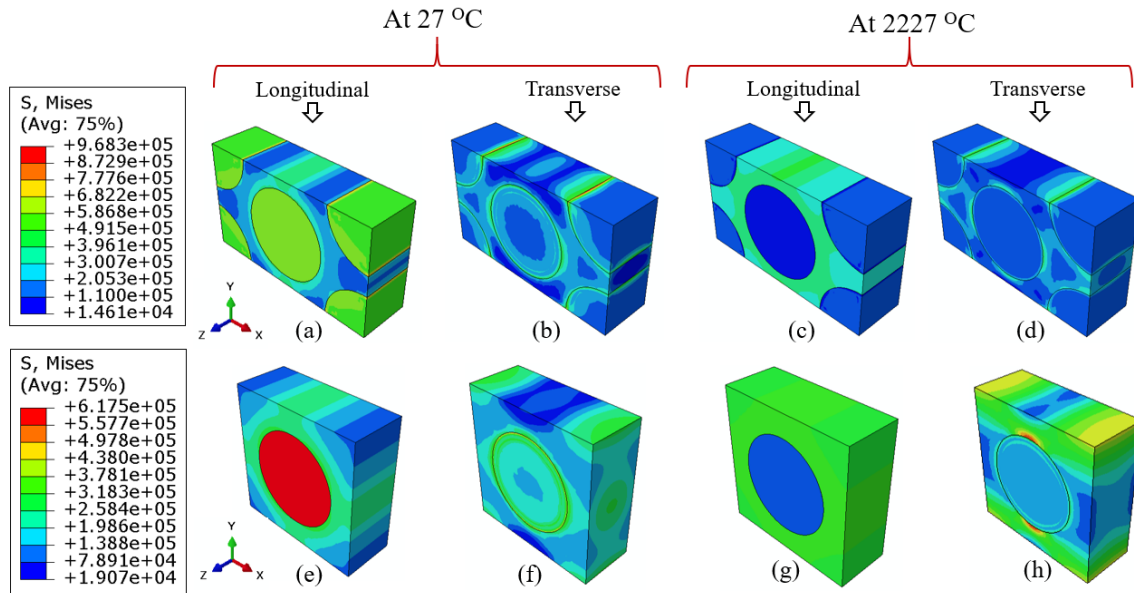


Fig. 5.9 Thermal stress distribution in micro-unit cells at extremum temperatures in different directions

The effective CTEs of the bundles in different directions are obtained for the entire temperature range (i.e. 27°C to 2227°C) through these micro-unit cells. They are presented as a function of temperature in Fig. 5.10. It is noticed that the effective CTE of the transverse direction of the circular bundle has initially increased up to a temperature of 640°C. Afterward, it remains almost constant up to 1627°C then slightly decreases. On the other hand, the transverse CTE of the rectangular bundle continuously increased with a gentler slope with a rise in temperature. The effective CTE in the longitudinal direction has a considerable effect of volume fraction variation (The circular bundle has less magnitude compared to the rectangular bundle). The CTE of the rectangular bundle has zero expansion at around 300°C and the same is noticed around 650°C for the circular bundle. The CTE variation in the longitudinal direction with respect to temperature for both unit cells is found to be similar (refer Fig. 5.10). Furthermore, the analytical model of Schapery [89] was also utilized to calculate the CTEs in longitudinal directions for both of the unit cells. It was found that the present FE analysis is in excellent agreement with the analytical model (see in Fig 5.10).

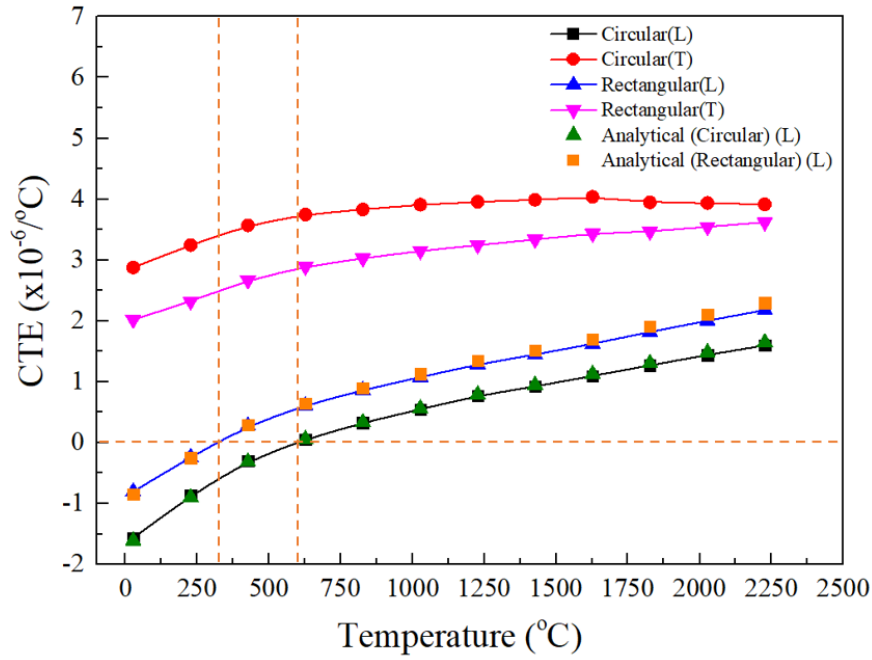


Fig. 5.10 Variation of effective CTE of bundles in 3DH C/C composite with temperature

5.6.1.2 Effective properties of 3DH C/C composite

At the upper scale, the effective CTEs of the 3DH C/C composite were predicted using lower scale effective properties and realistic microstructure in RVE under strongly imposed boundaries which were discussed earlier in section 5.2. The deformation contour of the 3DH composite's RVE is shown in Figs 5.II(a), (b), and (c).

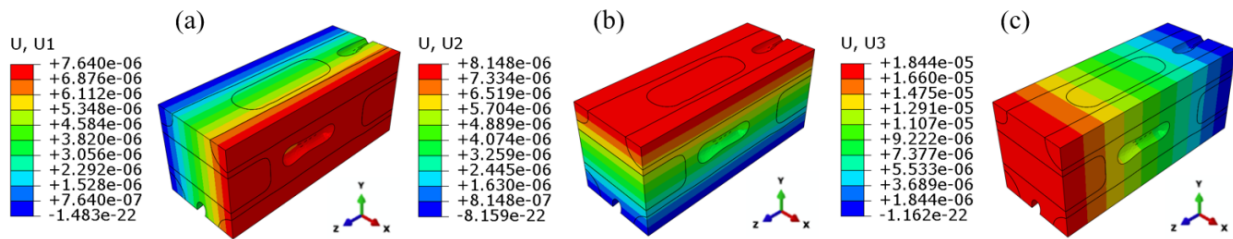


Fig. 5.II Thermal deformation in (a) x-direction, (b) y-direction, and (c) z-direction of 3DH C/C composite RVE at 2227°C

It is clear from the deformation contours of Fig 5.II that the parallel planes' assumption is maintained in the analysis (as the parallel planes are uniformly displaced). Although the composite RVE has expanded freely in three orthogonal directions, the local stresses still developed in the constituents due to the mismatch of their CTEs and geometric irregularities. Though the magnitude of such stresses is observed to be low, they still have an important role as residuals [121-126]. Their behavior with respect to temperature is studied as presented in Fig 5.12.

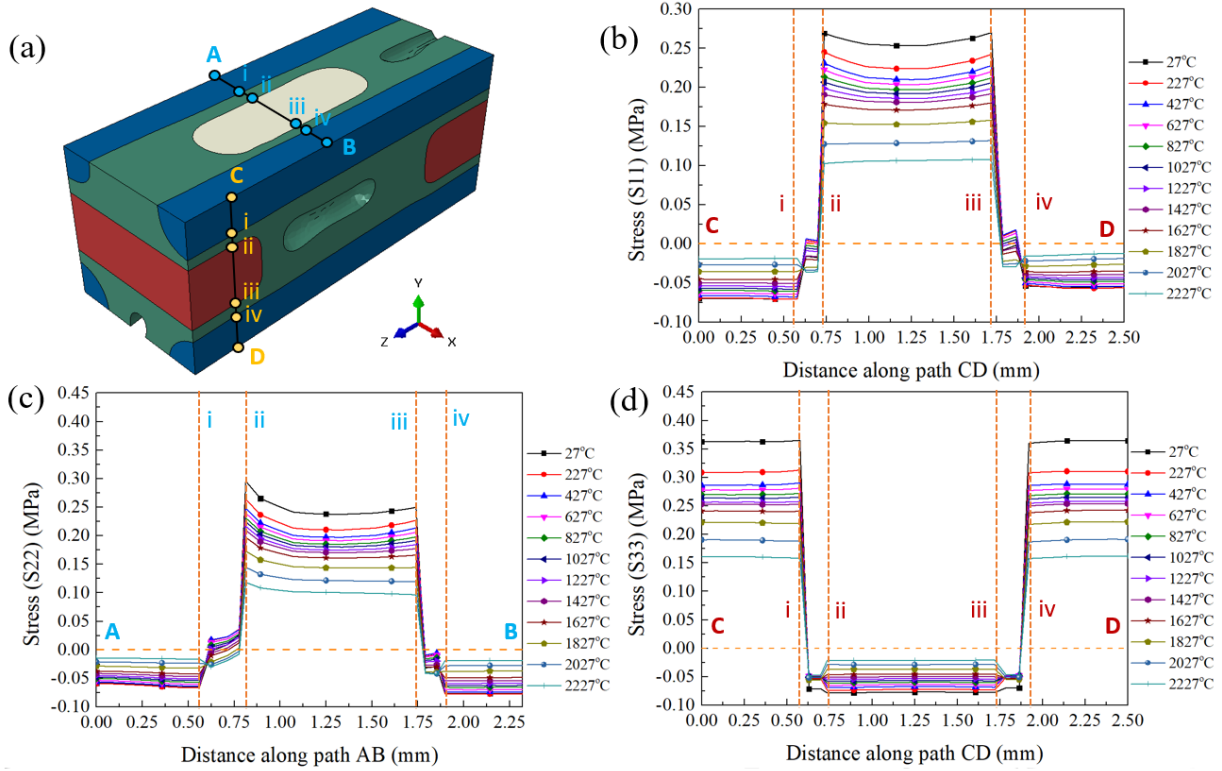


Fig 5.12 (a) Paths (A-B and C-D) crossing different phases of RVE and variation of stress components along them in (b) x-direction, (c) y-direction, and (d) z-direction

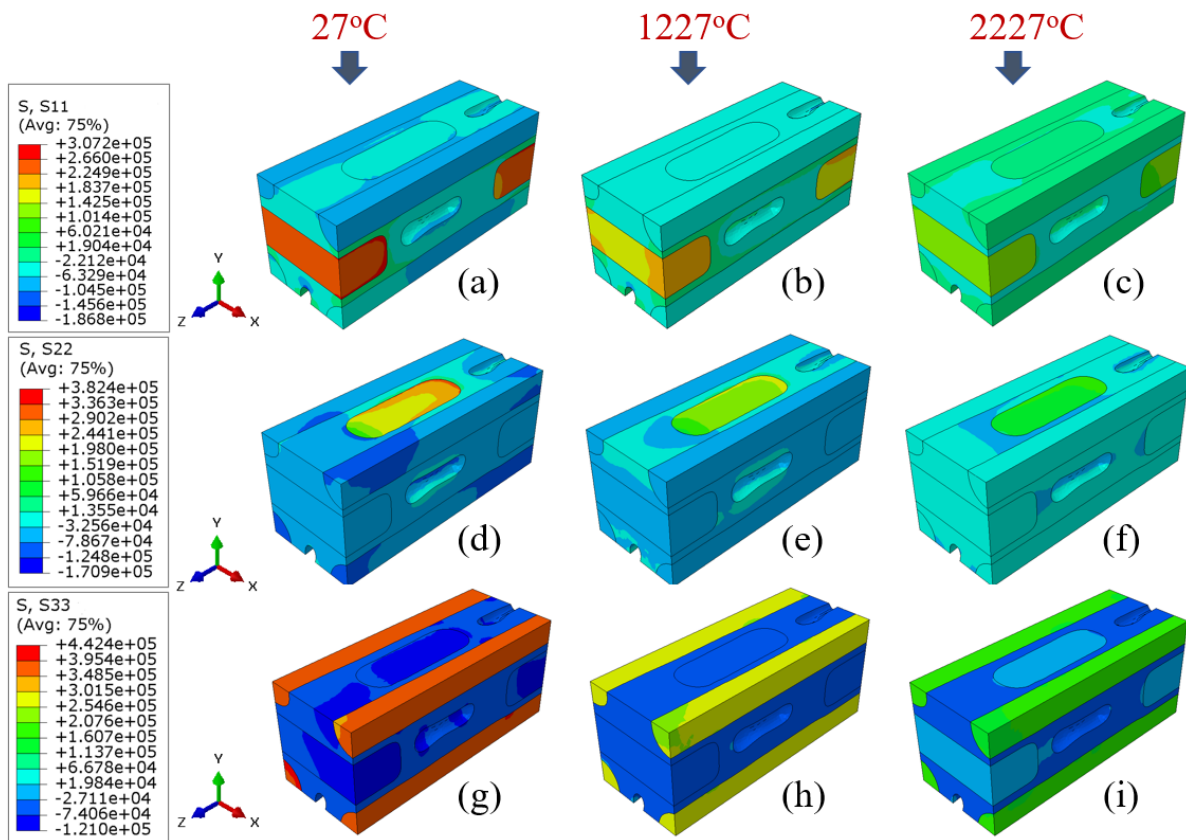


Fig 5.13 Stress distribution in 3DH C/C composite in (a, b, c) x-direction, (d, e, f) y-direction, and (g, h, i) z-direction at different temperatures

The residual stress distribution in x, y, and z directions (Fig 5.12(b), (c), and (d) respectively) is shown along the different paths (A-B and C-D) marked on the RVE as indicated in Fig 5.12 (a). It is observed that longitudinal bundles experience tensile stress while the stress that matrix and transverse bundles experience is mostly compressive. It is also clear from Fig.5.12 that the magnitude of stress jumps near the interface is significantly reduced as the temperature increases to maxima.

The local distribution of the residual stresses is shown in Fig. 5.13. Fig. 5.13 (a), (b), and (c) represent the local stress distributions in the 3DH C/C composite at 27°C, 1227°C, and 2227°C respectively corresponding to the deformation of RVE in the x-direction. Similarly, Fig. 5.13 (d), (e), and (f) are the local stress distributions corresponding to the y-deformation and Fig. 5.13 (g), (h), and (i) is the local stress distributions corresponding to the z-deformation of the RVE at respective temperatures.

Furthermore, the stress concentrations were observed in the vicinity of the irregularly shaped voids as depicted in Fig. 5.14 (a). Also, the magnitude of stress concentration near the voids is nearly one order higher than the far-field values. It is also clear from Fig. 5.14 (b (i), (ii), and (iii)) that the cross-sectional distortions resulted in the higher stresses near the reconstructed features included in the geometry.

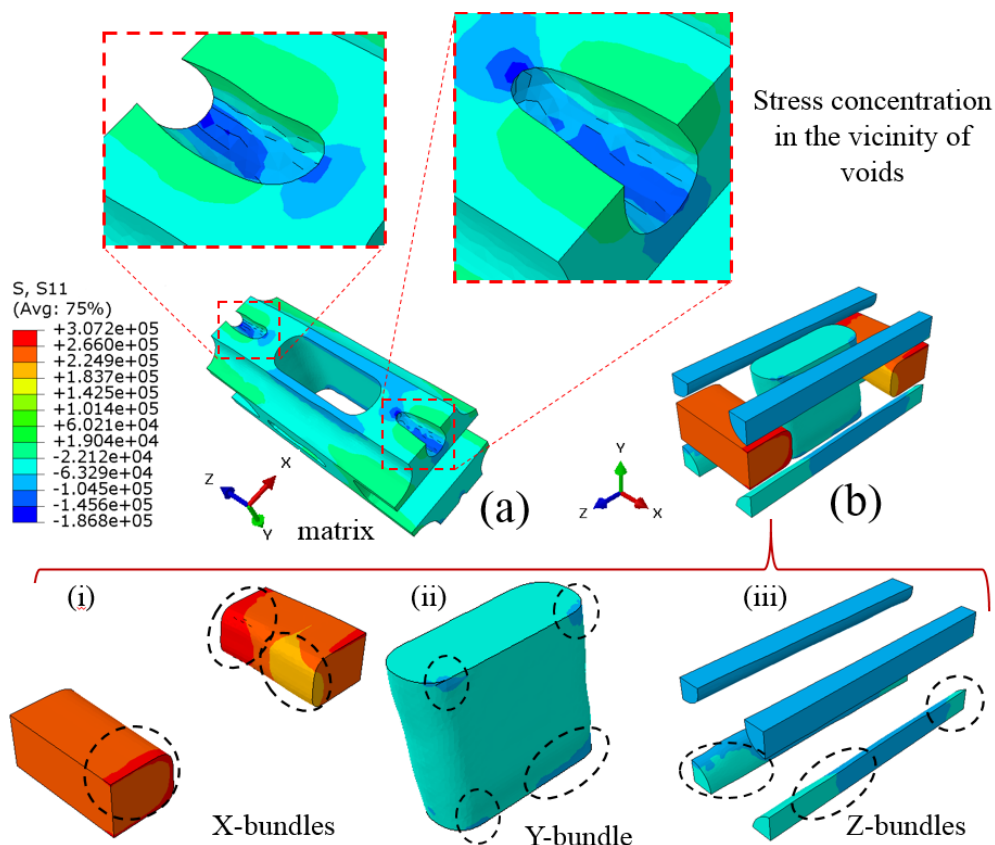


Fig. 5.14 (a) Localized stress concentration in the vicinity of irregularly shaped voids and (b) Uneven stress distribution in bundles due to bundle distortion imperfections

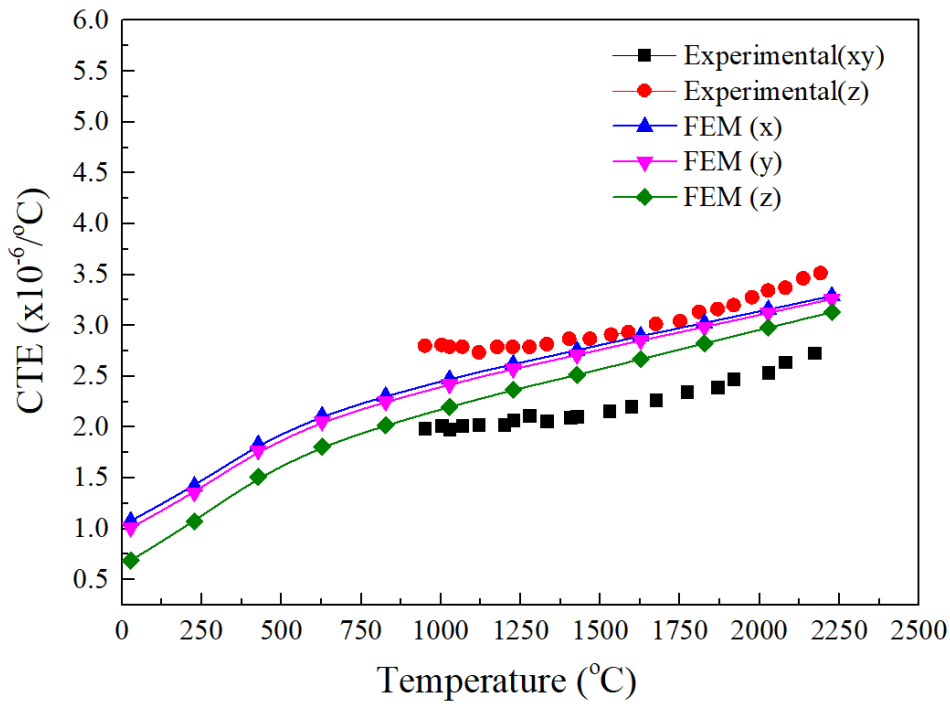


Fig. 5.15 Variation of the effective CTEs of 3DH C/C composite with respect to temperature (Experimental [85])

The predicted effective CTEs of the 3DH C/C composite in the in-plane (x and y) and the out-of-plane (z) directions are plotted in Fig. 5.15., The in-plane CTE is obtained as $1.07 \times 10^{-6}/^{\circ}\text{C}$ at room temperature, and the value is increased to $3.29 \times 10^{-6}/^{\circ}\text{C}$ at 2227°C . The out-of-plane CTE is obtained $0.688 \times 10^{-6}/^{\circ}\text{C}$ and $3.129 \times 10^{-6}/^{\circ}\text{C}$ at both extremum temperatures. The overall trend of CTE is found to be increasing with temperature which was also observed by Wang et al. [85] in their experimental study. In the present model, the in-plane CTE is greater than the out-of-plane CTE as the fiber volume fraction is low in the in-plane direction as compared to the out-of-plane direction.

5.6.2 Results of 4DIN C/C composite

5.6.2.1 Effective properties of bundles

Finite Element Analysis of the micro-unit cell was performed under the previously discussed loading and boundary conditions to obtain the effective CTE of bundles. Here, Young's modulus and Poisson's ratio for pitch-based matrix were considered as 7 GPa and 0.2, respectively from the experiments conducted by Bhagat et al. [127]. Other temperature-dependent material properties of constituents were taken from the literature [104] (refer to Table 2.2). Firstly, the effective elastic constants of bundles are obtained under six strain load cases and periodic boundary conditions. The obtained mean values of effective elastic constants for the bundles in the 4DIN C/C composite are tabulated in Table 5.4.

Table 5.4 Mean effective elastic constants of bundles in 4DIN C/C composite

Temperature (°C)	E_L (GPa)	E_T (GPa)	G_{LT} (GPa)	G_{TT} (GPa)	ν_{LT}	ν_{TT}
27	193.79	17.85	7.18	6.55	0.2	0.3586
227	192.94	17.83	7.18	6.55	0.2	0.3587
427	192.43	17.78	7.15	6.52	0.2	0.3587
627	192.11	17.74	7.13	6.51	0.2	0.3588
827	191.09	17.72	7.13	6.51	0.2	0.3588
1027	189.10	17.82	7.10	6.48	0.2	0.3589
1227	184.69	17.52	7.04	6.43	0.2	0.3591
1427	175.44	17.23	6.92	6.32	0.2	0.3595
1627	155.40	16.61	6.65	6.09	0.2	0.3605
1827	131.33	15.20	6.05	5.56	0.2	0.3625
2027	107.25	13.38	5.28	4.89	0.2	0.3652
2227	193.79	11.43	4.49	6.55	0.2	0.3679

The obtained thermal stress distribution in the hexagonal unit cell of the bundle is presented in Fig. 5.16 for three load cases at extremum temperatures (i.e., 27°C and 2227°C). Fig. 5.16 (a), (b), and (c) show the distribution of the stress at 27°C when the unit cell is subjected to thermal load in x, y, and z directions. Similar plots at 2227°C are shown in Fig. 5.16 (d), (e), and (f) in respective directions. The effect of the mismatch in thermal expansion coefficients of the phases (i.e., fiber and matrix) is evident from the stress distribution in the unit cell shown in Fig. 5.16. The distribution of the thermal stress in the unit cell under transverse thermal load at both extremum temperatures is found to be almost similar with a difference in the magnitude (refer Fig. 5.16(a), (b), (d), and (e)). The longitudinal CTE of the fiber is negative for lower temperatures up to 1027°C; therefore, the thermal stresses are much higher. It is also noticed in Fig 5.16(c) and (f) that the stresses are reversed to compressive nature at 2227°C. This shows that the bundle properties follow the trend of the fiber properties. To study the nature of the stress distribution in the unit cell in the longitudinal direction with respect to temperature, the thermal stresses were plotted along the path A-B (see Fig. 5.16(g)) in Fig. 5.16(h). It is clear from Fig. 5.16(h) that the jump in the stress values is observed to be the highest at 27°C and is reduced sharply to 827°C. The stress jump at the interface is observed to be negligible at a temperature of 1027°C. After that, it has again increased with a comparatively small magnitude up to a temperature of 2027°C. The temperature (1027°C) at which the thermal stress changes its sign is also known as transition temperature. This thermal point is also very near to the transition point of the fiber (the longitudinal CTE is negative at 1027°C and is positive at 1227°C for fiber). Next, the overall/effective CTEs of the fiber bundle were calculated using equation (5.18) for each temperature increment and are presented in Fig 5.17.

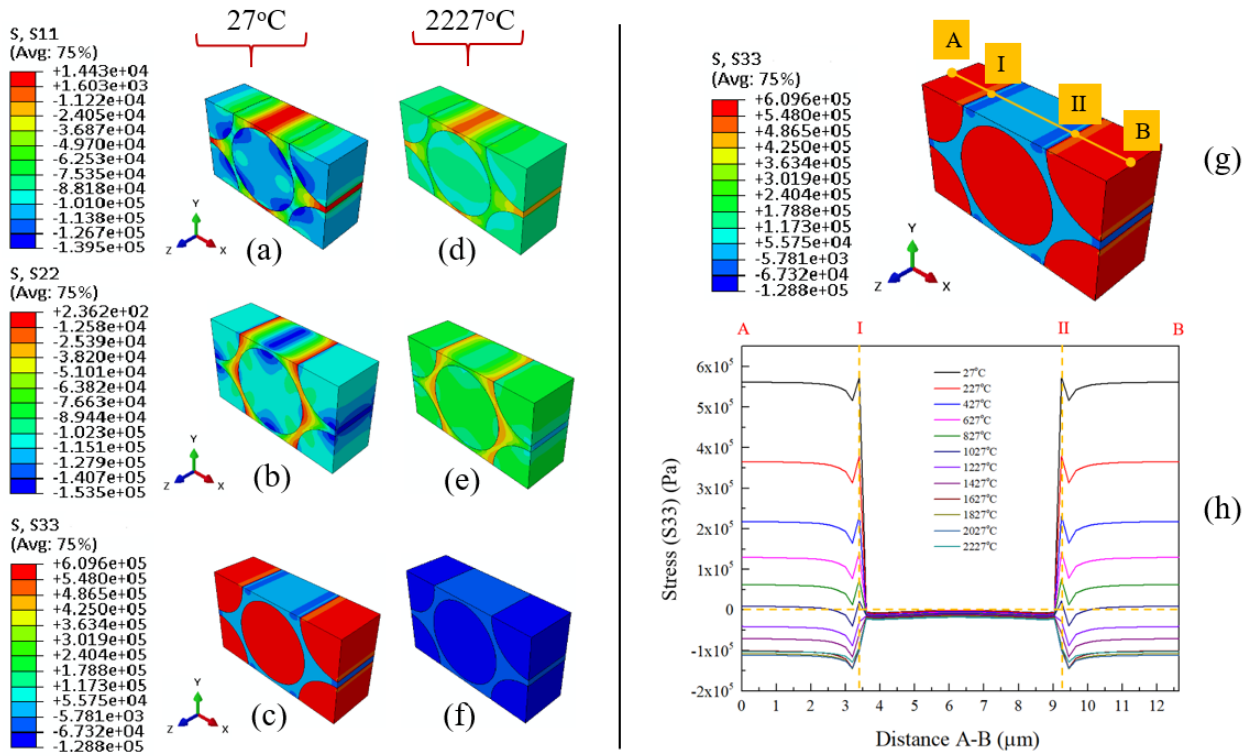


Fig. 5.16 Thermal stress distribution in the micro unit cell under unit temperature change at extremum thermal conditions: (a, b, d, e) Transverse direction (c, f) Longitudinal direction and (g, h) Longitudinal stress jump plot at the interface due to CTE mismatch at different temperatures

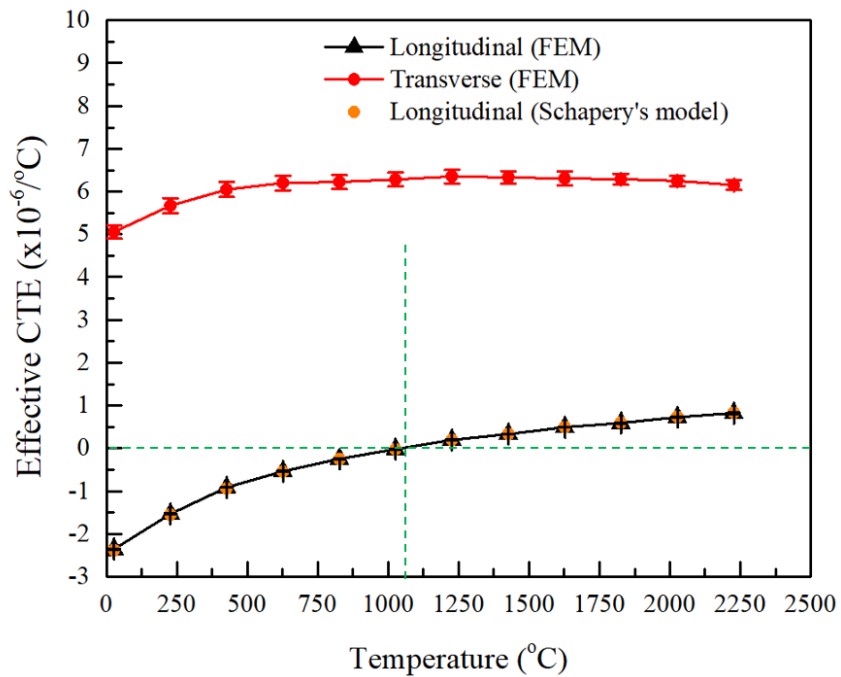


Fig. 5.17 Effective CTE of bundles as a function of temperature

Furthermore, it was observed in the reconstructed images of the composite that the fiber bundles were distorted during the fabrication processes; therefore, the fiber volume fraction in the different bundles inherently differs. These fluctuations in fiber volume fractions were incorporated in the analysis by varying the size of the unit cell for each reconstructed fiber bundle in the composite. All the micro-unit cells were analyzed separately for the effective CTEs over the full temperature range (27°C to 2227°C). Fig. 5.17 shows the mean curve of the effective longitudinal and transverse CTEs along with associated standard deviations. It is found that the transverse CTE has a significant effect on the fluctuations as compared to the longitudinal CTE (refer Fig. 5.17).

The effective longitudinal CTE for the fiber bundle is also calculated using the analytical equations given by Schapery's [89] considering the mean fiber volume fraction of micro-unit cells to be 82.72%. It was noticed that the predicted values are matching perfectly with those obtained through Schapery's model (see Fig. 5.17). The effective transverse CTEs of the bundle varies from $5.06 \times 10^{-6}/^{\circ}\text{C}$ at 27°C to $6.15 \times 10^{-6}/^{\circ}\text{C}$ at 2227°C. It is observed that the transverse CTE initially increases to a maximum value of $6.35 \times 10^{-6}/^{\circ}\text{C}$ at around 1227°C and then starts decreasing with a gentle slope with a further increase in temperature. The obtained variation of the CTEs of bundles was used as an input for the prediction of the effective CTEs of the composite at mesoscale. The results of the composite are discussed in detail in the next section.

5.6.2.2 Effective properties of 4DIN C/C composite

The Finite Element Analysis of composite unit cells was performed under appropriate boundary and loading conditions, as discussed in section 5.5.2. The contours of the thermal deformation in the RVE4B for all three orthogonal loads are presented at a higher temperature (2227°C) in Fig 5.18. Three interfacial conditions; perfectly bonded, imperfectly bonded, and completely debonded, are considered in the mesoscale analysis to conclude the effect of the interfacial behavior. The thermal deformation of RVE4B in the x-direction (in-plane) is shown in Fig 5.18 (a), (b), and (c) for the perfect, imperfect, and completely debonded interface. Similarly, Fig 5.18(d), (e), and (f) show the corresponding deformations in y, and Fig 5.18 (g), (h), and (i) shows them in the z-direction. It is observed in Fig 5.18 that the magnitude of deformation u is the highest for the perfectly bonded interface and is the lowest for the completely debonded case. Further, it can be noticed from the y-direction case that the magnitude of deformation v is the lowest for the perfect interface and the highest for the completely debonded interface. Also, the amount of deformation is approximately two times higher than that of x and z directions. The possible cause of this opposite behavior can be understood with the help of Fig. 5.19. In the case of deformation in the y-direction, the RVE is periodically constrained, keeping the upper face (face $y=L_y$) free to expand as shown in Fig. 5.19(a). The oblique bundles (i.e. 60° and 120° bundles) do not directly contribute to the deformation mechanism. They transferred the load through the matrix and interface between the bundle/matrix.

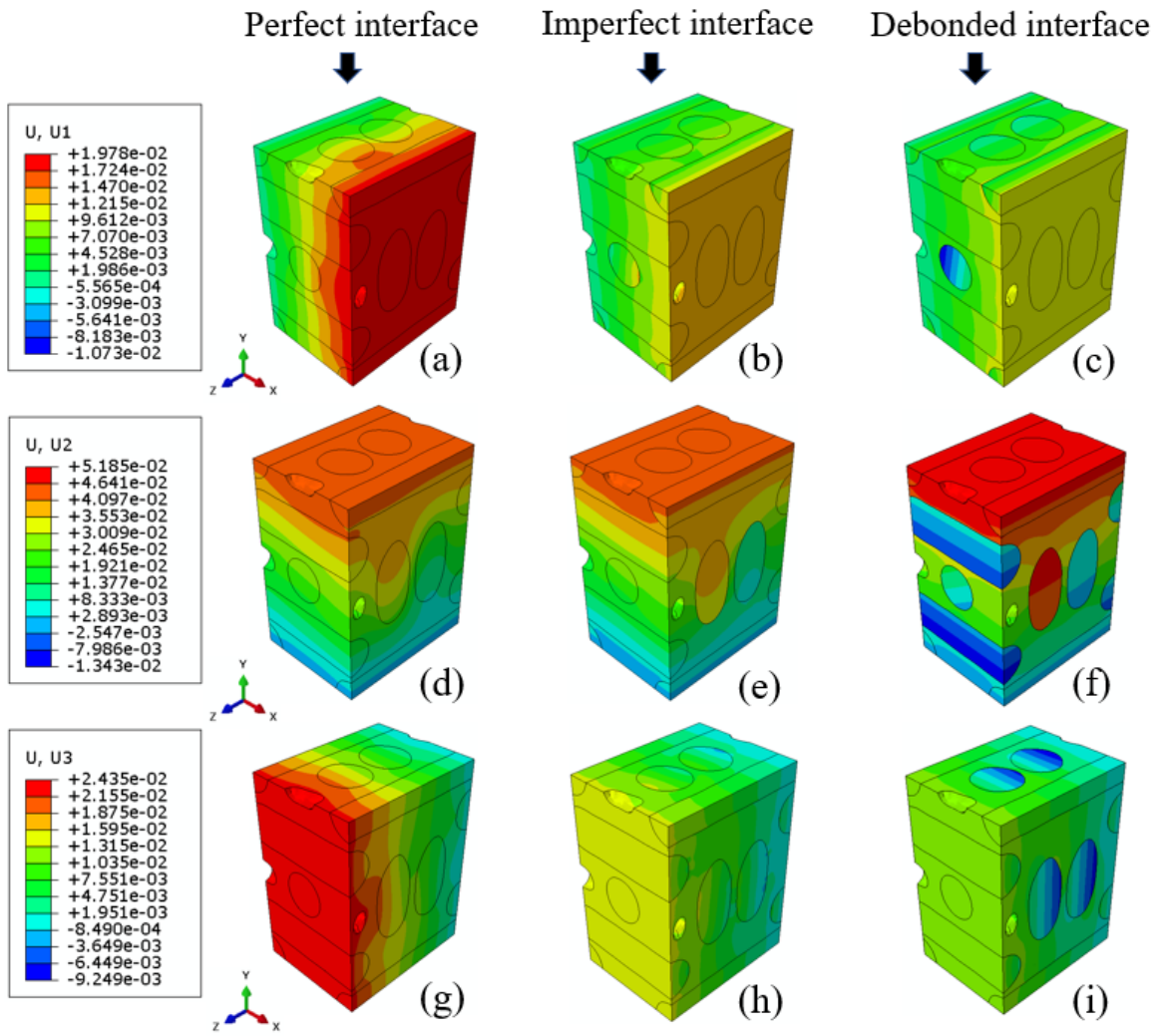


Fig. 5.18 Free thermal deformation in (a, b, c) x-direction, (d, e, f) y-direction, and (g, h, i) z-direction for different interfacial conditions

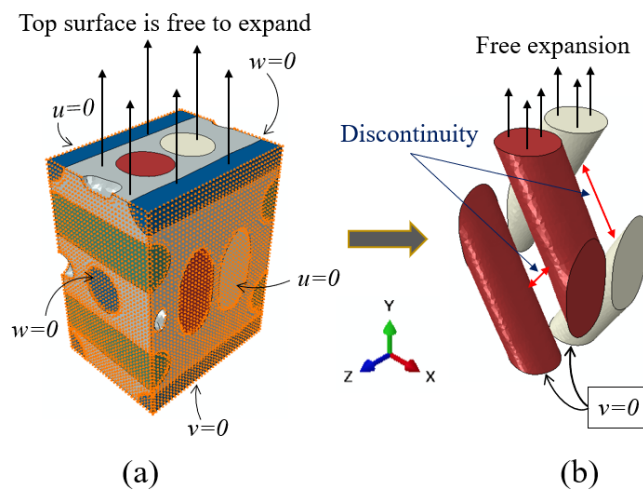


Fig. 5.19 (a) Boundary condition applied on RVE and (b) Boundary conditions contributed by oblique bundles

The bottom face of the RVE is constrained against deformation in the y -direction ($v=0$) and this face contains only two bundles (one from each direction) while the other two bundles are attached to the opposite face (see Fig. 5.19(b)). Hence, the deformation in the y -direction is mostly controlled by the weak interface between bundles/matrix that results in a higher deformation in the y -direction. Next, the effect of interfacial conditions in terms of displacement distribution in RVE at 2227°C is presented for all of three orthogonal cases in Fig. 5.20. Fig. 5.20 (b) describes the displacement field along the path 'J-K' in RVE4B (refer Fig. 5.20(a) for path) when deformation is allowed in the x -direction. Here, an increase in the magnitude of displacement jump near the bundle/matrix interfaces is observed as its condition changes from perfect to complete debond. In the case of a completely debonded interface, the magnitude of the displacement jump is almost the same at three interfaces (I, II, and IV) and much higher than that at interface III. Fig. 5.20(d) shows the displacement plots along the path 'L-M' (for path refer Fig 5.20 (c)) when the RVE deforms in the y -direction. It is clear from the plots that the variation in the displacement jump at the interface I and IV are negligible as compared to II and III.

Similar plots for ' w ' displacement are shown in Fig 5.20 (f) along the path 'N-O' (see Fig 5.20 (e) for path). In this case, the displacement jump is negligible at the interface II and IV as compared to I and III. Further, it was noticed that the displacement jumps increase drastically for the complete debond condition while the effect on the overall deformations is low. It is also clear from the displacement contours that the RVE also captures the effects of the bundle distortions and voids on the local field (displacements and strains) variations. It is observed from the study that the overall deformations of RVEs are reduced around 36.69% and 38.97% by using the imperfect interface (when compared to the perfectly bonded case) for the loads in x and z directions, respectively. Furthermore, the respective reduction is around 45.48% and 47.15% in the case of the completely debonded interface.

It is observed from the above study that the effect of the interface is more predominant in the local fluctuations as compared to the overall deformation.

Next, the contour plots of the cohesive scalar damage variable (CSDMG) are shown in Fig. 5.21 for certain temperatures to explore the extent of damage that occurred at the interfaces in the RVEs. The value of CSDMG varies from 0 (as perfectly bonded) to '1' (for completely debonded). Fig. 5.21(a) shows the contours of CSDMG for the load in the x -direction at different temperatures.

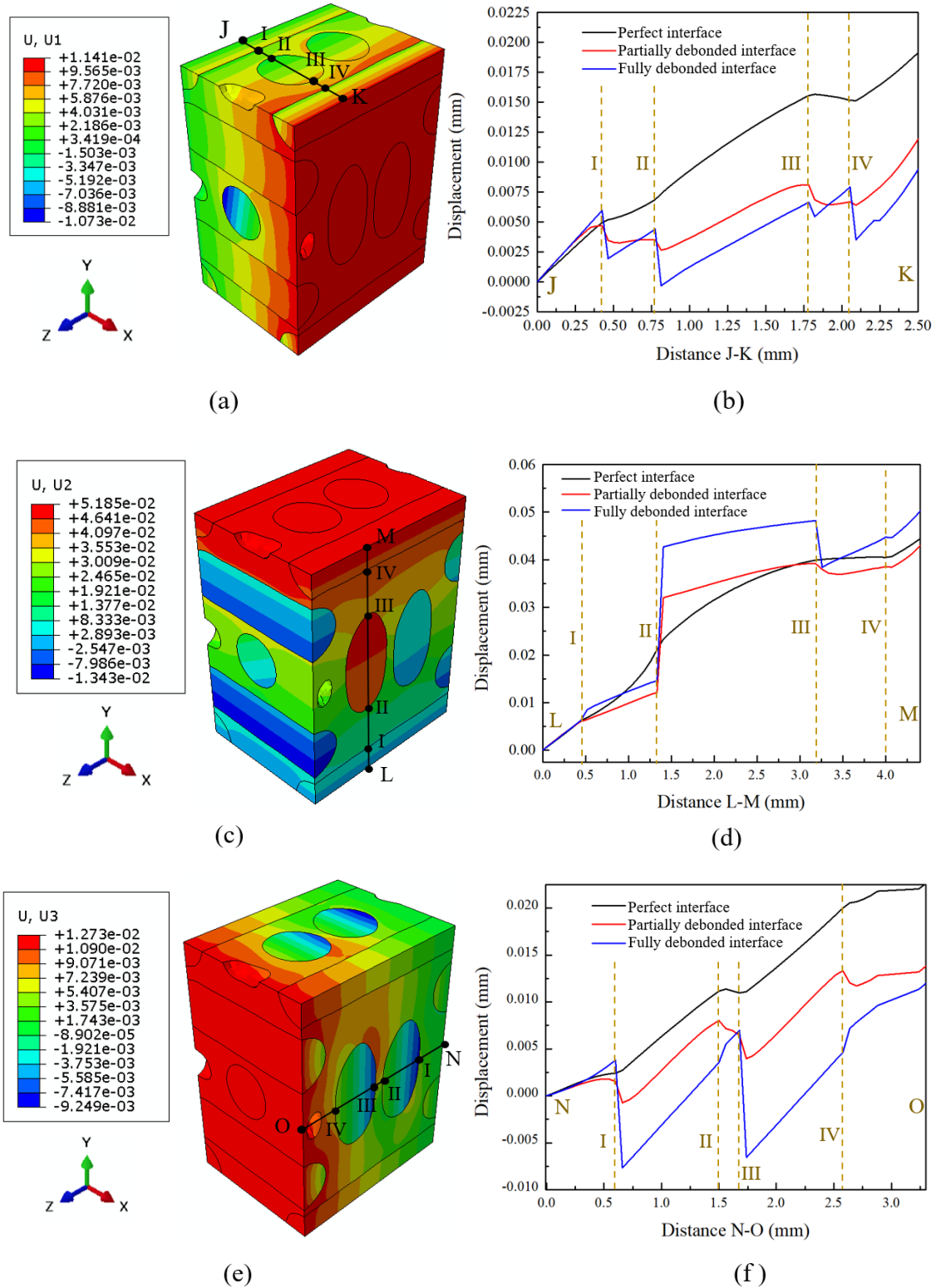


Fig. 5.20 Plot for interfacial displacement jump for three different interfacial conditions at 2227°C in (a, b) x-direction, (c, d) y-direction, and (e, f) z-direction in 4DIN C/C composite

It is revealed in Fig. 5.21(a) that the interfacial damage initiates at the ends of oblique bundles nearly at 247°C (corresponding thermal strain is 0.008%) and then the damage network enlarges with further increments in

temperature. The interfacial damage progressively increases with temperature and significant damage was observed at 2227°C (see Fig. 5.2I(a)) from left to right), where the corresponding overall thermal strain is 0.49%). A similar trend of the damage initiation and evolution was observed in the case of z-directional load (refer Fig. 5.2I(c)). The thermal strains corresponding to the temperatures, 247°C and 2227°C, are obtained as 0.009% and 0.42 %, respectively.

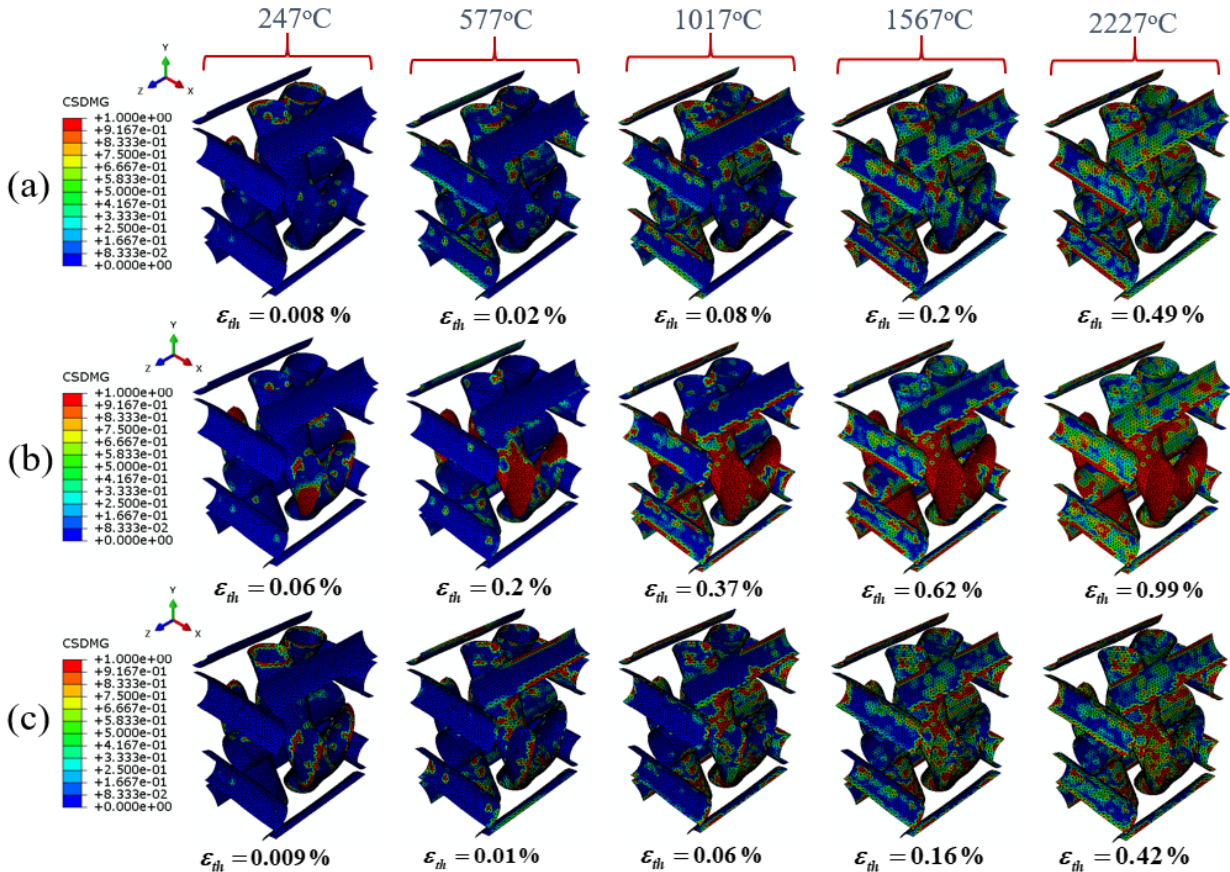


Fig. 5.2I Cohesive surface damage variable (CSDMG) plot when RVE deform in (a) x-direction, (b) y-direction, and (c) z-direction

It was observed earlier that the deformation pattern of the RVE in the y-direction is different from the other two directions; in the same way, similar behavior is also observed in the damage patterns. The interface damage has played a critical role and contributed to the increased thermal strains. The thermal strains at the temperatures 247°C and 2227°C are computed as 0.06% and 0.99% respectively (refer Fig. 5.2I(b)). These values are comparatively higher than those obtained for the cases of x and z directions. Therefore, the amount of damage at the interfaces of the oblique bundle is observed to be on the higher side as compared to other (x and z) bundles' interfaces (see Fig. 5.2I(b)). The extent of the damage at the interfaces of x and z bundles is almost similar to those obtained for the load cases of x and z directions. Finally, the effective thermal expansion coefficients of all the three RVEs of the 4DIN C/C composite were obtained as a function of temperature through the two-scale analysis for three interface conditions. The mean effective CTEs obtained from three

RVEs as a function of temperature (up to 2227°C) in three orthogonal directions are compared to those obtained through experiments in Fig 5.22.

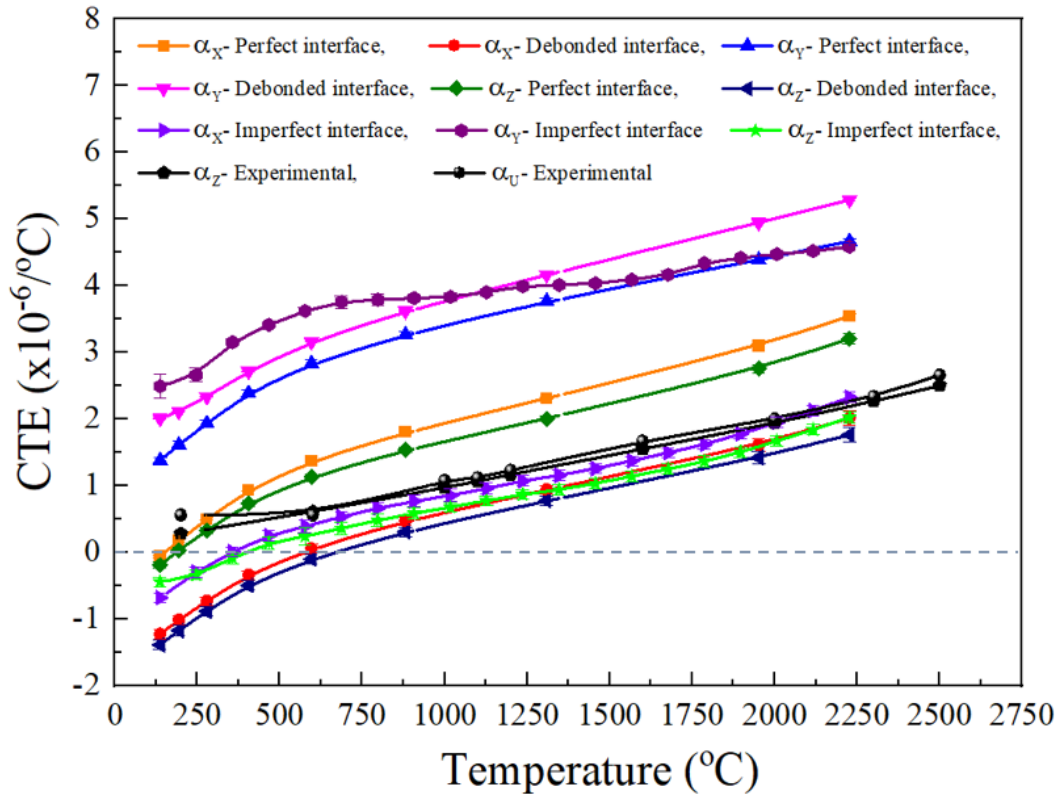


Fig. 5.22 The effective thermal expansion coefficient of 4DIN C/C composite in three orthogonal directions

The values of the effective CTE of the 4DIN C/C composite in the x-direction (α_x) is computed as -0.06×10^{-6} at 137°C and 3.546×10^{-6} at 2227°C for a perfectly bonded case. The same has reduced to -0.68×10^{-6} and $2.32 \times 10^{-6} / ^\circ\text{C}$ at the respective temperatures in case of the imperfectly bonded case. The values of α_x are further reduced to -1.22×10^{-6} and $2.016 \times 10^{-6} / ^\circ\text{C}$ for the completely debonded condition at respective temperatures. A similar trend was found for the effective CTE of the composite for z-direction (α_z). The values of α_z is computed as -0.187×10^{-6} at 137°C and $3.2 \times 10^{-6} / ^\circ\text{C}$ at 2227°C for a perfectly bonded interface, which is reduced to the -0.44×10^{-6} and 2.02×10^{-6} at respective temperatures for the imperfectly bonded case. α_x is always on the higher side as compared to α_z because it possesses a lower volume fraction of x-bundle than z-bundle in the composite. The variation of the computed α_x and α_z with respect to the temperature is also found to be in close proximity to experimental results. The values of α_x and α_z are especially in excellent agreement to experimental observations for temperatures higher than 627°C and also in the case of the imperfectly bonded interface. Apart from this, it is also observed that the behavior of α_y is different than

that of α_x and α_z for different interfacial conditions. Initially, the value of α_y is higher for the imperfectly bonded condition as compared to the perfectly and completely debonded conditions. The rate of increase of α_y with respect to the temperature is reduced after 675°C. The values of α_y almost match the values of those obtained for a perfectly bonded case for temperatures higher than 1500°C. The discontinuity in the oblique bundles in the y-direction (see Fig. 5.19) is the leading cause of this behavior of α_y . Finally, it can be concluded from the study that interfacial degradation has reduced the effective thermal expansion coefficients of the 4DIN C/C composite. The low thermal expansion coefficient is a favorable condition for composite performance. Simultaneously, the interfacial degradation also provides an active site for oxidation reaction and reduces the effective thermal conductivity of that composite, which are unfavorable conditions.

Chapter 6

Thermal shock resistance of 4DIN C/C composite

In this chapter, a FEM based numerical simulation was performed on a homogeneous sample of 4DIN C/C composite and its thermal shock resistance was estimated in terms of critical Laser power density. The temperature-dependent homogenized properties of the 4DIN C/C composite as predicted in previous chapters are used in the analysis. Firstly, the governing theory i.e. the classical theory of linear thermo-elasticity is briefly discussed. Next, the numerical framework is presented. In the last section, predicted FE results are compared to those that already exist in literature.

6.1 Thermal shock resistance

Thermal shock resistance of materials reflects their ability to sustain high thermal stresses generated due to sudden exposure to severe temperature changes. C/C composites are the most popular materials for high thermal applications in aerospace industries. They are used for the manufacturing of critical components of spacecraft where they have to endure thermal shock kind of loading. Therefore, it is very important to explore the thermal shock capability of these composite materials prior to the designing of such critical components. In the last few decades, the numerous analytical [7-11], experimental [13-26], and numerical [27-30] studies in this concern illustrate the valuable efforts of researchers worldwide. The main focus of these studies is to estimate the critical parameters that a material can sustain without fracture. These critical parameters are temperature change and heat flux. In the present study, the critical parameter has been discussed in terms of laser power density that the considered 4DIN C/C composite can sustain without showing any sign of fracture.

6.2 Governing equation and finite element formulation

In the present thermal shock analysis, the classical theory of linear thermo-elasticity [128] is used. In classical theory, the boundary value problem in the domain $\Omega \in R^d$ can be defined using the following set of differential equations. Let Γ be the boundary of the domain Ω such that $\Gamma = \Gamma^u \cup \Gamma^t \cup \Gamma^\theta \cup \Gamma^f$.

The superscripts u , t , θ , and f stand for displacement, traction, temperature, and heat flux imposed boundaries respectively.

Elastic initial boundary value problem:

$$\text{Equation of motion:} \quad \sigma_{ij,j} + \rho F_i = \rho \ddot{u}_i \quad \text{in } \Omega \quad (6.1)$$

$$\text{Constitutive relation:} \quad \sigma_{ij} = C_{ijkl}(e_{kl} - \alpha_{kl}\theta) \quad \text{in } \Omega \quad (6.2)$$

$$\text{Strain displacement relation:} \quad e_{kl} = u_{k,l} \quad \text{on } \Omega \quad (6.3)$$

$$\text{Displacement BC:} \quad u_i = \hat{u}_i \quad \text{on } \Gamma^u \quad (6.4)$$

$$\text{Traction BC:} \quad \sigma_{ij}n_j = \hat{p}_i \quad \text{on } \Gamma^t \quad (6.5)$$

$$\text{Initial conditions:} \quad u_i|_{t=0} = u_i^o \text{ and } \dot{u}_i|_{t=0} = \dot{u}_i^o \quad (6.6)$$

Transient thermal initial boundary value problem:

$$\text{Thermal energy equation:} \quad -q_{i,i} + \rho R + T_o \beta_{ij} \dot{e}_{ij} = \rho c \dot{\theta} \quad \text{on } \Omega \quad (6.7)$$

$$\text{Fourier's law:} \quad q_i = -k_{ij} \theta_{,j} \quad \text{on } \Omega \quad (6.8)$$

$$\text{Temperature BC:} \quad \theta = \hat{\theta} \quad \text{on } \Gamma^\theta \quad (6.9)$$

$$\text{Heat flux BC:} \quad q_i n_i = \hat{q}_n + h(\theta_w - \theta_\infty) \quad \text{on } \Gamma^f \quad (6.10)$$

$$\text{Initial condition:} \quad \theta|_{t=0} = \theta^o \quad (6.11)$$

Where σ_{ij} is the stress tensor, e_{kl} is the strain tensor, C_{ijkl} is the fourth-order stiffness tensor, u_i is displacement vector, p is the traction, α_{kl} is the thermal expansion coefficient ($\beta_{kl} = C_{ijkl}\alpha_{kl}$), ρ is the density, R is the heat generation per unit mass, F_i is the body force per unit mass, c is the specific heat, θ is the temperature difference, k_{ij} is thermal conductivity, q_i stands for heat flux, n_i is the unit vector normal to the surface, and h is the surface heat transfer coefficient. Here, i, j, k , and l are the tensorial indices. The subscripts w and ∞ show the body wall and ambient conditions, respectively. The symbols $(\dot{\cdot})$ and $(\cdot)_{,j}$ indicate the time derivative and the spatial derivative, respectively. The symbol $(\hat{\cdot})$ is used for the prescribed quantities.

Equation (6.2) (second term on the right-hand side) and equation (6.7) (the third term on the left-hand side) contain the terms responsible for thermal to mechanical and mechanical to thermal coupling, respectively. In a linear elastic range, the effect of mechanical deformation on thermal response is almost negligible. Therefore, we neglect the coupling term from equation (6.7), which then reduces the problem to only one-way couplings. Consider δu_i and $\delta \theta$ to be the test functions for elastic and thermal problem respectively, the weak form of the problems can be obtained by employing the concept of weighted residuals as (refer **Appendix-C(i)**)

$$\text{Weak form of the elastic problem:} \quad \int_V \sigma_{ij} (\delta u_i)_{,j} dv = \int_S \hat{p}_i \delta u_i ds + \int_V \rho F_i \delta u_i dv - \int_V \rho \ddot{u}_i \delta u_i dv \quad (6.12)$$

$$\begin{aligned} \text{Weak form of the} & \int_V q_i (\delta\theta)_{,i} dv + \int_V \rho R \delta\theta dt = \int_{S_1} \hat{q}_n \delta\theta ds + \int_{S_2} h(\theta_w - \theta_\infty) \delta\theta ds + \int_V \rho c \dot{\theta} \delta\theta dt \\ \text{thermal problem:} & \end{aligned} \quad (6.13)$$

The considered domain is assumed to be discretized into finite element mesh using n noded linear finite elements. If $[N^d]$ and $[N^\theta]$ are the displacement and the temperature shape function of the element respectively, $\{u_i^{(n)}\}$ and $\{\theta^{(n)}\}$ are the respective nodal unknowns; then, displacement and temperature fields within each finite element can be approximated as

$$\{u_i^{(e)}\} = \begin{Bmatrix} u_x^{(e)} \\ u_y^{(e)} \\ u_z^{(e)} \end{Bmatrix} = [N^d]^T \{u_i^{(n)}\} \quad (6.14)$$

$$\{\theta^{(e)}\} = [N^\theta]^T \{\theta^{(n)}\} \quad (6.15)$$

$$\text{Where } \{u_i^{(n)}\} = \left\{ u_x^{(1)} \quad u_y^{(1)} \quad u_z^{(1)} \quad u_x^{(2)} \quad u_y^{(2)} \quad u_z^{(2)} \dots \dots u_z^{(n)} \right\}^T$$

$$\{\theta^{(n)}\} = \left\{ \theta^{(1)} \quad \theta^{(2)} \quad \theta^{(3)} \dots \dots \theta^{(n)} \right\}^T$$

$$[N^d]^T = \begin{bmatrix} N_1^d & 0 & 0 & N_2^d & 0 & 0 & N_3^d & 0 & 0 \dots \dots N_n^d & 0 & 0 \\ 0 & N_1^d & 0 & 0 & N_2^d & 0 & 0 & N_3^d & 0 \dots \dots 0 & N_n^d & 0 \\ 0 & 0 & N_1^d & 0 & 0 & N_2^d & 0 & 0 & N_3^d \dots 0 & 0 & N_n^d \end{bmatrix}$$

$$[N^\theta]^T = [N_1^\theta \quad N_2^\theta \quad N_3^\theta \quad N_4^\theta \quad N_5^\theta \dots \dots N_n^\theta]$$

$$\{e_{ij}^{(e)}\} = [B^d]^T \{u_i^{(n)}\} \text{ and } \{\theta^{(e)}\}_{,i} = [B^\theta]^T \{\theta^{(n)}\} \quad (6.16)$$

$$\text{Let } [k] = \begin{bmatrix} k_{xx} & 0 & 0 \\ 0 & k_{yy} & 0 \\ 0 & 0 & k_{zz} \end{bmatrix}, \{\alpha^{(e)}\} = \{\alpha_{xx} \quad \alpha_{yy} \quad \alpha_{zz} \quad 0 \quad 0 \quad 0\}^T, [C_{ijkl}] = [D] \quad (6.17)$$

According to Galerkin's approach,

$$\{\delta u_i\} = [N^d]^T, \{\delta\theta\} = [N^\theta]^T, \{\delta u_{i,j}\} = [B^d]^T, \{\delta\theta_{,i}\} = [B^\theta]^T \quad (6.18)$$

Utilizing equations (6.14) - (6.17) in equation (6.12) and (6.13), the following finite element formulations are acquired (Refer **Appendix-C (ii)**).

$$[M^{dd}] \{\ddot{u}_i^{(n)}\} + [K^{dd}] \{u_i^{(n)}\} + [K^{d\theta}] \{\theta^{(n)}\} = \{\phi^d\} \quad (6.19)$$

$$[C^{\theta\theta}] \{\dot{\theta}^{(n)}\} + [K^{\theta\theta}] \{\theta^{(n)}\} = \{\phi^\theta\} \quad (6.20)$$

Where

$$\begin{aligned}
[K^{dd}] &= \int_{V^e} [B^d][D][B^d]^T dv & [C^{\theta\theta}] &= \int_{V^e} \rho c [N^\theta][N^\theta]^T dv \\
\{\phi^d\} &= \int_S [N^d] \{\hat{p}_i\} ds + \int_{V^e} \rho [N^d] \{F_i\} dv & [K^{\theta\theta}] &= \int_{V^e} [B^\theta][k][B^\theta]^T dv \\
[M^{dd}] &= \int_{V^e} \rho [N^d][N^d]^T dv & \{\phi^\theta\} &= \int_{V^e} \rho [N^\theta] \{R\} dv - \int_{S_1^e} [N^\theta] \{\hat{q}_n\} ds - \int_{S_2^e} [N^\theta] h(\theta_w - \theta_\infty) ds \\
[K^{d\theta}] &= - \int_{V^e} [B^d][D] \{\alpha^{(e)}\} [N^\theta]^T dv
\end{aligned}$$

Here, equation (6.19) and (6.20) are the finite element formulation for mechanical and thermal problems respectively. They were solved explicitly to get the displacement as well as the temperature distribution in the considered domain. In the present study, the explicit algorithm available in the commercial FE package “ABAQUS” that uses the explicit forward difference method to solve the thermal problem and the explicit central difference method to solve the mechanical problem [129] was utilized.

6.3 Material

A homogeneous sample of 4DIN C/C composite is considered for this study. Also, the numerically predicted effective thermal conductivity and the effective thermal expansion coefficients of the composite that were obtained in the previous Chapters 4 and 5 are utilized.

Table 6.I Mean effective elastic constants of 4DIN C/C composite

Temperature (°C)	E_{xx} (GPa)	E_{yy} (GPa)	E_{zz} (GPa)	G_{xy} (GPa)	G_{xz} (GPa)	G_{yz} (GPa)	ν_{xy}	ν_{xz}	ν_{yz}
27	25.5749	14.4623	30.2778	5.5753	3.8928	3.8925	0.2725	0.066	0.0802
227	25.5496	14.4563	30.2468	5.5733	3.8918	3.8914	0.2725	0.0661	0.0803
427	25.4831	14.439	30.1639	5.5665	3.8882	3.8844	0.2726	0.0662	0.0804
627	25.4166	14.4217	30.081	5.5596	3.8846	3.8844	0.2726	0.0663	0.0805
827	25.3863	14.4145	30.0412	5.5586	3.8836	3.8833	0.2726	0.0664	0.0806
1027	25.2457	14.3854	29.8993	5.5487	3.8782	3.878	0.2726	0.0667	0.0808
1227	25.0933	14.3395	29.6766	5.5322	3.8688	3.8685	0.2726	0.067	0.0812
1427	24.6618	14.2261	29.1378	5.4923	3.8463	3.846	0.2728	0.068	0.0822
1627	23.7556	13.9812	28.0083	5.4061	3.798	3.7976	0.273	0.07	0.0843
1827	21.7708	13.4048	25.5399	5.2011	3.6817	3.6812	0.2734	0.0749	0.0891
2027	19.3367	12.6106	22.5308	4.9157	3.5173	3.5164	0.2737	0.0817	0.0958
2227	16.8359	11.6773	19.4596	4.5762	3.3182	3.3168	0.2736	0.09	0.1037

The interface is assumed to be perfectly bonded. The mean effective elastic constants of the 4DIN C/C composite were obtained through the mechanical analysis of composite RVEs. The loading and periodic boundary conditions as discussed in chapter-5 (section-5.5.1, equations 5.21 to 5.25), were utilized during analysis. The obtained effective elastic constants of 4DIN C/C composite are given in Table 6.1. Apart from this, the temperature-dependent specific heat of the 4DIN C/C composite is taken from the literature [130] as given in Table 6.2.

Table 6.2 Specific heat of 4DIN C/C composite [130]

Temperature (°C)	23	100	200	300	400	500	600	700	800	900	1000	1100
Specific Heat (J/g°C)	0.65	0.95	1.35	1.62	1.8	1.95	2.1	2.2	2.25	2.28	2.281	2.282

6.4 Numerical model and thermal shock analysis

In this section, the laser irradiation test is simulated using the finite element based coupled thermomechanical analysis. It is assumed that the test is performed on a composite cylinder of 50mm diameter and 12 mm thickness that is similar to the test specimen used by Li et al. [98] (see Fig 6.1(a)).

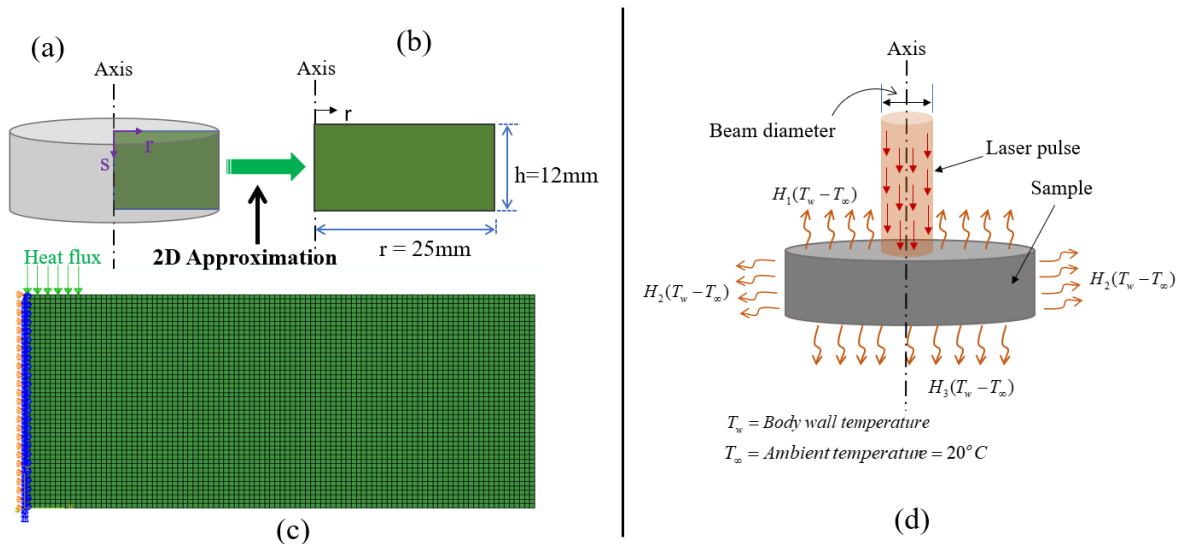


Fig. 6.1 (a) Cylindrical specimen, (b) 2D approximation, (c) 2D approximated finite element model with associated loading and boundary conditions, and (d) Schematic diagram of the laser pulse irradiation technique

Furthermore, the problem is reduced to the 2D axisymmetric case by exploiting the symmetric conditions (refer Fig 6.1(b)). Fig. 6.1(c) represents the discretized FE mesh of the composite that contains around 4800 axisymmetric elements (CAX4RT in ABAQUS/Explicit). The cylindrical body is centrally heated with a laser pulse for one second and then allowed to cool in the open air for two seconds. The power density of the laser pulse is varied from 10W/mm² to 230 W/mm² and the beam diameter is also in the range of 4-50 mm. The schematic diagram of thermal loading and boundary conditions is illustrated in Fig 6.1(d). Next, the temperature-dependent convective heat transfer coefficients for the top (H1), side (H2), and bottom surfaces (H3) of the body were taken from the literature [23] that are given by the equations (6.21), (6.22), and (6.23) respectively.

$$H_1 = 1.32 \left(\frac{\Delta T}{l_c} \right)^{0.25} \quad (6.21)$$

$$H_2 = 1.42 \left(\frac{\Delta T}{l_c} \right)^{0.25} \quad (6.22)$$

$$H_3 = 0.61 \left(\frac{\Delta T}{l_c} \right)^{0.25} \quad (6.23)$$

Here, l_c is the characteristic length and is defined as the ratio of the volume to the total surface area of the specimen. ΔT is the difference in the wall and the ambient temperatures. The emissivity ' ϵ ' for the composite surface is considered to be 0.9. The material is assumed to be failed under shear strength criteria as the shear strength of the 4DIN C/C composite is reported to be much lower than its tensile and compressive strength. The maximum shear strength of the composite is assumed from literature as 7.8 MPa [77].

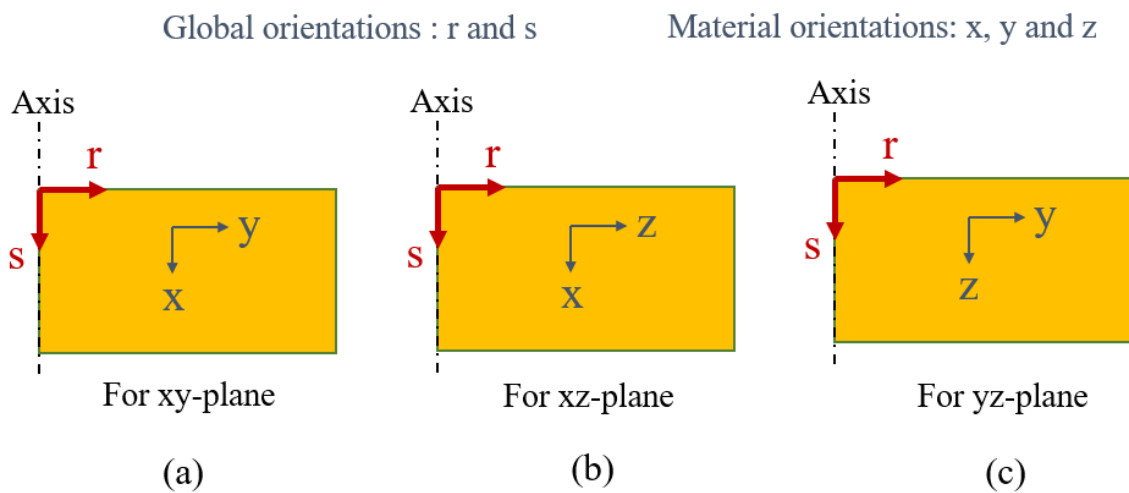


Fig. 6.2 Representation of (a) xy-plane, (b) xz-plane, and (c) yz-plane by assigning different material orientations along the r and s direction of the 2D approximated model

The magnitude of LPD at which the thermally induced shear stresses approach the shear strength is termed as critical laser power density. This is one of the measures of thermal shock resistance of the composite material and defines the capability of the material to sustain the laser power density up to the first sign of the fracture. In the present analysis, the material is assumed to be orthotropic. The shear strength of the composite was checked in three orthogonal directions (along xy , xz , and yz planes) individually. The representation of three different orthogonal planes by a 2D approximated model was achieved through assigning the different material orientations along 'r' and 's' directions (refer Fig 6.2). The detailed discussion on the critical laser power density for the 4DIN C/C composite corresponding to different beam diameters is presented in the next section.

6.5 Results and discussion

The discussion on the effect of the laser power density on the critical parameters i.e. the critical plane of failures, a critical time for laser pulse, and critical location on a critical plane, is presented in the next three subsections.

6.5.1 Critical laser power density and the critical plane

The critical power density depends on the two laser beam parameters: 1) the diameter of the laser beam and 2) heat flux density. The heat flux is varied from 10-230 W/mm² for different diameters of the beam to conclude the effect of laser power density on the composite. As stated earlier, the heat pulse is allowed on the specimen for 1 second followed by a cooling of 2 seconds. The temperature of the composite was increased to the maximum value during the 1 second that led to an increase in the shear stress within the composite. Fig. 6.3(a) shows the typical shear stress distribution in the composite for a 20mm beam diameter and 50 W/mm² heat flux. The maximum shear stress was attained in the specimen at 0.8 sec for this particular case. It is clear from Fig. 6.3(a) that there are two extreme conditions for the shear stresses: one near the top surface with a negative magnitude and another above the bottom surface with a positive magnitude. Therefore, it has been intended to study the stress distribution along the path (A-B) (refer Fig. 6.3 (a)) passing through these two extreme stress points. Fig.6.3 (b) shows the variation of the shear stresses along the path A-B for different flux densities. It is observed from Fig. 6.3(b) that the magnitude of the negative shear stress changes sharply along the line A-B as the flux is increased from 10-100 W/mm². Also, the results reveal that the point of the maximum shear stress slightly changed its position along the depth. However, the inflexion point does not change its position. Fig. 6.3(c) shows the variation of the shear stress along the path C-D (refer Fig. 6.3a) in the horizontal axis for different flux densities.

The maximum shear stress occurs just near the circumference of the beam (see Fig. 6.3(c)). It is observed in this study that the magnitude of the maximum shear stress sharply increases as the flux density is increased from 10-100 W/mm². Apart from this, the magnitude of the negative component of shear stress is around 2 times higher

than its positive counterpart. The location of absolute maximum shear stress lies within 0.5 to 2 mm in the depth from the irradiated surface near the beam periphery.

Next, the variation of the absolute maximum shear stress with the laser power density is observed. Fig. 6.4(a) shows the variation of the maximum shear stress (τ_{xy}) with respect to the laser power density for different beam diameters. A threshold value of 7.8 MPa that corresponds to the ultimate shear strength of the composite is also marked in Fig 6.4(a). The point at which the threshold line cuts the curves gives the power density of the beam required to reach the ultimate stress. This point is also referred to as the failure initiation point, and the corresponding beam power density is referred to as the critical laser power density that initiates the failure. Fig. 6.4(b) shows the requirement of the critical laser power densities for different beam diameters to initiate the failure in the composite.

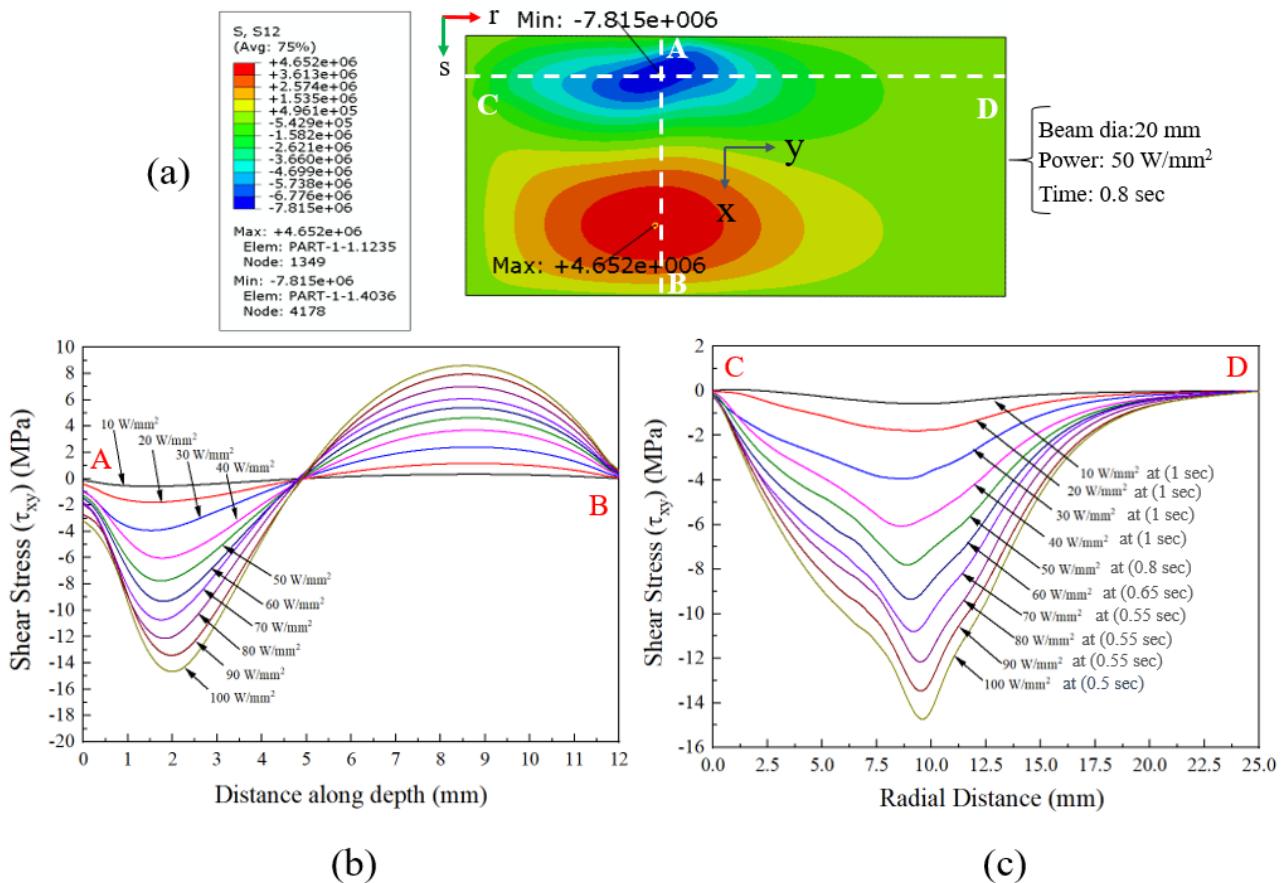


Fig. 6.3 (a) Shear stress contour plot in xy-plane and paths crossing the maximum stress point (b) Shear stress distribution along the path 'A-B' (c) Stress distribution along the path 'C-D'.

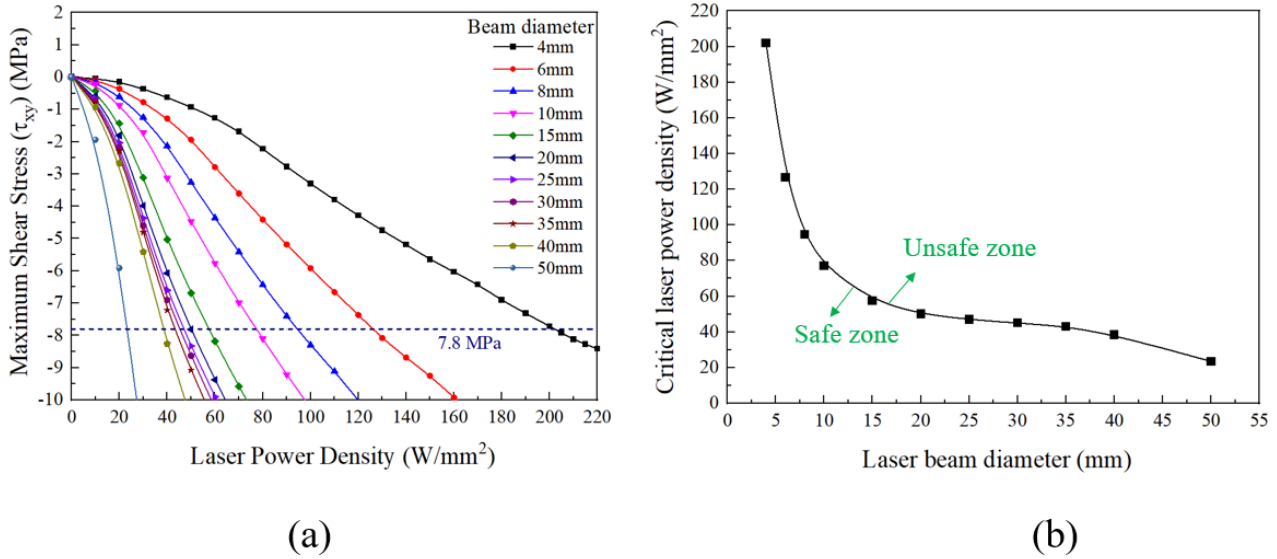


Fig. 6.4 (a) Maximum shear stress (τ_{xy}) Vs LPD curve and (b) Critical LPD curve

It is observed from Fig 6.4(b) that the slope of the critical laser density curve between the 15mm to 40 mm beam diameter is almost flat. The laser power density required to initiate the failure increases exponentially as the beam diameter is reduced from 15 mm to 5mm. Similarly, it decreases slowly as the beam diameter is increased to 40mm and above (this decrement is because of end effect i.e if we consider a test sample of bigger diameter, the slope of curve will remain flat beyond the 40 mm beam diameter and will go dawn at the end of the sample diameter). The area under the curve signifies the safe zone for the composite and the area above the curve is an unsafe zone, i.e., any combination of LPD and beam diameter that lies above this curve will cause thermal shock damage in shear mode. Fig. 6.5 shows the critical LPD curves obtained for the other two planes of the composite (i.e., Shear stresses τ_{xz} and τ_{yz}). It is clear from Fig 6.5 that the composite has almost similar behavior in all three planes under thermal shock.

The obtained response of the composite has also been compared to the one obtained by Li et al. [24] for a 2D laminated C/C composite. It is to be noted that the trend of the critical power density is very similar to the one obtained for the 2D laminated C/C composite. The critical LPD for the 4D C/C composite is around 10-18 times higher as compared to the 2D laminated composites. This means that the thermal shock resistance capability of the 4D C/C composite is around 10-18 times higher than that of the 2D laminated C/C composite. This enhanced thermal shock resistance of the 4D C/C composite is mainly due to the better arrangement of fibers and comparatively enhanced properties of the 4DIN composite as compared to the 2D composite (at 27°C, it possesses $TC=5.2$ W/mK and $CTE=4 \times 10^{-6}/^{\circ}C$ [24]).

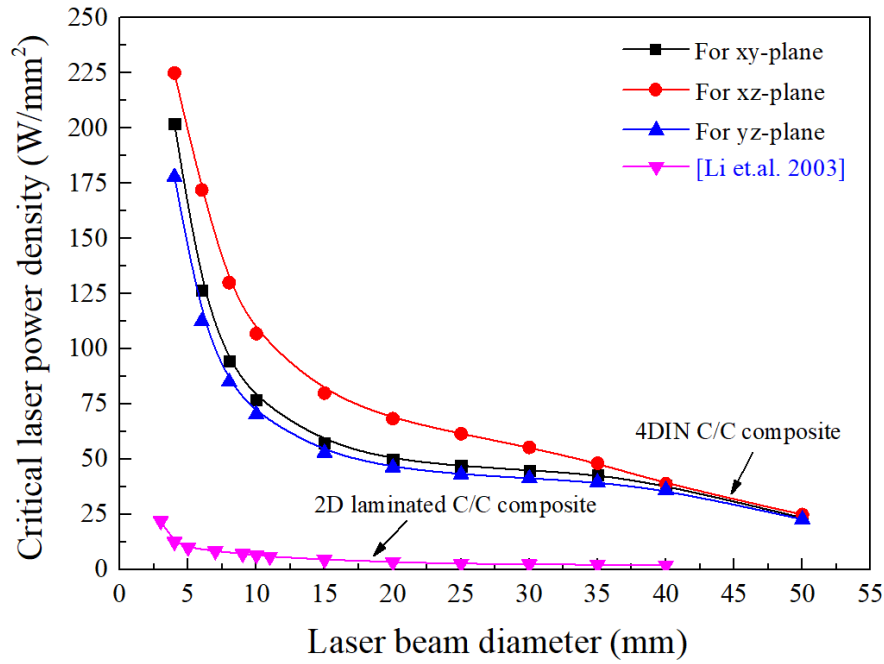


Fig. 6.5 Critical LPD curve for 4D C/C composite associated with three orthogonal planes and their comparison with critical LPD curve for 2D laminated C/C composite (Li et.al. [24]).

Furthermore, it is observed from Fig. 6.5 that the behaviors of the yz and xy planes are almost similar and lie slightly lower than the xz-plane. This suggests that the critical value of LPD is comparatively higher for the xz-plane as compared to the other two. Also, the yz-plane of the 4D C/C composite is the critical plane for shear failure under thermal shock loading. Therefore, the shear stress and temperature distribution on the yz-plane at critical LPD for different beam diameters are studied in detail in the next subsections.

6.5.2 The critical time of laser irradiation

The critical time of laser irradiation is another important parameter in thermal shock problems; hence, it was studied for critical yz-plane. Corresponding to the critical LPD values for the yz-plane, the variations of shear stress with time at the location of maximum shear stress were measured for different beam diameters and are presented in Fig 6.6(a). The locations of critical shear stress (where shear stress reaches the magnitude of strength at critical LPD) are termed critical locations. It is revealed in Fig. 6.6 (a) that the shear stress reaches the ultimate or limiting magnitude of the strength at different time instances in the pulse duration for a critical LPD. Such an instance of time is called a critical time of laser irradiation. It is also clear from Fig 6.6 (a) that critical time is also a function of the laser beam diameter. The critical time for the 4mm beam diameter is around 0.1 sec that increases with an increase in the diameter of beams. Fig. 6.6 (b) shows the variation of the critical time with the laser beam diameter. It is observed that the critical time increases almost linearly with an increase of beam diameter up to 20mm and afterward remains constant at 1 sec.

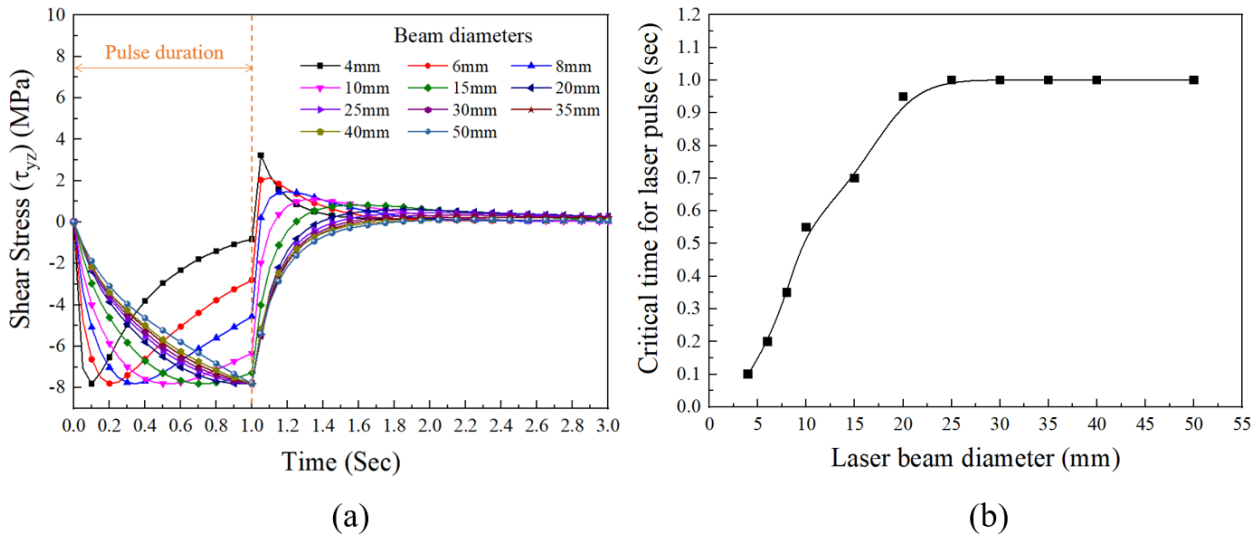


Fig. 6.6 (a) Shear stress vs time plot at the location of maximum stress and corresponding to critical LPD and (b) Critical time for different beam diameters.

6.5.3 Shear stress and temperature distributions at the critical laser power density

The critical time of laser irradiation varies with the beam diameter; therefore, the shear stress and the temperature distribution in yz -plane were studied at the corresponding critical times for different beam diameters, as shown in Fig. 6.7 (a) and (b) respectively. It is clear from Fig 6.7 (b) that the area in contact with the laser pulse on the irradiated surface is the region of maximum temperature and is further diffused toward the boundaries of the specimen.

The critical locations of the shear stress are marked on the contours for different diameters. It is observed that the locations shift towards the outer periphery of the specimen as the beam diameter is increased (see Fig 6.7(a)). On the other hand, the propagation of critical locations with respect to the beam diameter is comparatively very small in the thickness direction (s -direction). The shear stress distribution along the paths crossing the critical locations (refer Fig 6.3(a) for clarity about paths) is presented in Fig 6.8 (a) and (b) respectively as a function of coordinates.

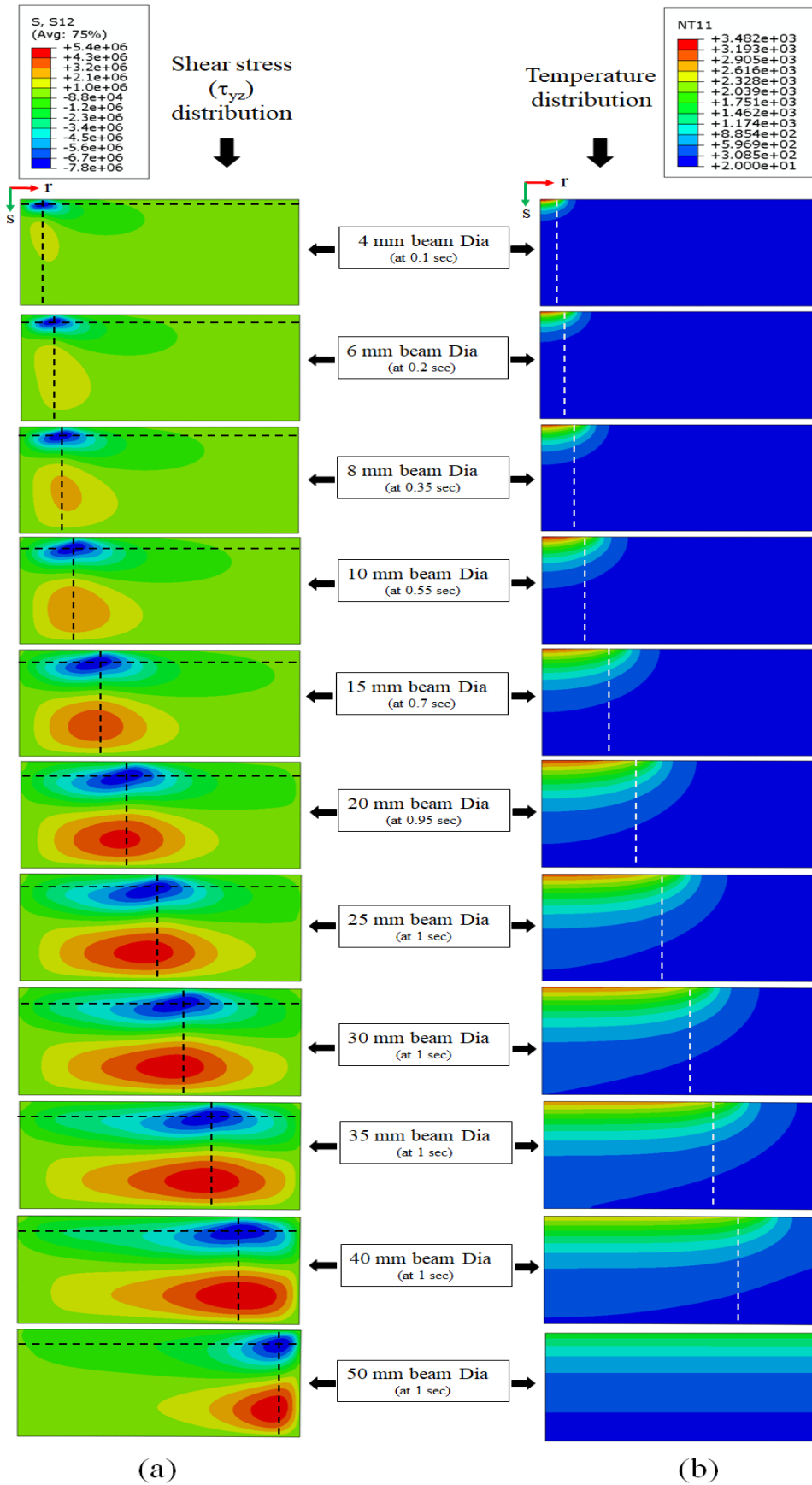


Fig. 6.7 (a) Shear stress distribution and (b) Temperature distribution at critical LPD at the critical time.

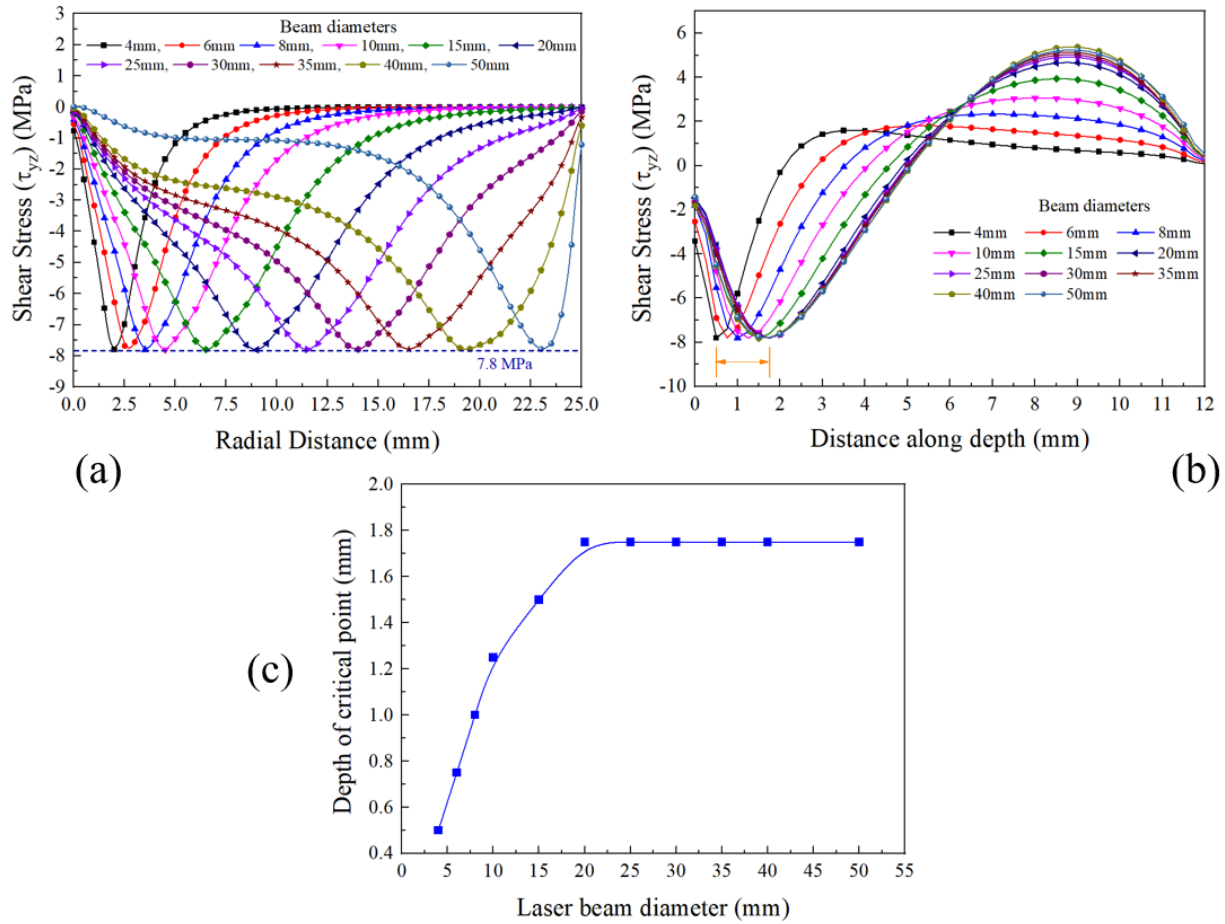


Fig. 6.8 (a) Shear stress distribution in the radial direction along the path crossing critical location, (b) Shear stress distribution in the thickness direction along the path crossing critical location, and (c) Depth of critical location for different beam diameters

Fig 6.8 (a) clearly shows that shear stress varies along the radial direction reaching the peak near the beam periphery. The peak assures the propagation of critical location in the radial direction with beam diameters. In Fig 6.8 (b), the shear stresses vary along the depth reaching their minima at 0.5-1.75 mm below the irradiated surface depending upon the beam diameter. Fig 6.8 (c) shows the critical depth as a function of the beam diameter. It is observed that it has increased from 0.5 mm to 1.75mm with an increase in the diameter of the beam from 4mm to 20mm respectively, and remains constant afterward.

Fig. 6.9 shows the variation of the temperature along the critical path in radial and thickness directions. It is observed that the temperature of the central area of the irradiated surface is around 3200°C for the beam diameters from 8mm to 25mm which has further decreased to 1700°C with an increase in diameters. It is clear from Fig. 6.9(a) that the temperature drops sharply just after the periphery of the beam. Fig 6.9(b) shows the variation of the temperature in the thickness direction. The temperature drops sharply in the depth for smaller beam diameters and attained a much gentler slope for beam diameters more than 20mm. It is noted that the sharp gradients of temperature drop in both directions define the critical location of the shear stresses.

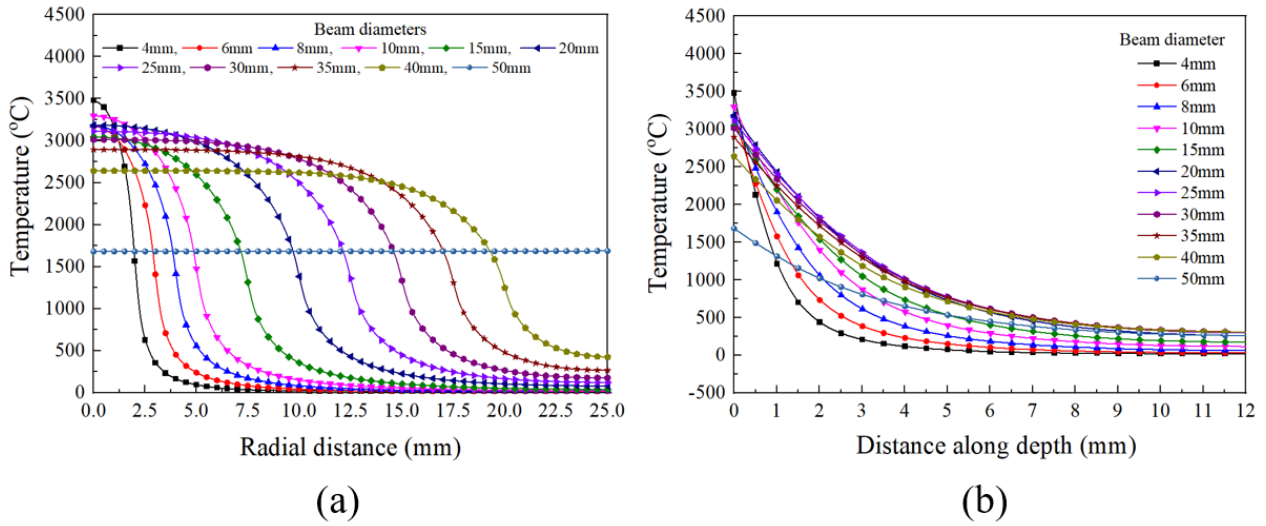


Fig. 6.9 (a) Radial temperature distribution on the irradiated surface and (b) Central temperature distribution along the thickness.

This study on the thermal shock behavior of the multidirectional composites is concluded in the next chapter.

Chapter 7

Conclusions

In this study, X-ray computed tomography was utilized to reconstruct the realistic microstructure of two complex architected multidirectional C/C composites namely: 3DH and 4DIN C/C composites. The inherent imperfections such as bundle distortion, bundle misalignment, irregular shaped big voids, and their distributions were successfully included directly in the finite element model. This omits the major gap between the real microstructure and the idealized geometries of the past studies to some extent. This is also a more realistic way of representing the microstructural characteristics rather than the random distribution of the properties to address the inhomogeneity. Next, the microstructural hierarchy of the material was also included through the two-scale AEH method sequentially. The two-scale formulation was utilized to predict the effective thermal conductivity and effective thermal expansion coefficients of the C/C composites as a function of temperature. The effect of interfacial imperfectness on the local field distributions as well as on the effective responses was also studied in detail. Some experiments were also performed for the validation of the proposed model. Finally, the predicted temperature-dependent effective properties were utilized for the thermal shock analysis at the macro scale. The typical observations and corresponding conclusions based on the current study are highlighted in the following four subsequent sections.

7.1 X-ray computed tomography

X-ray computed tomography is one of the most important tools that was used to explore the microstructural characteristics of materials. The image-based finite element models of composite unit cells were reconstructed using X-ray computed tomography and following major observations and conclusions are derived.

- I. The material microstructure of the 4DIN C/C composite was reconstructed with the help of a 2D image obtained through XCT and the inherent imperfections present in the material were studied in detail.
 - a. It is observed that the microstructure of the composite is observed highly fractured and the 3D network of the cracks and voids is complex. It is revealed from the image analysis that the pores are present in different locations and sizes in the composite. The big voids i.e., voids that are larger than 0.2 mm in diameter are located only in the matrix pockets. Apart from this, a significant porosity is also observed in the composite at different locations such as within bundles, matrix, and near the interfaces.

- b. It is also evident from the image analysis that the composite contains a variety of microcracks. Most of the interfaces of the bundles were found partially cracked. It is also observed through the image analysis that some of these interfacial cracks also propagate through the matrix and tend to merge into the cracks of adjacent interfaces.
 - c. Further, it is evident from the 2D images that the fiber bundles present in the composite are distorted due to the processing stress. These distortions are found in the form of misalignments, size, and shape changes.
 - d. It is observed from the histogram of the greyscale values of the images that the phases i.e. bundles and matrix, have a combined distribution of the grey values of the pixels. It was difficult to identify these phases based on the existing automatic segmentation tools. Hence, a semi-automatic procedure was utilized for the segmentation of these phases.
 - e. 3D segmented image of material microstructures is also reconstructed that ably includes most of the inherent imperfections in the geometry.
2. 3D reconstructed images were discretized into finite element meshes. It is found that a very dense or fine mesh was required to include the micro voids and micro-cracks that lead to a computationally inefficient FE mesh. To make the computations cost-effective, some compromises were made in the reconstructed 3D image.
 - a. Fiber bundles and matrix are considered homogenous materials at the mesoscale level. It is assumed that fiber bundles are free from voids, cracks, and other inhomogeneities. Micro voids (i.e. diameter less than 0.2mm) are ignored in the geometry of matrix and big voids (i.e. diameter greater than 0.2mm) are directly modeled.
 - b. The resolution of the image was compromised and reduced to 36 μm to make the reconstruction process easier and the FE mesh workable.
 - c. The uneven surface of the interface was optimized for the finite element meshing. Hence, very sharp features were ignored and made smoother.
 - d. The segmentation of the phases was carried out using semi-automatic operations. Therefore, there always are some manual errors associated with the processor which were neglected.
 3. The volume fractions of the fiber bundles are obtained $38.06 \pm 2 \%$ in 4DIN C/C composite.
 4. The voids were segmented using greyscale threshold value and the reconstructed FE meshes include around $2.03 \pm 0.35 \%$ of the void fraction.
 5. Furthermore, to include the effect of the microstructural hierarchy of the composite. Micro-unit cells were constructed for each bundle by considering them as a unidirectional composite. Fluctuation in fiber volume fraction was observed due to bundle distortion. The measured fiber volume fractions lie in the range of $82.72 \pm 5.12 \%$ in 4DIN C/C composite

The study on the effective thermal conductivity is concluded in the following section.

7.2 Effective Thermal conductivity

Fourier's Law of Heat Conduction derived from the AEH method is solved using FEM and periodic boundary conditions at two different levels of scales sequentially. The effect of imperfections such as irregular shaped big voids, bundle distortion, and misalignment, is directly included in the FE mesh. The interfacial imperfectness is considered in terms of the thermal gap conductance. The following major points are observed:

- 1) Effective thermal conductivity of the 3DH and the 4DIN C/C composites were successfully predicted as a function of temperature up to 1227°C. A decreasing trend of TC was found with respect to the temperature increase for both composites.
- 2) Temperature and heat flux contour plots obtained through simulations have suggested that the inherent imperfections significantly affected the local distribution of the field variables.
- 3) Imperfect interfaces caused the temperature jumps at the interface and the magnitude of the jumps inversely varied with the gap conductance values.
- 4) At the bundle level, the effect of an imperfect interface on effective thermal conductivity is negligible, especially in longitudinal directions.
- 5) The in-plane thermal conductivity of the 3DH C/C composite was experimentally measured through a laser flash method that is measured as 110.5 W/m°C at 51°C and 53.45 W/m°C at 998°C. On the other hand, the numerically predicted TC was calculated as 118.8 W/m°C at 27°C and 48.46 W/m°C at 1227°C for the perfect interface. The same for the imperfectly bonded case was obtained as 101.2 to 44.6 W/m°C for the imperfect interface in the same temperature range.
- 6) Due to the imperfect interface, around 14.85% and 7.98 % reduction in the in-plane TC of the 3DH C/C composite was observed at 27°C and 1227°C respectively. However, the out-of-plane TC was reduced by 6.2 % and 2.8 % at the respective temperatures. This suggests that the effect of the imperfect interface on the effective TCs of the 3DH C/C composite is more pronounced in the in-plane direction especially at lower temperatures.
- 7) The effective TC of the 4DIN C/C composite was numerically predicted as 116.13 W/m°C, 112.16 W/m°C, and 107.17 W/m°C in x, y, and z directions respectively at 27°C corresponding to the perfect interface. The same was reduced to 52.68 W/m°C, 51.06 W/m°C, and 47.79 W/m°C in x, y, and z directions respectively at 1227°C.
- 8) In the case of the 4DIN C/C composite, all three components of the effective TC were reduced by around 5% due to the imperfect interface for the full range of temperatures. This shows that the influence of gap conductance is quite low for the 4DIN C/C composite when compared to that of the 3DH C/C composite.

- 9) The current study concludes that the thermal gap conductance value $1.5 \times 10^3 \text{ W/m}^2\text{K}$ corresponds to the completely debond condition and $1.5 \times 10^5 \text{ W/m}^2\text{K}$ corresponds to the imperfect bond condition.
- 10) In the 3DH C/C composite, the out-of-plane TC is greater than the in-plane TC, which reflects its transversely isotropic behavior. However, in the case of the 4DIN C/C composite, the effective TCs in all three orthogonal directions are almost the same. Thus, it behaves like a quasi-isotropic material.
- 11) The proximity of the numerical results with experimental values makes evident the validity of the proposed model.

7.3 Effective thermal expansion coefficient

The same two-scale hypothesis was extended to study the thermo-mechanical property (thermal expansion coefficient) of the multi-directional C/C composites and the study is concluded as below.

- 1) The effective CTEs of the 3DH and the 4DIN C/C composites were predicted as a function of temperature up to 2227°C by considering the realistic microstructure. In both cases, CTEs were found to be very low and increases slowly with rising in temperature.
- 2) At low temperatures, the bundles possess negative CTE in the longitudinal direction and became positive as the temperature is increased. The transition temperature at which longitudinal CTE changes its sign is found to be 325°C and 605°C respectively for rectangular and circular bundles (which belongs to 3DH architecture). Such temperature is around 1100°C for the bundles of 4DIN C/C composite.
- 3) The in-plane CTE of the 3DH C/C composite varies from 1.07 to $3.29 \times 10^{-6}/^\circ\text{C}$ while the out-of-plane CTE varies from 0.688 to $3.13 \times 10^{-6}/^\circ\text{C}$ in the temperature range of 27°C - 2227°C . The trend of CTE variation is validated through the existing results of the 3D needle punched C/C composite and found to be in good agreement with.
- 4) Again, the CTE of the 3DH C/C composite shows a transversely isotropic behavior.
- 5) Significant interfacial stress jumps and residual stresses in the different phases were also observed due to the mismatch of the constituents' CTEs. Both quantities decrease with the rise in temperature.
- 6) The effective CTEs of the 4DIN C/C composite was predicted for the three interfacial conditions, namely: perfectly bonded, imperfectly bonded, and completely debonded using surface-based cohesive behavior.
- 7) It was observed that the degradation in the interfacial properties has reduced the effective CTEs of the 4DIN C/C composite in x and z directions while this nature was opposite in the y-direction.
- 8) The overall thermal deformations of the unit cells were reduced around 36.69% and 38.97% in x and z directions respectively for the completely debonded case as compared to the perfect interface case.
- 9) The imperfect interface also gave rise to significant displacement jumps at the bundle/matrix interfaces. It is observed that the local distribution of the field variables in the individual phases was also affected.

- 10) Significant damage was observed at the bundle/matrix interfaces of the 4DIN C/C composites in the thermomechanical simulations. It is observed that the interfacial damage initiates at around 247°C that corresponds to a thermal strain of 0.008%, 0.06 %, and 0.009% in x, y, and z directions respectively.
- 11) The contours of the scalar damage variable show that the interfaces of the in-plane bundles are significantly affected by the thermal stresses as compared to the other two directions.
- 12) In case of a perfectly bonded interface, the effective CTEs of the 4DIN C/C composite was found to be $-0.06 \times 10^{-6}/^{\circ}\text{C}$, $1.38 \times 10^{-6}/^{\circ}\text{C}$, and $-0.187 \times 10^{-6}/^{\circ}\text{C}$ respectively in x, y, and z directions at around 135°C which further increased to $3.546 \times 10^{-6}/^{\circ}\text{C}$, $4.66 \times 10^{-6}/^{\circ}\text{C}$, and $3.2 \times 10^{-6}/^{\circ}\text{C}$ at 2227°C in the respective directions.
- 13) In the case of the imperfect interfacial condition, α_x reduced to $-0.68 \times 10^{-6}/^{\circ}\text{C}$ and $2.324 \times 10^{-6}/^{\circ}\text{C}$ while the reduction in α_z was up to $-0.44 \times 10^{-6}/^{\circ}\text{C}$ and $2.025 \times 10^{-6}/^{\circ}\text{C}$ at 135°C and 2227°C respectively.
- 14) Unlike the values of α_x and α_z , the value of α_y increases due to imperfectness of interface and reached $2.49 \times 10^{-6}/^{\circ}\text{C}$ and $4.58 \times 10^{-6}/^{\circ}\text{C}$ at 135°C and 2227°C respectively.
- 15) The effective CTEs of the 4DIN C/C composite was measured experimentally using a dilatometer in the temperature range of 200-2500°C in in-plane (U) and out-of-plane (Z) directions. The obtained ranges of the CTEs are 0.56 to $2.66 \times 10^{-6}/^{\circ}\text{C}$ and 0.28 to $2.5 \times 10^{-6}/^{\circ}\text{C}$ in respective directions.
- 16) Corresponding to the imperfect interface, the predicted range of the CTEs of the 4DIN C/C composite in x and z directions are a good match with measured results. This shows that the interfacial properties adopted are appropriate.

7.4 Thermal shock resistance

Next, the thermal shock resistance of the 4DIN C/C composite was obtained in terms of critical laser power density through the simulation of the laser pulse irradiation method using the FE analysis. The major conclusions are as follows:

- 1) The thermal shock resistance of the 4DIN C/C composite was predicted in terms of critical Laser Power Density (LPD). The trend of the critical LPD curve for the 4DIN C/C composite was found to be very similar to those reported in the literature for the 2D laminated C/C composite. The thermal shock resistance of the 4DIN C/C composite was found 10-18 times higher than that of the 2D C/C composite because of enhanced thermo-mechanical properties.
- 2) The critical laser density was predicted as 178 W/mm² for a 4mm diameter beam that has been further reduced exponentially to 22.85 W/mm² for a beam diameter of 50mm.
- 3) The critical time of laser pulse irradiation was obtained for different beam diameters and it was observed that the range varied between 0.1–1 sec as diameter increased from 4 to 20 mm. It became constant as t_s beyond 20 mm beam diameter. The shear stress and temperature distribution were studied at critical laser

pulse irradiation. The maximum temperature is found around 3500 °C for a 4 mm beam diameter that reduces to 1700 °C for 50 mm beam diameter.

- 4) The critical laser power density curve was obtained based on all three components of shear stresses. The yz-plane is found as a critical plane and component τ_{yz} as a critical component of shear stress.
- 5) The temperature remained almost uniform inside the beam area and sharply decreases near the periphery along the radius on the irradiated surface. The critical location for shear stress was found near to the beam periphery and about 0.5–1.75 mm below the irradiated surface (where high thermal gradient exists) depending upon beam diameter.

7.5 Scope for the Future

- a) An appropriate efficient algorithm can be developed for the segmentation of phases such as bundles and matrix that possess poor contrast of greyscale.
- b) Effect of intra bundle pores, micropores and microcracks can be studied in detail
- c) The effect of matrix morphology on effective thermo-mechanical properties can be included into the model defining a new level of scale.
- d) A more refined voxel-based finite element model can be used to overcome the limitations of the present study by utilizing the extensive parallel programming FEM algorithms.
- e) More experiments can be performed to estimate the actual properties of the constituents.
- f) Thermal shock analysis can be performed on the reconstructed microstructure to conclude the effect of interfacial debond and imperfections on TSR.
- g) The present work can be extended to study the ablative behavior of the 4D C/C composite and its effect on effective thermo-mechanical properties.

References

- [1] Savage G. Carbon-Carbon composites, 1st edition, Chapman & Hall, Hong Kong 1993
- [2] Rohini Devi G and Rama Rao K. Carbon/Carbon Composites-An overview. Defense Science Journal 1993;43(4):369-383
- [3] Buckley JD and Edie DD. Carbon-Carbon materials and composites, Noyes Publication, New jersey, USA 1993.
- [4] Fitzer E and Manocha LM. Carbon reinforcements and Carbon/Carbon composites, 1st edition, Springer, Verlag Heidelberg, New York 1998.
- [5] J. Jortner. Macroporosity and interface cracking in multi-directional carbon-carbons Carbon, 24 (5) (1986), pp. 603-613
- [6] Sharma R, Deshpande VV, Bhgat AR, Mahajan P and Mittal RK. X-ray tomographical observations of cracks and voids in 3D carbon/carbon composites. Carbon 2013; 60: 335-345.
- [7] Kingery WD. Factors effecting thermal stress resistance of ceramic materials. Journal of American ceramic society 1955; 38:3-15
- [8] Deng J, Liu W and Du H. Thermal shock resistance of C/C composites. Carbon 1999; 37: 1868-1869
- [9] Lu TJ, and Fleck NA. The thermal shock resistance of solids. Acta Metallurgica 1998; 46(13):4755-4768
- [10] Hasselman DPH. Elastic energy at fracture vand surface energy as design criteria for thermal shock. Journal of the American Ceramic Society 1963; 46(11): 535-541
- [11] Hasselman DPH. Unified theory of thermal shock fracture initiation and crack propagation in brittle Ceramics. Journal of the American Ceramic Society 1969; 52(11): 600-604
- [12] Soboyejo WO. Materials Selection for Thermal Shock Resistance: Mechanical properties of engineered materials. Marcel Dekker, New York, 2003.
- [13] Sato S, Sato K and Imamura Y. Determination of the thermal shock resistance of graphite by Arc discharge heating. Carbon 1975; 13: 309-316
- [14] Log T, Melas J and Larsen B. Technique for determining thermal shock resistance of carbon materials. Carbon. 1993; 31(6) : 931-936

- [15] Li K, Wang D, Chen H and Guo L. Normalized evaluation of thermal shock resistance for ceramic materials. *Journal of Advanced Ceramics* 2014; 3(3): 250-258
- [16] Singh RN and Wang H. Thermal shock behavior of fiber reinforced ceramic matrix composites. *Composite Engineering* 1995; 5(10): 1287-1297
- [17] Wang H, Singh RN and Lowden RA. Thermal shock behavior of two-dimensional woven fiber-reinforced ceramic composites. *Journal of American Ceramic Society* 1996; 79(7): 1783-1792
- [18] Yan Z, Chen F, Xiong X, Xiao P and Huang B. Thermal Shock resistance of SiC/Si-Mo multilayer oxidation protective coating for Carbon/Carbon Silicon Carbide composites. *Journal of composite materials* 2010; 44(26): 3085-3092
- [19] Yin X, Cheng L, Zhang L and Xu Y. Thermal shock behavior of 3-dimensional C/SiC composite. *Carbon* 2002; 40: 905-910
- [20] Leanos AL and Prabhakar P. Experimental investigation of thermal shock effects on carbon-carbon composites. *Composite Structures* 2015; 132: 372-383
- [21] Benz R, Naoumidis A and Nickel H. Thermal shock testing of ceramics with pulsed laser irradiation. *Journal of nuclear materials* 1987; 150: 128-139
- [22] Qi ZM, Amada S, Akiyama S and Takahashi C. Evaluation of thermal shock strength of thermal sprayed coatings by the laser irradiation technique. *Surface and Coating technology* 1998; 110: 73-80
- [23] Amada S, Nong WY, Min QZ and Akiyama S. Thermal shock resistance of carbon-carbon composite by laser irradiation technique. *Ceramics International* 1999; 25: 61-67
- [24] Li H W, Amada S and Michel Epinat. Evaluation of the thermal shock shear strength of carbon-carbon (C/C) composite by laser irradiation technique. *Journal of material Processing and Technology* 2003; 138: 423-428
- [25] Kim JH, Lee YS, Kim DH, Park NS, Suh J, Kim OJ and Moon SI. Evaluation of thermal shock strength for graphite materials using a laser irradiation method. *Material Science and Engineering A* 2004; 387: 385-389.
- [26] Kim JH, Lee YS, Kim DH, Park NS and Moon SI. Evaluation of Thermal shock fracture toughness for ATJ graphite using Laser Irradiation Method. *Key Engineering Materials* 2004; 261: 93-98
- [27] Wang YR and Chou TW. Thermal shock resistance of laminated ceramic matrix composite. *Journal of Material Science* 1991; 26: 2961-2966
- [28] Li Z, Wang BL, Wang KF and Zheng L. A multiscale model for predicting the thermal shock resistance of porous ceramics with temperature dependent material properties. *Journal of European Ceramic Society* 2019; 39: 2720-2730

- [29] Burlayenco VN. Modeling Thermal shock in functionally graded plates with Finite Element Method. *Advances in Material Science and Engineering* 2016, DOI: 10.1155/2016/7514638
- [30] Henneberg D, Ricoeur A and Judt P. Multiscale modeling for the simulation of damage processes at refractory materials under thermal shock. *Computational material science* 2013; 70: 187-195
- [31] Whittaker AJ. and Taylor R. Thermal transport properties of carbon-carbon fiber composites I. Thermal Diffusivity Measurements. *Proc. R. Soc. Lond. A* 1990; 430(1878): 167-181.
- [32] Whittaker AJ. and Taylor R. Thermal transport properties of carbon-carbon fiber composites III. Mathematical Modeling. *Proc. R. Soc. Lond. A* 1990;430(1878):199-211.
- [33] Luo RY, Liu T, Li JS, Zhang H, Chen Z and Tian GL. Thermo-physical properties of carbon/carbon composites and physical mechanism of thermal expansion and thermal conductivity. *Carbon* 2004;42: 2887–2895.
- [34] Manocha LM, Warriar A, Manocha S, Sathiyamoorthy and Banerjee S. Thermo-physical properties of densified pitch-based carbon/carbon materials—I. Unidirectional composites. *Carbon* 2006; 44: 480–487.
- [35] Manocha LM, Warriar A, Manocha S, Sathiyamoorthy and Banerjee S. Thermo-physical properties of densified pitch-based carbon/carbon materials—II. Bidirectional composites. *Carbon* 2006;44:488–495.
- [36] Bhatt H, Donaldson KY and Hasselman DPH. Role of the Interfacial Thermal Barrier in the Effective Thermal Diffusivity/Conductivity of Sic-fiber-Reinforced Reaction-Bonded Silicon Nitride. *J. American Ceram Soc* 1990;73(2):312-316
- [37] Farhan S, Wang R and Li K. Directional thermophysical, ablative and compressive behavior of 3D carbon/carbon composites. *Ceramics International* 2015; 41: 9763-9769
- [38] Kumar S, Kumar A, Rohini Devi G and Gupta A K, Preparation of 3D orthogonal woven C–SiC composite and its characterization for thermo-mechanical properties. *Materials Science and Engineering A* 2011;528: 6210–6216.
- [39] Springer GS and Tsai SW. Thermal conductivity of Unidirectional composite. *J. Composite materials*.1967;1: 166-173.
- [40] Zou M, Yu B and Zhang D. An analytical solution for transverse thermal conductivities of unidirectional fiber composites with thermal barrier. *J. Phy D: Appl Phy* 2002;35(15):1867-1874.
- [41] Dasgupta A and Agarwal AK. Orthotropic thermal conductivity of plain-weave fabric composites using a homogenization technique. *J. of Composite materials* 1992;26(18):2736-2758
- [42] Ning QG and Chou TW. Closed-form solutions of the in-plane effective thermal conductivities of woven-fabric composites. *Composite Science and Technology* 1995; 55:41-48.

- [43] Kulkarni MR and Brady RP. A model of global thermal conductivity in laminated Carbon/Carbon composites. *Composite Science and Technology* 1997; 57:277-285.
- [44] Benveniste Y and Miloh T. The effective conductivity of composites With imperfect thermal contact at Constituent interfaces. *Int. J EnggSci* 1986;24(9):1537-1552,
- [45] Benveniste Y. Effective thermal conductivity of composites with a thermal contact resistance between the constituents: Nondilute case. *J Appl. Phy.* 1987;61: 2840-2843
- [46] Hatta H and Taya M. Thermal conductivity of coated filler composites. *Journal of Applied Physics* 1986;59(6):1851-1860
- [47] Hasselman DPH and Johnson LF, Effective thermal conductivity of composites with interfacial thermal barrier resistance. *Journal of Composite Materials* 1987;21(6): 508-515
- [48] Hasselman DPH, Donaldson KY and Thomas JR. Effective thermal conductivity of uniaxial composite with cylindrically orthotropic carbon fibers and interfacial thermal barrier. *Journal of Composite Materials* 1993;27(6): 637-644.
- [49] Benveniste Y, Chen T and Dvorek GJ. The effective thermal conductivity of composites-reinforced by coated cylindrically orthotropic fibers. *J Appl. Phy* 1990;67: 2878-2884
- [50] Lee YM, Yang RB and Gau SS. A generalized self-consistent method for calculation of effective thermal conductivity of composites with interfacial contact conductance. *International communications in Heat and Mass Transfer* 2006;33:142-150
- [51] Sejnoha M and Zeman J. Micromechanical modeling of imperfect textile composites. *Int J of Engg Sci* 2008;46:513-526.
- [52] Vorel J and Sejnoha M. Evaluation of homogenized thermal conductivities of imperfect carbon-carbon textile composites using the Mori-Tanaka method. *Structural Engineering and Mechanics* 2009;33(4):429-446.
- [53] Schuster J, Heider D and Sharp K. Measuring and modeling the thermal conductivities of three-dimensionally woven fabric composites. *Mechanics of composite materials* 2009;45(2): 165-174
- [54] Feng Z H, Zhi J Y, Fan Z, Sun D, Si C and Wang X D, An Analytical Model of Thermal Conductivity for Carbon/Carbon Composites with Pitch-Based Matrix, Hindawi Publishing Corporation *Advances in Mechanical Engineering* Article ID 242586
- [55] Islam MR and Pramila A. Thermal conductivity of fiber reinforced composites by FEM. *Journal of composite material* 1999;33(18):1699-1715
- [56] Klett JW, Ervin VJ and Edie DD. Finite-element modeling of heat transfer in carbon/carbon composites. *Composites Science and Technology* 1999;59:593-607.

- [57] Grujicic, M, Zhao CL, Dusel, EC, Morgan DR , Miller RS and Beasley DE. Computational analysis of the thermal conductivity of the carbon-carbon composite materials. *J. Mater Sci* 2006;41:8244–8256
- [58] Puglia PD, Sheikh MA and Hayhurst DR. Thermal transport property prediction of a CMC laminate from base materials properties and manufacturing porosities. *Proc R Soc. A*2005;461: 3575-3597.
- [59] Siddiqui OR and Sun D. Finite element analysis of thermal conductivity and thermal resistance behavior of woven fabric. *Computational Materials Science* 2013;75:45–51.
- [60] Alghamdi A, Mummery P and Sheikh M. Investigating the Effect of Porosity on Thermal Characteristics of a 3D Orthogonal C-SiC Composite Using Finite Element Method. *Advances in Ceramic Science and Engineering (ACSE)* 2013;2 (2):64-71
- [61] Shigang A, Rujie H and Yongmao P. A Numerical Study on the Thermal Conductivity of 3DWoven C/C Composites at High Temperature. *Appl Composite Materials* 2015;22(6)
- [62] Liu Z, Haiguo Z, Lu Z and Diansen Li. Investigation on the thermal conductivity of 3-Dimensional and 4-Directional Braided Composites. *Chinese Journal of Aeronautics* 2007; 20: 327-331.
- [63] Jiang L, Xu GD, Cheng S, Lu XM and Zeng T. Predicting the thermal conductivity and temperature distribution in 3D braided composites. *Composite Structures* 2014; 108: 578–583.
- [64] Lu Z, Wang C, Xia B and Zhou Y. Effect of Interfacial Properties on the Thermo-physical Properties of 3D Braided Composites: 3D Multiscale Finite Element Study. *Polymer composites* 2014;35: 1690-1700
- [65] Dong K, Zhang J, Jin L, Gu B and Sun B. Multi-scale finite element analyses on the thermal conductive behaviors of 3D braided composites. *Composite Structures* 2016;143: 9–22.
- [66] Dong K, Liu K, Pan L, Gu B and Sun B. Experimental and numerical investigation on the thermal conduction properties of 2.5D angle-interlock woven composites. *Composite Structures* 2016;154: 319-333.
- [67] Tsukrov I, Piat R, Novak J and Schnack E. Micromechanical modeling of porous Carbon/Carbon composites. *Mechanics of advanced materials and structures* 2005; 12: 43-54
- [68] Piat R, Tsukrov I, Mladenov N, Guellali M, Ermel R, Beck T, Schnack E and Hoffmann MJ. Material modeling of the CVI-infiltrated carbon felt II. Statistical study of the microstructure, numerical analysis and experimental validation. *Composite Science and Technology* 2006; 66: 2769-2775
- [69] More N, Basse-Cathalinat B, Baquey C, Lacroix F, Ducassou D. Application of novel techniques of medical imaging to the non-destructive analysis of carbon-carbon composite materials. *Nuclear Instruments and Methods in Physics Research* 1983;214(2–3):531–536.

- [70] Douarche N, Rouby D, Peix G, Jouin JM. Relations between X-ray tomography, density and mechanical properties in carbon–carbon composites. *Carbon* 2001;39(10):1455–1465.
- [71] Coindreau O, Vignoles G. Assessment of geometrical and transport properties of a fibrous C/C composite preform using X-ray computerized micro-tomography: Part I. Image acquisition and geometrical properties. *Journal of Materials Research* 2005;20(9):2328–2339.
- [72] Martin-Herrero J, Germain Ch. Microstructure reconstruction of fibrous C/C composites from X-ray microtomography. *Carbon* 2007;45(6):1242–1253.
- [73] Kosek M, Sejak P. Visualization of voids in actual C/C woven composite structure. *Composite Science and Technology* 2009;69(9):1465–1469.
- [74] Vorel J, Zeman J and Sejnoha M. Homogenization of plain weave composites with imperfect microstructure Part II. Analysis of real world materials. *International journal for Multiscale Computational Engineering* 2013; 11(5): 443-462
- [75] Drach B, Tsukrov I, Gross T, Dietrich S, Weidenmann K, Piat R and Bohlke T. Numerical modeling of carbon/carbon composites with nanotextured matrix and 3D pores of irregular shapes. *Int. J of solids and structures* 2011; 48(18): 2447-2457
- [76] Sharma R, Mahajan P and Mittal RK. fiber bundle push-out test and image-based finite element simulation for 3D carbon/carbon composites. *Carbon* 2012; 50 :2717-2725
- [77] Sharma R, Bhagat AR and Mahajan P. Finite element analysis for mechanical characterization of 4D Inplane Carbon/Carbon composite with imperfect microstructure. *Latin American Journal of Solids and Structures* 2014; 11:170-184.
- [78] Sharma R, Mahajan P and Mittal RK, Elastic modulus of 3D carbon/carbon composite using image-based finite element simulations and experiments. *Composite structures* 2013; 98: 69-78
- [79] Sharma R, Mahajan P and Mittal RK. Image-based finite element analysis of 3D-orthogonal Carbon-Carbon composite. *Proceedings of the world congress on Engineering*. Vol-2, June 30-July 2, 2010, London, UK.
- [80] Qi L, Chao X, Tian W, Ma W and Li H. Numerical study of the effects of irregular pores on transverse mechanical properties of unidirectional composites. *Composite science and technology* 2018; 159: 142-151
- [81] Ali J, Farooqi JK, Buckthorpe D, Cheyne A, Mummery P. Comparative study of predictive FE methods for mechanical properties of nuclear composites. *Journal of Nuclear Materials* 2009;383(3):247–53.
- [82] Alghamdi A, Mummery P and Sheikh M. Multi-scale 3D image-based modeling of a carbon/carbon Composite. *Modeling and Simulation in Material Sci. Eng.* 2013;21: 1-14
- [83] Kumar S, Kumar A, Shukla A, Devi GR and Gupta AK. Investigation of thermal expansion of 3D-stitched C-SiC composite. *Journal of European Ceramic society* 2009; 29: 2849-2855

- [84] Liao X, Li H, Xu W and Li K. Study on the thermal expansion properties of C/C composites. *J Mater Sci* 2007; 42: 3435-3439
- [85] Wang P, Zhang S, Li H, Kong J, Li W and Zaman W. Variation of thermal expansion of carbon/carbon composite from 850 to 2500°C. *Ceramics International* 2014; 40: 1273-1276
- [86] Voigt W. Theoretische studienuber die elastizitatsverhaltnisse der crystalle. *Annalen der Physic* 1889; 38: 573-587
- [87] Reuss A. Berechnung der fliebgrenze von crystallen auf Grund der Plastizitatsbedingung fur Einkristalle. *Zeitschrift fur angewandte Mathematik und Mechanik* 1922; 9: 49-58
- [88] Turner P S. Thermal expansion stresses in reinforced plastics. *Journal of research of the national bureau of standards* 1946; 37:239-250
- [89] Schapery RA. Thermal expansion coefficient of composite materials based on energy principles. *Journal of Composite Materials* 1968; 2: 380-404
- [90] Levin VM. Thermal expansion coefficient of heterogeneous material. *Mechanics of Solids* 1967; 2: 58-61
- [91] Chamis CC and Sendeckyj GP. Critique on theories predicting thermo-elastic properties of fibrous composite. *Journal of Composite Materials* 1968; 2(3):332-358.
- [92] Chamberlain NJ. Derivation of expansion Coefficients for a fiber reinforced composites. BAC SON(P) report 1968: 33, British Aircraft Corporation, London
- [93] Rosen BW and Hashin Z. Effective thermal expansion coefficients and specific heats of composite materials. *Int. J. Eng. Sci.* 1970; 8(2):157-173
- [94] Hashin Z. Analysis of properties of fiber composites with anisotropic constituents. *Journal of applied mechanics* 1979 ; 46(3):543-550
- [95] Gowayed Y, Zou W and Gross S. An Analytical Approach to Evaluate the Coefficients of Thermal Expansion of Textile Composite Materials. *Polymer Composites* 2000; 21(5):814-820
- [96] Bowles ED and Tompkins SS. Prediction of coefficients of thermal expansion for unidirectional composites. *Journal of Composite Materials* 1989; 23(4): 370-388
- [97] Islam R, Sjolind SG and Pramila A. Finite element anlysis of linear thermal expansion coefficient of unidirectional cracked composite. *Journal of Composite Materials* 2001; 35(19): 1762-1776
- [98] Karch C. Micromechanical Analysis of thermal expansion coefficients. *Modeling and Numerical Simulation of Material Science* 2014; 4: 104-118
- [99] Karadeniz ZH and Kumlutas D. A numerical study on the coefficients of thermal expansion of fiber reinforced composite materials. *Composite Structures* 2007; 78: 1-10

- [I00] Ran Z, Yan Y, Li J, Qi Z and Lei Y. Determination of thermal expansion coefficients for unidirectional fiber-reinforced composites. *Chinese Journal of Aeronautics* 2014; 27: 1180-1187
- [I01] Dong K, Zhang J, Cao M, Wang M, Gu B and Sun B. A Mesoscale study of thermal expansion behaviors of epoxy resin and carbon fiber/epoxy unidirectional composites based on periodic temperature and displacement boundary conditions. *Polymer Testing* 2016; 55: 44-60
- [I02] Dong K, Peng X, Zhang J, Gu B and Sun B. Temperature dependent thermal expansion behavior of carbon fiber/epoxy plain woven composite: Experimental and numerical studies. *Composite Structures* 2017; 176: 329-341
- [I03] Dasgupta A, Agarwal RK and Bhandarkar SM. Three-dimensional modeling of woven fabric composites for effective thermo-mechanical and thermal properties. *Composite Science and Technology* 1996; 56:209-223
- [I04] Ai S, Fu H, He R and Pei Y. Multiscale modeling of thermal expansion coefficient of C/C composites at high temperature. *Materials and Design* 2015; 82: 181-188
- [I05] Nasution MRE, Watanabe N, Kondo A and Yudhanto A. Thermomechanical properties and stress analysis of 3D textile composites by asymptotic expansion homogenization method. *Composites: Part B* 2014; 60: 378-391
- [I06] Zhai J, Cheng S, Zeng T, Wang Z and Jiang L. Thermo-mechanical behavior analysis of 3D braided composites by multiscale finite element method. *Composite Structures* 2017; 176: 664-672
- [I07] Wang H, Cao M, Siddique A, Sun B and Gu B. Numerical analysis of thermal expansion behaviors and interfacial thermal stress of 3D braided composite materials. *Computational Material Science* 2017; 138: 77-91
- [I08] Hu CX, Li HJ, Zhang SY and Song YS. Numerical simulation on thermal expansion coefficient of 3D braided C/C composites. *Rare Metals* 2013; 33: 99-106
- [I09] Jiang LL, Xu GD, Cheng S, Lu XM and Zeng T. Finite element analysis of thermo-mechanical properties of 3D Braided Composites. *Applied Composite Materials* 2014; 21: 325-340
- [I10] Mohajerjesbi S. Prediction for coefficient of thermal expansion of three-dimensional Braided Composites. *AIAA Journal* 1997; 35: 141-144
- [I11] Bay RS, Tucker CL. Stereological measurement and error estimates for three-dimensional fiber orientation. *Polymer Engineering & Science* 1992; 32(4): 240- 253
- [I12] Parker WJ, Jenkins RJ, Butler CP and Abbott GL. Flash Method of Determining Thermal Diffusivity, Heat Capacity, and Thermal conductivity. *Journal of Applied Physics* 1961; 32:1679-1684
- [I13] Bensoussan A, Lion JL, Papanicolaou G. Asymptotic analysis for periodic structures.- Amsterdam: North-Holland Pub. Co.; 1978

- [I14] Fish J. Practical Multiscale, First edition., John Wiley & sons, United Kingdom, 2014.
- [I15] Torquato S, Random Heterogeneous Material: Microstructure and Macroscopic properties, First edition., Springer, New York, 2002.
- [I16] Fish J and Shek K. Multiscale analysis of composite materials and structures. Composite science and Technology 2000;60:2547-2556.
- [I17] Xu R, Bouby C, Zahrouni H, Ben Zineb T, Hu H and Potier-Ferry M. A Multiscale analysis on the Superelasticity Behavior of Architected Shape Memory Alloy Materials. Materials 2018;11: 1746
- [I18] Xu R, Bouby C, Zahrouni H, Ben Zineb T, Hu H and Potier-Ferry M. 3D modeling of shape memory alloy fiber reinforced composites by multiscale finite element analysis. Composite structures 2018; 200:408-419.
- [I19] Li S. Boundary conditions for unit cells from periodic microstructures and their implications. Composite science and technology 2008; 68(9) :1962-1974.
- [I20] Rao MV, Mahajan P and Mittal RK. Effect of architecture on mechanical properties of carbon/carbon composites. Composite Structures 2008; 83: 131-142
- [I21] Shokrieh MM, Residual stresses in composite materials. First edition, Woodhead publishing limited, UK, 2014
- [I22] Liu HY, Zhang Xi, Mai YW and Diao XX. On steady state-fiber pull-outII Computer Simulation. Comp. Sci and Tech 1999; 59(15): 2191-2199
- [I23] Nath RB, Fenner DN, and Galiotis C. The progressional approach to interfacial failure in carbon reinforced composites: elasto-plastic finite element modeling of interface cracks. Composites Part A 2000; 31(9):929-943
- [I24] Deve HE and Maloney MJ, On the toughening of intermetallics with ductile fibers: Role of interfaces. Acta Metallurgica et Materialia 1991; 39(10): 2275-2284
- [I25] Nakamura T and Suresh S, Effects of thermal residual stresses and fiber packing on deformation of metal-matrix composites. Acta Metallurgica et Materialia 1993; 41(6): 1665-1681
- [I26] Mai YK and Jain LK, On Residual Stress Induced Distortions during Fabrication of Composite Shells. Journal of Reinforced Plastics and Composites 1996; 15(8):793-805
- [I27] Bhagat AR and Mahajan P. Characterization and Damage Evaluation of Coal Tar Pitch Carbon Matrix Used in Carbon/Carbon Composites. Journal of Materials Engineering and Performance 2016; 25: 3904-3911
- [I28] Balla M. Formulation of coupled problems of thermo-elasticity by finite elements. Periodica polytechnica mechanical engineering 1989; 33(1-2): 59-70
- [I29] ABAQUS analysis user's guide. <<http://ivtabaqusdoc.ivt.ntnu.no:2080/v6.I4/books/usb/default.htm>>.

- [130] Farhaan S, Wang R, Li K and Wang C. Sublimation and oxidation zone ablation behavior of carbon/carbon composites. *Ceramic International* 2015; 41(10): 13751-13758

Appendix-A

Asymptotic Expansion Homogenization for thermal problem

Following mathematical facts have been utilized during derivation [113, 115]

Fact 1 Derivative of periodic function is also periodic with the same length of period.

Fact 2 The integral of derivative of periodic function over the period is zero

Fact 3 For the equation

$$A^0 u = F \quad \text{in } \Theta \quad \text{where } A^0 = -\frac{\partial}{\partial y_i} \left(a_{ij}(y) \frac{\partial}{\partial y_j} \right)$$

The Θ -periodic function 'u' will be a unique solution iff

$$\langle F \rangle = \frac{1}{|\Theta|} \int_{\Theta} F d\Theta = 0$$

Where ' \int ' and ' $\langle \rangle$ ' are showing volume and volume average quantity over the domain Θ respectively.

Fact 4 for any function $\varphi^\psi = \varphi(x, y)$, chain rule of partial differentiation yields

$$\frac{\partial \varphi^\psi}{\partial x_i} = \frac{\partial \varphi}{\partial x_i} + \frac{1}{\xi} \frac{\partial \varphi}{\partial y_i} \quad \text{where, } \xi = \frac{x_i}{y_i}$$

Consider a thermal boundary value problem in a 3-dimensional composite domain as described in Chapter-5 (section-4.3). One can refer to this section also for the definition of symbols.

$$\text{Steady state heat equation:} \quad -\frac{\partial}{\partial x_i} \left(K_{ij}^\psi \frac{\partial T^\psi}{\partial x_j} \right) = f \quad \text{in } \Omega^\psi \in R^d \quad (\text{A1})$$

$$\text{Temperature BC:} \quad T^\psi = c_1 \quad \text{on } \partial\Omega_1^\psi$$

$$\text{Heat flux BC:} \quad K_{ij}^\psi \frac{\partial T^\psi}{\partial x_j} n_i = c_2 \quad \text{on } \partial\Omega_2^\psi$$

$$\text{Fourier's law of conduction:} \quad q_i^\psi = -K_{ij}^\psi \frac{\partial T^\psi}{\partial x_j} \quad \text{on } \Omega^\psi \quad (\text{A2})$$

Where, $\partial\Omega_1^\psi$ and $\partial\Omega_2^\psi$ are the temperature and heat flux prescribed boundaries respectively such that $\partial\Omega_1^\psi \cup \partial\Omega_2^\psi = \partial\Omega^\psi$.

The asymptotic expansion approximation of temperature field can be written as

$$T^\psi(x) = T_0(x, y) + \xi T_1(x, y) + \xi^2 T_2(x, y) + \dots \quad (\text{A3})$$

Substituting expansion (A3) into equation (A1) and using **Fact 4**, we get

$$-\left(\frac{\partial}{\partial x_i} + \frac{1}{\xi} \frac{\partial}{\partial y_i}\right) \left[K_{ij}(y) \left(\frac{\partial}{\partial x_j} + \frac{1}{\xi} \frac{\partial}{\partial y_j} \right) (T_0(x, y) + \xi T_1(x, y) + \xi^2 T_2(x, y) + \dots) \right] = f$$

$$\text{or } -\frac{\partial}{\partial x_i} \left[K_{ij}(y) \left(\frac{\partial}{\partial x_j} + \frac{1}{\xi} \frac{\partial}{\partial y_j} \right) (T_0(x, y) + \xi T_1(x, y) + \dots) \right] - \frac{1}{\xi} \frac{\partial}{\partial y_i} \left[K_{ij}(y) \left(\frac{\partial}{\partial x_j} + \frac{1}{\xi} \frac{\partial}{\partial y_j} \right) (T_0(x, y) + \xi T_1(x, y) + \dots) \right] = f$$

on further simplifications, we get

$$\left[\frac{1}{\xi^2} A_0 + \frac{1}{\xi} A_1 + A_2 + \dots \right] [T_0(x, y) + \xi T_1(x, y) + \xi^2 T_2(x, y) + \dots] = f \quad (\text{A4})$$

where,

$$A_0 = -\frac{\partial}{\partial y_i} \left(K_{ij}(y) \frac{\partial}{\partial y_j} \right)$$

$$A_1 = -\frac{\partial}{\partial y_i} \left(K_{ij}(y) \frac{\partial}{\partial x_j} \right) - \frac{\partial}{\partial x_i} \left(K_{ij}(y) \frac{\partial}{\partial y_j} \right) = -\frac{\partial}{\partial y_i} \left(K_{ij}(y) \frac{\partial}{\partial x_j} \right) - K_{ij}(y) \frac{\partial^2}{\partial x_i \partial y_j}$$

$$A_2 = -\frac{\partial}{\partial x_i} \left(K_{ij}(y) \frac{\partial}{\partial x_j} \right) = -K_{ij}(y) \frac{\partial^2}{\partial x_i \partial x_j}$$

Here, $K_{ij}(y)$ has been assumed to vary locally and preserve periodicity in the domain Θ .

Equating the terms of equation (A4) with a similar power of ξ both sides up to the third term of expansion, we get

$$A_0 T_0(x, y) = 0 \quad (\text{A5})$$

$$A_0 T_1(x, y) + A_1 T_0(x, y) = 0 \quad (\text{A6})$$

$$A_0 T_2(x, y) + A_1 T_1(x, y) + A_2 T_0(x, y) = f \quad (\text{A7})$$

Now consider the equation (A5)

From **Fact 3**, T_0 will be a unique solution and one of the obvious solutions is

$$T_0(x, y) = T_0(x) \quad (\text{A8})$$

i.e first term of asymptotic expansion depends only on global coordinate which is a global solution field and does not vary locally.

Next, equation (A6) can be written as

$$A_0 T_1(x, y) = -A_1 T_0(x)$$

or
$$A_0 T_1 = \frac{\partial}{\partial y_i} \left(K_{ij}(y) \frac{\partial T_0(x)}{\partial x_j} \right) + K_{ij}(y) \frac{\partial^2 T_0(x)}{\partial x_i \partial y_j} = \frac{\partial K_{ij}(y)}{\partial y_i} \frac{\partial T_0(x)}{\partial x_j} \quad (\text{A9})$$

In equation (A9), it is to be noted that on right hand side, variables are separated and derivative of conductivity tensor is also a periodic term in Θ (from **Fact 1**). So, its volume average over the local domain will be zero. Hence, from **Fact 3**, it is obvious that $T_1(x, y)$ will be a unique solution up to an additive constant and can be written as

$$T_1 = \chi_j(y) \frac{\partial T_0}{\partial x_j} + \zeta(x) \quad (\text{A10})$$

where, $\chi_j(y)$ is the solution of following local problem

$$A_0 \chi_j(y) = \frac{\partial K_{ij}(y)}{\partial y_i} \text{ in } \Theta \quad (\text{A11})$$

The term $\chi_j(y)$ is termed as temperature influence function which acts as a bridging term to establish the relation between the local temperature field $T_1(x, y)$ with the global temperature gradient $\frac{\partial T_0(x)}{\partial x_j}$.

Now consider the equation (A7)

$$A_0 T_2(x, y) = f - A_2 T_0(x) - A_1 T_1(x, y)$$

Since, T_2 is y-periodic (Local temperature field), So, this will be a unique solution (from **Fact 3**) iff

$$\langle f - A_2 T_0(x) - A_1 T_1(x, y) \rangle = 0$$

or
$$\frac{1}{|\Theta|} \int_{\Theta} (f - A_2 T_0(x) - A_1 T_1(x, y)) d\Theta = 0 \quad (\text{A12})$$

Where $|\Theta|$ is the volume of the unit cell domain Θ . Expanding each term of equation (A12), we have

$$\begin{aligned} A_1 T_1 &= -\frac{\partial}{\partial y_i} \left(K_{ij}(y) \frac{\partial}{\partial x_j} \right) T_1(x, y) - K_{ij}(y) \frac{\partial^2 T_1(x, y)}{\partial x_i \partial y_j} \\ &= -\frac{\partial}{\partial y_i} \left(K_{ij}(y) \frac{\partial}{\partial x_j} \left(\chi_j(y) \frac{\partial T_0(x)}{\partial x_j} + \zeta(x) \right) \right) - K_{ij}(y) \frac{\partial^2}{\partial x_i \partial y_j} \left(\chi_j(y) \frac{\partial T_0(x)}{\partial x_j} + \zeta(x) \right) \\ &= -\frac{\partial}{\partial y_i} \left(K_{ij}(y) \chi_j(y) \frac{\partial^2 T_0(x)}{\partial x_j \partial x_j} + K_{ij}(y) \frac{\partial \zeta(x)}{\partial x_j} \right) - K_{ik}(y) \frac{\partial \chi_j(y)}{\partial y_k} \frac{\partial^2 T_0(x)}{\partial x_i \partial x_j} \end{aligned}$$

$$= -\frac{\partial(K_{ik}(y)\chi_j(y))}{\partial y_k} \frac{\partial^2 T_0(x)}{\partial x_i \partial x_j} - \frac{\partial K_{ij}(y)}{\partial y_i} \frac{\partial \zeta(x)}{\partial x_j} - K_{ik}(y) \frac{\partial \chi_j(y)}{\partial y_k} \frac{\partial^2 T_0(x)}{\partial x_i \partial x_j} \quad (\text{A13})$$

$$A_2 T_0 = -K_{ij}(y) \frac{\partial^2 T_0}{\partial x_i \partial x_j} \quad (\text{A14})$$

Substituting expressions (A13) and (A14) in equation (A12), we get

$$\frac{1}{|\Theta|} \int_{\Theta} \left(f + \frac{\partial(K_{ik}(y)\chi_j(y))}{\partial y_k} \frac{\partial^2 T_0(x)}{\partial x_i \partial x_j} - \frac{\partial K_{ij}(y)}{\partial y_i} \frac{\partial \zeta(x)}{\partial x_j} + K_{ik}(y) \frac{\partial \chi_j(y)}{\partial y_k} \frac{\partial^2 T_0(x)}{\partial x_i \partial x_j} + K_{ij}(y) \frac{\partial^2 T_0(x)}{\partial x_i \partial x_j} \right) d\Theta = 0$$

or

$$\begin{aligned} \frac{1}{|\Theta|} \int_{\Theta} f d\Theta + \frac{1}{|\Theta|} \frac{\partial^2 T_0(x)}{\partial x_i \partial x_j} \int_{\Theta} \frac{\partial(K_{ik}(y)\chi_j(y))}{\partial y_k} d\Theta + \frac{1}{|\Theta|} \frac{\partial \zeta(x)}{\partial x_j} \int_{\Theta} \frac{\partial K_{ij}(y)}{\partial y_i} d\Theta + \frac{1}{|\Theta|} \frac{\partial^2 T_0(x)}{\partial x_i \partial x_j} \int_{\Theta} K_{ik}(y) \frac{\partial \chi_j(y)}{\partial y_k} d\Theta \\ + \frac{1}{|\Theta|} \frac{\partial^2 T_0(x)}{\partial x_i \partial x_j} \int_{\Theta} K_{ij}(y) d\Theta = 0 \end{aligned}$$

The second and third terms vanish as per **Fact 2**. The expression reduces to

$$\langle f \rangle + \frac{1}{|\Theta|} \frac{\partial^2 T_0(x)}{\partial x_i \partial x_j} \int_{\Theta} \left(K_{ij}(y) + K_{ik}(y) \frac{\partial \chi_j(y)}{\partial y_k} \right) d\Theta = 0$$

$$\text{or} \quad \left[\frac{1}{|\Theta|} \int_{\Theta} \left(K_{ij}(y) + K_{ik}(y) \frac{\partial \chi_j(y)}{\partial y_k} \right) d\Theta \right] \frac{\partial^2 T_0(x)}{\partial x_i \partial x_j} = -\langle f \rangle$$

$$\text{or} \quad \left[\frac{1}{|\Theta|} \int_{\Theta} K_{ij}(y) \left(\delta_{jk} + \frac{\partial \chi_j(y)}{\partial y_k} \right) d\Theta \right] \frac{\partial^2 T_0(x)}{\partial x_i \partial x_j} = -\langle f \rangle$$

$$\text{or} \quad -K_{ij}^H \frac{\partial^2 T_0(x)}{\partial x_i \partial x_j} = \langle f \rangle$$

$$\text{or} \quad -\frac{\partial}{\partial x_i} \left(K_{ij}^H \frac{\partial T_0(x)}{\partial x_j} \right) = \langle f \rangle \quad (\text{A15})$$

Here, δ_{jk} is Kronecker delta and equation (A15) is the heat conduction equation in an equivalently homogenized domain with constant effective thermal conductivity K_{ij}^H which is defined as

$$K_{ij}^H = \frac{1}{|\Theta|} \int_{\Theta} K_{ij}(y) \left(\delta_{jk} + \frac{\partial \chi_j(y)}{\partial y_k} \right) d\Theta \quad (\text{A16})$$

Substituting the expansion (A3) into Fourier's law (A2) and applying chain rule (**Fact 4**), we obtain

$$\begin{aligned}
q_i^y(x, y) &= -K_{ij}(y) \left\{ \left(\frac{\partial}{\partial x_j} + \frac{1}{\xi} \frac{\partial}{\partial y_j} \right) (T_0(x) + \xi T_1(x, y) + \xi^2 T_2(x, y) + \dots) \right\} \\
&= -K_{ij}(y) \left\{ \frac{\partial}{\partial x_j} (T_0(x) + \xi T_1(x, y) + \xi^2 T_2(x, y) + \dots) + \frac{1}{\xi} \frac{\partial}{\partial y_j} (T_0(x) + \xi T_1(x, y) + \xi^2 T_2(x, y) + \dots) \right\} \\
&= -K_{ij}(y) \left\{ \frac{1}{\xi} \frac{\partial T_0(x)}{\partial y_j} + \left(\frac{\partial T_0(x)}{\partial x_j} + \frac{\partial T_1(x, y)}{\partial y_j} \right) + \xi \left(\frac{\partial T_1(x, y)}{\partial x_j} + \frac{\partial T_2(x, y)}{\partial y_j} \right) + \dots \right\} \\
&= \frac{1}{\xi} q_i^{(-1)}(x, y) + q_i^{(0)}(x, y) + \xi q_i^{(1)}(x, y) + \xi^2 q_i^{(2)}(x, y) + \dots
\end{aligned}$$

Here, $q_i^{(-1)} = 0$ as $\frac{\partial T_0(x)}{\partial y_j} = 0$ and the leading term of heat flux expansion is $q_i^{(0)}(x, y)$ which is the function of global temperature gradient and local temperature. So, the average heat flux in unit cell domain Θ can be written as

$$\begin{aligned}
\langle q_i \rangle &= \frac{1}{|\Theta|} \int_{\Theta} q_i^{(0)}(x, y) d\Theta \\
&= \frac{1}{|\Theta|} \int_{\Theta} \left\{ -K_{ij}(y) \left(\frac{\partial T_0(x)}{\partial x_j} + \frac{\partial T_1(x, y)}{\partial y_j} \right) \right\} d\Theta \\
&= \frac{1}{|\Theta|} \int_{\Theta} \left\{ -K_{ij}(y) \left(\frac{\partial T_0(x)}{\partial x_j} + \frac{\partial}{\partial y_j} \left(\chi_j(y) \frac{\partial T_0}{\partial x_j} + \zeta(x) \right) \right) \right\} d\Theta \quad (\text{from (A10)}) \\
&= \frac{1}{|\Theta|} \int_{\Theta} \left\{ -K_{ij}(y) \left(\frac{\partial T_0(x)}{\partial x_j} + \frac{\partial \chi_j(y)}{\partial y_j} \frac{\partial T_0}{\partial x_j} + \frac{\partial \zeta(x)}{\partial y_j} \right) \right\} d\Theta \\
&= \frac{1}{|\Theta|} \int_{\Theta} \left\{ -K_{ij}(y) \left(\delta_{jk} + \frac{\partial \chi_j(y)}{\partial y_k} \right) \right\} d\Theta \frac{\partial T_0(x)}{\partial x_j} \\
&= -K_{ij}^H \frac{\partial T_0(x)}{\partial x_j} \quad (\text{from (A16)})
\end{aligned}$$

Hence, Fourier's Law in terms of average quantities and effective thermal conductivity can be written as

$$\langle q_i \rangle = -K_{ij}^H \left\langle \frac{\partial T}{\partial x_j} \right\rangle$$

Appendix-B

Asymptotic expansion homogenization for thermo-elastic problem

Consider an elastostatics problem in the composite domain $\Omega^\Psi \in R^d$ (Refer Ch-5, section5.3)

$$\text{Stress equilibrium equation:} \quad \frac{\partial \sigma_{ij}^\Psi}{\partial x_j} + b_i^\Psi = 0 \quad \text{in } \Omega^\Psi \in R^3 \quad (\text{B1})$$

$$\text{Displacement BC:} \quad u_i^\Psi = c_1 \quad \text{on } \partial\Omega_1^\Psi$$

$$\text{Traction BC:} \quad \sigma_{ij}^\Psi . n_j = c_2 \quad \text{on } \partial\Omega_2^\Psi$$

$$\text{Constitutive relation:} \quad \sigma_{ij}^\Psi = C_{ijkl}^\Psi (e_{kl}^\Psi - \alpha_{kl}^\Psi \Delta T) = C_{ijkl}^\Psi e_{kl}^\Psi - \beta_{kl}^\Psi \Delta T \quad (\text{B2})$$

$$\text{Strain-displacement relation:} \quad e_{kl}^\Psi = \frac{\partial u_k^\Psi}{\partial x_l} \quad (\text{B3})$$

Here, the material properties are assumed to vary locally i.e. $C_{ijkl}^\Psi = C_{ijkl}(y)$ and $\alpha_{kl}^\Psi = \alpha_{kl}(y)$ [II 6]

Displacement field in the composite domain can be approximated through asymptotic expansion as

$$u_i^\Psi(x, y) = u_i^{(0)}(x) + \xi u_i^{(1)}(x, y) + \xi^2 u_i^{(2)}(x, y) + \dots \quad (\text{B4})$$

Inserting the expansion (B4) in equation (B3) and using chain rule (**Fact 4**), we get

$$\begin{aligned} e_{kl}^\Psi &= \left(\frac{\partial u_k^{(0)}}{\partial x_l} + \frac{1}{\xi} \frac{\partial u_k^{(0)}}{\partial y_l} \right) + \xi \left(\frac{\partial u_k^{(1)}}{\partial x_l} + \frac{1}{\xi} \frac{\partial u_k^{(1)}}{\partial y_l} \right) + \xi^2 \left(\frac{\partial u_k^{(2)}}{\partial x_l} + \frac{1}{\xi} \frac{\partial u_k^{(2)}}{\partial y_l} \right) + \dots \\ &= \frac{1}{\xi} \frac{\partial u_k^{(0)}}{\partial y_l} + \left(\frac{\partial u_k^{(0)}}{\partial x_l} + \frac{\partial u_k^{(1)}}{\partial y_l} \right) + \xi \left(\frac{\partial u_k^{(1)}}{\partial x_l} + \frac{\partial u_k^{(2)}}{\partial y_l} \right) + \dots \\ &= \frac{1}{\xi} e_{kl}^{(-1)} + e_{kl}^{(0)} + \xi e_{kl}^{(1)} + \dots \end{aligned} \quad (\text{B5})$$

Where $e_{kl}^{(-1)} = \frac{\partial u_k^{(0)}}{\partial y_l}$, $e_{kl}^{(0)} = \left(\frac{\partial u_k^{(0)}}{\partial x_l} + \frac{\partial u_k^{(1)}}{\partial y_l} \right)$, $e_{kl}^{(1)} = \left(\frac{\partial u_k^{(1)}}{\partial x_l} + \frac{\partial u_k^{(2)}}{\partial y_l} \right)$ and so on...

Inserting the expansion of strain (B5) into the constitutive relation (B2), we obtain

$$\sigma_{ij}^\Psi = C_{ijkl} \left(\frac{1}{\xi} e_{kl}^{(-1)} + e_{kl}^{(0)} + \xi e_{kl}^{(1)} + \dots \right) - C_{ijkl} \alpha_{kl} \Delta T$$

$$\text{or} \quad \sigma_{ij}^\Psi = \frac{1}{\xi} \sigma_{ij}^{(-1)} + \sigma_{ij}^{(0)} + \xi \sigma_{ij}^{(1)} + \dots \quad (\text{B6})$$

Where,

$$\sigma_{ij}^{(-1)} = C_{ijkl} e_{kl}^{(-1)} = C_{ijkl} \frac{\partial u_k^{(0)}}{\partial y_l} \quad (\text{B7})$$

$$\sigma_{ij}^{(0)} = C_{ijkl} (e_{kl}^{(0)} - \alpha_{kl} \Delta T) = C_{ijkl} \left(\frac{\partial u_k^{(0)}}{\partial x_l} + \frac{\partial u_k^{(1)}}{\partial y_l} - \alpha_{kl} \Delta T \right), \dots \text{and so on} \quad (\text{B8})$$

Now chain rule of partial differentiation can be applied on stress equilibrium equation (BI) as

$$\frac{\partial \sigma_{ij}^{\psi}}{\partial x_j} + \frac{1}{\xi} \frac{\partial \sigma_{ij}^{\psi}}{\partial y_j} + b_i = 0$$

$$\text{or} \quad \frac{\partial}{\partial x_j} \left(\frac{1}{\xi} \sigma_{ij}^{(-1)} + \sigma_{ij}^{(0)} + \xi \sigma_{ij}^{(1)} + \dots \right) + \frac{1}{\xi} \frac{\partial}{\partial y_j} \left(\frac{1}{\xi} \sigma_{ij}^{(-1)} + \sigma_{ij}^{(0)} + \xi \sigma_{ij}^{(1)} + \dots \right) + b_i = 0$$

$$\text{or} \quad \frac{1}{\xi^2} \frac{\partial \sigma_{ij}^{(-1)}}{\partial y_j} + \frac{1}{\xi} \left(\frac{\partial \sigma_{ij}^{(-1)}}{\partial x_j} + \frac{\partial \sigma_{ij}^{(0)}}{\partial y_j} \right) + \left(\frac{\partial \sigma_{ij}^{(0)}}{\partial x_j} + \frac{\partial \sigma_{ij}^{(1)}}{\partial y_j} \right) + \dots + b_i = 0 \quad (\text{B9})$$

Now, equating the terms with a similar power of ξ on both sides of equation (B9) up to the third term, we get three coupled partial differential equations as follow

$$\frac{\partial \sigma_{ij}^{(-1)}}{\partial y_j} = 0 \quad (\text{B10})$$

$$\frac{\partial \sigma_{ij}^{(-1)}}{\partial x_j} + \frac{\partial \sigma_{ij}^{(0)}}{\partial y_j} = 0 \quad (\text{B11})$$

$$\frac{\partial \sigma_{ij}^{(0)}}{\partial x_j} + \frac{\partial \sigma_{ij}^{(1)}}{\partial y_j} + b_i = 0 \quad (\text{B12})$$

Now considering equation (B10), we have

$$\frac{\partial}{\partial y_j} \left(C_{ijkl} \frac{\partial u_k^{(0)}}{\partial y_l} \right) = 0$$

From **Fact 3**, $u_k^{(0)}$ must be a unique solution and one of the obvious solutions is

$$u_k^{(0)}(x, y) = u_k^{(0)}(x) \quad (\text{B13})$$

i.e first term of asymptotic expansion depends only on global coordinate 'x'. This gives $\sigma_{ij}^{(-1)} = 0$.

Now, using the expressions for $\sigma_{ij}^{(0)}$ and $\sigma_{ij}^{(-1)}$, equation (B11) can be written as

$$\frac{\partial}{\partial y_j} \left\{ C_{ijkl} \left(\frac{\partial u_k^{(0)}}{\partial x_l} + \frac{\partial u_k^{(1)}}{\partial y_l} - \alpha_{kl} \Delta T \right) \right\} = 0 \quad (\text{BI4})$$

Here $u_k^{(1)}(x, y)$ is the local displacement field. According to the method of separation of variable, one can assume the local displacement field as

$$u_k^{(1)} = -\phi_k^{pq}(y) \frac{\partial u_p^{(0)}}{\partial x_q} + \eta_k(y) \Delta T \quad (\text{BI5})$$

In equation (BI5), the local displacement field is related to the global strain and temperature change through two arbitrary influence functions $\phi_k^{pq}(y)$ and $\eta_k(y)$ respectively and are known as displacement influence function and temperature influence function.

Substituting (BI5) in (BI4), we get

$$\frac{\partial}{\partial y_j} \left\{ C_{ijkl} \left(\frac{\partial u_k^{(0)}}{\partial x_l} + \frac{\partial}{\partial y_l} \left(-\phi_k^{pq}(y) \frac{\partial u_p^{(0)}}{\partial x_q} + \eta_k(y) \Delta T \right) - \alpha_{kl} \Delta T \right) \right\} = 0$$

$$\text{or} \quad \frac{\partial}{\partial y_j} \left[\left(C_{ijpq} - C_{ijkl} \frac{\partial \phi_k^{pq}}{\partial y_l} \right) \frac{\partial u_p^{(0)}}{\partial x_q} + \frac{\partial}{\partial y_j} \left[C_{ijkl} \left(\frac{\partial \eta_k}{\partial y_l} - \alpha_{kl} \right) \right] \Delta T \right] = 0 \quad (\text{BI6})$$

Since $\phi_k^{pq}(y)$ and $\eta_k(y)$ are arbitrary, equation (BI6) can be split into two decoupled problem in the local domain as follows

$$\frac{\partial}{\partial y_j} \left(C_{ijpq} - C_{ijkl} \frac{\partial \phi_k^{pq}}{\partial y_l} \right) = 0 \quad \text{in } \Theta \quad (\text{BI6.a})$$

and

$$\frac{\partial}{\partial y_j} \left[C_{ijkl} \left(\frac{\partial \eta_k}{\partial y_l} - \alpha_{kl} \right) \right] = 0 \quad \text{in } \Theta \quad (\text{BI6.b})$$

Equation (BI6.a) and (BI6.b) are the elastic and thermal problems respectively and can be solved separately in local domain for corresponding influence functions.

Averaging the equation (BI2) over the volume of local domain Θ , we obtain

$$\frac{1}{|\Theta|} \int_{\Theta} \left(\frac{\partial \sigma_{ij}^{(0)}}{\partial x_j} + \frac{\partial \sigma_{ij}^{(1)}}{\partial y_j} + b_i \right) d\Theta = 0$$

$$\text{or} \quad \frac{1}{|\Theta|} \int_{\Theta} \left(\frac{\partial \sigma_{ij}^{(0)}}{\partial x_j} \right) d\Theta + \frac{1}{|\Theta|} \int_{\Theta} \left(\frac{\partial \sigma_{ij}^{(1)}}{\partial y_j} \right) d\Theta + \frac{1}{|\Theta|} \int_{\Theta} b_i d\Theta = 0 \quad (\text{BI7})$$

The second term of equation (BI7) is zero according to the **Fact 2**. After further simplifications, we get

$$\begin{aligned}
& \frac{1}{|\Theta|} \int_{\Theta} \frac{\partial}{\partial x_j} \left\{ C_{ijkl} \left(\frac{\partial u_k^{(0)}}{\partial x_l} + \frac{\partial u_k^{(1)}}{\partial y_l} - \alpha_{kl} \Delta T \right) \right\} d\Theta + \frac{1}{|\Theta|} \int_{\Theta} b_i d\Theta = 0 \\
\text{or } & \frac{\partial}{\partial x_j} \left[\frac{1}{|\Theta|} \int_{\Theta} C_{ijkl} \left(\frac{\partial u_k^{(0)}}{\partial x_l} + \frac{\partial}{\partial y_l} \left(-\phi_k^{pq}(y) \frac{\partial u_p^{(0)}}{\partial x_q} + \eta_k(y) \Delta T \right) - \alpha_{kl} \Delta T \right) d\Theta \right] + \frac{1}{|\Theta|} \int_{\Theta} b_i d\Theta = 0 \\
\text{or } & \frac{\partial}{\partial x_j} \left[\left\{ \frac{1}{|\Theta|} \int_{\Theta} \left(C_{ijkl} \frac{\partial u_k^{(0)}}{\partial x_l} - C_{ijkl} \frac{\partial \phi_k^{pq}}{\partial y_l} \frac{\partial u_p^{(0)}}{\partial x_q} \right) d\Theta \right\} - \left\{ \frac{1}{|\Theta|} \int_{\Theta} C_{ijkl} \left(\frac{\partial \eta_k}{\partial y_l} - \alpha_{kl} \right) d\Theta \right\} \Delta T \right] + \frac{1}{|\Theta|} \int_{\Theta} b_i d\Theta = 0 \\
\text{or } & \frac{\partial}{\partial x_j} \left[\left\{ \frac{1}{|\Theta|} \int_{\Theta} \left(C_{ijpq} - C_{ijkl} \frac{\partial \phi_k^{pq}}{\partial y_l} \right) d\Theta \right\} \frac{\partial u_p^{(0)}}{\partial x_q} - \left\{ \frac{1}{|\Theta|} \int_{\Theta} C_{ijkl} \left(\frac{\partial \eta_k}{\partial y_l} - \alpha_{kl} \right) d\Theta \right\} \Delta T \right] + \frac{1}{|\Theta|} \int_{\Theta} b_i dy = 0 \\
\text{or } & \frac{\partial}{\partial x_j} \left[\langle C_{ijpq} \rangle \frac{\partial u_p^{(0)}}{\partial x_q} - \langle \beta_{kl} \rangle \Delta T \right] + \langle b_i \rangle = 0 \\
& \frac{\partial}{\partial x_j} \left[\langle C_{ijkl} \rangle \left\{ \frac{\partial u_k^{(0)}}{\partial x_l} - \langle \alpha_{kl} \rangle \Delta T \right\} \right] + \langle b_i \rangle = 0 \tag{B18}
\end{aligned}$$

Clearly, equation (B18) is nothing but stress equilibrium equation in an equivalently homogenized domain with constant effective properties $\langle C_{ijkl} \rangle$ and $\langle \alpha_{kl} \rangle$.

Here the equivalent homogenized properties are defined as

$$\langle C_{ijpq} \rangle = \frac{1}{|\Theta|} \int_{\Theta} \left(C_{ijpq} - C_{ijkl} \frac{\partial \phi_k^{pq}}{\partial y_l} \right) d\Theta$$

$$\langle \beta_{ij} \rangle = -\frac{1}{|\Theta|} \int_{\Theta} C_{ijkl} \left(\frac{\partial \eta_k}{\partial y_l} - \alpha_{kl} \right) d\Theta$$

$$\langle b_i \rangle = \frac{1}{|\Theta|} \int_{\Theta} b_i d\Theta$$

and

$$\langle \alpha_{kl} \rangle = \langle C_{ijkl} \rangle^{-1} \langle \beta_{kl} \rangle$$

Hence the constitutive relation in terms of homogenized effective properties and average quantities can be written as

$$\langle \sigma_{ij} \rangle = \langle C_{ijkl} \rangle \left(\langle e_{kl} \rangle - \langle \alpha_{kl} \rangle \Delta T \right)$$

Appendix-C

(i)

Considering elastic problem (equation 6.1)

$$\int_V (\sigma_{ij,j} + \rho F_i - \rho \ddot{u}_i) \delta u_i dv = 0$$

or
$$\int_V \sigma_{ij,j} \delta u_i dv + \int_V \rho F_i \delta u_i dv - \int_V \rho \ddot{u}_i \delta u_i dv = 0$$

Applying integration by parts on the first term, we obtain

$$\int_V (\sigma_{ij} \delta u_i)_{,j} dv - \int_V \sigma_{ij} \delta u_{i,j} dv + \int_V \rho F_i \delta u_i dv - \int_V \rho \ddot{u}_i \delta u_i dv = 0$$

Implementing Gauss divergence theorem, we get

$$\int_S \sigma_{ij} \delta u_i n_j ds - \int_V \sigma_{ij} \delta u_{i,j} dv + \int_V \rho F_i \delta u_i dv - \int_V \rho \ddot{u}_i \delta u_i dv = 0$$

or
$$\int_S (\sigma_{ij} n_j) \delta u_i ds - \int_V \sigma_{ij} \delta u_{i,j} dv + \int_V \rho F_i \delta u_i dv - \int_V \rho \ddot{u}_i \delta u_i dv = 0$$

or
$$\int_S \hat{p}_i \delta u_i ds - \int_V \sigma_{ij} \delta u_{i,j} dv + \int_V \rho F_i \delta u_i dv - \int_V \rho \ddot{u}_i \delta u_i dv = 0$$

or
$$\int_V \sigma_{ij} \delta u_{i,j} dv = \int_S \hat{p}_i \delta u_i ds + \int_V \rho F_i \delta u_i dv - \int_V \rho \ddot{u}_i \delta u_i dv$$

Similarly, for the heat transfer problem (equation 6.7)

$$\int_V (-q_{i,i} + \rho R - \rho c \dot{\theta}) \delta \theta dv = 0$$

or
$$-\int_V q_{i,i} \delta \theta dv + \int_V \rho R \delta \theta dv - \int_V \rho c \dot{\theta} \delta \theta dv = 0$$

applying integration by parts on the first term

$$-\left(\int_V (q_i \delta \theta)_{,i} dv - \int_V q_i (\delta \theta)_{,i} dv \right) + \int_V \rho R \delta \theta dv - \int_V \rho c \dot{\theta} \delta \theta dv = 0$$

Implementing Gauss divergence theorem

$$-\left(\int_S q_i \delta \theta n_i ds - \int_V q_i (\delta \theta)_{,i} dv \right) + \int_V \rho R \delta \theta dv - \int_V \rho c \dot{\theta} \delta \theta dv = 0$$

or
$$-\left(\int_S (q_i n_i) \delta \theta ds - \int_V q_i (\delta \theta)_{,i} dv \right) + \int_V \rho R \delta \theta dv - \int_V \rho c \dot{\theta} \delta \theta dv = 0$$

or
$$-\left(\int_{S_1} \hat{q}_n \delta \theta ds + \int_{S_2} h(\theta_w - \theta_\infty) \delta \theta ds - \int_V q_i (\delta \theta)_{,i} dv \right) + \int_V \rho R \delta \theta dv - \int_V \rho c \dot{\theta} \delta \theta dv = 0$$

or
$$\int_V q_i (\delta \theta)_{,i} dv + \int_V \rho R \delta \theta dv = \int_{S_1} \hat{q}_n \delta \theta ds + \int_V \rho c \dot{\theta} \delta \theta dv + \int_{S_2} h(\theta_w - \theta_\infty) \delta \theta ds$$

(ii)

Term wise FE discretization in elastic problem (equation 6.12)

$$\begin{aligned}\int_V \sigma_{ij} \delta u_{i,j} dv &= \int_V (C_{ijkl} e_{kl} - C_{ijkl} \alpha_{kl} \theta) \delta u_{i,j} dv \\ &= \int_V ([D][B^d]^T \{u_i^{(n)}\} - [D]\{\alpha^{(e)}\}\theta) [B^d]^T dv \\ &= \int_V [B^d][D][B^d]^T dv \{u_i^{(n)}\} - \int_V [B^d][D]\{\alpha^{(e)}\}[N^\theta]^T dv \{\theta^{(n)}\} \\ \int_S \hat{p}_i \delta u_i ds &= \int_S \{\hat{p}_i\}^T [N^d]^T ds = \int_S [N^d] \{\hat{p}_i\} ds \\ \int_V \rho F_i \delta u_i dv &= \int_V \rho \{F_i\}^T [N^d]^T dv = \int_V \rho [N^d] \{F_i\} dv \\ \int_V \rho \ddot{u}_i \delta u_i dv &= \int_V \rho [N^d]^T \{\ddot{u}_i^{(n)}\} [N^d]^T dv = \int_V \rho [N^d][N^d]^T \{\ddot{u}_i^{(n)}\} dv\end{aligned}$$

Term wise FE discretization in thermal problem (equation 6.13)

$$\begin{aligned}\int_V q_i (\delta \theta)_{,i} dv &= \int_V (-k_{ij} \theta_{,j}) (\delta \theta)_{,i} dv \\ &= - \int_V ([k][B^\theta]^T \{\theta^{(n)}\}) [B^\theta]^T dv \\ &= - \int_V [B^\theta][k][B^\theta]^T dv \{\theta^{(n)}\} \\ \int_V \rho R \delta \theta dv &= \int_V \rho \{R\}^T [N^\theta]^T dv = \int_V \rho [N^\theta] \{R\} dv \\ \int_{S_1} \hat{q}_n \delta \theta ds &= \int_{S_1} \{\hat{q}_n\}^T [N^\theta]^T ds = \int_{S_1} [N^\theta] \{\hat{q}_n\} ds \\ \int_V \rho c \dot{\theta} \delta \theta dv &= \int_V \rho c [N^\theta]^T \{\dot{\theta}^{(n)}\} [N^\theta]^T dv = \int_V \rho c [N^\theta][N^\theta]^T dv \{\dot{\theta}^{(n)}\} \\ \int_{S_2} h(\theta_w - \theta_\infty) \delta \theta ds &= \int_{S_2} h(\theta_w - \theta_\infty) [N^\theta]^T ds = \int_{S_2} [N^\theta] h(\theta_w - \theta_\infty) ds\end{aligned}$$

List of publications

1. **Zahid M**, Sharma R, Bhagat AR, Abbas S, Yadav A and Mahajan P. Micro-Structurally Informed Finite Element Analysis of Carbon/Carbon Composites for Effective Thermal Conductivity. Composite Structures, DOI: <https://doi.org/10.1016/j.compstruct.2019.111221>
2. **Zahid M** and Sharma R. Thermal Shock resistance of 4D-inplane carbon/carbon composite based on microstructurally informed effective properties. Materials Today Communications, DOI: <https://doi.org/10.1016/j.mtcomm.2020.101637>
3. **Zahid M**, Sharma R and Bhagat AR. Realistic microstructure based two scale finite element analysis of 3D C/C composite for effective thermal expansion coefficient. International Journal of Advances in Engineering Sciences and Applied Mathematics. DOI: [10.1007/s12572-020-00272-8](https://doi.org/10.1007/s12572-020-00272-8)
4. **Zahid M**, Sharma R, Bhagat AR and Priyanka K. Image based numerical modelling for effective thermo-elastic property of 4D Carbon/Carbon composite at high temperature. Composite structures. (**Under revision**)
5. **Zahid M**, Sharma R, Bhagat AR, Abbas S and Mahajan P. Microstructure based thermal expansion coefficient of 3D C/C composite. Proceedings of 4th Indian Conference on Applied Mechanics-2019(725-728), IISc Bangalore.

Author's Biography

Mohammad Zahid was born on 14th January of 1990 in Patna, the capital city of Bihar, India. He started his journey of education from Madrasa where he learned and hifz (memorize) the Holy Quran. Later, he completed his higher secondary level education in science stream. He completed his Bachelor of Technology (B.Tech) in Mechanical Engineering in 2012 from Maulana Azad College Of Engineering and Technology (MACET), Patna (Bihar) achieving the highest marks in college. He went to the Indian Institute of Technology (IIT (ISM)) Dhanbad, Jharkhand, India for his Post graduation (M. Tech) in Mechanical Engineering (with specialization in machine design) in the session 2014-16. During this period, he got motivation for research in composite materials and structures. Later he joined IIT Mandi, Mandi, Himachal Pradesh, India as a Research Scholar in School of Engineering in August-2016.